

Hydrocarbon Seeded ABS - Nitrous Hybrid Engine Development

Experimental Validation of an Analytical Design Tool

R. Wubben

MSc Aerospace Engineering
AE5810 Thesis Space



Hydrocarbon Seeded ABS - Nitrous Hybrid Engine Development

Experimental Validation of an Analytical Design Tool

by

R. Wubben

to obtain the degree of Master of Science
at the Delft University of Technology,
to be defended publicly on Tuesday July 5, 2022 at 9:30 AM.

Student number: 4469100
Project duration: November, 2021 – July, 2022
Thesis committee: Dr. B. V. S. Jyoti, TU Delft, Supervisor
Prof. Dr. E. K. A. Gill, TU Delft, Chair
Dr. ir. W. van der Wal, TU Delft, Examiner

An electronic version of this thesis is available at <http://repository.tudelft.nl/>.

Preface

With this thesis work, the past 7 years of studying have come to an end. A large part of which I spent in the student rocketry society Delft Aerospace Rocket Engineering (DARE) where I have had the chance to build and test small rockets, a hydrogen-oxygen spark torch igniter, an ethalox liquid engine and a variety of nitrous oxide based hybrid engines ranging from 40N to 26kN. Without all the lessons I have learnt at DARE over these years this thesis would not have been possible. I have really come to appreciate the support in the society where knowledge is selflessly passed on to the next generation, making sure everyone gets a chance to learn and grow in the field of small rocket systems and, if interested, can boost the start of their career in the space industry. In the end, the intrinsic motivation that is brought out in students by DARE is the reason for the start of this thesis. The inherent challenge in designing propulsion systems and the fine balance between, high pressures, temperatures, heat fluxes and the material properties is the only thing keeping the engine from failing, making it such a challenging environment. Experimental engine test campaigns are known for their failure intolerance. Getting 99% right will more often than not be insufficient for a successful result, but making mistakes is ultimately the only way to succeed. Apart from unintentional cold flows (read misfires), explosions are thus simply a part of rocket science and they will have to be dealt with. As a fellow safety officer in particular it is the most rewarding feeling when you can sit back and enjoy the show while knowing all the precautions to fail safely have worked flawlessly (though reflection is always essential to keep improving).

First of all I would like to thank my supervisor, Jyoti for all her support throughout the project and the freedom she provided to let the project develop itself. The scope of the project has been broad and without nudges in the right direction by Jyoti the final result would not have been the same.

Second of all, the team members of project Chimera (Franco, Jesse Martijn, Moana, Oszkar, Roderick and Thijmen) have been an enormous help. While most of them were still learning the ropes of testing rocket propulsion systems they have made really large steps in a small amount of time. They quickly took their responsibility and ownership of their work. Without their help this thesis would never have the amount of valuable data that has been fundamental to the final result. An honourable mention goes out to Andrew for setting up the work spaces in the Aircraft Hall as otherwise no machines would have been available to DARE in the transition from the Dreamhall.

Furthermore, none of the tests could have been executed without safety officers so my thanks go out to Nathaniel Stebbins Dahl, Francesca van Marion, Jonathan Neeser, Dion van Strijconck and Jeije van den Wijngaart for being present at the multitude of tests. Jeije also has been a great help with developing the data acquisition system and in general helped raising the quality of the work by the interesting discussions we had throughout the project.

Also a big thank you goes out to the TU Delft staff that have helped out throughout the project. Fred Bosch and Viktor Horbowiec for their help in the Aircraft Hall during the production of the components and setting up or improving production plans. Johan Bijleveld en Marlies Nijemeisland for their support in the investigation of the ABS material properties and making use of the lab equipment. Bart Hoek for his guidance in using the bomb calorimeter. Also the team at Logistics and Environment (L&M) for allowing us to use their facilities, letting us borrow their gas regulators (for extended periods of time) and storing our gas bottles.

Finally, these past 8 months would not have been successful without the support I received my parents, brother, friends and family while I was pouring hours and hours in this research as well as the projects in the years before. Especially towards the end with the time pressure of writing up the results I would like to thank my partner for her patience as 7 years of studying have come to a satisfying end.

*R. Wubben
Delft, June 2022*

Executive Summary

This thesis on ABS-Nitrous Hybrid Engine Development was performed at Delft Aerospace Rocket Engineering. This topic surfaced during the development of the Stratos IV rocket, one of DARE's flagship projects. After the breakup of the Stratos III vehicle, inertial roll coupling was pinpointed to be the root cause as determined by Wubben et al. [1]. In order to battle the problem a propulsive roll control system was suggested to keep the roll rate under acceptable bounds. After the possibilities to develop a nitrous based monopropellant thruster were exhausted, the option of a restartable ABS-Nitrous hybrid was found in literature. It features a higher performance and still allows for the engine to be restarted multiple times. This study continues on the work performed for Stratos IV with the long term goal to increase the technology readiness level (TRL) for future applications, both within and outside DARE. The short term goal is to develop a validated first order analysis tool to easily generate and optimise the required geometry for a particular application. The aim is to enable future projects to use this concept by having a rapid development tool available and ready to be used. Whether this is for an engine ignition system; a satellite attitude control, orbit maintenance or orbit transfer system; a sounding rocket roll control system or main engine. A coherent set of requirements was established to support design decisions throughout the development of the full experimental test setup and engine hardware. These were separated in heritage, safety, test setup, propulsion and software requirements.

A literature study into the history of hybrid rocket systems was conducted. Student projects and university initiatives have been determined to be a perfect breeding ground where experience with these systems is gained and the technology can be further researched to further increase its TRL especially in the high thrust range. Designs have been proven to work on smaller scales up to a few tens of kN. Scaling effects together with costs are the current complicating factor, but the new space approach is facilitating new opportunities whose results will be available in the upcoming years. After all, no prohibitive technological boundaries have been encountered.

The unique properties that 3D printed ABS has make it a very suitable candidate for applications where hybrids are otherwise not usable. It features restartability with an ignition system that use no toxic propellants or explosives. This makes it a valuable alternative to HTPB or paraffin, even though performance is slightly lower. The TRL from literature is sufficiently high to implement the concept in an integrated design study.

An investigation into the propellant was conducted in order to establish the appropriate burn parameters for chemical equilibrium equations. The ratio of monomers has been evaluated using 3 different methods showing globally consistent results. More accurate results can be achieved using an AutoStepwise TGA machine. This allows for an accurate determination of the SAN-butadiene ratio and can verify FTIR based measurements. Bomb calorimetry gives the higher heating value which can be used to find the heat of formation through chemical equilibrium equations. The deviation in fuel properties is below 1%. This is deemed sufficient for the purpose of this study.

A selection of the most applicable and/or crucial sources have been included for now. The tool is made with such modularity that additional models can easily be added and interchangeably selected by the user to compare results. A very complete set of infrastructure is present within the rocket society DARE that is ready to be used for exactly this application. The results can be used by future teams to expand the body of knowledge further.

The collected data, though incomplete or anomalous at times, was of sufficient quality to use for partial validation of the tool. Values for the feed system pressures and thrust output have been proven to be within $\pm 10\%$ of the measured values. However, some of the parameters contributing to these overarching values, such as fuel and oxidiser mass flow and OF ratio show a larger deviation. This can be partially attributed to the data analysis method. The second cause may be the use of a simple regression rate model. Proper implementation of more sophisticated models may be able to capture the effects currently treated as a bulk property. This error is further increased when helical structures

are attempted to be modelled. A low ignition delay can be assured with a sufficiently low ignition mass flow and controlled conditions by shielding the system from environmental effects. Control of the grain burn profile has been achieved by adjusting the grain geometry. Due to the both large scope of the project and the fact that this study is an initialisation for further potential studies there is a multitude of aspects that can be improved upon. Either, simplifying model assumptions can be dropped or further experimental studies can be used to further develop and characterise the system. Due to how the software tool was built up from the start, many engineering models can be added. They can each be represented in a module and interchangeably used with the existing pool of models. The data collected in this study as well as the software written to model the system can be requested from the author at rolf.wubben@gmail.com for future research.

Contents

Preface	ii
Executive Summary	iv
Nomenclature	viii
List of Figures	xiv
List of Tables	xv
1 Introduction	1
1.1 Research Objective and Questions	1
1.2 Project Chimera	2
1.3 Requirements.	3
1.3.1 Heritage Requirements.	3
1.3.2 Safety Requirements	3
1.3.3 Test Setup Requirements	4
1.3.4 Propulsion Requirements	4
1.3.5 Software Requirements	5
1.4 Report Structure	5
2 Overview & History	6
2.1 Early attempts	6
2.2 New Revival	6
2.3 New Space	7
2.4 Student Projects	7
2.5 Conclusion	7
3 ABS-Nitrous Hybrid System	8
3.1 Hybrid Rocket Engine Fundamentals	8
3.2 Regression Rate	10
3.2.1 Port design	10
3.2.2 Liquefying Fuels	10
3.2.3 Oxidising Additives	11
3.2.4 Swirl Injection.	11
3.2.5 Helical Ports	12
3.3 Combustion Process	12
3.3.1 Thermochemistry	12
3.3.2 Flow Analysis	13
3.4 Combustion Instabilities & Acoustics	14
3.5 Diaphragm - Mixer	14
3.6 Oxidiser Comparison	15
3.7 Fuel comparison	16
3.7.1 Hydrocarbon seeding effect	18
3.7.2 Ignition	19
3.8 Conclusion	20
4 ABS Characterisation	21
4.1 ABS Material Structure	21
4.2 Material Specifications	22
4.3 Additives	22
4.4 FTIR.	23
4.5 Thermogravimetric analysis	25

4.6	Bomb Calorimeter	29
4.7	Heat of Formation	31
4.8	Conclusion	34
5	Chimera Hybrid Engine Simulation Software	35
5.1	Software Structure	35
5.2	Packages used	37
5.2.1	PyQt.	37
5.2.2	Combustion Equilibrium	37
5.3	Engineering Models	37
5.3.1	Tank modelling liquid nitrous	38
5.3.2	Tank modelling vapour nitrous	39
5.3.3	Injector modelling liquid nitrous	39
5.3.4	Injector modelling vapour nitrous	41
5.3.5	Saturated properties of nitrous oxide	41
5.3.6	Regression Modelling	42
5.3.7	Nozzle Modelling	44
5.4	Conclusion	44
6	Test setup	45
6.1	Engine Assembly	45
6.1.1	Injector manifold	46
6.1.2	ABS fuel grain	46
6.1.3	Nozzle Assembly	47
6.1.4	Injector configurations	48
6.1.5	Grain configurations	48
6.2	P&ID and system overview	48
6.3	Thrust bench	50
6.4	Data Acquisition	52
6.4.1	IFM pressure sensors	53
6.4.2	Load cells	53
6.4.3	Thermocouples	54
6.4.4	Piezoelectric sensors	55
6.4.5	Ignition power	55
6.5	High voltage generator	56
6.6	LabView program	57
6.7	Conclusion	57
7	Results	58
7.1	Test Data Analysis Method	58
7.1.1	Time synchronisation	58
7.1.2	Mass flow estimate	58
7.1.3	Performance estimate	59
7.1.4	Feed system performance estimate	59
7.1.5	Output plots	60
7.2	Summary of collected test data and results	60
7.2.1	Test data summary	60
7.2.2	Hot fire data summary	61
7.3	Complications during testing	64
7.3.1	Sensor noise	64
7.3.2	Nozzles exploding	64
7.3.3	Ignition relay	64
7.3.4	Ignition data logging	65
7.3.5	Main valve opening	65
7.3.6	Misfires	66
7.3.7	Pressure sensor malfunctioning	68
7.4	Validation	68
7.4.1	Validation procedure	69

7.5	Discussion of Results	74
7.5.1	Injector effect	74
7.5.2	Discharge and flow coefficients	75
7.5.3	Nozzle Model	75
7.6	Conclusion	76
8	Conclusion and Recommendations	78
8.1	Research Conclusions	78
8.2	Recommendations for future work	80
8.2.1	ABS quantification	80
8.2.2	Regression rate modelling	80
8.2.3	Expand propellant combinations	80
8.2.4	Combustion instabilities	81
8.2.5	Scalability	81
8.2.6	Ignition properties	81
8.3	Future applications	81
	Bibliography	81
A	COTS Datasheets	86
B	Engineering drawings and production	109
B.1	Manifold	109
B.2	HV Pressfit	112
B.3	HV Connector	112
B.4	Nozzle Insert	115
B.5	Nozzle Retainer	116
B.6	ABS grain printing	120
C	CHESS	125
C.1	Installing rocketCEA	125
C.2	Example Output	126
C.3	Graphical User Interfaces	129
D	Data	132
D.1	TGA results	132
D.2	Data Analysis Output Example	134
D.3	Compilation of all test data	143

Nomenclature

Acronyms

ADC	Analog to Digital Converter
ADR	European Agreement concerning the International carriage of Dangerous Goods by Road
AMROC	American Rocket Company
BOM	Bill Of Materials
CEA	Chemical Equilibrium Applications (CEA)
CFD	Computational Fluid Dynamics
CHESS	Chimera Hybrid Engine Simulation Software
cRIO	CompactRIO
DARE	Delft Aerospace Rocket Engineering
DC	Direct Current
FDM	Fused Deposition Modeling
FIFO	First In, First Out
FPGA	field-programmable gate array
FS	Full Scale
FTIR	Fourier-transform Infrared spectroscopy
HEM	Homogeneous Equilibrium Model
HHV	Higher Heating Value
HPDP	Hybrid Propulsion Demonstration Program
LEO	Low Earth Orbit
MEOP	Maximum Expected Operating Pressure
MOSFET	Metal–Oxide–Semiconductor Field-Effect Transistor
NASA	National Aeronautics and Space Administration
NHE	Non-Homogeneous Equilibrium Model
NHNE	Non-Homogeneous Non-Equilibrium Model
NiCr	Nickel Chromium
NIST	National Institute of Standards and Technology
O/F	Oxygen-to-Fuel or Mixture Ratio
P&ID	Piping and Instrumentation Diagram
PEEK	Polyether ether ketone

R&D	Research and Development
REFPROP	Reference Fluid Thermodynamic and Transport Properties Database
RPA	Rocket Propulsion Analysis
SAN	Styrene-acrylonitrile
SPI	Single Phase Incompressible Model
TGA	Thermogravimetric Analysis
TRL	Technology Readiness Level
USA	United States of America
WECG	'Wet Explosieven Civiel Gebruik', or 'Law on Explosives for Civil Use'.

Propellants

ABS	Acrylonitrile Butadiene Styrene
GOX	Gaseous Oxygen
HDPE	High Density Poly Ethylene
HTP	High Test Peroxide
HTPB	Hydroxyl-Terminated Polybutadiene
IRFNA	Inhibited Red Fuming Nitric Acid
LOX	Liquid Oxygen
NTO	Nitrogen Tetroxide
PLA	Polylactic Acid
PMMA	Poly Methyl Methacrylate
SAN	Styrene-Acrylonitrile
TEA-TEB	Triethylaluminum-Triethylboron

Feed System

BV	Bleed valve
CGR	Compressed Gas Regulator
CGRV	Compressed Gas Regulator Valve
CV	Check Valve
DPS	Differential Pressure Sensor
DV	Dump valve
ESV	Emergency Safety Valve
FV	Fill valve
MV	Main valve
NC	Normally Closed
NO	Normally Open

PRV	Pressure Relief Valve
SV	Service valve
TC	Thermocouple
XV	Extinguisher Valve

Greek Symbols

α	Absorptivity	[-]
ϵ	Emissivity	[-]
ϵ	Expansion ratio	[-]
γ	Heat capacity ratio	[-]
μ	Dynamic viscosity	[Pa · s]
ρ	Density	[kg/m ³]
σ_b	Stefan Boltzmann constant	W/m ² K ⁴
τ	Characteristic Time	[-]

Roman Symbols

$\Delta_f H^\circ$	Heat of Formation	[kJ/mol]
\dot{m}	Mass flow	[kg/s]
\dot{r}	Regression Rate	[mm/s]
A	Amplification factor	[-]
A	Area	[m ²]
A	Optical density	[-]
a	Regression rate model scale factor	[(mm/s)/(kg/(m ² s)) ⁿ]
c	Speed of Sound	[m/s]
C_d	Discharge Coefficient	[-]
C_F	Thrust coefficient	[-]
C_f	Skin friction factor	[-]
C_p	Specific heat capacity	[J/(kg K)]
c^*	Characteristic velocity	[m/s]
f	Frequency	[Hz]
G	Mass flux	[kg/m ² s]
h	Specific Enthalpy	[J/kg]
h_v	Enthalpy of pyrolysis	[J/kg]
I_{sp}	Specific Impulse	[s]
k	Non-equilibrium Parameter	[-]
k_v	Valve flow coefficient	[-]

l	Effective throat length	[m]
n	Regression rate model burn exponent	[-]
P	Helix pitch	[m]
P	Pressure	[Pa]
Pr	Prandtl Number	[-]
Q	Volumetric flow rate	[m ³ /s]
R	Gas constant	[J/kg K]
R_c	Helix radius of curvature	[m]
$R_{c_{eff}}$	Helix effective radius of curvature	[m]
Re	Reynolds number	[-]
SG	Specific gravity	[-]
T	Temperature	[K]
V	Volume	[m ³]
x	Distance from injector	[cm]
Z	Compressibility factor	[-]

Subscripts

0	initial
b	bubble
f	fuel
hm	Helmholtz mode
l	liquid
r	residence
t	throat
v	vapour

Molecules

H_2	Hydrogen
H_2O	Water
H_2O_2	Hydrogen Peroxide
N_2	Nitrogen
N_2O	Nitrous Oxide
N_2O_4	(Di)Nitrogen Tetroxide
NO	Nitric Oxide
O_2	Oxygen

List of Figures

3.1	Typical classical hybrid propulsion system Chiaverini and Kuo [4, p 39].	8
3.2	Hybrid combustion boundary layer. Chiaverini and Kuo [4, p18].	9
3.3	Typical regression rate behaviour [6]	10
3.4	Blowing effect as a function of entrainment. Chiaverini and Kuo [4, p 26].	11
3.5	Physical processes involved in hybrid rocket combustion from Chiaverini and Kuo [4, p 46.]	12
3.6	Stream-traces and axial velocity [15, p.9]	13
3.7	Temperature field with streamlines (not to scale) [16, p.34]	13
3.8	Performance curves of selected oxidisers over a range of mixtures ratios.	15
3.9	Performance curves of selected fuels over a range of mixtures ratios.	17
3.10	Arc-path properties for unset and set fuel grains [43]	18
3.11	Initial theory based on Paschen's law [42]	18
3.12	Revised theory including char path [44]	19
4.1	Representation of the combination of ABS monomers, retrieved from ¹	21
4.2	Distribution of phases in ABS, retrieved from ²	21
4.3	Calibration curves to convert absorption to ABS component mass ratios	23
4.4	ABS sample constrained on FTIR spectrometer	24
4.5	Absorption spectrum of the analysed ABS plastic	24
4.6	Mass over temperature of an ABS sample [49]	25
4.7	TGA4000 machine	26
4.8	Samples before	26
4.9	Samples after	26
4.10	Mass over temperature of an ABS sample	27
4.11	peculiarities of mass over temperature data of an ABS sample	27
4.12	Mass over temperature of an ABS sample including Gaussian fit	28
4.13	Schematic of a bomb calorimeter retrieved from ¹	29
4.14	Bomb calorimetry test setup. Note the press to assemble benzoic acid discs for calibration purposes. On the right, the bomb water bath with brown top can be seen.	30
4.15	Contents of bomb	30
4.16	High pressure 'bomb'	30
4.17	White inert residue	30
4.18	Flow diagram to determine heat of formation.	31
4.19	Diagram showing convergence of heat of formation	32
4.20	Convergence of heat of formation of nominal case	33
4.21	Convergence of heat of formation of adjusted mass ratios case =	33
4.22	Convergence of heat of formation of adjusted HHV case	34
5.1	Software flow diagram	36
5.2	CHESS Folder Structure	37
5.3	Diagrams showing the nodes and the heat and mass transfer processes between them for classical equilibrium and non-equilibrium models [55]	38
5.4	Diagrams showing the nodes and the heat and mass transfer processes between them for the proposed model by Zimmerman [61]	38
5.5	Conceptual Injector Element Pressure History [63]	40
5.6	Example port cross sections for five different mean linear regression values from Whitmore and Walker [13]	43
6.1	Cross section of side view (left) and top view (right)	45

6.2	Manifold cross section	46
6.3	Application of silicone elastomer for temperature sensitive components	46
6.4	Initial spark	47
6.5	Formed flame	47
6.6	Final char path	47
6.7	Back view of two nozzle parts	47
6.8	Front view of two nozzle parts	47
6.9	Two injector configurations visualised in one part	48
6.10	ABS fuel grain with a straight port	48
6.11	ABS fuel grain with a helical port	48
6.12	P&ID of the test setup	49
6.13	Layout of the thrust bench including vertical sensor cable guide	51
6.14	Layout of the full test setup	51
6.15	The National Instruments cRIO-9035	52
6.16	Verification of the pressure sensors	53
6.17	Calibration of the load cells	54
6.18	Layout of the high voltage system on the back of the vertical sensor cable guide	55
6.19	Assembled High Voltage Generator	56
6.20	The diagram of the ZVS Mazzili driver [74]	56
6.21	GUI used to control the hybrid engine test setup and log data	57
7.1	Remaining nozzles and fuel grains of all 10 burns counting horizontally from left top to right bottom	61
7.2	Nozzle at the end of test 2	64
7.3	Nozzle at the end of test 5	64
7.4	Nozzle at the end of test 6	64
7.5	Snapshot of the small, subsonic pulsating flame	65
7.6	Filtered ignition voltage. Red indicates a hot fire, blue a misfire or cold flow. The numbers represent each test.	66
7.7	Weather report of the test days with wind speed given in km/h, retrieved from ¹	67
7.8	Spectrogram of the static pressure during test 21	67
7.9	Spectrogram of the static pressure during test 26	67
7.10	Performance comparison of all 8 second burns	68
7.11	Temperature comparison of all 8 second burns	69
7.12	Straight grain model comparison absolute values	70
7.13	Straight grain model comparison percentage error	71
7.14	Helical grain model comparison absolute values	72
7.15	Helical grain model comparison percentage error	73
7.16	Pre-chamber remnants of test 2	74
7.17	Fuel grains of tests 3 (left) and 4 (right)	74
7.18	Logarithmic curve fit of ignition over main flow ratio to ideal regression factor	74
7.19	Estimated valve discharge coefficient over valve pressure ratio for test 26	75
7.20	Estimated valve discharge coefficient over tank (upstream) pressure for test 26	75
7.21	Nozzle at $t = 0$	75
7.22	Nozzle at $t = 3$	75
7.23	Nozzle at $t = 4$	75
7.24	Nozzle at $t = 5$	76
7.25	Nozzle at $t = 6$	76
7.26	Nozzle at $t = 7$	76
7.27	Nozzle of hot fire 9 at end of burn	76
7.28	Visibly higher temperature during hot fire 10	76
B.1	Close up of the clamping of the manifold and alignment of the diagonal injection hole.	109
B.2	The Bridgeport mill set at a 25 degrees angle to drill two injector holes. Also note the clamping setup of the chuck.	110
B.3	Vertical clamping setup of chuck on the mill bed.	110

B.4 Sanding of the edges on a HV connector as it is clamped in a collet and suspended in a rotating center	112
B.5 Graphite dust collection setup on a lathe	115
B.6 Machining of nozzle divergent using a conical mill and custom hard stop.	115
B.7 Clock dial showing less than 10 micron misalignment over a full rotation.	116
B.8 Machining of external conical surface.	116
B.9 Bad layer adhesion	120
B.10 Small amount of layer separation	120
B.11 No layer separation	120
B.12 Ultimaker 5S 3D printer	120
C.1 Use exactly these settings that have been shown to work	125
C.2 CHESS engine properties output	126
C.3 CHESS grain cross sections output	127
C.4 CHESS nozzle cross sections output	127
C.5 CHESS species mass ratio output	128
C.6 CHESS sizing GUI	129
C.7 CHESS solving GUI	130
C.8 CHESS post-processing GUI	131
D.1 Mass over temperature of an ABS sample at 5 °C/min including Gaussian fit	132
D.2 Mass over temperature of an ABS sample at 2 °C/min including Gaussian fit	133
D.3 Mass over temperature of an ABS sample at 0.5 °C/min including Gaussian fit	133
D.4 Mass over temperature of an ABS sample at 5 °C/min with isothermal step including Gaussian fit	134
D.5 Mass over temperature of an ABS sample at 0.1 °C/min including Gaussian fit	134
D.6 Raw and filtered data comparison of test 26	135
D.7 Calculated engine performance of test 26	136
D.8 Calculated feed system performance of test 26	137
D.9 Piezoelectric data from dynamic pressure sensor, microphone and accelerometer of test 26	138
D.10 Power data of test 6	139
D.11 Spectrogram of accelerometer recording of test 6	140
D.12 Spectrogram of microphone recording of test 6	140
D.13 Spectrogram of dynamic pressure sensor recording of test 6 in the range 0-10,000Hz	141
D.14 Spectrogram of dynamic pressure sensor recording of test 6 in the range 0-50,000Hz	141
D.15 Spectrogram of chamber pressure recording of test 6	142
D.16 Performance comparison of all flows	143
D.17 Temperature comparison of all flows	144

List of Tables

3.1	Comparison of selected oxidisers combined with ABS. The source of the data is Taylor [35] unless otherwise indicated	15
3.2	Comparison of selected fuels combined with nitrous oxide	17
4.1	A collection of additives potentially used in this ABS blend.	22
4.2	FTIR results in terms of percentage weight	24
4.3	Property comparison between 1970's ABS resins and the modern Trinseo resin [52] . . .	25
4.4	Overview of the percentage contribution of 4 Gaussian curves fitted to the mass loss rate	28
4.5	Values of bomb calibration run	31
4.6	Values of ABS bomb calorimetry measurement	31
4.7	Enthalpy of formation contribution of ABS copolymers retrieved from Whitmore, Peterson, and Eilers [37]	32
4.8	Summary of inputs of heat of formation determination cases	33
4.9	Summary of outputs of heat of formation determination cases	34
5.1	Physical nitrous constants from [56]	41
5.2	Constants used in equations from [56]	42
6.1	Tank failure calculations	50
6.2	Overview of data acquisition hardware used for the Chimera test setup	52
7.1	Test data summary of all 27 tests	62
7.2	Test data summary of all 10 hotfires	63
7.3	Overview of success rate of each injector configuration both before and on the 25th of May	67

Introduction

This thesis on ABS-Nitrous Hybrid Engine Development was performed at Delft Aerospace Rocket Engineering. DARE is a student rocketry society associated with Delft University of Technology. Its main goal is to provide unique hands-on experience on rocketry systems to its members to complement the theoretical material taught at the university faculties. There are many teams with different specialities from electronics and parachutes to structures and propulsion. The team sizes range from small, long term research and development (R&D) teams to large flagship projects. This topic surfaced during the development of the Stratos IV rocket, one of DARE's flagship projects. After the breakup of the Stratos III vehicle, inertial roll coupling was pinpointed to be the root cause as determined by Wubben et al. [1]. In order to battle the problem a propulsive roll control system was suggested to keep the roll rate under acceptable bounds. After the possibilities to develop a nitrous based monopropellant thruster were exhausted, the option of a restartable ABS-Nitrous hybrid was found in literature. It features a higher performance and still allows for the engine to be restarted multiple times. It is therefore a very suitable option for roll control purposes, but it can prove to be suitable for other applications as well. Due to time constraints for a system this complex, it could not be fully developed before the launch date of Stratos IV. This study continues on the work performed for Stratos IV with the long term goal to increase the technology readiness level (TRL) for future applications, both within and outside DARE. The short term goal is to develop a validated first order analysis tool to easily generate and optimise the required geometry for a particular application. The aim is to enable future projects to use this concept by having a rapid development tool available and ready to be used. Whether this is for an engine ignition system; a satellite attitude control, orbit maintenance or orbit transfer system; a sounding rocket roll control system or main engine.

1.1. Research Objective and Questions

The research objective for this study is:

To experimentally validate a modular analytical design tool for restartable ABS-N₂O hybrid engines.

In order to reach this objective, sub-goals are required that tie in with the research questions. First the past problems with hybrid engines need to be identified to ensure there is a mitigation strategy for the issues that might come up through development and to assess why hybrids have not yet taken a firm place in the commercial market. Secondly, the performance of ABS-N₂O needs to be assessed in comparison to alternative hybrid configurations. This should prove the suitability and benefit of the technology for this application. Thirdly, if a model is to be developed it is important to quantify the propellants that are being used. Thus, in order to establish an accurate model of the fuel used in the motor two parameters need to be determined: the composition ratio of the three monomers and the heat of combustion. Both are needed for chemical equilibrium calculations that are used to estimate motor performance. The former influences the formation of certain species and their ratios, the latter mainly determines the (adiabatic) flame temperature. Since ABS plastic is a commercial product the exact composition is a trade secret and the manufacturer could not disclose any details on the ratio of the constituents. Therefore, the composition will be attempted to be determined using experimental

methods. Using these fuel parameters as an input, the next step is to collect engineering models in an easy-to-use tool. In order for the tool to be validated, its results will need to be compared to experimental data. This data has been gathered over a series of testing campaigns and allows to answer question 5: full validation of the code and the feasibility of the technical application. In order for these points to be addressed, the following research questions, grouped per sub-goal with their relevant sub-questions, require an answer:

1. Why do very few hybrid systems exist in the professional rocketry business?
 - (a) What can be learned from past initiatives?
 - (b) Is there a use case for hybrids outside of student designs?
2. How suitable is ABS-Nitrous for this application?
 - (a) How does ABS performance compare to other fuels?
 - (b) What other useful traits does ABS have?
3. Can the ABS fuel be characterised?
 - (a) Can the composition of ABS be determined with sufficient accuracy?
 - (b) Can the heat of formation of ABS be determined with sufficient accuracy?
4. Do existing equations and models offer sufficient accuracy for a preliminary design model?
 - (a) Which models of self-pressurised tanks are applicable and of sufficient accuracy?
 - (b) Which models of injector mass flow (single/two-phase) exist?
 - (c) Which models describe the hybrid engine regression rate and combustion characteristics?
5. How can the system be experimentally validated?
 - (a) What boundary conditions exist for ignitability?
 - (b) How do different options compare to promote restartability?
 - (c) How can a low ignition delay be assured?
 - (d) How do different designs compare to enable control of the grain burn profile and thrust curve?
 - (e) Can a consistent, predictable, igniter input power be achieved?

Before the answer to the questions are covered, section 1.2 will explain the context of this study within DARE. Then, based on the formulated research questions and given context, a set of requirements will be given in section 1.3. In order to then start addressing these questions, a literature study was performed. Over 300 sources for the tool, and this study in general, have been collected and sorted in a well-structured library for future reference by Wubben [2].

1.2. Project Chimera

Student rocketry teams are in the unique position where systems with high development risks can be worked on without significant consequences. Mistakes can be made that do not impact larger timelines, big budgets or shareholders. As long as the safety of everyone involved is ensured, the learning goals of the students will be fulfilled: experience the practical application of engineering theory. In particular hybrid rocket engines have a very strong use case for student teams: they are complicated enough to challenge students in topics such as feed system design, thermodynamics as well as test rig commissioning and executing operational procedures. At the same time they do not suffer the complexity of liquid rocket systems. Although they are becoming more popular in student teams as well, they come at an elevated cost of hardware and development times. With the high turnover rate inherent to student teams very few team members are involved from the beginning to the end during the development of an engine. Arguably one of the strongest aspects in a student team is being able to observe and participate in the entire design cycle of a product to increase the understanding of the full engineering process in a relatively small setting. As such, hybrids can be the perfect stepping stone to work with larger systems in the future.

In DARE however, work on experimental hybrid systems has been reduced in the society since the end of Stratos III. The Stratos IV engine had identical internals, but the casing and nozzle were improved from aluminium and graphite to carbon composite and 3D printed titanium. This meant that most of the team members learnt very well how to built this large complicated engine and analyse and improve external features greatly, but no study was pursued in the fundamental design and development of hybrid engines.

In order to reintroduce the interest in and expertise of hybrid engine development at the end of Stratos IV project Chimera was started. It's purpose is to advance the use of ABS propellant for hybrid propulsion systems in particular. There is a lot of potential for student teams specifically due to ABS' capabilities, which will be further elaborated upon in chapter 3.

So to strengthen the use case of the proposed technology, the project is set up around this study. While the team gains practical experience in testing hybrid rocket engines they work on their own design for a small rocket. The output of this thesis can be used for the project to start a detailed design. For now as the main engine of a small rocket, but in the future it may be applied to igniters or roll control systems for more advanced student systems as well. As such, the project will not be part of this study, but rather an initial attempt to get new students up to speed on the topic and lower the threshold required to get started on a design.

The benefit of starting directly after the end of Stratos IV is that the hardware used for Stratos IV project is now available and can be used for this study as well as for project Chimera later on. It does imply that the exact sizing of the system is heavily dependent on the work that was done within Stratos IV before the start of the thesis and many aspects of the system have been derived from earlier designs. These constraints are acceptable for this study as no particular size is required for the validation of the tool. It does however put limits on the size range for which the tool is validated and thus any future tests of systems can be used to strengthen the tool by increasing its validated range.

1.3. Requirements

With the project scope defined in and the research questions known a comprehensive set of requirements can be generated to guide the direction of the project and ensure its goals are reached. The requirements are split up in different sections. First of all the relevant heritage requirements from Stratos IV that have driven the sizing of the original system are collected to understand the framework in which this project has been set up. Secondly, concrete requirements for the test setup and hardware is

1.3.1. Heritage Requirements

This set of requirements was imposed by the Stratos IV project. Either from system sizing constraints due to the design envelope of the roll control system or from the testing equipment that is used .

Identifier	Requirement	Traceability
STRA-1	Four thrusters shall fit in the circumference of the Stratos IV rocket	-
STRA-2	The roll control system shall be located on the top of the nitrous tank	-
STRA-3	Each thruster shall produce an average thrust of at least 40N	-
STRA-4	The ignition power shall be below 20W	-
STRA-5	The existing 3L 'phoenix' tank shall be used as a run tank	-
STRA-6	The existing DARE thrust bench shall be used to mount the engine and testing equipment	-
STRA-7	A National Instruments cRIO shall be used for data acquisition	-
STRA-8	The system shall be small enough to be tested on the fellowship field	-

1.3.2. Safety Requirements

The single most important set of requirements are those concerning the safety of the testing personnel and spectators/bystanders in the public spaces used for testing rocket systems in Delft. Operational safety practises have a long history in DARE and are facilitated by an independent safety officer attending test campaigns. Safety design features are reviewed by the safety board before any system is allowed to be tested. This set of requirements gives an overview of the physical design aspect of implementing safety. The implementation of these requirements into the design of the system will be given in section 6.2.

Identifier	Requirement	Traceability
SAFE-1	The test shall impose no significant risk to anyone in its direct vicinity	-
SAFE-2	Operation of the rig shall be done at a distance of at least 40m	SAFE-1
SAFE-3	The primary failure mode of the thruster shall be nozzle shear out	SAFE-1
SAFE-4	The primary failure mode of the tank shall be bulkhead shear out	SAFE-1
SAFE-5	The tank shall have a pressure relief valve	SAFE-1
SAFE-6	The tank shall have a normally-open bleed valve	SAFE-1
SAFE-7	The main line shall have an emergency safety valve to independently shut down the engine	SAFE-1
SAFE-8	The emergency safety valve shall be battery powered	SAFE-7
SAFE-9	The emergency safety valve shall be manually operated	SAFE-7
SAFE-10	The emergency safety valve shall be normally-closed	SAFE-7
SAFE-11	The system shall have a means of purging the thruster with nitrogen	SAFE-1
SAFE-12	The thruster shall be confined using a shrapnel box	SAFE-1
SAFE-13	Shrapnel from the nozzle shall be contained using sandbags	SAFE-1
SAFE-14	Every hot fire test shall be supervised by an independent safety officer	SAFE-1

1.3.3. Test Setup Requirements

The test setup requirements define the hardware used to test the engine. This includes the data acquisition system

Identifier	Requirement	Traceability
TEST-1	The system shall be able to operate on an empty grass field	STRA-8
TEST-2	The system shall be controlled from a laptop at a distance of at least 40 meters	SAFE-2
TEST-3	The system shall use an engine-generator as the electric power source	STRA-8
TEST-4	There shall be no electrical connection between the high voltage system and cRIO	-
TEST-5	The system shall measure tank, injector and combustion pressure at 2500Hz	STRA-7
TEST-6	The system shall measure tank mass and thrust produced at 50,000Hz	STRA-7
TEST-7	The system shall measure vibration, dynamic pressure and sound at 100,000Hz	STRA-7
TEST-8	The system cabling shall be organised on a vertical cable guide	-
TEST-9	The vertical cable guide shall be detachable from the thrust bench	STRA-6
TEST-10	The system shall use an Arduino to measure the ignition voltage, input voltage and input current	TEST-4
TEST-11	The Arduino shall log its measurements to an SD card at over 400 Hz	TEST-10

1.3.4. Propulsion Requirements

The propulsion requirements define aspects of the engine internals this includes propellant and material selection as well as re-usability.

Identifier	Requirement	Traceability
PROP-1	The thruster shall use ABS as its fuel	-
PROP-2	The thruster shall use nitrous vapour as its oxidiser	STRA-2
PROP-3	The thruster shall use the hydrocarbon seeding effect for ignition	-
PROP-4	The thruster shall have an internal diameter of 40mm	STRA-1
PROP-5	The nozzle shall withstand the operating conditions of the thruster for at least 16 seconds	-
PROP-6	The nozzle shall be made of graphite	PROP-5
PROP-7	The thruster internals shall be replaceable within 30 minutes	-
PROP-8	The manifold shall be reusable	PROP-7
PROP-9	The nozzle retainer shall be reusable	PROP-7
PROP-10	The engine casing shall be reusable	PROP-7

1.3.5. Software Requirements

The software requirements have been broken up in two parts. First of all, the user requirements are defined. As the tool is intended for future use it needs to be intuitive and easy to use. Secondly, the functional requirements are listed. They define the capabilities of the software in the background.

Identifier	Requirement	Traceability
USER-1	The software shall be usable without knowledge of the source code	-
USER-2	All input parameters shall be editable by the user in the form of a GUI	-
USER-3	No variables shall be hard coded	-
USER-4	All in- and outputs shall be able to be saved by the user	-
USER-5	All in- and outputs shall be able to be loaded by the user	-
USER-6	The calculated system parameters shall be able to be overridden manually by the user	-
USER-7	The software shall visualise the generated preliminary design	-
USER-8	The tank pressure shall be able to be overwritten by an external file	-
USER-9	The ambient pressure shall be able to be overwritten by an external file	-
USER-10	The user shall be able to set termination criteria for the simulation	-
USER-11	The user shall be able to set the discretization of the grain length	-
USER-12	The user shall be able to set the discretization of time of the simulation	-
USER-13	The user shall be able to select which outputs to plot	-

Identifier	Requirement	Traceability
FUNC-1	The software shall be entirely open source	-
FUNC-2	The software shall make use of open source packages only	-
FUNC-3	The software shall generate a preliminary design based on the user's input parameters	-
FUNC-4	The software shall evaluate system performance over time	-
FUNC-5	The software shall incorporate at least two modular engineering models for the tank, injector and combustion process	-
FUNC-6	The software shall model liquid or vapour nitrous to be stored and/or drained from the tanks	FUNC-5
FUNC-7	The software shall model straight port hybrid engine	FUNC-5
FUNC-8	The software shall model helical port hybrid engine	FUNC-5
FUNC-9	The software shall output relevant system parameters in a csv	-
FUNC-10	The software shall output relevant system parameters in the form of graphical plots	-
FUNC-11	The software shall be able to compare data between runs and experimental values	-
FUNC-12	The software shall be able to log the exhaust products over time	-

1.4. Report Structure

As mentioned in section 1.1 each research question is addressed in it's own part of the report. First of all, question one will be addressed by summarising the history of hybrid rocket engines in chapter 2. Secondly, the ABS-N₂O technology and it's applicability will be discussed in chapter 3 as per question two. Thirdly, an investigation into the propellant properties of ABS will be described in chapter 4. It covers the structure, composition and the determination of the heat of formation and thus provides the answer to research question three. Question four is answered in chapter 5. It describes the software used to model the system and gives an overview of the structure: which packages have been used, how have the python files been organised and what does the software flow diagram look like. Then the engineering models used are elaborated upon and the software's sensitivity is tested. The following two chapters document everything surrounding the rocket engine's testing campaign. chapter 6 presents the setup that was used in terms of hardware and software. This includes the different configurations that have been tested together with the common engine internals. Lastly, the results are presented and discussed in chapter 7. With all five research questions covered, chapter 8 provides the conclusion of the work performed under this thesis.

2

Overview & History

Hybrid rocket engine technology has been employed by many different parties for many different reasons throughout history. Generally speaking, the most successful applications have been in student teams or smaller projects as the simplicity of the system is attractive compared to a liquid and the performance benefits of a hybrid over a solid motor tend to justify the slight increase in complexity. However, other projects have existed over the years as well and their technology and success rate are discussed in this chapter to serve as a source of lessons learned. Please note that a lot of cases have been left out in order to keep this chapter concise and focus on the key takeaways. Please consider the indicated sources for a more complete overview.

2.1. Early attempts

The usage of hybrid engines has been described and tested since 1920 according to Oiknine [3]. Many different propellant combinations have been tried, mostly in the USA and Europe. The tests were experimental in nature and no real commercial application was being considered. The interest in hybrids was however revived in the mid 80's for two reasons. The first was the expectation of a huge commercial satellite market. With low-cost launchers being required to fill the market hybrids soon surfaced to be a potential low cost alternative to traditional liquid engines. The second reason was the Space Shuttle Challenger fatal accident of 1986. NASA commissioned several design teams to investigate the idea to replace the Space Shuttle's external solid rocket boosters by Hybrid Space Shuttle Boosters as an inherently safer option compared to the solid boosters. AMROC was one of the significant players for the time. In 1989 they attempted the launch of their SET-1 rocket. Moisture had frozen the main valve, however and thus it failed to lift off. As far as AMROC could tell, all other systems behaved nominally [4, Chapter 14]. However, the launch failure in combination with the death of their founding president George Koopman months earlier meant the end for the program. Similarly, the feasibility studies on hybrid booster replacements for the space shuttle were conducted, but never implemented as they were ultimately rejected after a more advanced solid rocket motor concept was pursued [4]. A similar concept was suggested by AMROC in 1992 when they investigated upgrading the strap-on boosters of the Titan and Delta rockets. No designs were actually pursued in the end.

2.2. New Revival

In the late 90's and beginning 00's the interest in hybrids increased again. In research the benefit of liquefying fuels was first explained in 1995. This will be elaborated upon in subsection 3.2.2. The effect was a regression rate of 3-5 times higher as for classical hybrids. This allowed for the construction of larger hybrids without the necessity of the more complex multiport design, with all the complications that follow. In the mean time NASA ran the Hybrid Propulsion Demonstration Program 250K Hybrid Motor [5]. The results with a 250,000 pound vacuum thrust HTPB-LOX hybrid were very promising, but some additional work was required. Two engines were built. The first one only fired for 8 seconds and the second engine went through 3 burns. The first motor had a passive design which resulted in unstable operation. The instabilities were countered by introducing a heat source, 2 small GOX hybrid engines, into the head end of the motor to aid in vaporise the incoming LOX to stabilise the combustion

process. This mostly worked, but so far could not stabilise the motor for the full 80 second burn time. On the commercial side work had started based on the previous efforts of AMROC. In 1997 SpaceDev Company was founded after acquiring their technology rights. They developed a hybrid motor for SpaceShipOne of Scaled Composites. As expected from this hand down of technology, they used a classical hybrid design using HTPB as fuel. However, they used nitrous oxide instead of LOX for practical purposes. In 2003 SpaceShipOne made it's first powered flight and in 2004 it performed the first commercial astronaut flight over 100km. Although it was very successful, the vehicle did undergo anomalous behaviour such as a high roll rate and chugging of the engine. Again, these are signs that hybrid engines have many applications, but require additional work to make them function reliably and consistently. Scaled Composites' SpaceShipOne was the basis for SpaceShipTwo that is used by Virgin Galactic for the purpose of space tourism today[3].

2.3. New Space

With the dawn of the new space age, a new opportunity for hybrids has emerged. RocketLab has proven the feasibility of a small satellite launcher that is commercially viable. Over the world new small launchers are being developed that intend to take a share of the market by abandoning the old space approach. This approach included long timelines at large scales with high budget, performance and development risk. Instead they develop small options cheaply and accept a failure rate and slightly lower performance, that allows for a much quicker development time and reduced costs. An example of this is Hyimpulse. They are a small launch vehicle start-up from Germany. Their members carry experience from the HEROS student rockets and are now scaling up their engines. They have so far tested a 75kN paraffin LOX hybrid engine. Another example is Gilmour space, based in Australia. They also intend to use the hybrid engine as an affordable option to launch to LEO ¹. A last example is the Nucleus rocket from the Norwegian company Nammo. It runs on HTPB and hydrogen peroxide producing 30kN of thrust ².

2.4. Student Projects

Nowadays, many student rocketry teams working on hybrid engines exist all around the world. Some teams who have developed relatively large hybrid rockets are Stanford with their Peregrine Hybrid, CNES with the Perseus rocket, HyEnD with their HEROS rockets and DARE with the Stratos rockets. This is far from a complete list, these are just the largest and well-known hybrid rocket projects. Hybrid rockets tend to be popular due to their relative simplicity. This is especially the case when nitrous oxide is used as the oxidiser as a decent performance can be achieved without adding a separate tank for a pressurant gas. In addition, hybrid rocket engine fuels tend to be far more benign next to a solid motor with comparable performance. HDPE, PMMA, HTPB, paraffin and sorbitol have been used most frequently and all do not pose major health concerns. This means it is safe for students to work with the materials and the budget remains relatively low since no special licenses or facilities are required.

2.5. Conclusion

While commercial ventures have been unsuccessful in the past, more and more companies are getting in the business of large hybrid motors. New space is reopening the opportunities seen in the 80's that could allow for smaller scale systems to find their way into the space business as well. After all, no prohibitive technological boundaries have been encountered. Large hybrids do have complications with regards to stability, but promising results have followed after attempting fixes. In the mean time all the student projects and university initiatives are a perfect breeding ground where experience with these systems is gained and the technology can be further researched to further increase its TRL especially in the high thrust range. Designs have been proven to work on smaller scales up to a few tens of kN. Scaling effects together with costs are the current complicating factor, but the new space approach is facilitating new opportunities whose results will be available in the upcoming years. The hybrid engine developed for this study is of a scale small enough not to have to deal with the complications of costs. Also, there is a large body of knowledge available from student efforts at this scale. The lessons learned from this chapter would be mainly important for potential up-scaled versions of the concept.

¹<https://www.gspacetechnology.com/>

²<https://www.nammo.com/product/nucleus-sounding-rocket/>

ABS-Nitrous Hybrid System

This chapter gives an overview of hybrid rocket engine fundamentals and goes more in-depth on the combustion and regression mechanisms in a hybrid rocket engine in sections 3.2 and 3.3. The ABS-nitrous propellant combination is compared to common current propulsion configurations in sections 3.7 and 3.6.

3.1. Hybrid Rocket Engine Fundamentals

In this section the fundamentals of hybrid rocket engine technology are laid out as an introduction before the ABS-N₂O concept is discussed in detail. From top to bottom (left to right on Figure 3.1) a hybrid propulsion system consists of the following:

- A **pressurisation system** to pressurise the tank and push the liquid propellant, usually the oxidiser, out of the tank
- An **oxidiser tank** that stores the propellant, usually at a relatively high pressure.
- **Valve and feed system** between the tank and the engine. Optionally this section can contain a turbopump in order to allow for a higher combustion pressure and reduced tank pressure and thus dry mass.
- **Injector** element that introduces the fluid into the chamber. A variety of patterns can be used.
- An **ignition system** to start the combustion process. These are often pyrotechnics for hybrid systems.
- A **pre-combustion chamber** where the spray from the injector is expanded. It also contains room for vortices that can aid in dampening out combustion instabilities.
- The **fuel grain & port** comprise the bulk of the combustion chamber. The oxidiser flow travels through the port(s) and regresses the fuel outwards
- The **post-combustion chamber** is the area just before the nozzle where the fuel grain ends. Here some additional mixing takes place before the combustion products are expelled. A diaphragm/mixer may be implemented to increase the turbulence and residence time of the flow to allow for more complete combustion at the cost of increased system mass.
- A **nozzle** that expands and accelerates the flow outwards, thereby generating thrust.

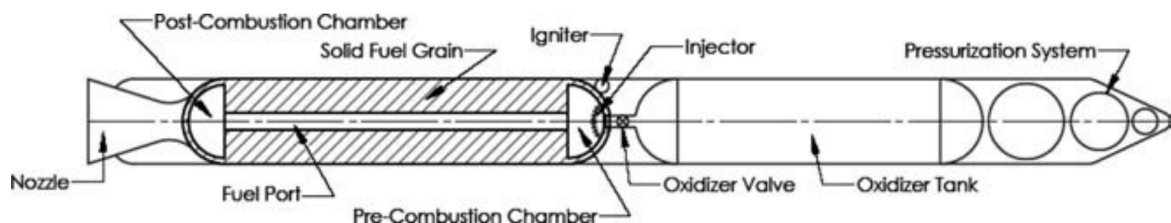


Figure 3.1: Typical classical hybrid propulsion system Chiaverini and Kuo [4, p 39.].

A major advantage of hybrid propulsion is the safety of the system. The fuel and oxidiser are stored separately and thus operational safety is hugely improved over solid rocket motors. The danger of cracks is also significantly smaller as the surface area will only burn where an oxidiser is present, which is in the grain port. A crack may result in a thermal failure of the wall, but that event is still far less explosive as the result of a crack in a solid motor grain. In addition, it does not have the sensitivity to temperature that solid motors are subject to. All these features significantly reduce the development cost of a hybrid system. Lastly, as the fuel regression rate is coupled to the oxidiser flow through the port, throttling can be achieved by simply reducing the flow rate of one liquid instead of the simultaneous throttling of two fluids in a liquid engine.

On the other hand, throttling will still cause a slight O/F shift lowering efficiency. This is also present without throttling as the fuel port keeps increasing over the burn time of the motor. However, proper design of the system can minimise the effect. Where liquid and solid rocket motors burn relatively uniformly throughout the entire chamber a hybrid rocket engine has a distinct zone where the two separate propellants mix. This zone is referred to as the flame zone and resides between the fuel surface and the oxidiser flow through the port as shown in Figure 3.2. A fuel rich boundary layer exists on the surface of the grain which transitions in to a vaporised fuel rich zone. On the other side of the flame zone a (mostly) vaporised oxidiser rich flow travels to the aft end of the chamber. The mass flow rate of oxidiser does not change over distance travelled, but more fuel will be mixed in as the flow travels. The bulk O/F will therefore shift over grain length and the final value reached at the end of the motor will determine its performance properties together with the completion of combustion which heavily depends on mixing properties in the port and post combustion chamber. This physical separation between the two propellants in the combustion process cause a performance loss compared to liquid propulsion alternatives. Within the combustion process there is another inhibiting mechanism: fuel regression rate. For hybrids this rate is relatively low meaning they require a large surface area to reach a certain specified mass flow rate. This means either a very long and slender design is required or multiple ports need to be present, both which introduce their own set of complications. However, some design features exist that can improve the regression rate.

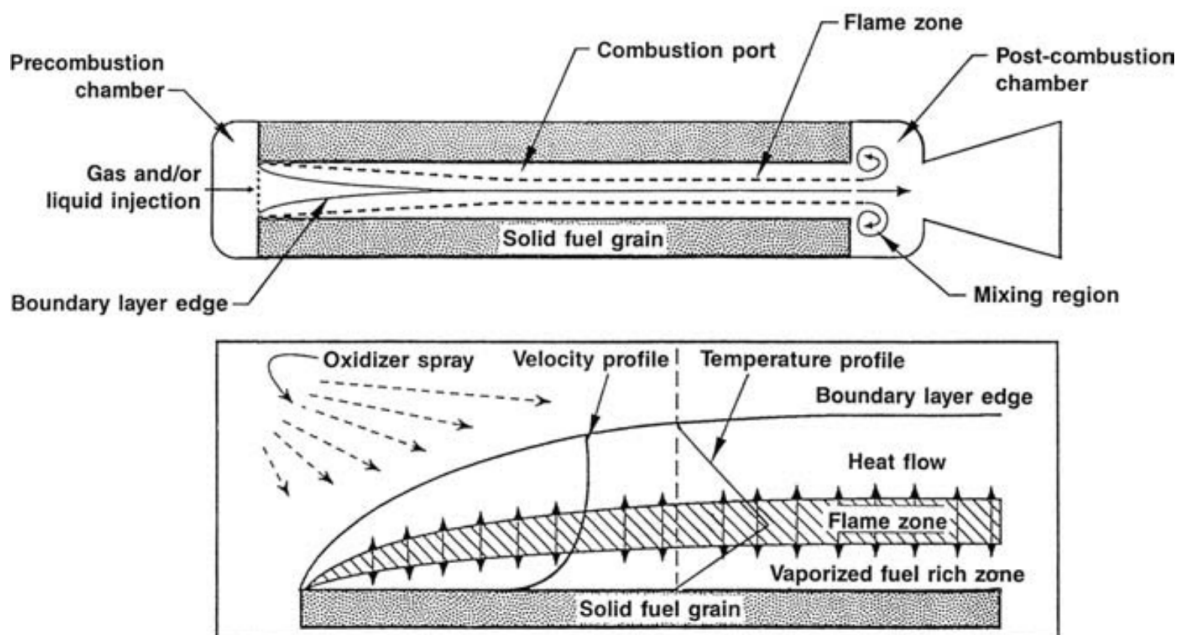


Figure 3.2: Hybrid combustion boundary layer. Chiaverini and Kuo [4, p18.].

3.2. Regression Rate

A fundamental problem with hybrids is their low regression rate compared to solid rocket boosters. The low regression rate implies a very long and slender geometry is required which can be disadvantageous for them to fit the requirements of a launch vehicle. Several options have been investigated and attempted over time. Before going into details, it is important to understand the driving mechanisms of fuel regression. Figure 3.3 shows three major regimes of regression rate that can be distinguished. In the middle range the regression rate is dominated by diffusion and it is a function of the mass flux. Convective heat transfer is the dominant mode of heat transport. When the mass flux is very high, chemical kinetics take over and regression rate becomes mainly a function of pressure. A flooding limit exists, that depends on the pressure and propellant combination, where the mass flux is so high that the flame extinguishes. When the mass flux is low, radiative heat transfer is dominant. Here the regression rate is affected by the partial pressure of emitting species and the port diameter. A lower bound exists below which the engine would be cooking. The fuel then resides in a thermal semi-molten layer for a long time. A chuffing instability can occur by the repeated mechanical removal of this melt layer [6].

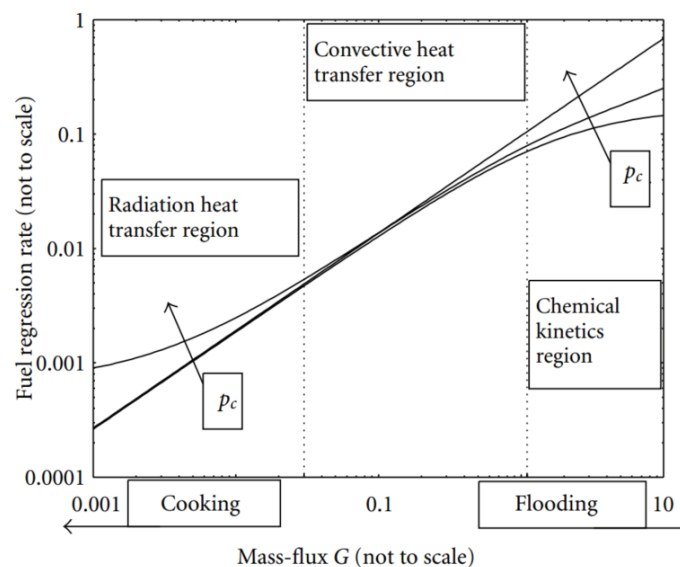


Figure 3.3: Typical regression rate behaviour [6]

3.2.1. Port design

The first and most obvious solution is the construction of multiple ports in a fuel grain. This increases the surface area of the fuel that is in contact with the oxidiser flow. However, it yields a larger empty mass as all the internal motor walls are required to remain structurally sound at burnout. Otherwise the consequence would be the fuel coming loose resulting in a highly unpredictable burning process behind of those segments as well as a risk of clogging the nozzle throat. Another difficulty that comes with this design is the production process. A complicated geometry requires a significant increase in tooling and production time, both of which drive up the cost. Lastly, there is the risk of the ports showing asymmetric burning between ports. However, as stated in Chiaverini and Kuo [4, p. 19]: "The uniformity of burning was quite remarkable, an important observation confirming the practicality of multiport fuel grains".

3.2.2. Liquefying Fuels

Another way to increase the regression rate is by using liquefying fuels. Using a traditional fuel such as HTPB brings along the problem of a very low heat transfer into the material. As the fuel burns, its surface simply ablates away giving very little time to transfer the heat from the outermost layer to the inside of the fuel grain. This is called blowing. Liquefying fuels however tend to conduct this

heat a lot faster. A thin liquid layer exists between the burning flow through the port and the solid fuel. This liquid layer keeps conducting the heat very effectively and is subjected to entrainment (liquid droplets detaching from the surface into the flow) which increases the speed of vaporisation of the fuel and thereby increases the regression rate. Fundamentally, the heat transfer reduction is correlated to blowing. Sutton and Biblarz [7, p. 737] gives a clear definition: "The blowing coefficient β is an important parameter affecting boundary layer heat transfer. It is interesting to note that, although it is defined as the non-dimensional fuel mass flow rate per unit area normal to the fuel surface, it is also a thermochemical parameter equivalent to the non-dimensional enthalpy difference between the fuel surface and the flame zone." This means that there is a fundamental link between the fuel generation and enthalpy difference between the fuel and flame zone. A high blowing coefficient causes a large reduction in heat transfer. According to Karabeyoglu et al. [8] a regression rate increase of 3 to 4 times that of classical hybrid fuels can be achieved.

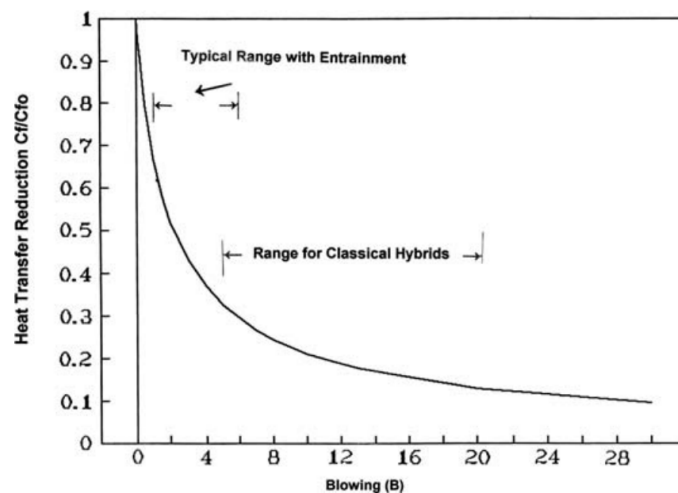


Figure 3.4: Blowing effect as a function of entrainment. Chiaverini and Kuo [4, p 26].

3.2.3. Oxidising Additives

Oxidising additives are generally metal particles such as aluminium or magnesium. They burn a lot hotter than the fuels they are suspended in and thus they aid in their melting or dissociation process. Zaseck et al. [9] tried several additives to an opposed flow burner test setup. As expected, polymeric additives decrease the regression rate. This is likely due to a viscosity increase of the liquid layer. Nano- and flake aluminium, ammonia borane, mechanically activated titanium carbon and pyrophoric titanium chromium manganese have been used with mixed the results. The latter two did increase the regression rate as they reacted or decomposed in or near the melt layer. The decomposition time of ammonia borane was too slow to see a noticeable change. For the aluminium the residence time was too low and a more relevant test setup is required. This was done by Evans et al. [10]. They compared HTPB and paraffin fuels with and without metal additives. HTPB with 13% tungsten nano-powder showed a 38% increase in regression rate. Gotzmer et al. [11] showed that the addition of 13% aluminium yields on increase of 15% in the regression rate of a paraffin nitrous hybrid. They also established a multiplication factor of 3 in the regression rate of a paraffin fuel compared to HTPB. This was raised to 4 after the addition of the aluminium powder.

3.2.4. Swirl Injection

Swirl injection is a widely used method, since it is a relatively simple feature to implement. The injector orifices are to be machined under an angle with respect to the axial and radial direction of the motor. The oxidiser is then "pushed" against the fuel grain, which has a twofold effect: the radial component of the flows velocity vector reduces the liquid layer of the fuel which increases the heat flux into the grain. Secondly, a certain amount of flow will pass by a much larger amount of fuel wall as the helical flow path is simply longer than a straight line through the grain. As shown by Pucci [12], the regression rate increased up to 38% by swirling the flow at 30°. Using swirl at 60° caused the regression rate to

increase by as much as 182%.

3.2.5. Helical Ports

A solution to achieve higher regression rates, that is particularly suitable for 3D printed grains, is the use of helical ports. The effect of helical ports with an axial injector is similar to that of a swirl injector on a straight port as explained before. Implementation is even simpler though and especially useful for smaller motors that lack the space requirements for swirl injection elements or have only one injection element. Whitmore and Walker [13] has developed an engineering model for regression rate amplification by helical ports. Two contributing factors were identified: helix induced skin friction increase and helical flow suppression of radial wall blowing. About 75% of the amplification was determined to be due to skin friction increase.

3.3. Combustion Process

The combustion process in a hybrid rocket engine is a complicated mechanism that switches its dominating physical mechanisms over different engine sizes, flow regimes and/or engine types. An overview of these mechanisms is given in Figure 3.5. It gives a very clear summary of possible mass and heat transfer locations within the hybrid combustion process. It is recommended to refer back to this overview when any of these processes are dealt with in more detail in the following sections.

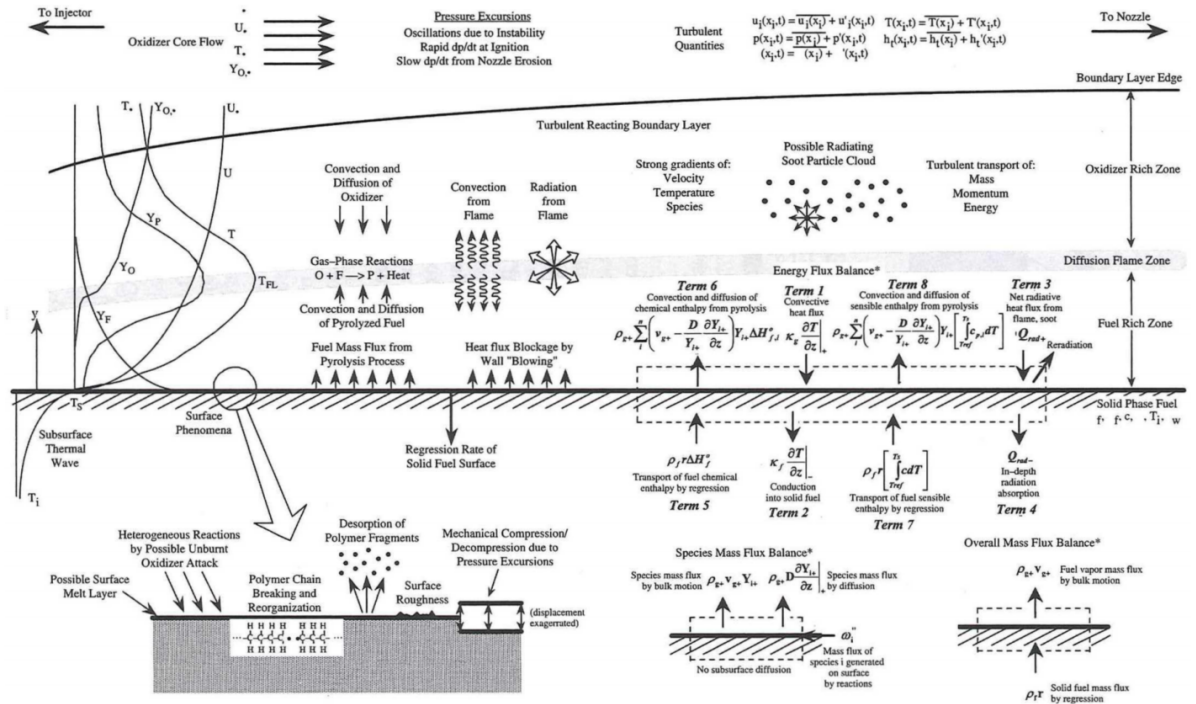
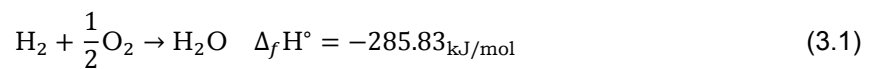


Figure 3.5: Physical processes involved in hybrid rocket combustion from Chiaverini and Kuo [4, p 46.]

3.3.1. Thermochemistry

The thermochemistry of rocket motors is well summarised by Zandbergen [14, ch. 7]. It includes, amongst others, chemical formula, reaction equations, heat of formation of species, adiabatic flame temperature calculations and chemical equilibrium equations. A very simple example will be given here to show the concept:



The standard heat of formation of the components from the elemental components are known and serve as an input. Checking the mass balance left and right (molar amounts) the heats of formation can be

used to find the heat of combustion. Taking into account phase transitions, the initial temperature and the heat capacity of the components the adiabatic flame temperature can be found. At higher temperatures or different mixture ratios these equations will become more complex as multiple species need to be taken into account such as radicals and products of partial combustion. The principle however stays the same. In the nozzle the situation is slightly different as two conditions can be taken into account: equilibrium flow or frozen flow. Equilibrium flow means that the exhaust products still react in the exhaust stream. This equilibrium reaction is caused by the steep temperature drop as the flow contracts before and is expanded after the throat. The shift in temperature will cause a shift in the ratio of species in the flow. Frozen flow means the flow does not react anymore. Temperature changes still define the gas properties, but no longer the ratio of species. A better approximation of a real nozzle is to combine both assumptions. Up and until the throat the flow can be considered to be in equilibrium as there is a sharp drop in temperature at low flow velocities. After the throat frozen flow can be assumed as the residence time goes down significantly due to the gas accelerating beyond the speed of sound. This is called Bray's approximation [14, p.138].

3.3.2. Flow Analysis

Analysing the flow in a hybrid rocket engine is key to understanding instabilities and acoustic effects as discussed in section 3.4 and the regression rates which are separately addressed in section 3.2. Evaluating flow paths in hybrid engines requires per definition at least a 2D or 2D axisymmetric mesh and Computational Fluid Dynamics (CFD) are used. For the scope of this study a CFD analysis of the hybrid is too complicated and not necessary. After all, the goal is to develop a fast and simple to use tool. The examples in this section thus serve as a resource to understand the flow field inside a hybrid. In figures 3.6 and 3.7 two examples of flow fields are given. In the left hand figure from Leccese, Bianchi, and Nasuti [15] a recirculation zone at the injector side is clearly present, even without a step change from the fuel grain in the outer geometry. It shows that the recirculation zone is a potential hot spot, depending strongly on the O/F of the local flow. This needs to be taken into account in the design of the pre-chamber, depending on the regime that the engine runs at. Daniele and Giuliano [16] go further and adjusts the injection velocity to compare the resulting flow field distributions. A secondary recirculation zone at the beginning end of the fuel can be observed, which reduces in size as the inlet velocity goes down. This is due to a high turbulence level caused by the high inlet velocity, resulting in a higher fuel concentration, and therefore temperature, in the pre-chamber as fuel goes back upstream. Finally, another vortex is expected at the end of the fuel as the flows expands from the fuel port into the post chamber. It is not as strongly present as the one near the injector as the flow velocities are significantly lower.

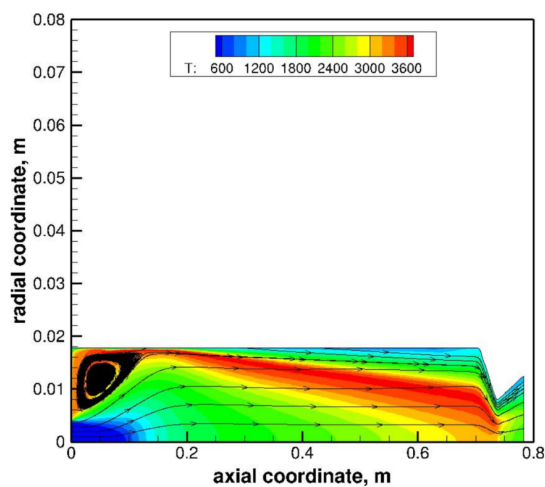


Figure 3.6: Stream-traces and axial velocity [15, p.9]

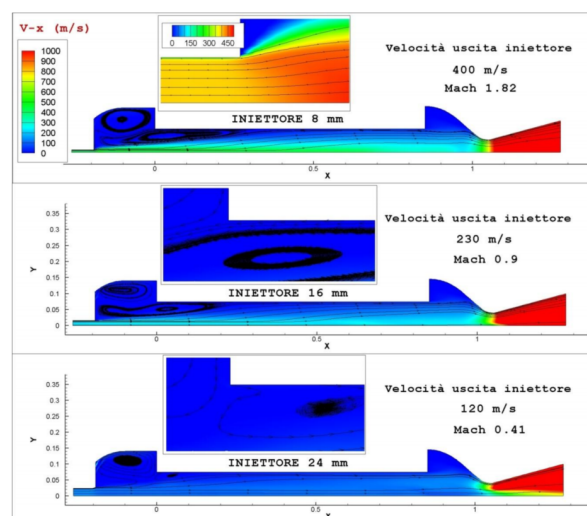


Figure 3.7: Temperature field with streamlines (not to scale) [16, p.34]

3.4. Combustion Instabilities & Acoustics

Hybrid engines are notorious for generating low frequency combustion instabilities that increase the heat flux through the walls. This can cause thermal failure of the walls in combination with the pressure spikes. There are two research groups that have paid a particular interest in investigating and attempting to model these instabilities. The first is Karabeyoglu at Stanford University. The authors worked on a range of different phenomena. In Karabeyoglu et al. [17] a linearised transient model was developed and validated using test data. The instabilities considered were related to thermal effects being: wall heat transfer blocking due to the regression rate and heat transients in the fuel as well as in the boundary layer. In De Zilwa et al. [18] 3 modes of instability were considered: a non-acoustic mode at 30Hz at the natural frequency of fuel-production oscillations triggered by vortex shedding of the oxidiser flow when expanded in the pre-chamber, the Helmholtz mode at 100Hz and a longitudinal acoustic half-wave in the chamber at 350Hz. The Helmholtz mode corresponds to a large volume terminating at a small throat and is the same as the sound a glass bottle produces when air is blown over it. The natural frequency of this phenomenon can be calculated using Equation 3.2 from De Zilwa et al. [19]

$$f_{hm} = \frac{c}{2\pi} \sqrt{\frac{A_t}{Vl}} \quad (3.2)$$

De Zilwa et al. [20] continued with this principle and established a method to determine the instantaneous, bulk averaged port diameter by measuring the Helmholtz instability. The frequency shift of this instability over time corresponds to the port diameter change due to the fuel grain regressing away. Lastly in Karabeyoglu, Stevens, and Cantwell [21] the authors investigate the low frequency combustion instabilities caused by feed system coupling. Waxman et al. [22] proposes a solution to these instabilities that have hampered the Peregrine hybrid programme for years: intentionally causing critical flow in your injector such that the mass flow is insensitive to the back pressure in the chamber, thereby removing the feed system coupled combustion instabilities. Carmicino and Pastrone from Napoli and Torino respectively [23, 24, 25, 26] had a focus on vortex shedding causing an acoustic instability. In this case vortex shedding at the end of the fuel grain, where the flow is suddenly expanded into the post combustion chamber, was considered. The vortices that are being formed can burn vigorously and may drive acoustic waves into the chamber. The authors worked on an analysis and modelling of this instability. Additional work by Akyuzlu [27] and Uddanti [28] has been performed on the topic as well. To summarise, acoustics and low to high instabilities are a well known and researched problem in hybrid rocket engines. In this study they have two applications: firstly solving issues during the development phase to identify the source of any excessive instabilities that need to be resolved and secondly they could serve as an output design parameter to warn the user of the model that the design may be prone to certain instabilities and potentially give recommendations to resolve them.

3.5. Diaphragm - Mixer

A key component to increase the efficiency in any hybrid system is the use of a diaphragm /protrusion or mixer. Both are a component that obstructs the flow of combustion gases and increases their turbulence and residence time. This obstruction can be within the grain itself, where it is called a diaphragm or protrusion, or behind the fuel in the post-chamber where it is referred to as a mixer. Both options increase mixing and the completion of combustion of the oxidiser and fuel, which is a fundamental limit of hybrids compared to solid and liquid motors. The two fuels are in a different state and are thus separated, even in the combustion process. A significant amount of work on quantifying the effect of diaphragms and mixers was done by Grosse et al. [29, 30] in Germany and Bellomo et al. [31, 32, 33, 34] in Italy. Combustion efficiency increases of 6% have been found using mixers.

3.6. Oxidiser Comparison

The most common oxidisers used for rocket engines are nitrous oxide, LOX, nitrox, nitrogen tetroxide, hydrogen peroxide and IRFNA in no particular order. Their performance is traded off together with the fuel ABS. A trade-off for all the different fuels is given later in section 3.7. Table 3.1 gives an overview of the input data for the comparison as well as the optimum O/F ratio that resulted. This is the optimum with regards to the specific impulse of the propellant combination. The analysis was performed using rocketCEA, a python wrapper of the NASA program Chemical Equilibrium Applications (CEA) [35]. The resulting plots are shown in Figure 3.8.

Table 3.1: Comparison of selected oxidisers combined with ABS. The source of the data is Taylor [35] unless otherwise indicated

Oxidiser	Components	Formula	ρ [g/cm ³]	$\Delta_f H^\circ$ [kJ/mol]	$\Delta_f H^\circ$ [cal/mol]	$(O/F)_{opt.}$
N2O	Nitrous Oxide	N2O (L)	0.780	81.450	19467.0	6.61
LOX	Oxygen	O2 (L)	1.146	-12.98	-3102.	1.98
Nitrox	Oxygen Nitrous Oxide	60% O2 (L) 40% N2O (L) [36]	0.950 [36]	43.6784	10439.4	3.46
NTO	Nitrogen Tetroxide	N2 O4 (L)	1.433	-19.56	-4676.0	3.19
HTP	Hydrogen Peroxide	H2 O2 (L)	1.407	-187.778	-44880.0	5.51
IRFNA	Nitric Acid Nitrogen Tetroxide Water Hydrogen Fluoride	H 1.57216 N 1.62945 O 4.69505 F 0.02499 (L)	1.48	-271.37	-64860.0	3.98

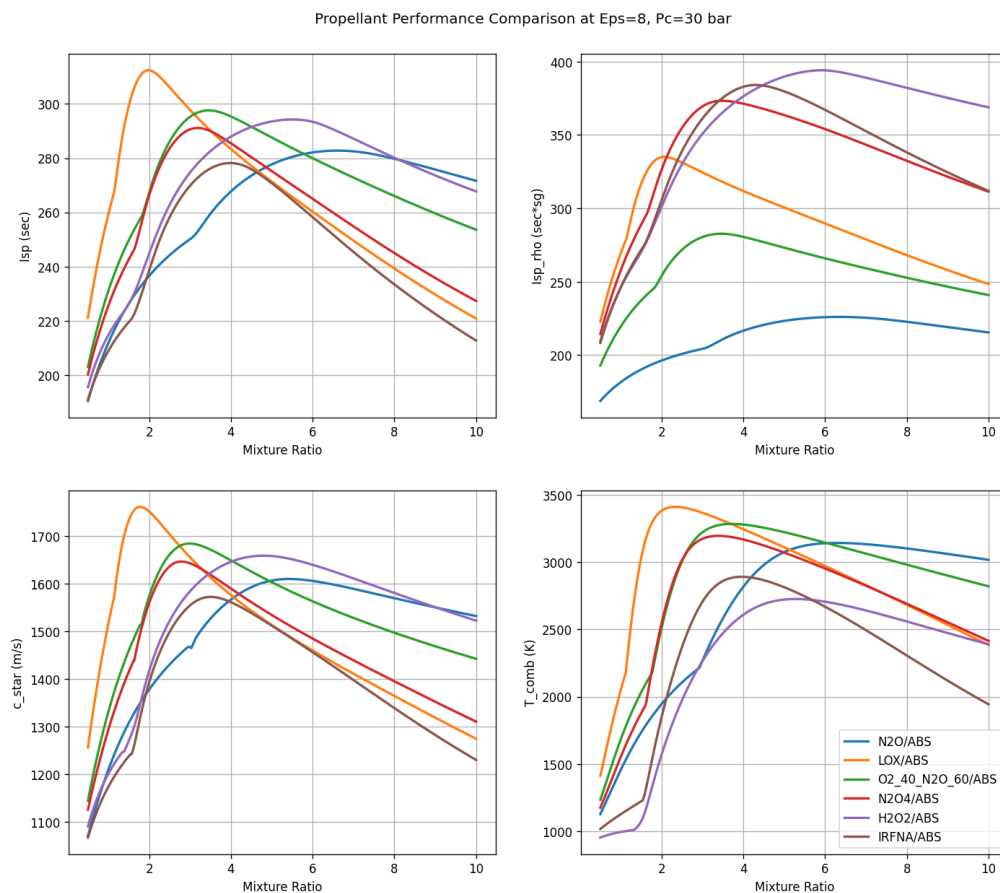


Figure 3.8: Performance curves of selected oxidisers over a range of mixtures ratios.

What stands out is the peak of the LOX curve. It is far higher and shifted further to the left. This is due to the fact that there is no part of the molecule that does not take part in the oxidation reaction. This makes its performance very mass efficient and thus also shifts the O/F ratio down.

The third on the list is Nytrox. It is a mixture between nitrous oxide and oxygen and has been described by Karabeyoglu [36]. The mixture has a combination of benefits that the separate species do not possess. The oxygen serves as the pressurising agent whereas the nitrous adds to the density while keeping a non-cryogenic operational temperature at a higher specific impulse than nitrous alone. In addition, the safety of the propellant has improved since the oxygen does not participate in the exothermic decomposition reaction of pure nitrous oxide. Some combustion behaviour benefits have also been identified such as an efficient gas phase combustion and more stable operation due to the nitrous decomposition aiding in reliable LOX vaporisation. This is similar to the small hybrid engines adding heat to the HPDP program mentioned in section 2.2. A downside is the fact that nitrous will tend have a higher concentration at the bottom of the tank, whereas the oxygen is mostly vaporised at the temperature of the mixture leaving it mostly in the top of the tank. Nytrox, as expected, sits in between the curves of nitrous and LOX. As the mixture ratio of the two is adjusted the performance curve will shift between the two pure performance curves.

The last three oxidisers are known for their density and therefore perform very well in the density specific impulse. However, of these NTO and IRFNA are highly toxic and therefore difficult to work with. In addition, they are known environmental hazards and therefore the space industry should work towards replacing these for green alternatives. HTP is good option as it features the highest density specific impulse.

From the propellants without environmental concerns only nitrous oxide and nytrox have self - pressurising properties. For this study this property is deemed crucial as it helps simplifying the system a great deal. In addition, before attempting applying a propellant in a thesis, some experience should be built with the working fluid. In order for LOX, HTP or nytrox to be considered, it is required to first build and commission test equipment that can work with these fluids. Finally, nytrox is still very experimental and additional research is required before implementing it in other designs. For example, the O/F shift over burn time, caused by the spatial distribution of the mixture, needs to be identified more accurately.

3.7. Fuel comparison

Similarly to section 3.6 for oxidisers, this section gives an overview of some common hybrid fuels and their performance with nitrous oxide. These are ABS, HTPB, paraffin, PMMA and a DARE formulation. Since there are some variations in the formulation of paraffin and HTPB, for both 2 different values were used and plotted separately. There are minor differences in the formulations of HTPB, but for the paraffin for all practical purposes the differences are negligible. The properties of the fuels considered are summarised in Table 3.2. Paraffin for it's lack of oxygen in the molecules has a very high optimum mixture ratio, followed by HTPB that has some oxygen in its terminating group. Their performance is closely followed by ABS, though it under-performs slightly in comparison. It however requires slightly less oxygen due to the presence of nitrogen in the acrylonitrile group shifting the mixture ratio further left. Even shifted further to the left are PMMA and the DARE formulation based on sorbitol. Both contain a lot more oxygen in their fuel and at the same time are a lot more dense than the alternatives. Although both, and especially the DARE propellant formulation, do not perform very well compared to the others in terms of I_{sp} , the high density of the fuel raises the volumetric specific impulse to be the highest. The DARE formulation was selected for the Stratos rockets since a constraint on the size of the oxidiser tank was present. The oxygen in sorbitol shifts the optimum O/F so far to the left that a sufficient total impulse can be achieved with the constraint in oxidiser volume available.

HTPB and paraffin marginally outperform ABS, but there are other aspects to be taken into account. For example, HTPB is not a liquefying fuel and therefore the regression rate is drastically lower than that of ABS. This necessitates the use of more complicating design features such as multiport design, swirl injection or additives for larger scale designs. If a further increase in regression rate of ABS is required this can easily be achieved by printing a helical port. This is far harder to manufacture for paraffin grains. In addition, ABS grains show a higher degree of consistency between produced grains [37, 38].

Table 3.2: Comparison of selected fuels combined with nitrous oxide

Fuel	Components	Formula	ρ [g/cm ³]	$\Delta_f H^\circ$ [kJ/mol]	$\Delta_f H^\circ$ [cal/mol]	(O/F) _{opt.}
ABS	Acrylonitrile Butadiene Styrene	C3 H3 N (S) C4 H6 (S) C8 H8 (S) [39]	1.04	98.31 32.00 63.31 [37]	23496.7 7648.18 15131.5	6.61 [35]
HTPB	Hydroxyl Polybutadiene	C7.3165 H10.3360 O0.1063 (S) [35]	0.922 [35]	-	1200.0 [35]	7.21 [35]
HTPB2	Hydroxyl Polybutadiene	C3.8462 H5.8077 O0.0385 (S) [37]	0.930 [37]	23.99 [37]	5733.74	7.24 [35]
Paraffin	Paraffin	C50 H102 (S) [40]	0.924 [40]	-1438.2 [40]	-343738	8.17 [35]
Paraffin2	Paraffin	C20 H42 (S) [41]	0.924 [40]	-594.57 [41]	-142106	8.21 [35]
PMMA	Plexiglass	C5 O2 H8 (S) [41]	1.19 [39]	-348.7 [41]	-83341.3	4.66 [35]
DARE	Sorbitol Paraffin Aluminium	80% C6H14O6 (S) [39] 10% C50H102 (S) [40] 10% Al(S)	1.49 [39] 0.924 [40] 2.7 [39]	-1353.7 [39] -1438.2 [40] 0.0	-323540 -343738 0.0	3.36 [35]

Propellant Performance Comparison at Eps=8, Pc=30 bar

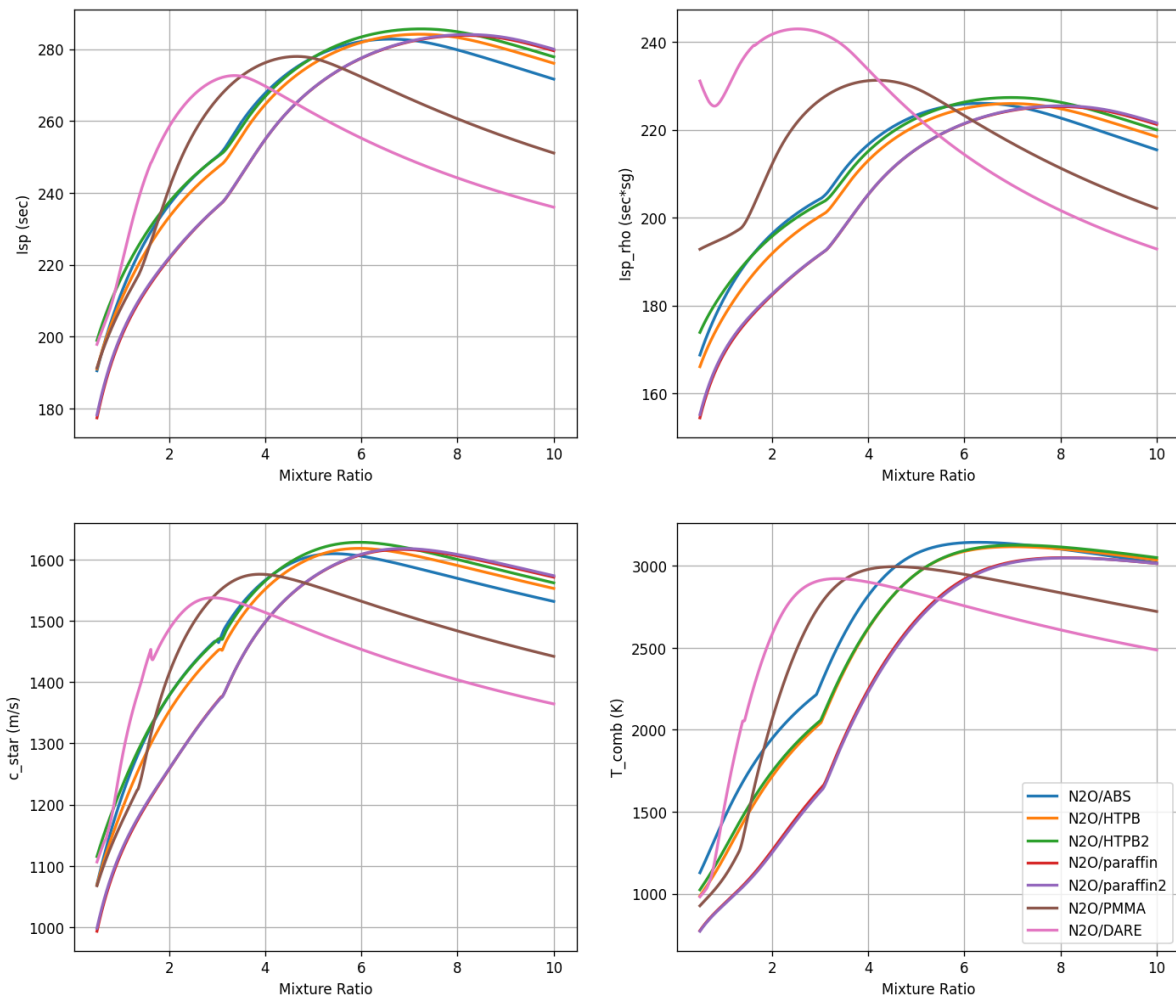


Figure 3.9: Performance curves of selected fuels over a range of mixtures ratios.

3.7.1. Hydrocarbon seeding effect

FDM processed ABS plastic has unique electrolytic breakdown properties. The effect was serendipitously discovered by Whitmore et al. [42]. When a high voltage is applied to the plastic's surface, it starts letting off smoke after an initial period of atmospheric arcing. This smoke consists of hydrocarbons that have been released from the plastic fuel in a process called pyrolysis: thermochemical decomposition of a material at elevated temperatures. This effect is shown in Figure 3.10 from Whitmore et al. [43].

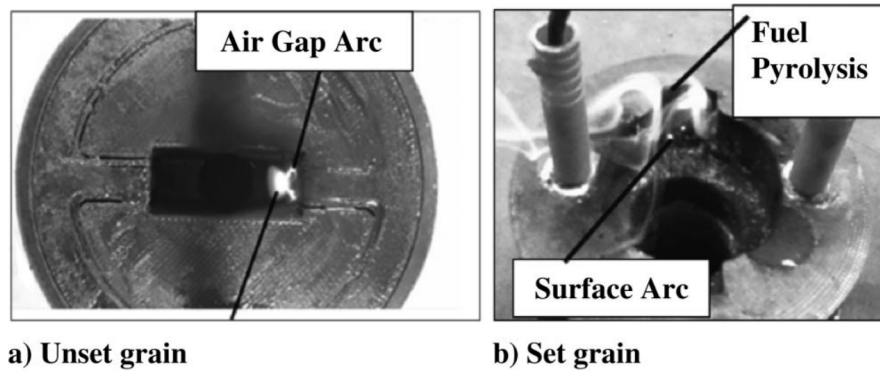


Figure 3.10: Arc-path properties for unset and set fuel grains [43]

In [42], the effect was tested using three articles: a machined extruded rod of ABS, horizontally printed ABS and vertically printed ABS. The two printed articles showed significant sparking and hydrocarbon vapour generation, but the machined ABS showed none whatsoever even at over 1kV. This indicates that the 3D printing process has a significant role in the functionality of the effect. The suggested theory explains that the ridges of the plastic layers function as micro-electrodes aiding in the electrical breakdown of the material. This effect is illustrated in Figure 3.11. The spark would follow Paschen's law that defines the electrical breakdown voltage of an insulator (such as air).

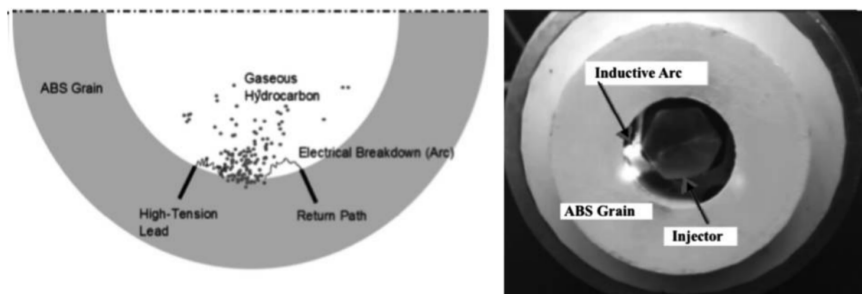


Figure 3.11: Initial theory based on Paschen's law [42]

Whitmore, Mathias, and Harvey [44] revisited the previous theory after more tests were performed. The arcs previously observed occurred at significantly lower voltages than predicted by Paschen's law. In addition, the required voltage dropped further as the grain was used more often. This is exactly the effect of the previously shown setting of a grain in Figure 3.10. Initially the arc travels through the air. This pyrolyses a small amount of fuel on the surface, a process referred to as charring. This char actually conducts very well and the spark gap drops to the surface of the fuel. This process repeats until the entire path between the electrodes has been charred as is shown in Figure 3.12. The high voltage is now fully conducted through the material and joule heating occurs that releases hydrocarbon vapours in a process called pyrolysis. In conclusion, the effect is likely a combination of Paschen's law and the electrostatic breakdown properties including charring of a weak conductor such as ABS plastic. This theory is strengthened by tests performed on PLA. Normally 3D printed PLA would not show this behaviour, but when the surface is doped in graphite it would ignite in the presence of GOX. When the graphite powder was burned away the effect stopped again.

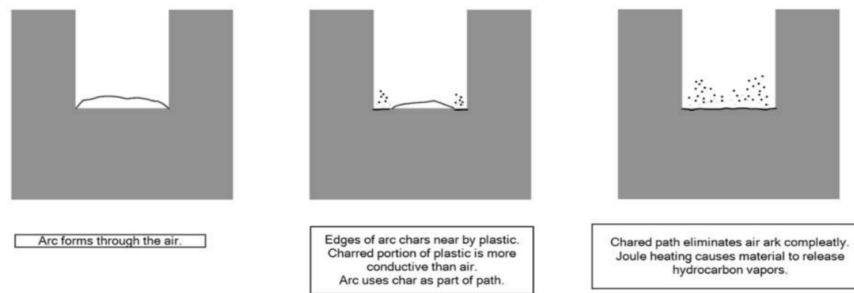


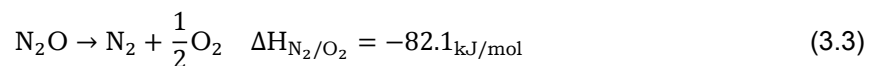
Figure 3.12: Revised theory including char path [44]

3.7.2. Ignition

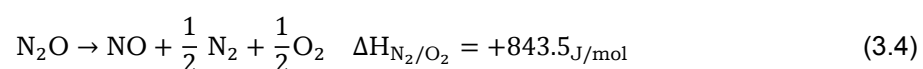
Now that the hydrocarbon seeding effect is understood it can be compared to other ignition options. Some common options that have been used or are considered for hybrid engines include:

1. Pyrotechnic
2. Bipropellant
3. Pyrophoric
4. Hypergolic
5. Catalytic
6. Hydrocarbon seeding

Pyrotechnic igniters are classified as ADR class 1 dangerous goods. They are a significant explosive hazard that would complicate rideshare options on satellite launchers. In addition, they are almost exclusively single use devices and would not allow the system to be used for multiple restart applications. A bi-propellant igniter has the option to ignite a motor multiple times, depending on the tank size. The downsides are the complexity and mass of the system required as well as the development time of a reliable, consistent system. Another option is pyrophoric ignition. This can be achieved using TEA-TAB which is forced out of an ampule into the engine at start-up. It is a well established and reliable method of ignition, but it defeats the whole use of green non-toxic propellants. In addition, just as pyrotechnic igniters, it would disqualify the system for rideshare applications. The same goes for hypergolic systems, where two propellants spontaneously combust on contact. They also carry the additional downside of a complex bi-propellant system. Finally, catalytic ignition is a tried and tested option. In particular catalytically decomposed hydrazine has been used. A reusable catalyst to decompose the nitrous has been proposed as well by Zakirov et al. [45] However, the system proposed by Whitmore, Mathias, and Harvey [44] offers a much simpler low power solution than all these options. In addition, it doesn't use any dangerous goods making it a safe system to work with and qualify it for rideshare applications. This restartable behaviour still functions properly with nitrous as well as the standard testing oxidiser GOX as illustrated in Whitmore [46]. The decomposition of nitrous is exothermic and generates nitrogen and oxygen gas.



There is however an endothermic reaction of nitrous at a temperature below 400°C where nitric oxide is created that needs to be taken into account. So the combustion chamber temperature should be above that threshold, especially at startup as the endothermic reaction would otherwise cool the incoming propellant stream and delay or quench the startup reaction.



On top of that, nitrous must be vaporised before any decomposition reaction takes place. For most hybrid motor applications nitrous is introduced as a two-phase liquid. On top of that, the nitrous will expand over the injector significantly lowering the temperature below even -40°C. Thus, nitrous oxide based hybrid systems need a large enthalpy source to vaporise the cold liquid. This is where the hydrocarbon seeding effect comes into play. The high temperature hydrocarbon vapour that is released

significantly lowers the activation energy for a nitrous oxide reaction. This is likely due to a number of different oxygen radicals being released when the hydrocarbon vapour burns. This creates additional oxidation reaction pathways that enable combustion at a relatively low ignition power input. This effect has proven to overcome the theoretical technical challenges, as up to twelve restarts have been successfully performed [46]. Finally, a large benefit of the propellant combination nitrous oxide and ABS is that it can be considered a green fuel [47, 48]. Neither are toxic or need expensive equipment to handle. Its reaction products are also relatively benign.

3.8. Conclusion

The unique properties that 3D printed ABS has make it a very suitable candidate for applications where hybrids are otherwise not usable. It features restartability with an ignition system that use no toxic propellants or explosives. This makes it a valuable alternative to HTPB or paraffin, even though performance is slightly lower. The TRL from literature is sufficiently high to implement the concept in an integrated design study.

ABS Characterisation

Analysing plastics is not straightforward. In this chapter four different approaches have been applied in order to find the component mass ratio and heat of formation of the selected ABS material with varying results. In order to understand the limitations of each method first of all, the structure of ABS will be elaborated upon in section 4.1. Secondly, some known properties of the used plastic will be given in section 4.2. Then some complications arising from the use of additives are discussed in section 4.3 after which the first method to quantify the plastic monomer ratio will be treated in section 4.4: Fourier-transform Infrared spectroscopy (FTIR). This is followed by (TGA) in section 4.5. The next step is to quantify the heat of combustion with a bomb calorimeter which is done in section 4.6. From these values and the suggested monomer ratios the heat of formation is calculated in section 4.7. Finally the results will be concluded in section 4.8.

4.1. ABS Material Structure

ABS is a thermoplast that is composed of three different monomers: acrylonitrile, butadiene and styrene. A representation of this molecule is given in Figure 4.1. Each of the three monomers contributes to specific quality of the final product. Acrylonitrile offers chemical resistance and thermal stability. Styrene is known for its rigidity and makes the plastic easy to process. Finally the butadiene offers toughness and impact resistance. Unlike the image suggests, ABS is not a homogeneous material. It exists as a two-phase system with a styrene-acrylonitrile copolymer (SAN) as the main phase with polybutadiene rubber dispersed through it [49]. This structure is shown in Figure 4.2. The two phases are connected through a process called grafting. The SAN provides the backbone upon which chains of polybutadiene are growing. These structures are suspended in a matrix of ungrafted SAN.

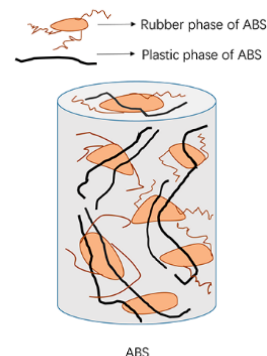
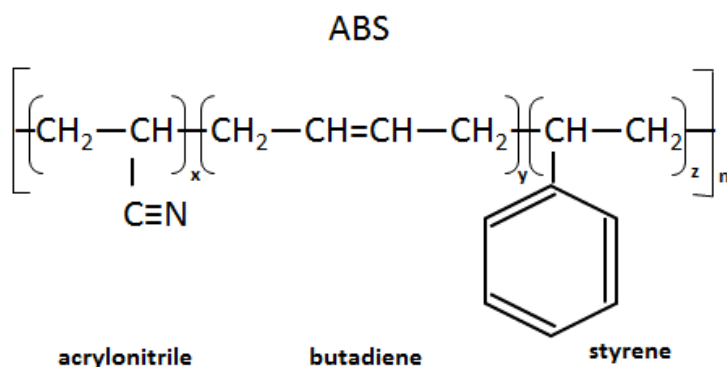


Figure 4.1: Representation of the combination of ABS monomers, retrieved from ¹

Figure 4.2: Distribution of phases in ABS, retrieved from ²

¹https://www.researchgate.net/figure/Chemical-structure-of-ABS-PS-and-PVC_fig2_328589758

²<https://www.mdpi.com/2073-4360/11/12/2048/htm>

4.2. Material Specifications

During the production process the ratio of these three monomers as well as radical initiators can be varied in order to influence the degree of polymerisation, length of polymers and product properties. A superior final product depends on the careful selection of these parameters and these are therefore usually not public knowledge. As mentioned in chapter 1, the manufacturer could not disclose any details on the ratio of the constituents and within the time span of this thesis no NDA could be achieved. Therefore an experimental approach was taken in order to attempt to quantify the ABS plastic used: REAL filament ABS gray. REAL is the retailer that sells the final reels with filament. The filament itself is produced by Reprapworld, who in turn receive the ABS pellets, used to extrude this filament, from Trinseo. Throughout the communication with these three parties it has become clear that:

- The 3D filament data sheet states:
 - > 98 % Styrene-acrylonitrile-butadiene copolymer
 - < 0.1 % Styrene
- The plastic contains 2-4% masterbatch (additives) according to Reprapworld
- The resin is Trinseo MAGNUM™3453 AB
- According to their help desk, its composition is in the range¹:
 - 15% to 35% acrylonitrile
 - 5% to 30% butadiene
 - 40% to 60% styrene

With the >98 % requirement on ABS copolymer content from the data sheet it can be assumed that the masterbatch is 2%. More details including mechanical properties are given in the data sheets of the filament on page 107 and of the resin on page 108.

4.3. Additives

Additives are combined to enhance the properties of plastics. For example to prevent UV degradation, increase fire safety or to add a colour to the plastic resin. The combination of additives selected for a certain product is called masterbatch. When analysing plastics these additives can be problematic as they interfere with the instrument. They could absorb certain wavelengths that are interesting for the FTIR analysis performed in Figure 4.3. Or they could leave an inert residue in either the sample for TGA or even that of the bomb calorimeter. For the latter this only concerns metallic additives as their oxides will remain in solid form. Organic compounds will combust in the presence of oxygen at elevated temperatures and pressures. Table 4.1 gives a summary of additives that are either very likely present in the ABS blend or potentially present and metallic.

Table 4.1: A collection of additives potentially used in this ABS blend.

Name	Typical amount range (% w/w)	Element	Function	Source
Carbon Black	0.25-5	C (s)	Black colour	[50]
Titanium oxide		TiO ₂	White colour	
Boric acid	0.7–3	H ₃ BO ₃	Flame retardants	[51]
Brominated flame retardants with antimony as synergist	3–25 (for brominated)	Br, Sb		
Cadmium compounds	0.05-3	Cd	Stabilisers, Antioxidants and UV stabiliser	
Lead compounds		Pb		

From these, the two colourants are most likely to have been used to create the dark grey colour of the plastic. The others may be present in lower amounts. Due to the high percentage range of brominated flame retardants it is unlikely that they have been included. In order to prevent interference of any additive, an attempt was made to separate them from the plastic. Multiple solvents were used to try and dissolve the ABS sample. These include:

¹These align with the values of Wikipedia: https://en.wikipedia.org/wiki/Acrylonitrile_butadiene_styrene

- Dichloromethane (DCM)
- Methyl isobutyl ketone (MIK or MIBK)
- Chloroform
- Aniline
- Tetrahydrofuran (THF)
- Acetone
- Benzoyl dichloride

All of them dissolved the plastic to some extent, but left some swollen components floating in the solution. Given the wide range of solvents used and their known capacity to dissolve ABS plastic leads to the conclusion that the sample contains a relatively high degree of cross-links between its butadiene strings in the rubber phase. This is plausible given the desired mechanical properties resulting from these cross-links that are useful for 3D printed components: impact resistance and toughness. This can be confirmed by Table 4.3, which tabulates some of the mechanical properties of this resin given in the data sheet on page 108. The resin far outperforms the older variants. Filtering and drying the dissolved sample would result in the removal of the carbon and metallic additives, but leaves a ratio containing considerably less butadiene as this will also be filtered out. Therefore, this approach has been disbanded. Instead the sample has been analysed as is, with all the additives included.

4.4. FTIR

The first method was developed by Gesner [52] in 1970, specifically for ABS. It used to be common procedure to break up a sample in it's original components and analyse them individually to find the component ratio. This tends to be a tedious procedure however so the study compares three methods that turn out to be in agreement within their respective standard deviations. It validates the use of the calibration curve method which is the most accessible and most applicable for grafted polymers. It was made by analysing ABS plastics with known ratios including a degree of grafting. It uses the absorption spectrum of a sample of ABS obtained by Fourier-transform infrared spectroscopy. With calibration curves it relates the observed corrected optical density at to the composition of the material by percent weight. This relation and the curves are shown in Figure 4.3.

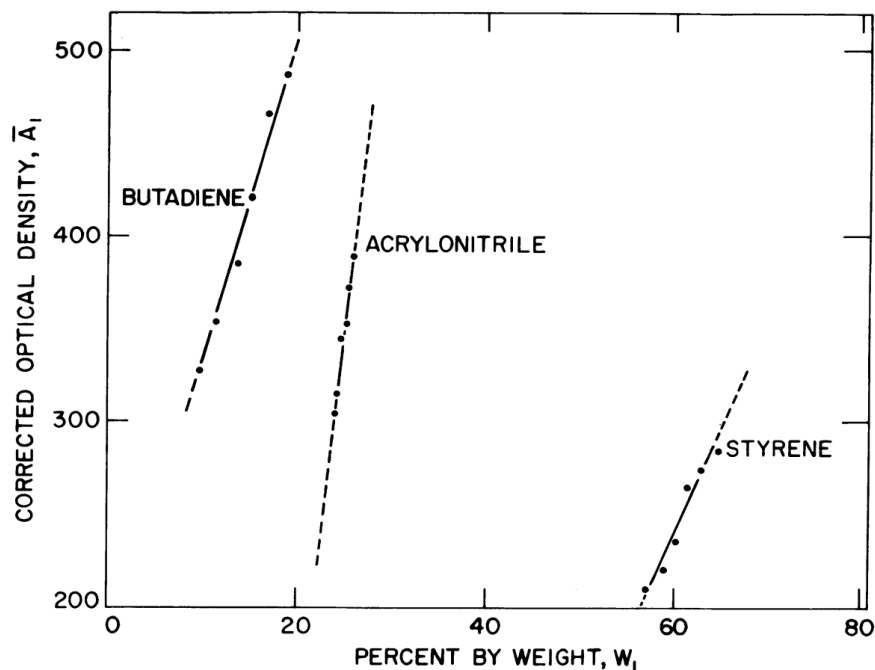


Figure 4.3: Calibration curves to convert absorption to ABS component mass ratios

Essentially, certain molecular bonds are known to show up as peaks in the spectrum at certain wave numbers. As acrylonitrile, butadiene and styrene are all distinctly different molecules after polymerisation. Double carbon bonds are only found in polybutadiene without cross-links. A carbon nitrogen triple bond only exists in acrylonitrile and styrene is the only molecule to contain a benzene ring. The calibration curves use the fact that the higher the peak, the larger the quantity of the molecular bonds matching this wavelength. The wave numbers of interest are 2239, 965 and 1584 cm^{-1} for acrylonitrile, butadiene and styrene respectively. The magnitude of the peaks at the indicated locations are then used to find the corrected optical density defined as

$$\overline{A}_1 = A_1 / \sum_{i=1}^n A_i \quad (4.1)$$

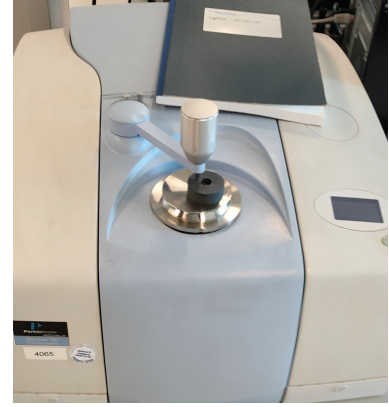


Figure 4.4: ABS sample constrained on FTIR spectrometer

The spectra used here are made with a PerkinElmer Spectrum 100 FT-IR Spectrometer shown in Figure 4.4. Before every run a calibration run is required. The final results are then the subtraction of the calibration run from the plastic spectrum. These are shown in Figure 4.5 with a zoom in of each of the three peaks of interest. Dividing each peak by the sum of all peaks considered and averaging the results of the two runs, yields the values given in Table 4.2.

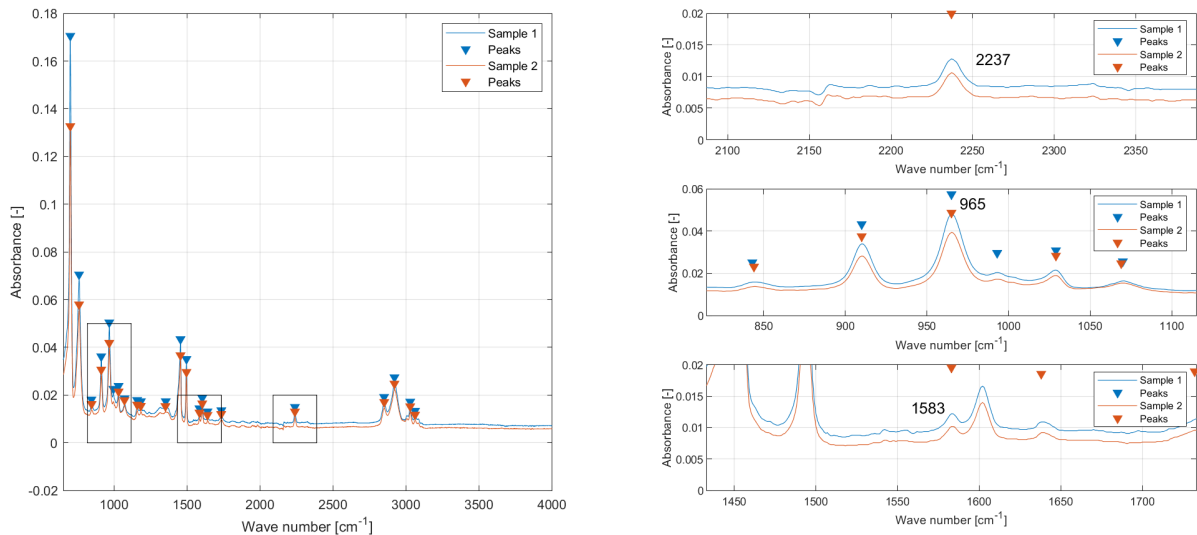


Figure 4.5: Absorption spectrum of the analysed ABS plastic

Table 4.2: FTIR results in terms of percentage weight

Molecule	Run 1	Run 2	Average
Acrylonitrile	20.9	20.8	20.8%
Butadiene	25.2	25.5	25.4%
Styrene	53.9	53.7	53.8%

The acrylonitrile ratio is on the lower end of the range analysed in the paper. It is not far off compared to the ratios of butadiene and styrene. Butadiene is far over its range and styrene is far under. All three values are however still well within the range indicated in section 4.2 and lay within boundaries of expected commercially available ABS formulations. It should be noted that the plastics used in the 1970's study are very different from modern formulations. From Table 4.3 it is evident that the modern resin has far superior mechanical properties over its predecessors from the 1970's. In particular the impact strength is over twice as high. Although this can also be attributed to better polymerisation processes, it is deemed very likely that an increased amount of butadiene will have been required

for this large an increase. This is in agreement with the obtained results. Gesner [52] argues that the developed method is specifically intended to differentiate plastics by their mechanical properties and has shown that with the values of the three resins in Table 4.3. Though the Trinseo resin is an extrapolation, it follows the same trend as validated previously. This trend is potentially slightly further away due to a broadened peak at $\approx 1600\text{ cm}^{-1}$. It indicates the presence of carbon black that could have increased the magnitude of the peak otherwise attributed to styrene content. However, even a 50% decrease in the absorbance will yield an only 1.2% reduction in absolute mass percentage of styrene, with the bulk going to an increase of butadiene. This means the sample potentially contains more butadiene than indicated, further pushing the sample out of the measurement range. A broad band at 445 cm^{-1} that can be attributed to TiO_2 was just out of range of the instrument and the theory of its presence could not be strengthened with the FTIR measurements. Thus, there is also no indication it could have interfered with the measurements.

Table 4.3: Property comparison between 1970's ABS resins and the modern Trinseo resin [52]

	Trinseo Magnum 3453	Resin I	Resin V	Resin VI
Impact Strength (23°C) [kJ/m ²]	18	9.0	8.4	7.8
Tensile Strength [MPa]	45.0	39.3	38.6	36.5
Flexural Strength [MPa]	68.0	65.5	62.7	62.0
Flexural Modulus [MPa]	2300	2230	2300	2500

Nonetheless, extending the range this far for a quantitative analysis of the mass ratios cannot be done with sufficient confidence without a full validation campaign following the same procedures as Gesner [52]. However, this would be out of the scope of this thesis and instead the validity of the results will be attempted to be validated using different methods.

4.5. Thermogravimetric analysis

Another method, as described in PerkinElmer [49], is thermogravimetric analysis. Simply put, the device heats up a sample and records its mass and temperature over time until the sample (mostly) disappeared. Components of the sample will start to decompose vaporise at specific temperatures and thus, if the temperature increase is slow enough a distinction can be made between the different components of the sample. This process will be performed under an inert nitrogen atmosphere to prevent combustion of the sample. Only at 700 °C the flow of nitrogen will be changed to oxygen in order to facilitate the removal of carbon until only ash remains. In the heterogeneous ABS material, the SAN copolymer will vaporise first after which the butadiene rubber will follow. The ideal process is illustrated in Figure 4.6. The step in temperature between larger mass loss events indicates a mixture is present and allows for an accurate estimate of the ratio of the two.

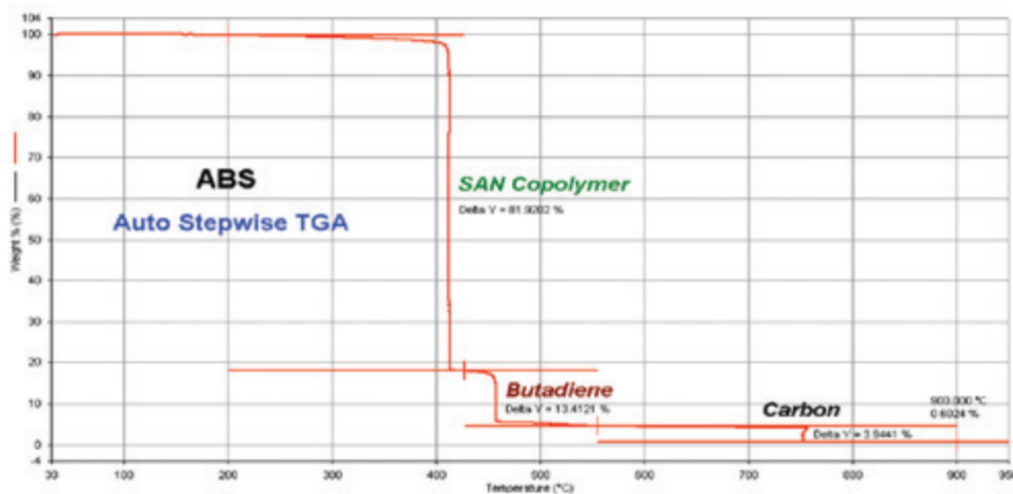


Figure 4.6: Mass over temperature of an ABS sample [49]

In this thesis the PerkinElmer Thermogravimetric Analyser TGA 4000 was used, shown in Figure 4.7. PerkinElmer [49] used the PerkinElmer® Pyris™ 1 TGA. It is important to note that the Pyris is more advanced than the TGA 4000. It uses an AutoStepwise function which can automatically hold the temperature steady when a larger mass loss event is detected. In the case of ABS it holds the heating process for at least 10 minutes when the mass loss exceeds 1.25%/min and continues again when it is less than 0.10%/min. The result is a much finer record of mass loss around the transition time between evaporation of each components in the mixture. The TGA 4000 is calibrated as standard practice by the lab technicians. This was verified by the final sample mass which was recorded to be between 2.0-2.1mg by a separate high accuracy scale, whereas the TGA 4000 recorded an initial mass of 2.05mg. The slowest setting it is capable of is 0.1°C/min. It has the option to hold the temperature stable at a manually set point, but not dynamically by analysing the mass loss rate. Therefore, the first step is to observe how the samples behave under different heating rates. The campaign started with 5°C/min, 2°C/min and 0.5°C/min runs. As a reference, in PerkinElmer [49] a nominal heating rate of 50 °C was used. The samples before and after the analysis can be seen in Figure 4.8 and Figure 4.9. Note the residue left in the cups. Since oxygen is introduced towards the end, it is expected that all the carbon burns away. This oxygen flow is also the likely contributor to the stepped increase of mass at exactly the same temperature for each run, seen in the bottom right plot of Figure 4.11. The white residue could refer to the TiO_2 mentioned in section 4.3. It could however also indicate the presence of one of the non-oxidised metal additives. The mass seems to slowly increase above 700 °C which could be due to oxygen being added as the metals oxidise and stay in the cup. Correcting for the step up this mass is estimated to be around 1 %.

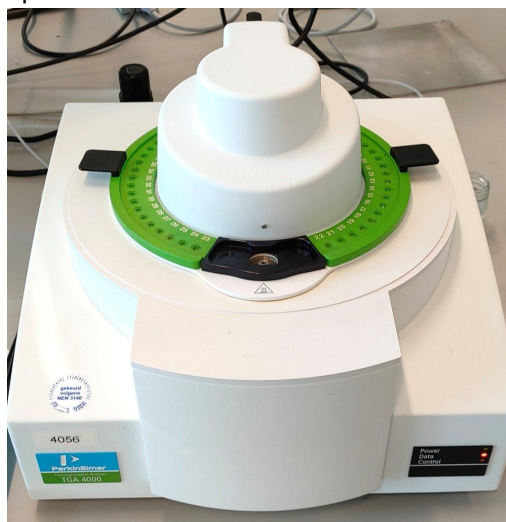


Figure 4.7: TGA4000 machine



Figure 4.8: Samples before



Figure 4.9: Samples after

The mass temperature plot is shown in Figure 4.10 with several zoomed views of critical locations given in Figure 4.11. There is an evident trend between the temperature at which the maximum mass loss rate occurs and the heating rate. The higher the heating rate, the higher the temperature of the largest mass loss event. This is an indication that the heating process is too fast compared to the decomposition and evaporation process in the ABS. As the curve had been shifting left, an isothermal step at 390°C was added in the hope that it would resolve the transition between two fractions. Note that the rate was already sufficient to resolve a small step at 260 °C. However, the isothermal was both too late and of too short a duration to resolve a step change as significant mass loss continued throughout the isothermal. The next experiment was set to the slowest setting of 0.1°C/min. At this rate, the experiment took so long that it stopped logging data when the file reached the maximum size that the program is able to create. The temperature range was sufficient to evaluate the results around the large mass loss event however. A shallow change in slope could now be observed at 400 °C and the mass loss event again shifted further to the left. This is an indication that the heating rate is approaching a sufficiently low value, but with the machine at the lowest setting this trend could not be continued. Instead it was argued that a reduction in sample size could help to resolve the phases. A smaller sample might need a smaller amount of time to decompose and vaporise.

The final run was again with a rate of $0.1^\circ\text{C}/\text{min}$ but with a lower data rate to ensure logging would not stop until the end. The result is a slightly noisier signal that almost exactly follows the previous run.

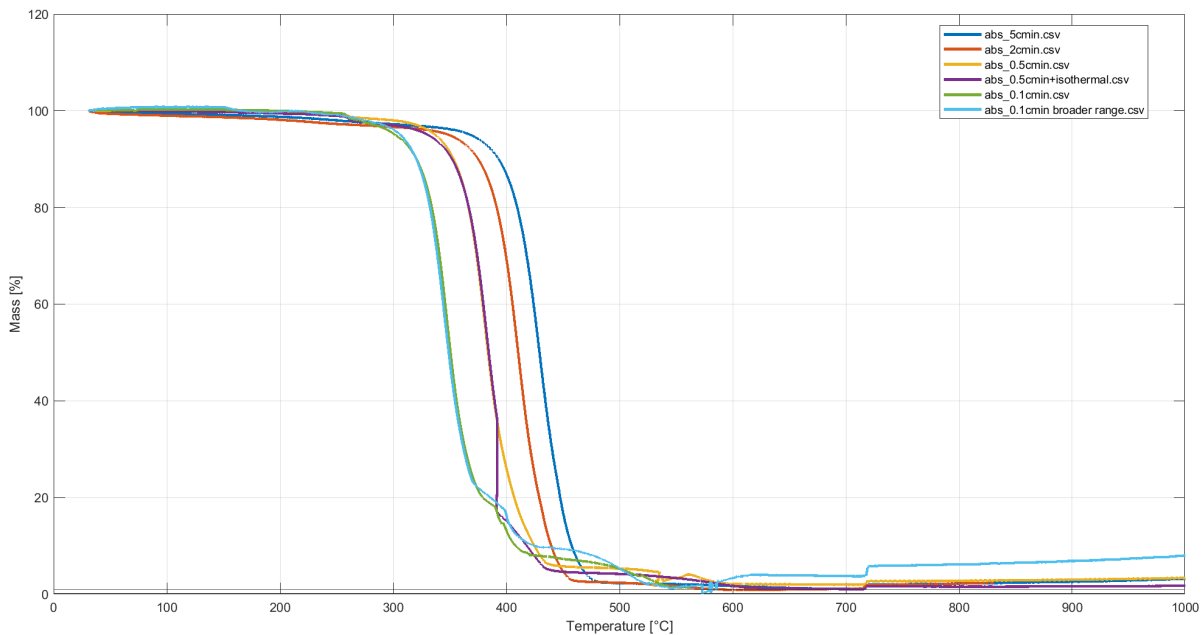


Figure 4.10: Mass over temperature of an ABS sample

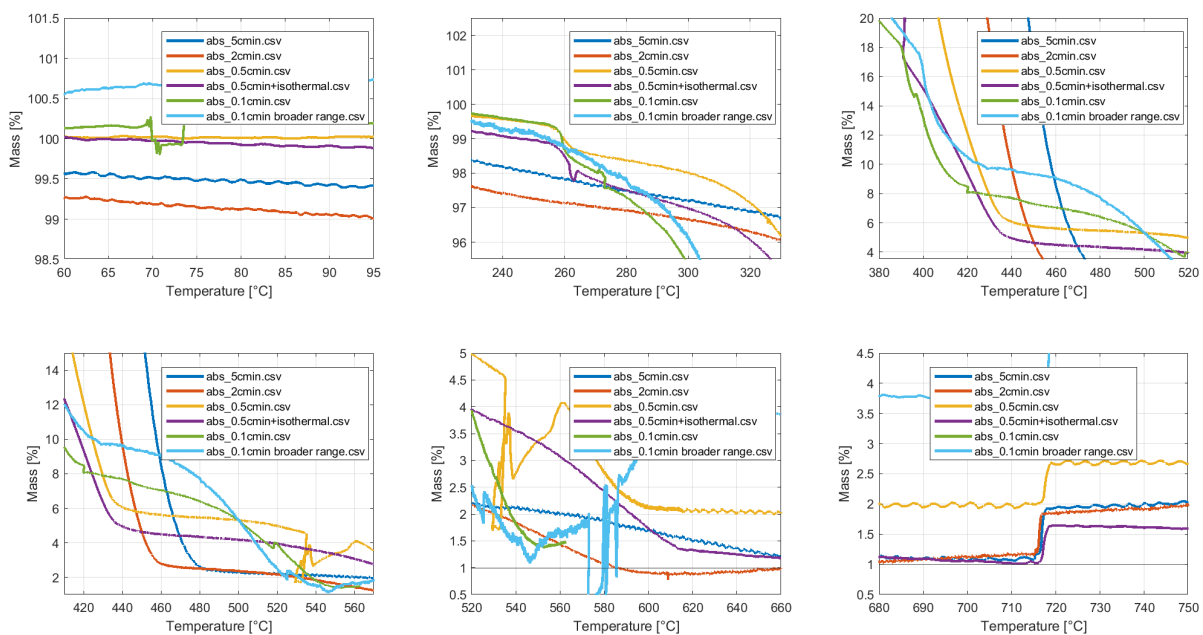


Figure 4.11: peculiarities of mass over temperature data of an ABS sample

One final attempt to separate the phases with the current limitations of the testing equipment available is to assume that the vaporisation of a fraction is normally distributed. Taking the derivative of the absolute mass over temperature curve results in a curve that can be fitted with a sum of multiple Gaussian normal distributions. It was found that for each heating rate a sum of exactly 4 distributions fits the data of the large mass loss very well. This indicates 4 different fractions are present in the large mass loss event. Since the two larger and the two lower peaks overlap, it is possible that they represent (co)polymers with a different degree of polymerisation, or cross-linking in the case of butadiene. As expected, the slower the heating rate the more distinct their peaks are and the further they are sepa-

rated from one another. The isothermal run has been excluded from the summary as the mass loss at this one temperature causes the Gaussian assumption to become invalid. For each run 7 plots are generated. On the left top the standard mass temperature plot is given as a reference. Below it are 4 plots given the derivatives of the total mass over time and over temperature both on the full range and zoomed in on the large mass loss event. On the right hand side a zoom in of the filtered temperature derivative of the mass can be seen twice. On the top is the plot of the initial guesses of the summation of Gaussian curves. The script will iterate this initial estimate to reduce the residuals. This result is shown in the bottom right. A very good set of initial conditions is required for the script to converge so the peak location, height and width need to be guessed iteratively by looking at the peaks in the data.

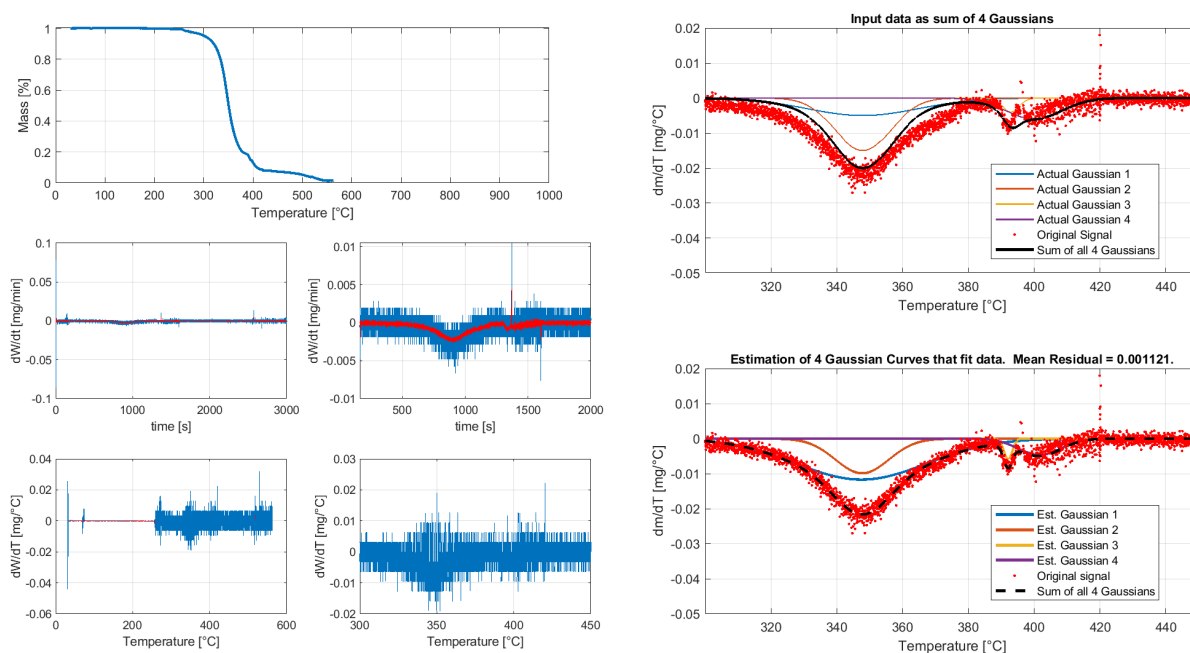


Figure 4.12: Mass over temperature of an ABS sample including Gaussian fit

The Gaussian fits of the other runs have been added in Appendix D. When the ratio of the area of each Gaussian curve with respect to the sum of all curves is taken the values in Table 4.4 are found. It lists the heating rate of each run, the sample mass and the ratios of all the 4 Gaussian curves separately and that of the first two and the last two summed. What can be observed is a large variance in the weight ratios of each individual Gaussian, however the summed ones show some consistency. It suggests a butadiene content of just over 10 %, significantly lower than the 25.4% from FTIR measurements. The run with a heating rate of 0.5 °C/min however indicates a potential contribution of 20 %. It also lacks the sharp peak all the other runs do contain. Finally, the mass loss from 400-550 °C remains unexplained. This could potentially be a polybutadiene rubber phase with a higher degree of cross-links. If these are included the total goes up again to around 20 % which does agree with the FTIR based estimation. Again, these phases will need to be resolved as well in order to draw any definite well supported conclusions.

Table 4.4: Overview of the percentage contribution of 4 Gaussian curves fitted to the mass loss rate

Heating rate	Sample mass [mg]	Gaussian 1 [%]	Gaussian 2 [%]	Gaussian 3 [%]	Gaussian 4 [%]	Gaussian 1+2 [%]	Gaussian 3+4 [%]
5°C/min	5.39	40.9	22.3	1.1	35.7	63.2	36.8
2°C/min	6.88	32.0	58.0	0.7	9.4	90.0	10.0
0.5°C/min	6.23	43.9	38.5	11.5	6.1	82.4	17.6
0.5°C/min	6.85	-	-	-	-	-	-
0.1°C/min	6.81	66.4	23.0	2.2	8.4	89.4	10.6
0.1°C/min	2.06	25.8	62.9	2.0	9.3	88.7	11.3

Some suggestions can be made to resolve the phases using the current machine. For example, a few isothermal steps at lower temperatures could be tried to identify when exactly one phase ends and the next starts. This could be at for example 250 °C to better resolve the initial mass loss event or at 300 °C which is the approximate decomposition temperature indicated by the manufacturer. This process can then be repeated to resolve the step around 400 °C. However, this will have to be a repetitive time consuming process as it takes 7 days to reach 1000 °C at 0.1 °C/min. This could be optimised by neglecting the range over 600 °C and increase heating rates in between isothermal steps. However, with a complex polymorph as ABS it is expected that different unexpected complications will elongate this process. Instead it is advised to source an actual AutoStepwise TGA that is particularly designed to solve this type of problem.

4.6. Bomb Calorimeter

The heat of combustion can be determined using a bomb calorimeter. In this device a small piece of fuel with known mass is combusted in an excess of oxygen in a capsule suspended in an isolated water bath. The water is stirred around while the temperature increase of the system is measured and used to find the heat of combustion of the sample. Figure 4.13 shows a schematic of a bomb calorimeter.

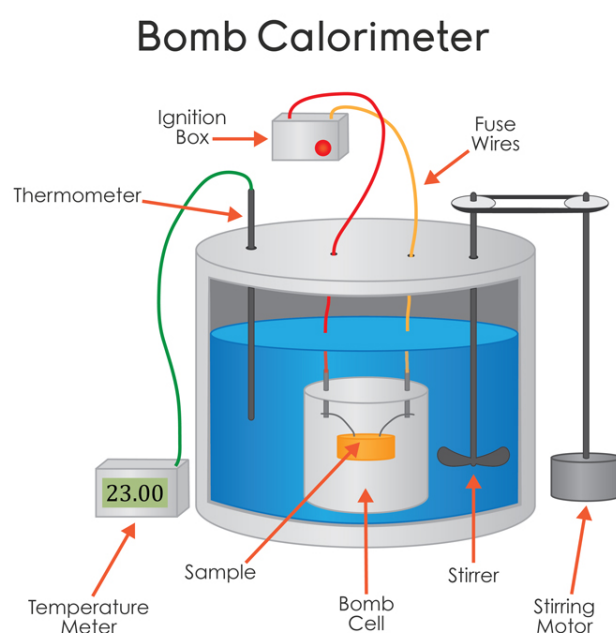


Figure 4.13: Schematic of a bomb calorimeter retrieved from ¹

Within the TU Delft two bomb calorimeters were located in the same facility. One lower end calorimeter that is used for bachelor projects and a high end Parr 6772 Bomb calorimeter. Since ABS was an unknown material for the lab where the bomb calorimeter was located some trial runs on a more accessible model were attempted first. This setup is shown on Figure 4.14. The goal was to determine how complete the combustion of the material was and if there is any potential to damage the hardware. Three runs were attempted of which only the first one is deemed representative, due to its consistency with the initial calibration run. Afterwards a series of accurate tests could be performed to accurately determine the HHV without any risk of damaging the apparatus. Unfortunately, due to repeated occupancy of the machine, it being nonoperational due to broken hardware and unavailability of personnel, the additional sequence of higher accuracy tests could not be performed. As explained in section 4.7, the value obtained does agree with heat of formation calculations. Figure 4.15 shows the preparation of the ABS in the cup. A string of cotton is tied around a NiCr wire and lead down in between the ABS segments to aid the ignition process. The closed bomb assembly is shown in Figure 4.16. Note the two adaptors for the ignition leads and the closed off oxygen inlet. Finally, the cup after combustion is

¹<https://socratic.org/questions/581e5a5511ef6b4a10d7a18b>

shown in Figure 4.17. Similarly to what was observed after the TGA, a white residue can be found in the cup of the bomb calorimeter. The mass increase of the cups in the first and third run are 0.003g and 0.006g or 0.35% and 0.68% respectively. It should be noted that there was a splash pattern observed that implies that some material was shot out of the cup into the bomb. This means that the total amount is potentially higher.



Figure 4.14: Bomb calorimetry test setup. Note the press to assemble benzoic acid discs for calibration purposes. On the right, the bomb water bath with brown top can be seen.



Figure 4.15: Contents of bomb



Figure 4.16: High pressure 'bomb'



Figure 4.17: White inert residue

As mentioned before, the bomb calorimeter requires calibration before use. This is commonly done using benzoic acid. Equation 4.2 is used to calculate the heat capacity of the calorimeter.

$$C = \frac{\text{HHV}_{\text{benzoic acid}} \times m_{\text{benzoic acid}} + (\text{HHV}_{\text{NiCr}} \times m_{\text{NiCr}} + \text{HHV}_{\text{cotton}} \times m_{\text{cotton}})}{\Delta T} \quad (4.2)$$

The equation can then be reversed to find the higher heating value of the ABS instead of the known benzoic acid. It is important to keep the total heat of combustion in a similar range to ensure the calibration run is valid. This means that of a fuel with an higher expected caloric value, a lower amount should be inserted. The results of the calibration run and ABS analysis test are given in tables 4.5 and 4.6 respectively. Their temperature increase is very similar indicating they total heat of combustion was similar as well.

Table 4.5: Values of bomb calibration run

m_{Water}	1753	g
dm_{ABS}	1.093	g
dm_{NiCr}	0.007	g
m_{cotton}	0.019	g
$\text{HHV}_{\text{Benzoic acid}}$	26.454	kJ/g
HHV_{NiCr}	1.4	kJ/g
$\text{HHV}_{\text{cotton}}$	17.5	kJ/g
dT	3.165	°C
C	9.243767	kJ/C

Table 4.6: Values of ABS bomb calorimetry measurement

m_{Water}	1754	g
dm_{ABS}	0.865	g
dm_{NiCr}	0.001	g
m_{cotton}	0.019	g
$m_{\text{cup},0}$	14.115	g
$m_{\text{cup},1}$	14.118	g
m_{residue}	0.003	g
dT	3.610	°C
HHV_{ABS}	38.19	kJ/g

4.7. Heat of Formation

With the bomb calorimeter measurement the heat of combustion has been found. For CEA, however, the heat of formation is required instead. This allows for an analysis with different oxidisers, mixture ratios and pressures. This means that the results from the oxygen rich and thus complete combustion in the bomb calorimeter can be extrapolated to scenarios where no complete combustion takes place. The heat of combustion is the difference between the heat of formation of the fuel and oxidiser, the reactants, and the products. Thus, in order to find the heat of formation, an analysis must be performed to find out which species are being formed under an excess of oxygen at a certain pressure. An input of this set of chemical equilibrium equations is the heat of formation of the ABS itself and thus an initial guess needs to be provided after which an iterative process should converge on the solution. The flow diagram for this process is shown in Figure 4.18.

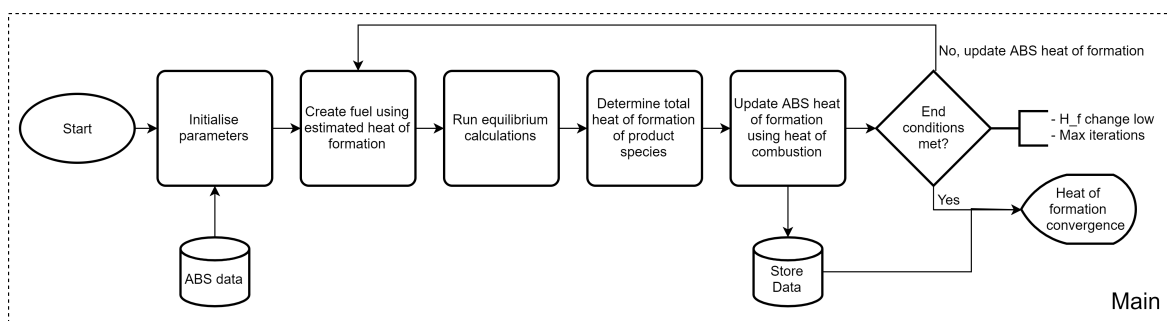


Figure 4.18: Flow diagram to determine heat of formation.

First the input parameters are initialised and a propellant combination is created. Then, chemical equilibrium equations are solved using these input parameters. Two outputs will be further analysed: the molecular weight of all the species that have been formed and the combustion temperature. The temperature will then be used to calculate the enthalpy change of the reaction products from their formation to the combustion temperature. This should be equal to the heat of combustion acquired from the bomb calorimetry measurement.

$$\epsilon = \sum_{i=1}^n m_i \cdot \Delta_f H_i^\circ - m_i \cdot \Delta H_i \quad (4.3)$$

This process is visualised in Figure 4.19. In the initial step there is an offset between the estimated heat of formation of the products based on the heat of formation of the reactants and the heat of combustion and the actual heat of formation of the products. This error is reduced with each iteration and as such, the second step shows a corrected heat of formation of the reactants.

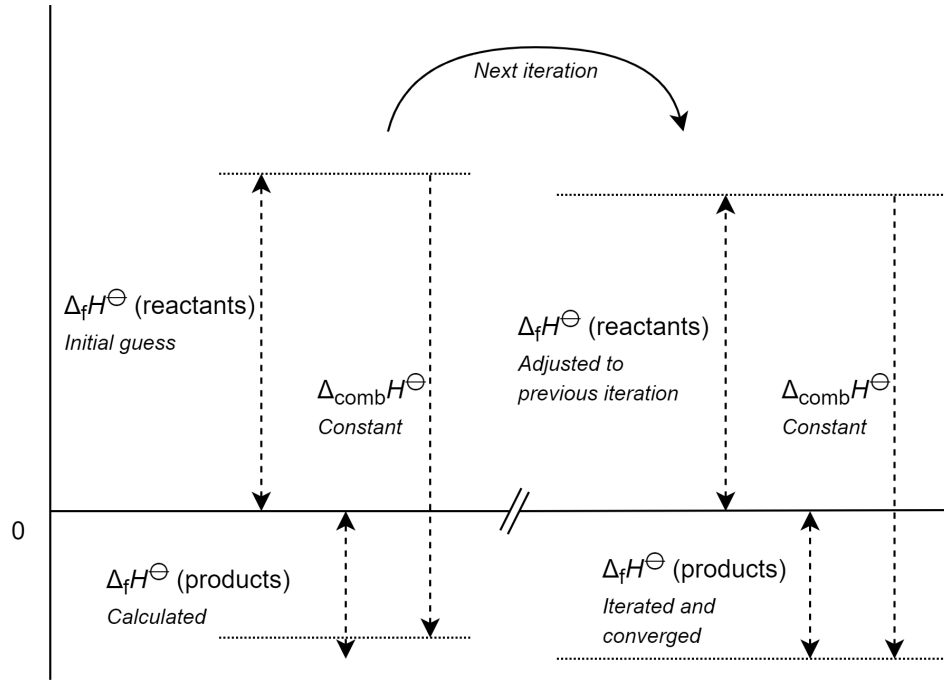


Figure 4.19: Diagram showing convergence of heat of formation

An initial guess is the final value required to start the analysis. This can be acquired from literature. The solver has shown to converge very reliably even with poor initial guesses, but a proper estimate is still required to verify the the output is sensible. An offset from the theoretical value is expected, but the deviation is not expected to be considerably large. The total heat of formation of ABS can be estimated using 9 parameters. First there is the heat of formation of the three individual monomers. In ABS however, these monomers have been polymerised and thus a heat of polymerisation should be taken into account. Intuitively, this is the parameter that induces the largest amount of uncertainty. The degree of polymerisation, grafts and cross-linking all influence this value and will be different for each ABS resin. Finally the ABS mole fraction is required to calculate the contribution of each of the three components. The two last columns are the values of the ratio determined in this chapter. The other two columns are an example from [37].

Table 4.7: Enthalpy of formation contribution of ABS copolymers retrieved from Whitmore, Peterson, and Eilers [37]

Monomer	ΔH_f monomer [kJ/g·mol]	ΔQ_f poly- merisation [kJ/g·mol]	ΔH_f polymer [kJ/g·mol]	ABS mole fraction	Enthalpy contribution [kJ/g·mol]	ABS mole fraction	Enthalpy contribution [kJ/g·mol]
Acrylonitrile	172.62	74.31	98.31	0.43	42.27	0.28	27.53
Butadiene	104.10	72.10	32.00	0.50	16.00	0.35	11.20
Styrene	146.91	84.60	63.31	0.07	4.36	0.37	23.42
ABS total					62.63		62.15

Three cases will be compared. First there is the nominal run with its parameters set to the values

that have been determined throughout this chapter. Secondly, there is a run where the ratios have been adjusted until the solution is relatively close to the initial guess. Finally, the third run had its heat of combustion varied such that it also closely matches the initial guess. All their inputs are summarised in Table 4.8. The resulting convergence plots are Figure 4.20, Figure 4.21 and Figure 4.22.

Table 4.8: Summary of inputs of heat of formation determination cases

Parameter	Nominal	Adjusted mass ratios	Adjusted HHV	Units
Heat of combustion	38192	38192	38560	kJ/kg
Mole fraction Acrylonitrile	26.8	31.4	26.8	%
Mole fraction Butadiene	32.0	19.2	32.0	%
Mole fraction Styrene	35.2	39.3	35.2	%
Mole fraction Carbon	5.8	9.8	5.8	%
Mole fraction Titanium Dioxide	0.3	0.3	0.3	%

It is evident that the final heat of formation is highly sensitive to the estimated heat of combustion. An increase of the estimated heat of combustion of only 0.97% will cause it to converge rapidly on the initial value estimated with the values from Table 4.7 instead of reducing with 80 %. Contrarily, the mass ratios need to be significantly edited in order to make a significant change. The butadiene mole fraction had to be reduced with 40% to get a comparable result.

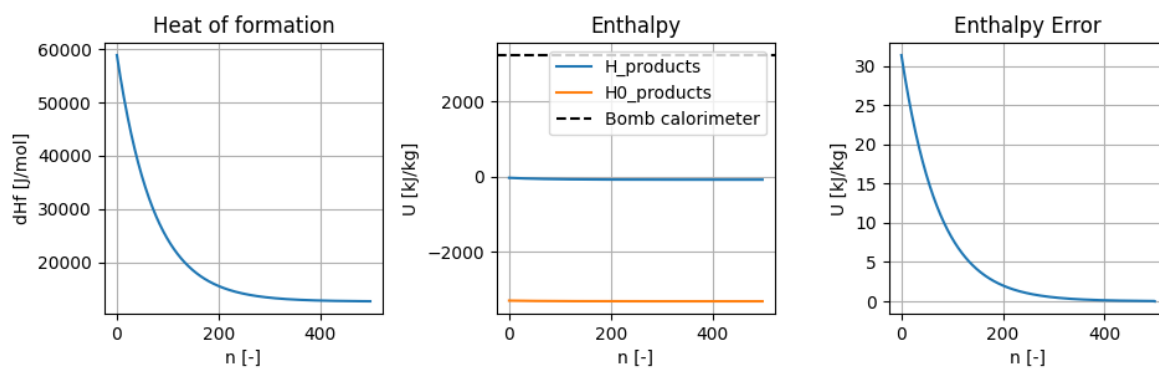


Figure 4.20: Convergence of heat of formation of nominal case

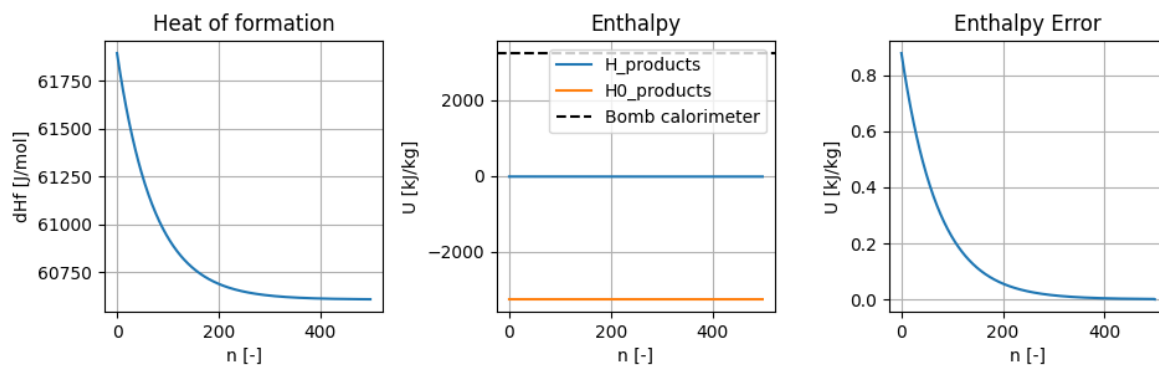


Figure 4.21: Convergence of heat of formation of adjusted mass ratios case =

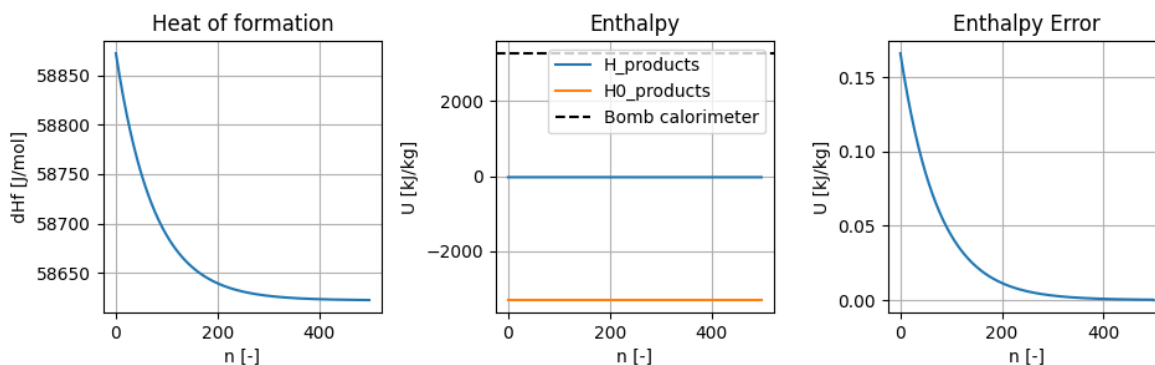


Figure 4.22: Convergence of heat of formation of adjusted HHV case

When the output performance parameters, shown in Table 4.9 are compared however, all differences are insignificant except for the heat of formation. This indicates that the final result is relatively insensitive to the input parameters which allows for a larger uncertainty of the input parameters.

Table 4.9: Summary of outputs of heat of formation determination cases

Parameter	Nominal	Adjusted mass ratios	Adjusted HHV	Units	Percentage error
Vacuum Specific Impulse	193.3	193.3	194.6	s	0.67
Characteristic Velocity	1295.8	1295.9	1304.0	m/s	0.98
Combustion Temperature	2726.3	2732.9	2753.6	K	0.99
Molar mass	32.5	32.6	32.5	mol	0.31
Isentropic exponent	1.2	1.2	1.2	-	0.00
Heat of formation	12.64	60.61	58.62	kJ/mol	79.1

In order to improve the accuracy of the estimated heat of formation more accurate bomb calorimeter measurements are essential. If the bomb calorimeter is to be used as a method to validate the fuel composition as well, improved accuracy of the TGA suffice. This will set the SAN-butadiene-C-ash ratio and allows to vary the S-A ratio until the results converge. Alternatively, a larger campaign as described in Gesner [52] could be performed to validate or adjust the calibration curve method.

4.8. Conclusion

The ratio of monomers has been evaluated using 3 different methods showing globally consistent results. More accurate results can be achieved using an AutoStepwise TGA machine. This allows for an accurate determination of the SAN-butadiene ratio and can verify FTIR based measurements. Bomb calorimetry gives the higher heating value which can be used to find the heat of formation through chemical equilibrium equations. The ratio can be verified using this method as a different ratio of nitrogen, carbon and oxygen atoms will yield a different total enthalpy of the combustion products when the same heat of formation is used, assuming the final heat of formation will be close to the initial condition based off of theoretical equations. The deviation in fuel properties is below 1%. This is deemed sufficient for the purpose of this study. For the future however it is recommended to follow up on the results presented in this chapter. The collected methods have the potential to form a even more reliable basis once accurate results are obtained and compared.

5

Chimera Hybrid Engine Simulation Software

This chapter presents the setup of the Chimera Hybrid Engine Simulation Software (CHESS). It is based on the requirements of subsection 1.3.5. This chapter aims to prove that these requirements have been fulfilled. In section 5.1 the software flow diagram and the organisation of all the different python files are given. Then the python packages that were used in the program are listed and elaborated upon in section 5.2. A range of engineering models was implemented to describe the physics of the system, these are explained in section 5.3. Finally, a sensitivity study was performed to verify the functionality of the software.

5.1. Software Structure

Upon analysis of the requirements three main functions of the software package can be identified. The software flow diagram of each of these functions is given in Figure 5.1. First of all a preliminary design needs to be generated. This design should be aided by sizing calculation based on the input of some global variables. The output of these calculations need to be summarised, visualised and presented to the user in a fashion that allows them to be overridden. The next step is to take this preliminary design and propagate the initial conditions over time using a variety engineering models that should be interchangeable and selectable by the user. These results then need to be stored for the final step: post processing. The data should be able to be easily visualised so that the user can assess the output and decide if different engineering models need to be selected or input parameters adjusted. Some examples of these output plots are given in section D.2. The first one gives some engine properties over time such as the chamber pressure, thrust produced and mass flows. More graphs of this type can be generated for tank and injector properties as well. Figure C.3 and Figure C.4 show the cross sections of the grain and nozzle over time respectively. The time step between lines can be manually adjusted by the user. In addition, they each show three relevant variables plotted alongside. Finally the mass species over time are shown in Figure C.5. This can be used to keep track of the species that are produced at certain OF ratios and combustion pressures. Especially at lower OF ratios, the fuel is not burned to completion and some more toxic products such as hydrogen cyanide can be produced in low quantities. Depending on the application this can become a design constraint that can be checked with this graph.

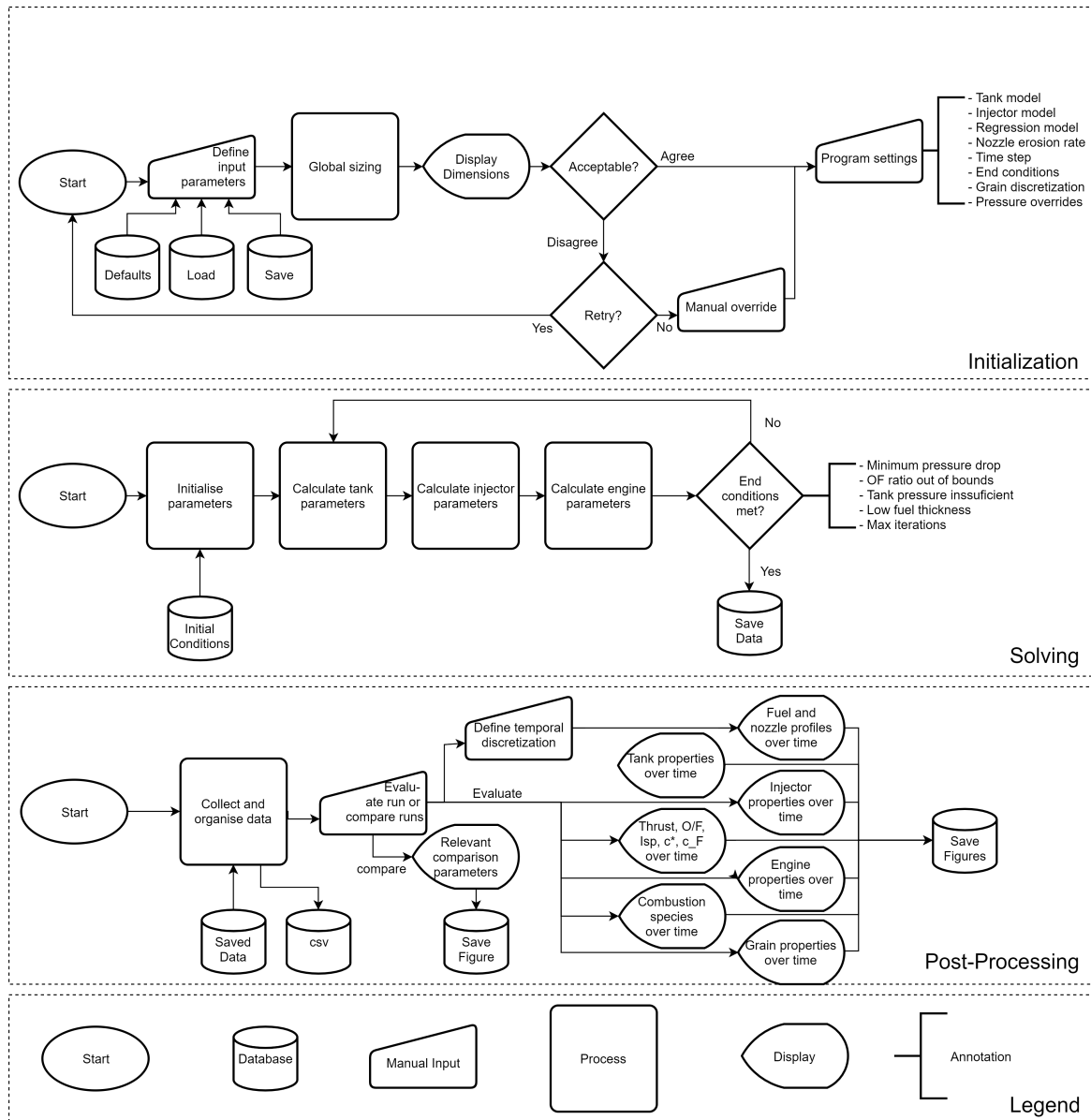


Figure 5.1: Software flow diagram

Each of the three processes described in Figure 5.1 use similar or the same equations and physical phenomena interchangeably. In order to minimise code duplication and thereby lose traceability, the structure in Figure 5.2 has been implemented. There are three folders that each contain code uniquely used for each of the three processes. One folder named `myEngines` stores the data of as many designs as desired each with sub folders of each run that was performed. This structure makes it easy to locate and compare older runs with the most recent ones. The folder `system_models` contains the full collection of engineering models and instantiates the data structures for the sub-components tank, injector and engine. The `physics` folder stores the scripts that deal with physical phenomena that are shared by all these processes. For example, the saturated properties of nitrous and rocketCEA fuel combinations and functions are defined there. Finally, the top folder contains the code that works with the three Graphical User Interfaces (GUIs). It performs no calculations itself, but handles all the user inputs and directs the triggers accordingly. These three GUIs are shown in section C.3

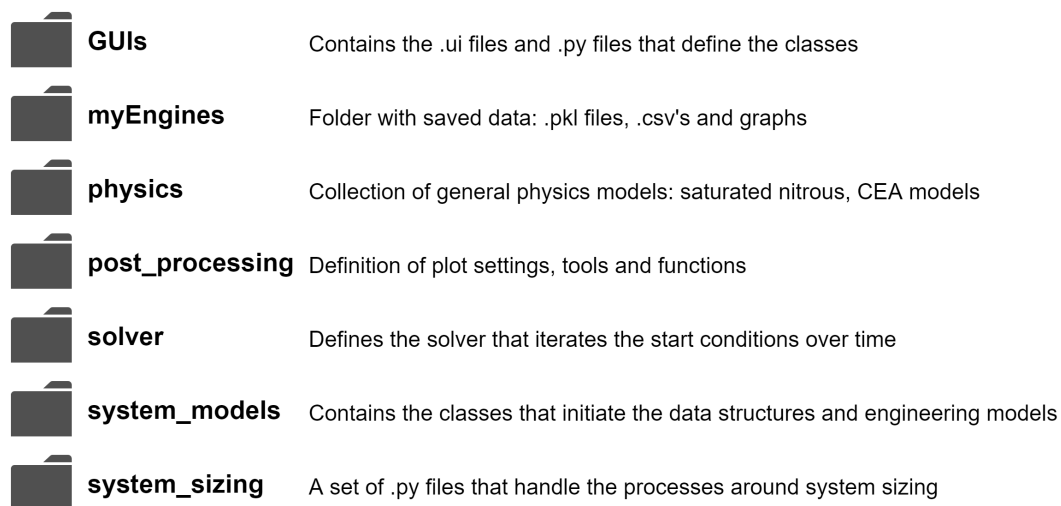


Figure 5.2: CHESS Folder Structure

5.2. Packages used

This section briefly mentions the four packages used in the development of CHESS. The way data and parameters are handled in CHESS are based on Numpy¹. It is used to export data as csv and load multiple previous runs to visualise and compare with current data. It is also the major structure used to internally store, transfer and manipulate data between the different processes running. Numpy 1D and 2D arrays are used to store temporal and spatial data efficiently and allows for fast data manipulation to speed up the software. Finally, data visualisation is done using the Matplotlib².

5.2.1. PyQt

PyQt³ is a powerful software package that allows users to develop highly customisable graphical user interfaces. Especially in combination with QT designer to develop the layout. The resulting widgets, buttons and values can be connected, calculated and manipulated in python code. This offers a high amount of flexibility and results in an interface that has been tailor made for its application. The structure of CHESS has therefore been built around the class structure of PyQt objects.

5.2.2. Combustion Equilibrium

Two combustion equilibrium software packages are often used: Chemical Equilibrium Applications (CEA) and Rocket Propulsion Analysis (RPA). The former is built by NASA and is freely available online. Its functioning is described in great detail by Gordon and McBride in [53, 54]. The principle has briefly been addressed in subsection 3.3.1. The latter, RPA, has a free option which allows only for a small amount of analysis and its use is then limited for small back-of-the-envelope calculations. In order to implement combustion equilibrium equations in python rocketCEA⁴ may be used. It "wraps The NASA Fortran CEA code and provides some useful tools" [35]. It is very useful for a more extensive analysis of propellant combinations or shifting O/F ratios through a motor's length or over time as it can very simply be run many times integrated in a larger python code. Since it wraps a Fortran code, some additional work is required to install the package. This has been documented in Appendix C.

5.3. Engineering Models

A multitude of engineering models is available to describe the processes in a hybrid engine. A selection of accessible and promising models is given here for implementation into CHESS. A distinct differentiation between models describing liquid or vapour nitrous has been made as it becomes a fundamentally different problem for each case.

¹<https://numpy.org/>

²<https://matplotlib.org/>

³<https://pypi.org/project/PyQt5/>

⁴<https://rocketcea.readthedocs.io/>

5.3.1. Tank modelling liquid nitrous

In order to model liquid nitrous oxide run tanks a deeper investigation into it's self-pressurising properties is required. An excellent overview of available models is given in Zimmerman et al. [55]. All the models run on the simplified nodes as shown in Figure 5.3, 4 in total. The propellant is split up in two nodes: vapour and liquid. The area outside of the tank is divided at the same place. Then a series of locations where heat and mass transfer occurs are identified. Using conservation of mass and energy, a set of equations can be constructed to solve the problem. All the different variations of this model can globally be split into two categories: phase equilibrium models and non-equilibrium models. The former assumes that the vapour and liquid inside the tank are saturated throughout time. This means that their temperature and pressure is equal and that the relevant gas properties are purely a function of temperature. These saturated conditions of nitrous are very well documented by ESDU [56] and will be discussed in subsection 5.3.5. Examples of such an equilibrium model are Whitmore & Chandler [57] and Casalino & Pastrone [58]. The non-equilibrium models all increase the complexity of the problem by removing certain assumptions. For example, Zilliac & Karabeyoglu [59] allow the liquid and vapour phase to be at different temperatures and directly calculate the heat and mass transfer between the two. Fernandez [60] evaluated this model in detail and added the option of using helium pressurant to increase the pressure of the tank over time. Casalino & Pastrone [58] also present a non-equilibrium model which uses the same basics, but applies a series of simplifying assumptions so the fluid properties can still be found at saturation conditions.

Zimmerman evaluates the performance of some of these models against experimental data and identifies that the authors may be able to get accurate results for their particular system, but only through the use of system-dependent empirical factors. There is a need for a robust and accurate tank model that can be used in a wide variety of systems. Zimmerman therefore proposes his own model in [61] where one of the key differences is that bubble formation is taken into account. A transparent tank has been constructed that shows the physical process inside the tank during emptying. Based on the experimental data a 1D linear model is set up that takes bubble formation, count and growth into account to estimate the pressure loss and recovery observed at the start of experimental tank emptying data. A diagram for this model is shown in Figure 5.4.

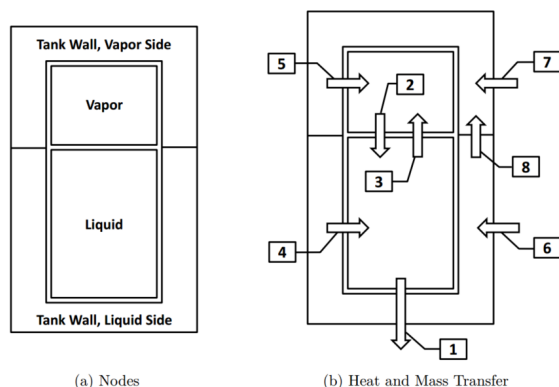


Figure 5.3: Diagrams showing the nodes and the heat and mass transfer processes between them for classical equilibrium and non-equilibrium models [55]

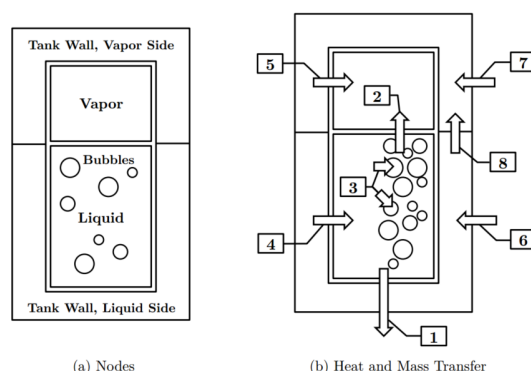


Figure 5.4: Diagrams showing the nodes and the heat and mass transfer processes between them for the proposed model by Zimmerman [61]

In short, the complexity and required computational power is the lowest for the equilibrium model. The non-equilibrium models are built on the same basic principles, but each with more realistic assumptions that increase the computational cost. The amount of complexity required for a certain application heavily depends on the required accuracy. The equations of the models described here have not been included as only tanks filled with vapour were attempted to be modelled for this study. It is recommended however that they be included in the modular software in the future to broaden the number of use cases.

5.3.2. Tank modelling vapour nitrous

Once the tank only contains vapour the problem becomes a lot simpler. The modelling of this process has been well described by Newlands [62]. It assumes an isentropic process meaning no energy is lost by heat transfer into or out of the walls of the tank. The isentropic relations are given in Equation 5.1

$$\frac{T_2}{T_1} = \left(\frac{P_2}{P_1} \right)^{\frac{\gamma-1}{\gamma}} = \left(\frac{\rho_2}{\rho_1} \right)^{\gamma-1} \quad (5.1)$$

next up, the vapour cannot be treated as an ideal gas as intermolecular forces are significant. A compressibility factor is required to describe their effect: $P = Z\rho RT$. The compressibility factor has been approximated as a single line from $Z = 1$ at 0 bar to the critical point. Using $\rho = \frac{m}{V}$ Equation 5.2 gives the following for a ratio of temperatures at the initial time and an arbitrary time later:

$$\frac{T_2}{T_1} = \frac{\frac{P_2}{Z_2 m_2} \left(\frac{V_{\text{tan}}}{R} \right)}{\frac{P_1}{Z_1 m_1} \left(\frac{V_{\text{tan}}}{R} \right)} \rightarrow \frac{T_2}{T_1} = \frac{P_2}{P_1} \left(\frac{Z_1 m_1}{Z_2 m_2} \right) \quad (5.2)$$

Substituting the temperature ratio for pressure using the isentropic equations in 5.1 yields Equation 5.3

$$\frac{T_2}{T_1} = \left(\frac{T_2}{T_1} \right)^{\frac{\gamma}{\gamma-1}} \left(\frac{Z_1 m_1}{Z_2 m_2} \right) \rightarrow \left(\frac{T_2}{T_1} \right) = \left(\frac{Z_1 m_1}{Z_2 m_2} \right)^{\frac{\gamma-1}{-1}} = \left(\frac{Z_2 m_2}{Z_1 m_1} \right)^{\gamma-1} \quad (5.3)$$

Here Z_2 is required to be known although it is a function of the outcome of this ratio. An iterative approach is therefore used where Z_2 is initially estimated to be equal to Z_1 after which it is allowed to converge to its updated value. The final temperature ratio can be used to calculate the other fluid properties using the isentropic relations in Equation 5.1

5.3.3. Injector modelling liquid nitrous

The tank emptying process is dictated by the amount of nitrous flowing out of the system. However, since nitrous is a two-phase system, it complicates the behaviour. At the pressures used for propulsion the liquid phase is not compressible and the vapour phase is not an ideal gas. Dyer et al. [63] suggests a viable model to predict two-phase injector flow relations and compares it to experimental data. Two different models are incorporated: a Single Phase Incompressible model (SPI) and a Homogeneous Equilibrium Model (HEM). Figure 5.5 shows a comparison of the static pressure history between a high- and low-vapour pressure liquid injector to illustrate the difficulty of modelling a two-phase flow due to the difference in physical behaviour.

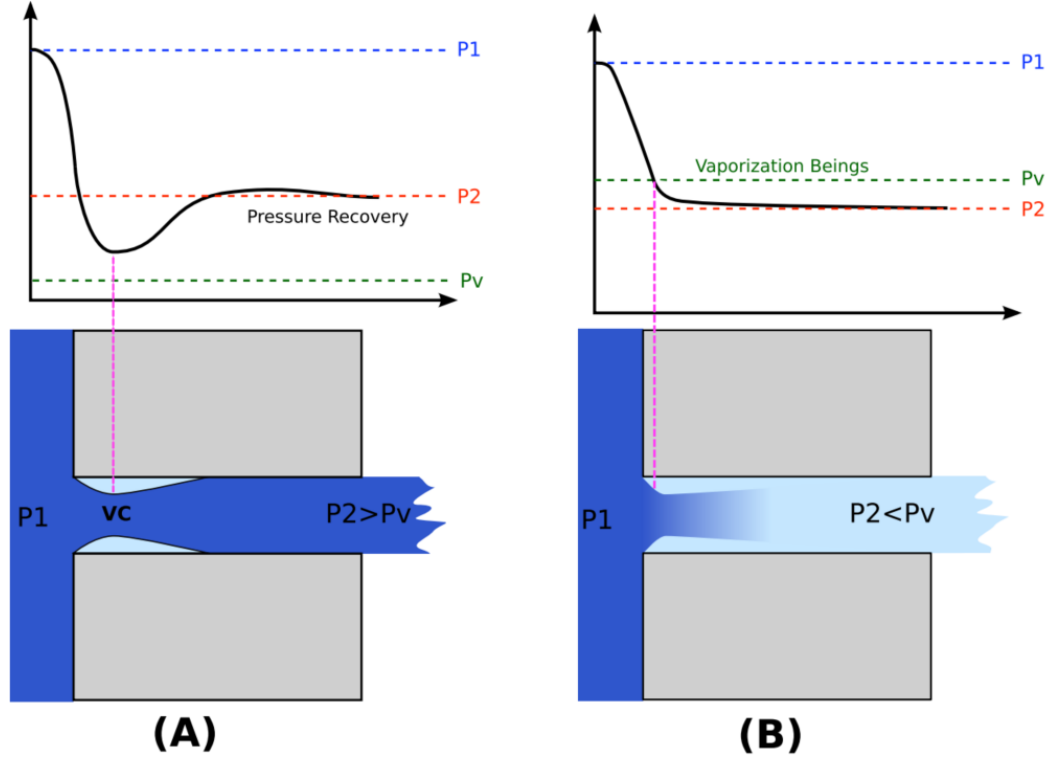


Figure 5.5: Conceptual Injector Element Pressure History [63]

It then follows the assumption that the flow rate should follow smoothly between the two, which results in the following set of equations:

$$G = C_d \left(\frac{1}{1+k} G_{SPI} + \left(1 - \frac{1}{1+k} \right) G_{HEM} \right) \quad (5.4)$$

$$G_{SPI} \equiv \frac{\dot{m}}{A} = \sqrt{2\rho_1 \Delta P}, \quad G_{HEM} = \rho_2 \sqrt{2(h_1 - h_2)} \quad \text{and} \quad k = \frac{\tau_b}{\tau_r} = \sqrt{\frac{P_1 - P_2}{P_v - P_2}} \quad (5.5)$$

Solomon [64] continues this work by first making a correction to Dyer's final equation of the Non-Homogeneous Non-Equilibrium Model (NHNE). It is assumed that this equation was originally intended by Dyer et al. since it is consistent with the physical explanation given. The factor k will increase when the bubble formation time τ_b is large and the liquid residence time τ_r is small. A fluid with a low amount of bubbles formed will correspond more to a single phase incompressible fluid. Therefore it seems that the factors need to be swapped. While rewriting mass flux to mass flow this correction yields:

$$\dot{m}_{NHNE} = C_d \cdot A_c \cdot \left(\left(1 - \frac{1}{1+\kappa} \right) \dot{m}_{SPI} + \frac{1}{1+\kappa} \dot{m}_{HEM} \right) \quad (5.6)$$

Solomon then continues to describe a two-phase enthalpy algorithm based off of the two-phase entropy model suggested by Whitmore and Chandler [57]. This entropy model was constructed to overcome mass flow inaccuracies for both the HEM and NHE models. The enthalpy algorithm takes the total fluid enthalpy and propagates it over time instead of the entropy as the assumption of isentropic expansion over the injector plate is known to be physically incorrect [64, p. 12]. A key parameter of the injection system of a liquid system is atomisation, as it defines the combustion process that follows as well as stability characteristics. Waxman, Cantwell, and Zilliac [65] gives a good overview on the effects of injector design on a self pressurising oxidiser such as nitrous oxide and the effects should be taken into account for an injector model. The equations described in this section have been included in the model, but could not be validated as only vapour flow is used in this study.

5.3.4. Injector modelling vapour nitrous

A simple vapour nitrous injection model was used by Whitmore and Chandler [57]. It uses the choked flow compressible version of the discharge coefficient equation, given in Equation 5.7, when the pressure ratio over the orifice is below the critical ratio.

$$\dot{m}_{V, out} = A_{out} C_{d_{out}} \cdot \sqrt{\gamma P_{\text{tank}} \cdot \rho_v \left(\frac{2}{\gamma + 1} \right)^{(\gamma+1)/(\gamma-1)}} \quad (5.7)$$

When this ratio is higher the pressure drop is insufficient to choke the flow and thus downstream conditions need to be taken into account. This results in the subsonic version given in Equation 5.8

$$\dot{m}_{v, out} = A \cdot C_d \sqrt{\frac{2\gamma}{\gamma - 1} \rho_v P_{\text{tank}} \left[\left(\frac{P_2}{P_{\text{tank}}} \right)^{2/\gamma} - \left(\frac{P_2}{P_{\text{tank}}} \right)^{(\gamma+1)/\gamma} \right]} \quad (5.8)$$

5.3.5. Saturated properties of nitrous oxide

The following set of equations has in its entirety been retrieved from ESDU [56]. This selection of available equations provide the thermophysical properties of nitrous oxide on the saturation line. On the saturation line all these properties are dependant on the temperature only and can therefore be scaled to the ratio of the temperature to the critical temperature $T_r = T/T_c$. These physical constants are given in Table 5.1, whereas the empirical constants used in equations 5.9-5.16 are given in Table 5.2

Table 5.1: Physical nitrous constants from [56]

Physical Constants	Symbol	Value
Molecular Weight	M_c	44.013
Critical Temperature	T_c	309.57 K (36.42 \Degree C)
Critical Pressure	p_c	7251. kPa
Critical Density	ρ_c	452. kg/m ³

$$\log_e \left(\frac{p}{p_c} \right) = \frac{1}{T_r} \left[b_1 (1 - T_r) + b_2 (1 - T_r)^{3/2} + b_3 (1 - T_r)^{5/2} + b_4 (1 - T_r)^5 \right] \quad (5.9)$$

Density of the Saturated Liquid:

$$\log_e \left(\frac{\rho(l)}{\rho_c} \right) = b_1 (1 - T_r)^{1/3} + b_2 (1 - T_r)^{2/3} + b_3 (1 - T_r) + b_4 (1 - T_r)^{4/3} \quad (5.10)$$

Density of the Saturated Vapour:

$$\log_e \left(\frac{\rho(g)}{\rho_c} \right) = b_1 \left(\frac{1}{T_r} - 1 \right)^{1/3} + b_2 \left(\frac{1}{T_r} - 1 \right)^{2/3} + b_3 \left(\frac{1}{T_r} - 1 \right) + b_4 \left(\frac{1}{T_r} - 1 \right)^{4/3} + b_5 \left(\frac{1}{T_r} - 1 \right)^{5/3} \quad (5.11)$$

Specific Enthalpy of the Saturated Liquid:

$$h(l) = b_1 + b_2 (1 - T_r)^{1/3} + b_3 (1 - T_r)^{2/3} + b_4 (1 - T_r) + b_5 (1 - T_r)^{4/3}. \quad (5.12)$$

Latent Heat of Vaporisation (Specific Enthalpy of Vaporisation):

$$\Delta_{\text{vap}} h = h(g) - h(l). \quad (5.13)$$

Specific Enthalpy of the Saturated Vapour:

$$h(g) = b_1 + b_2 (1 - T_r)^{1/3} + b_3 (1 - T_r)^{2/3} + b_4 (1 - T_r) + b_5 (1 - T_r)^{4/3} \quad (5.14)$$

Isobaric Specific Heat Capacity of the Saturated Liquid:

$$c_p(l) = b_1 \left[1 + b_2 (1 - T_r)^{-1} + b_3 (1 - T_r) + b_4 (1 - T_r)^2 + b_5 (1 - T_r)^3 \right]. \quad (5.15)$$

Isobaric Specific Heat Capacity of the Saturated Vapour:

$$c_p(g) = b_1 \left[1 + b_2 (1 - T_r)^{-2/3} + b_3 (1 - T_r)^{-1/3} + b_4 (1 - T_r)^{1/3} + b_5 (1 - T_r)^{2/3} \right] \quad (5.16)$$

Table 5.2: Constants used in equations from [56]

Property	b_1	b_1	b_1	b_1	b_1	Range of Applicability \degree C
p	-6.71893	1.35966	-1.3779	-4.051	-	-90 to 36
$\rho(l)$	1.72328	-0.83950	0.51060	-0.10412	-	-90 to 36
$\rho(v)$	-1.00900	-6.28792	7.50332	-7.90463	0.629427	-90 to 36
h(l)	-200.	116.043	-917.225	794.779	-589.587	-90 to 35
h(v)	-200.	440.055	-459.701	434.081	-485.338	-90 to 36
$c_p(l)$	2.49973	0.023454	-3.80136	13.0945	-14.5180	-90 to 30
$c_p(v)$	132.632	0.052187	-0.364923	-1.20233	0.536141	-90 to 30

5.3.6. Regression Modelling

Marxman [66, 67] developed a regression rate model in the 60's that still serves as a basis for contemporary models. Adjustments and additions are frequently made but the fundamental theory still stands. An overview of Marxman's diffusion-limited theory as well as additional applicable models for certain hybrid engine configurations is given by Marquardt and Majdalani [68]. In general, a large amount of papers have been published on the analysis of regression rate as it is so fundamental to hybrid combustion. Most, however, are very detailed and only apply to a particular system. This gives them a narrow range in engine size and only for a certain propellant combination. For any study of hybrid engines, the exact application needs to first be determined before an applicable model can be selected. As a basis for this study the simple exponential model for the regression rate is used.

$$\dot{r} = a \cdot G_{ox}^n \quad (5.17)$$

This equation can give a good approximation only if the values have been retrieved from comparable experimental data. These have been retrieved from Whitmore [69] by applying a least squares exponential fit to the mass flux versus regression rate plots. This yielded the values $a = 0.312040 \text{ (mm/s)/(kg/(m}^2 \text{ s))}^n$ and $n = 0.272200$. For the purpose of this study these values were deemed sufficient with the addition of two models discussed in the next paragraphs: regression rate amplification due to helical fuel port geometries and the addition of radiant heat transfer. In the future though, it is recommended to add more sophisticated base models as well.

Helical fuel port

A model for the regression rate amplification due to helical fuel ports is suggested by Whitmore and Walker [13]. The model is based on two amplification factors. This means that multiple regression rate models can be used as a base which allows for increased modularity of the software. The application of these factors is given in Equation 5.18

$$\dot{r}_{\text{helical port}} = (A_{C_f} A_{\beta}) \dot{r}_{\text{straight port}} \quad (5.18)$$

The first increase can be attributed to the increased skin friction coefficient. In order to model this effect, first the geometry of the helix needs to be defined. This geometry changes over time as the fuel regresses away. This understandably, erodes the helical profiles and attenuates the amplification. Over time, the profile will look more like a wide port with distinct ridges. This is visualised in Figure 5.6[13].

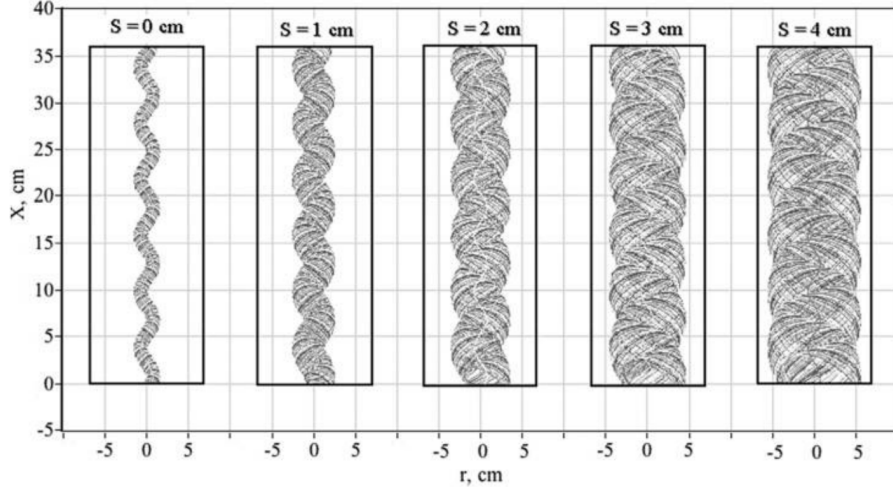


Figure 5.6: Example port cross sections for five different mean linear regression values from Whitmore and Walker [13]

This effect can be modelled using the effective radius of curvature which is derived from the actual radius of curvature based on the helix radius and pitch length. These relations are given in Equation 5.19.

$$R_c = r_{\text{helix}} \left[1 + \left(\frac{P}{2\pi \cdot r_{\text{helix}}} \right)^2 \right] \rightarrow R_{c_{\text{eff}}} = R_c \sqrt{1 + \frac{\pi}{2} \left(\frac{D - D_o}{R_c} \right)^2} \quad (5.19)$$

Implementing these in the skin friction estimation of helical coils by Mishra and Gupta yields Equation 5.20.

$$A_{C_f} = \left(C_{f_{\text{straight port}}} + 0.0075 \sqrt{\frac{D}{2R_{c_{\text{eff}}}}} \right) / C_{f_{\text{straight port}}} \quad (5.20)$$

$$= 1 + \frac{0.0075}{C_{f_{\text{straight port}}}} \sqrt{\frac{(1/2) \frac{D}{R_c \left[1 + (\pi/2) (D - D_o)/R_c \right]^2}}{1/2}}$$

Here it is required to find the skin friction factor for straight ports. Whitmore and Walker [13] uses the simple Blasius turbulent skin friction model given in Equation 5.21. Here Re_l is the Reynolds number based on fuel port length.

$$C_{f_{oL}} = \frac{0.074}{(Re_L)^{1/5}} \quad (5.21)$$

The Reynolds number can be found using the mass flux and the fluid viscosity. The latter is retrieved from rocketCEA. The simple derivation is shown in Equation 5.22.

$$\dot{m} = \rho A V \quad \text{and} \quad G = \frac{\dot{m}}{A_{\text{port}}} \rightarrow G = \rho V \quad (5.22)$$

$$Re_L = \frac{\rho V L}{\mu} \rightarrow Re_L = \frac{G L}{\mu}$$

The second factor originated from suppressed radial wall blowing. The radial flow velocity is increased due to the swirling motion of the oxidiser. This radial component will reduce the effect of wall blowing as described in subsection 3.2.2. Whitmore and Walker [13] uses Boardman's radial wall blowing correlation, that states that regression rate is inversely proportional to the blowing coefficient to the 0.77 power. The result is the blowing suppression amplification factor in Equation 5.23.

$$A_\beta = \left[1 + 2(2\pi N)^2 \left(\frac{\rho_{\text{wall}}}{\rho_{\text{ox}}} \right) \left(\frac{G_{\text{ox}}}{G_{\text{fuel}}} \right)^2 \left(\frac{2r_{\text{helix}}}{D} \right) \right]^{0.77} \quad (5.23)$$

$$= \left[1 + 2 \cdot (2\pi N)^2 \left(O/F^2 \frac{M_{w_{\text{wall}}}}{M_{w_{\text{ox}}}} \right) \left(\frac{2r_{\text{helix}}}{D} \right) \right]^{0.77}$$

Radiant Heat Transfer

ABS is a liquefying fuel, same as paraffin. However, as discovered by Whitmore and Merkley [70] their behaviour is different from legacy hybrid fuels. It shows a strong correlation to the diameter of the motor, where smaller motors tend to burn fuel rich. An extension to the Marxman regression rate model, as discussed in section 3.2, was developed to account for radiant heat transfer to the material surface. This results in the following equation:

$$\dot{r} = \frac{0.635}{\rho_f \cdot P_r^{2/3}} \left(\frac{\Delta h_f}{h_v} \right) \cdot \left(G_{ox}^n \cdot \left(\frac{\mu}{x} \right)^{1-n} \right) \cdot \left(\frac{G_{ox}^n \cdot (\mu/x)^{1-n}}{2 \cdot \rho_f \cdot \dot{r}} \right)^{0.77} + \frac{\sigma_B \cdot (\varepsilon \cdot T_0^4 - \alpha \cdot T_f^e)}{\rho_f \cdot h_v} \quad (5.24)$$

Here the basis of the regression rate model is the Marxman model, but for the purposes of this study only the addition of the radiative term is used. Here h_v is the enthalpy of pyrolysis of the fuel material which has been found to be 3.070 MJ/kg by Whitmore et al. [71]. The fuel surface absorptivity has been set at 0.93, to take the lower bound of a black plastic given that a dark grey fuel is used, but can be adjusted manually in the user interface. The plume emissivity however varies from 0.53 to 0.15 in Whitmore and Merkley [70]. This wide range can likely be attributed to the variance of combustion products over grain length. The plume will mainly contain the optically more transparent nitrous at the oxidiser rich start of the grain whereas the products from the pyrolysed fuel will cause the plume to become more opaque. Improved accuracy might be achieved by making the emissivity a function of the O/F ratio at a certain position along the length of the grain. Finally, the fuel surface temperature is assumed to be equal to the chamber temperature. This assumption is deemed valid due to the insulation provided by the surface film layer on the ABS. This film layer is formed due to the glass transition process of ABS and prevents almost any heat from conducting into the fuel itself, which would cool down the actual fuel surface temperature. For situations where this assumption does not hold, it can be estimated using classical Arrhenius reaction kinetics parameters. These are described in Equation 5.25 from Eilers and Whitmore [72].

$$\dot{r} = A_k e^{-\frac{E_a}{R_u T_s}} \rightarrow T_s = \frac{E_a}{R_u (\ln(A_c) - \ln(\dot{r}))} \quad (5.25)$$

5.3.7. Nozzle Modelling

Since a graphite nozzle is used, some erosion is to be expected. Mainly the throat diameter will be affected, significantly influencing the chamber pressure and therefore also the mass flow, regression rate and thrust produced. The nozzle divergent section is also expected to erode, though at a much lower rate since the heat flux and stress on the material are much lower. A change in exit diameter will influence the thrust level through a change in expansion ratio. Both these effects will be modelled using a linear erosion constant. This will cause the diameter of the nozzle throat and exit to increase linearly and their respective areas quadratically.

5.4. Conclusion

In this chapter the design of an easy to use preliminary design tool has been described. It's structure has been described and the used packages and their merits listed. Most importantly it offers the beginning of the answer to research question 4. In section 5.3 a list of models, with recommendations for potential future improvements, has been given. Multiple models for self-pressurised tanks are available and are expected to offer sufficient accuracy. These models are strongly coupled to the injector models of which plenty are available for both vapour and liquid phases of nitrous. In terms of hybrid regression rates, only a simple formula has been applied so far but the potential exists to add a large set of more sophisticated models and increase the reliability of the current tool.

6

Test setup

In this chapter the experimental test setup that has been used is described. First of all, the thruster assembly will be treated in section 6.1. In order to assess research question 5 a variety of engine configurations was tested and as such it includes a discussion and justification of the different configurations that have been tested. The P&ID and tank design are given in section 6.2. It gives an overview of the system and allows for an introduction of the test bench, high voltage generator and sensors used in section 6.3, section 6.4 and section 6.5 respectively. With an overview of the setup and its requirements a brief overview of the LabView program that was developed to operate the setup is given in section 6.6. Finally the results are concluded in section 6.7.

6.1. Engine Assembly

Figure 6.1 shows the engine assembly in two cross sections in two different 90 ° offset orientations. The two engineering drawings, one with the cross sections and one exploded view with Bill Of Materials (BOM), that these are based on can be found in Appendix B on pages 123 and 124. The production plans and engineering drawings of all the individual components discussed in this section have been worked out in Appendix B. This section will therefore focus only on giving a rationale as to why design decisions were made and clarify the overall result and not explain the machinability and production design considerations.

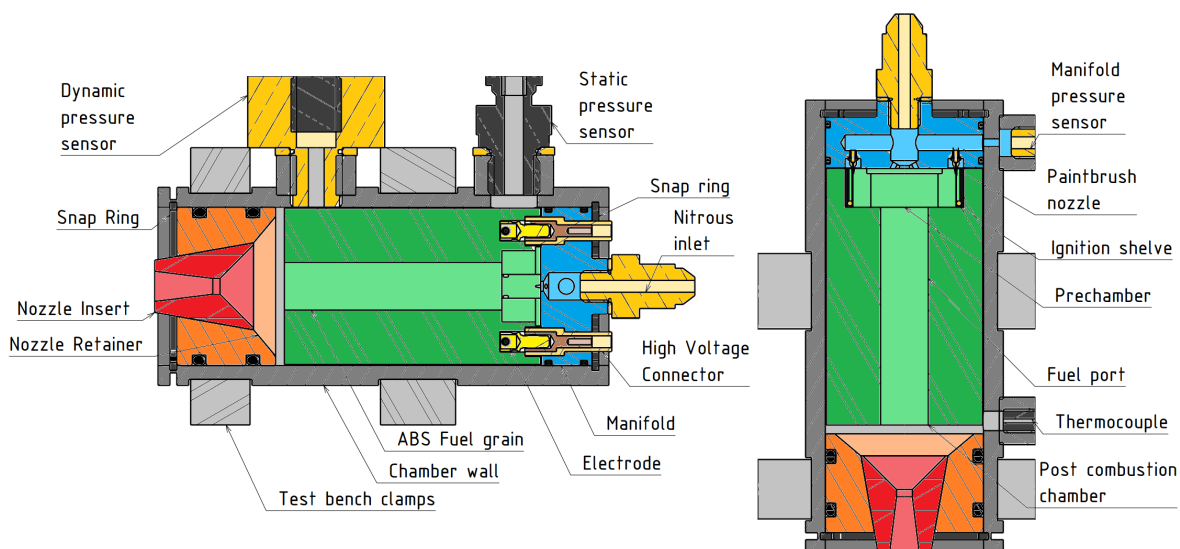


Figure 6.1: Cross section of side view (left) and top view (right)

Globally the design is made up of 3 components: the injector manifold, fuel grain and nozzle assembly. The nozzle insert (red) is supported by the nozzle retainer (orange). The grain (green) sits almost directly on top. The embedded ignition electrodes are shown in yellow. Thirdly, the injector manifold (blue) sits in the top of the chamber and has insulated connectors for the electrodes (brown and yellow) and the brass feed system adaptor in the top (yellow). On the side view the static and dynamic pressure sensor adaptors are shown. The top view shows the manifold static pressure sensor and combustion chamber thermocouple inlet. These sensors will be treated later in section 6.4. Here the three main parts will be further worked out in their three respective subsections 6.1.1, 6.1.2 and 6.1.3. Subsequently, subsections 6.1.4 and 6.1.5 elaborate on the exact difference between the injectors and grain geometry of the configurations.

6.1.1. Injector manifold

The injector manifold is inserted in the chamber and constrained by a snap ring. The oxidiser is introduced from the back and a hole is present on the side to measure the pressure just before the injector. It features two high pressure, high temperature resistant, non-conductive interfaces that are used to lead the ignition power into the metal chamber. Although they are made from PEEK (Polyether ether ketone), a relatively temperature resistant plastic, they still need to be well insulated from the high temperature combustion gases. For this purpose silicone elastomer is used. It covers the entire face plate of the injector and provides a glued and inhibited surface between the manifold and the grain.

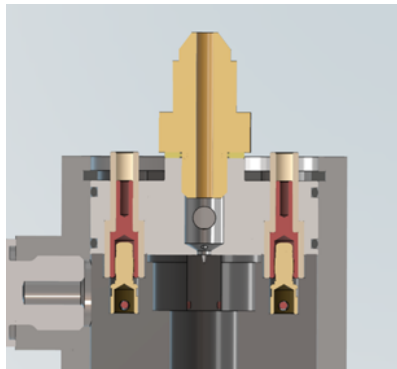


Figure 6.2: Manifold cross section

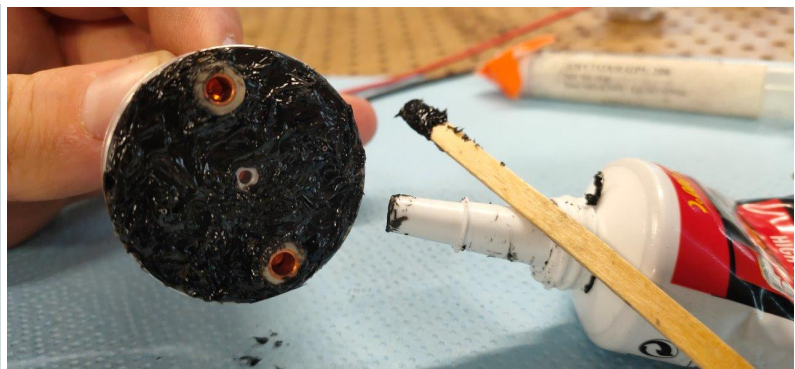


Figure 6.3: Application of silicone elastomer for temperature sensitive components

6.1.2. ABS fuel grain

Most of the fuel grain comes ready from the printer. However a few steps need to be performed still. The grain has to be set and its electrodes inserted and glued with ABS cement. The setting of the grain is done before electrode insertion since that allows setting of both the ignition shelves individually. This potentially increases the chances of ignition, especially when multiple restarts are attempted. After electrode insertion, the grain setting may be repeated to ensure proper operation of the full assembly, but once the electrode is in, even a small difference in distance will cause the air gap to break only on one side. That happens because initially a spark is formed between the two electrodes through the air. After a few iterations and by potentially reducing the voltage to prevent the spark from forming, a flame will start. During combustion of the flame the fuel surface will be carbonised and finally a char path may be formed that carries all the current through the plastic enabling the release of high temperature hydrocarbon vapour. This process is shown in images 6.4, 6.5 and 6.6.



Figure 6.4: Initial spark



Figure 6.5: Formed flame



Figure 6.6: Final char path

Please note that the crocodile clips have been partially burnt during a demo where oxygen was blown through the grain in atmospheric conditions. When the high voltage is only applied for a short duration of a few seconds no sustained flame will form and the process can be carried out in a lab under a few safety precautions. First of all, proper ventilation is required to ensure none of the combustion products are inhaled. A suction hood with sufficient flow rate has shown to be very effective. Second of all, since high voltage is applied this process is never to be carried out alone and can only be performed with permission from or under supervision of an officer of the safety board. Finally, the high voltage leads need to be discharged and the system disarmed before anything is touched and the grains can be switched out.

6.1.3. Nozzle Assembly

As per requirements PROP-5 and PROP-6 the nozzle needs to survive the harsh thermal conditions of the exhaust flow for a duration of 16s and thus the nozzle will be made from graphite. Graphite is specifically known for it's high heat resistance and a common nozzle material in both the amateur and professional community due to it's accessibility and relative low cost, compared to alternative solutions. It is still not a cheap material however and machining larger components costs a significant effort due to the fine carbon particles and dust that are released during machining operations. In addition, this motor has relatively large diameter for the thrust it produces due to the sizing requirement STRA-1. The graphite nozzle has therefore been made smaller than the full diameter of the motor. The graphite insert is suspended in a reusable retainer ring that is the full diameter of the engine. This retainer ring is made of simple steel and thermally insulated using the same silicone elastomer as used for the adhesion between the grain and the manifold. The O-rings are lubricated using standard bearing grease and the top O-ring has another thick layer of silicone elastomer between it and the engine internals. In total 10 graphite inserts and 3 retainers have been made.



Figure 6.7: Back view of two nozzle parts



Figure 6.8: Front view of two nozzle parts

6.1.4. Injector configurations

The heritage injector design featured one central hole and two diagonal holes aimed from the centre at the two ignition shelves on the fuel grain. This design is limited by manufacturing constraints. Using the available manual machines the rotation speed is limited to 3000 rpm and no accurate clamping solutions exist for drills under 1mm in diameter. Without an accurately centered drill with the appropriate rotation speeds (at or over 10000rpm) the likelihood of the drill breaking in the work piece is unacceptable. A solution was found by using paint brush nozzles. They feature an M1.8 thread and have nozzle diameters of 0.2, 0.3 and 0.5mm, the smallest and largest of which were chosen to be tested. It was chosen to test three different injector designs to investigate two parameters: upper and lower mass flow boundaries for successful ignition as per research question 5(a) and radial burn symmetry to reduce ignition shelf regression and promote restartability as per research question 5(b). This is achieved by a reduced ignition to main flow ratio, which could only be achieved using smaller injector nozzles. The two different designs are shown together in Figure 6.9. The red ellipses indicate the two radial airbrush nozzles located directly above the ignition shelves. The blue circles in the center show the two diagonal holes in the center of the injector. The detailed engineering drawing can be found on 111.

6.1.5. Grain configurations

Two different grain geometries have been tested. One is the standard straight port design. For the second it was decided to use the helical port design. The helical port amplifies the regression rate and is a feature that is currently unique for 3D printed fuel grains. As the regression rate is an inherent complication for hybrid engines and 3D printing offers a unique solution, it was decided that this benefit should be attempted to be quantified. The difference between these two grains should give an answer to research question 5(c). The straight port is designed to be 12mm in diameter with a length of 55mm and a pre-chamber of 10mm. The helical grain has a 1.5mm offset from the center and a 20mm phase.

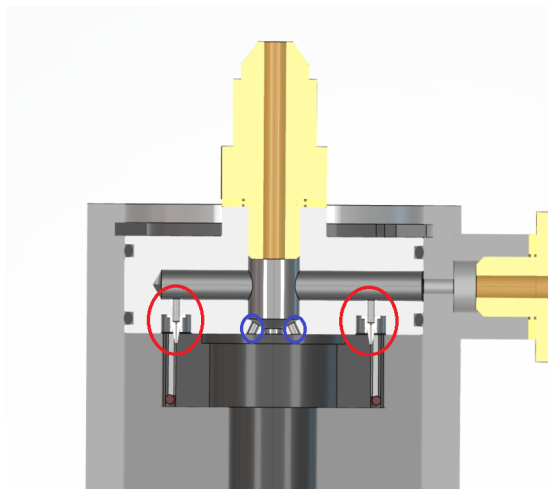


Figure 6.9: Two injector configurations visualised in one part

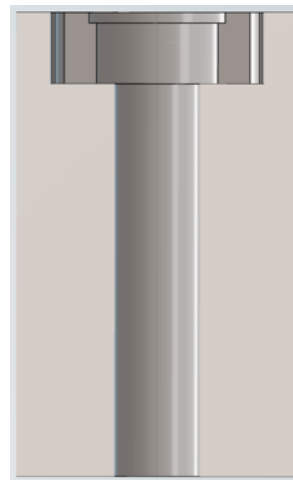


Figure 6.10: ABS fuel grain with a straight port

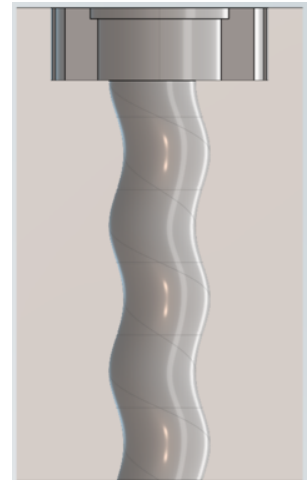
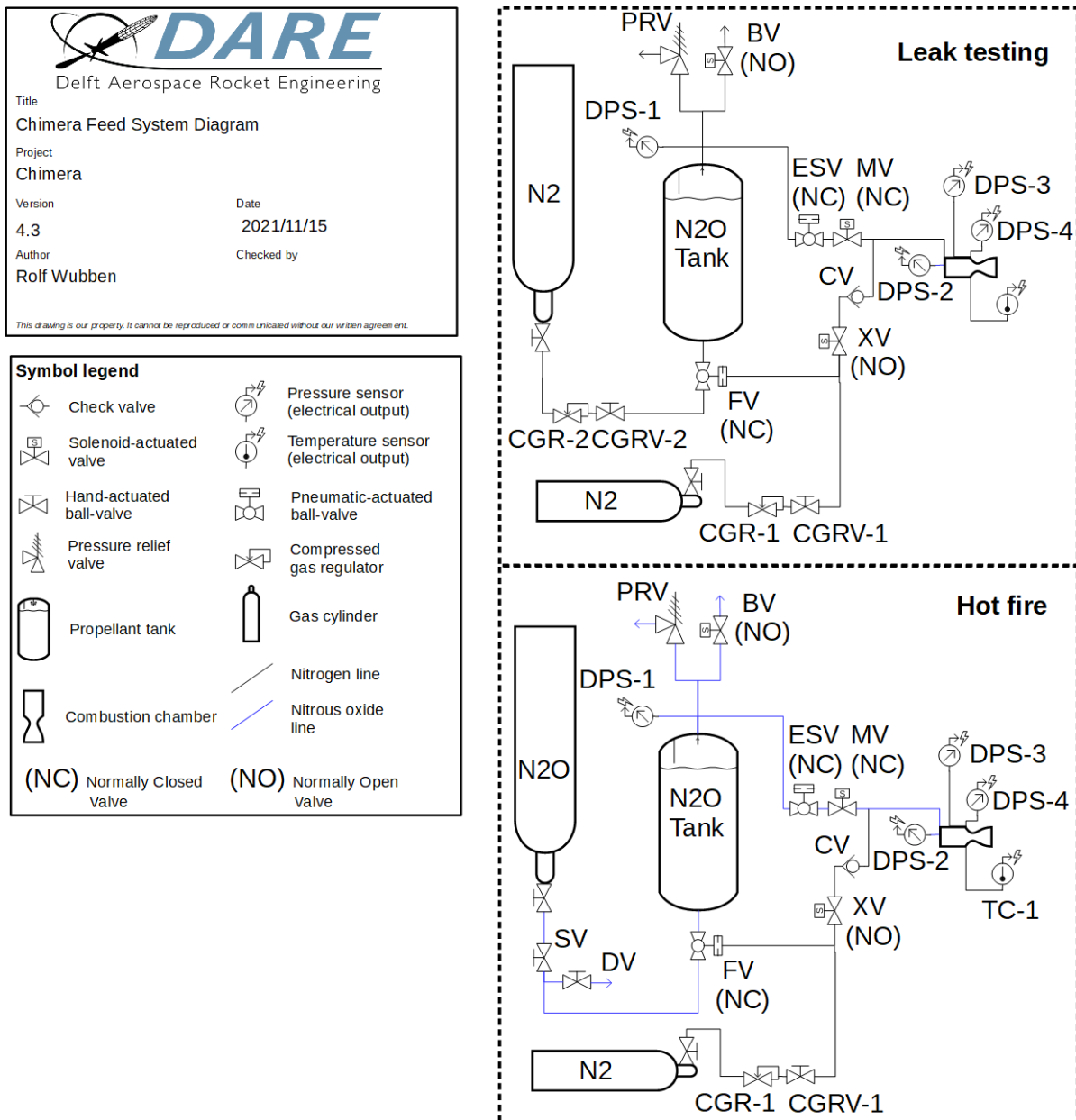


Figure 6.11: ABS fuel grain with a helical port

6.2. P&ID and system overview

An overview of a feed system is given in a Piping and Instrumentation Diagram or P&ID. It shows all the valves and their physical locations as well as the instrumentation of the system associated with the feed system. It is used to design the system, address the safety of the system and to keep an overview and troubleshoot when problems arise during testing. Two feed system configurations are being used: one to allow for step wise leak testing the system with a nitrogen bottle before nitrous is introduced and the other for a hot fire configuration with nitrous oxide supplied to the run tank. Both configurations are shown in Figure 6.12.



Many of the elements are associated with the safety requirements of subsection 1.3.2. A pressure relief valve is present that will blow off pressure when it reaches maximum expected operating pressure (MEOP) at 70 bar. A normally open bleed valve is present to vent the tank and reduce the pressure at command. It is essential that it is normally open. In case control of the system is lost the power can be removed from a distance, returning the system to a safe predictable state after which it can be approached again. A normally open extinguisher valve is used to safe the system by extinguishing any remaining fire and as a bonus preserves the state of the fuel grain at shutdown by cooling and solidifying it. Once again the NO design enables the system to be able to return to a safe state while testing personnel can keep their distance. A check valve is installed in parallel to prevent the high pressure nitrous oxide from flowing into the low pressure nitrogen system. On the main line an emergency safety valve is installed in parallel to the main valve. This valve is normally closed and its operation is entirely independent of the rest of the system. It is powered by a battery and actuated with a physical switch. This implies that even when system control is lost, the engine can be shut off from a distance. Any fault in the ESV system means power will be cut and the valve closes. The battery will be at 40m distance

together with the laptop controlling the system. Two gas bottles are attached to the system. The larger bottle is used to fill the tank whilst the small nitrogen bottle is used to pressurise the pneumatic fill valve as well as supply nitrogen to the extinguisher valve. Both nitrogen bottle output pressures are regulated, whereas the nitrous pressure depends on the temperature and sunlight conditions of the day. The tank pressure is regulated by filling and venting operations. For colder weather, a heating wire is installed around the tank that can be used to increase the pressure. The nitrous oxide is drawn from the top of the tank. The classical concept is to use the vapor pressure in the top of the tank to push out the liquid on the bottom. However, this design originated from Stratos IV and as per requirement STRA-2 the roll control system has to be placed on top of the tank and drawing nitrous vapour (PROP-2). This legacy item is decided to be kept as it simplifies orifice manufacturing due to the prohibitively small diameters otherwise required for denser liquid flows at this thrust scale. However, also a larger valve is required to allow for the mass flow of the less dense vapour. The Pulsoid X-10 350 BHP ¹ is therefore used as the main valve of the system. It has a fast cycle time and still allows for a significant volumetric flow. The pressure relief valve comes from the same manufacturer as the valve and is the Nitrous Safe Pressure Relief Valve (SPRV) 1/8 BSP thread ². A linear bearing constrains the tanks movement within the frame and an S-type load cell keeps it in place and measures the mass. It should be noted that due to the low mass flows and relatively high tank mass this data is relatively noisy compared to the other sources. The tank itself is made of a 5mm thick aluminium tube with two bolted bulkheads sealed with O-rings and suspended in a aluminium frame. The frame is secured rigidly by 3 tension straps that are anchored into the field using steel pegs. The tank has been inherited from project Stratos and has been designed to fail in the axial direction. This has been validated by a destructive test. It's analysed failure modes and dimensions are summarised in Table 6.1.

Table 6.1: Tank failure calculations

Material	Aluminium 6082	–
MEOP	70	bar
Tank inner diameter	100	mm
Wall thickness	5	mm
Radial burst pressure	272	bar
Radial burst SF	3.89	–
Bolt configuration (top & bottom)	6x M8, 10.9	–
Bolt failure pressure	144.5	bar
Bolt failure SF	2.06	–
Bolt spacing to edge (top & bottom)	13	mm
Shear-out failure pressure	118	bar
Shear-out SF	1.69	–

6.3. Thrust bench

The thrust bench was designed and built previously by another project for general use. The design process and resulting hardware are documented in [73]. It is a multipurpose modular test bench that allows for a wide range of setups to be tested. The top plate features a 50mm matrix of M8 tapped holes that allow for a variety of clamps to be attached. This plate is suspended on two solid rods and slides on linear bearings. The bottom frame is anchored in the ground using steel rods. On the bottom a mounting structure is present to allow for a load cell to be attached. In addition, a spring with turnbuckle is present to set some pretension on the load cell. This requires a new offset calibration for every test campaign, but ensures that the measured data is away from the non-linear behaviour of the load cell around it's zero value. On the bench a vertical cable guide was constructed to organise the large amount of cables from the different sensor that were used. The cables and sensors can also be removed from the bench and suspended from the back of the plate which allows for easy removal of the testing equipment when the multipurpose bench is needs to be used by another team in between testing campaigns. The equipment is shown in Figure 6.13. On the left hand side the thruster with all

¹<https://www.noswizard.com/nitrous-control/nitrous-solenoids/x-10-nitrous-solenoid-350-bhp.html>

²<https://www.noswizard.com/nitrous-sprv-1-8-bsp.html>

its pressure and temperature sensors can be seen. The acoustic sensor is inserted in a machined and threaded piece of plastic to allow for dampening of vibration from the hot fire. The large emergency safety valve features as a mounting point for the feed system to the bench. The much smaller blue main valve is also directly attached to the rigid ESV using swivelled feed system connectors.

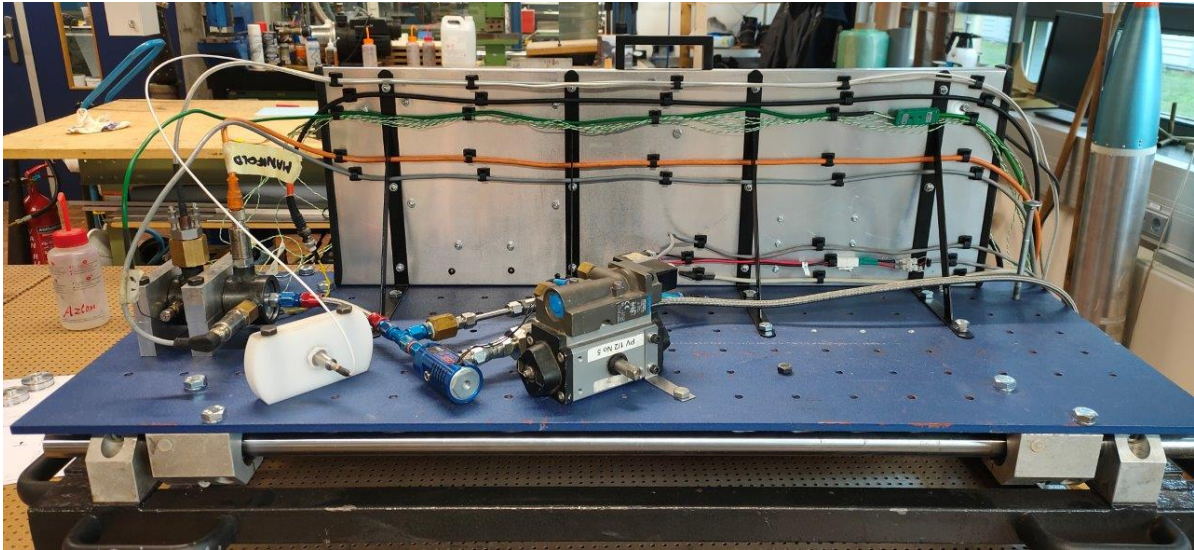


Figure 6.13: Layout of the thrust bench including vertical sensor cable guide

The full setup on the field is shown in Figure 6.14. It includes the data acquisition system on the right front, the tank in the right back and the thruster with the exhaust aimed left. A shrapnel box was placed around the thruster to ensure no shrapnel could spread radially from the thruster.



Figure 6.14: Layout of the full test setup

6.4. Data Acquisition

Data is acquired using a cRIO module from National Instruments. It is housed in a rigid stainless steel box that is able to sustain anomalies during rocket engine test campaigns. It features valve control as well as data inputs for load cells, pressure sensors, thermocouples and vibration sensors. An overview is given in Table 6.2. Each of these features is facilitated by another module that can be slotted into the main. These are shown in Figure 6.15.



Figure 6.15: The National Instruments cRIO-9035

Table 6.2: Overview of data acquisition hardware used for the Chimera test setup

Application	Model	Range/Specifications	Sensor Error
DAQ main	NI cRIO-9035 ¹	CPU, FPGA	N/A
Pressure Sensors	NI 9203	200 kS/s, ± 20 mA	N/A
Tank, Injector &	ifm PT5423 ²	0-60 bar	$\pm 0.5\%$ FS
Load cells	NI 9237	50 kS/s/channel	N/A
Thrust	FUTEK LCM500 ³	± 222 N	$\pm 0.25\%$ FS
Tank	Celtron STC-25 ⁴	± 25 kg	$\pm 0.25\%$ FS
Thermocouples	NI 9213	75 S/s Aggregate, ± 78 mV	N/A
Combustion chamber	RS PRO Type K Thermocouple 150mm ⁵	$+1100$ °C	N/A
Surface	RS Pro K Type ⁶ Thermocouple	-75 °C - $+250$ °C	N/A
Power	Arduino UNO ⁷	0-5V	
Voltage output	UNO ADC + voltage divider	0-1200V	$\pm 0.5\%$ FS
Voltage and current in	INA 219 ⁸	0-26V, 0-3.2A	$\pm 0.5\%$ FS
Dynamic signals	NI 9232	102.4 kS/s/channel 3 AI, ± 30 V, 24 Bit	N/A
ICP® pressure sensor	PCB 124A21 ⁹	0-1,724kPa 0.034 kPa Resolution	$\pm 1.0\%$ FS
ICP® microphone	PCB 106B52 ¹⁰	0-6.89kPa 0.00013 kPa resolution	$\pm 1.0\%$ FS
Vibration Sensor	LDT0-028K ¹¹	50 mV/g Baseline Sensitivity	N/A
Valve Control	NI 9375	6-30 V, 7 μ s (Input) 500 μ s (Output)	

6.4.1. IFM pressure sensors

Some relevant pages of the datasheet of these sensors can be found in Appendix A on pages 87 to 91

The pressure sensors used are supplied by IFM. They work in multiple different pressure ranges and always output 4-20mA. For a sensor with the range of 0-60 bar, this results in a slope of 3750 and an offset of -14. This type is an industry standard and have been proven to work very reliably over the years. Calibration can only be done with sensors of superior accuracy, but these are the most accurate sensors available. However, a qualitative assessment on test days can be done by reading off the analog dials on the pressure regulators during pressure testing. These analog values can then be compared with the data that is logged by the sensors. In Figure 6.16 the comparison between the two values and their calibration curves are given for 5 separate test days. Linear regression has also been performed for all 5 days together. What can be concluded is very strong linearity on each day, but weak correlation between days. This is likely due to non-ideal effects in the analog dials. As the ambient temperature changes their values may vary and they generally only require accuracy in the order $\pm 10\%$. The combined slope and offset is the closest to manufacturer specifications. These two observations strengthen the reliability of the sensors as it indicates they behave consistently linear together with analog dials and the average of 5 runs is closer to the expected values than each individual run. Therefore the manufacturer's calibration is justified to be used.

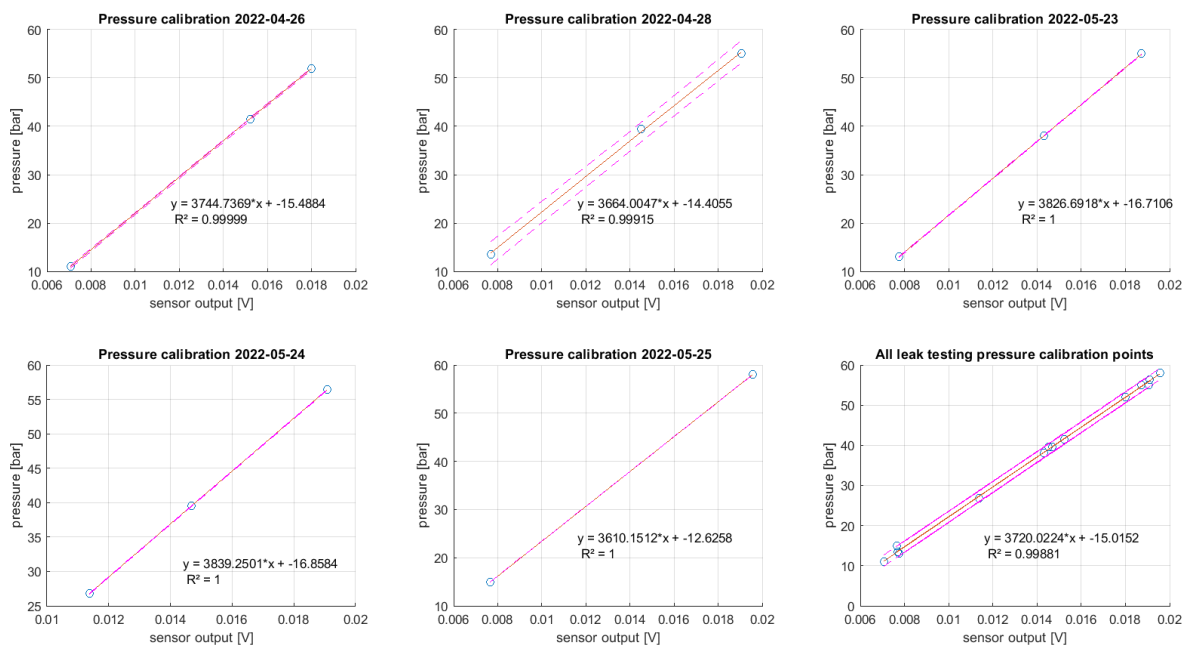


Figure 6.16: Verification of the pressure sensors

6.4.2. Load cells

The tank is suspended from a load cell in tension while being constrained by vertical bearings. The thrust bench features a load cell which has been pretensioned by a spring. The spring and the dry mass of the tank ensure that the load cells are not used around their zero point. Unlike the pressure sensors, these sensors are incorporated into a structure that induces a potentially slightly different slope, due

¹<https://www.ni.com>

²<https://www.ifm.com/nl/nl/product/PT5423>

³<https://www.futek.com/store/load-cells/threaded-in-line-load-cells/miniature-threaded-in-line-LCM300>

⁴<https://stekon.nl/products/celtron-stc/>

⁵<https://nl.rs-online.com/web/p/thermocouples/7877696>

⁶<https://nl.rs-online.com/web/p/thermocouples/3630250>

⁷<https://store.arduino.cc/products/arduino-uno-rev3/>

⁸<https://www.ti.com/product/INA219>

⁹<https://www.pcb.com/products?m=124a21>

¹⁰<https://www.pcb.com/products?m=106b52>

¹¹<https://www.rs-online.vn/p/vibration-sensor-ldt0-028k-pcb/8937086/>

to for example bearing friction, and a significantly different offset due to the spring and tank dry mass. The load cells are calibrated using 4 weights of 1kg each. The tank is loaded with four known masses directly whereas the thrust load cell uses a rope over a pulley. In total 18 data points are collected per load cell. First a zero measurement is taken after which 4 different loads are applied. These loads are then removed one by one totalling 9 initial samples. A major contributor to the accuracy of the load cells is the application of strain relief before the application of a load, especially when the load is reduced. Therefore a second set of 9 measurements will be taken where strain relief is applied between each measurement. Linear regression is then utilised to find the calibration constants slope and offset for three cases: 5 data points on load increase, 5 data points on load decrease and 9 data points both up and down with strain relief. The results of the calibration run are shown in Figure 6.17. The strongest correlation is found in the calibration case with strain relieve as is to be expected. These values will be applied to the sensors and are valid as long as the load cells themselves are also strain relieved just before each hot fire attempt.

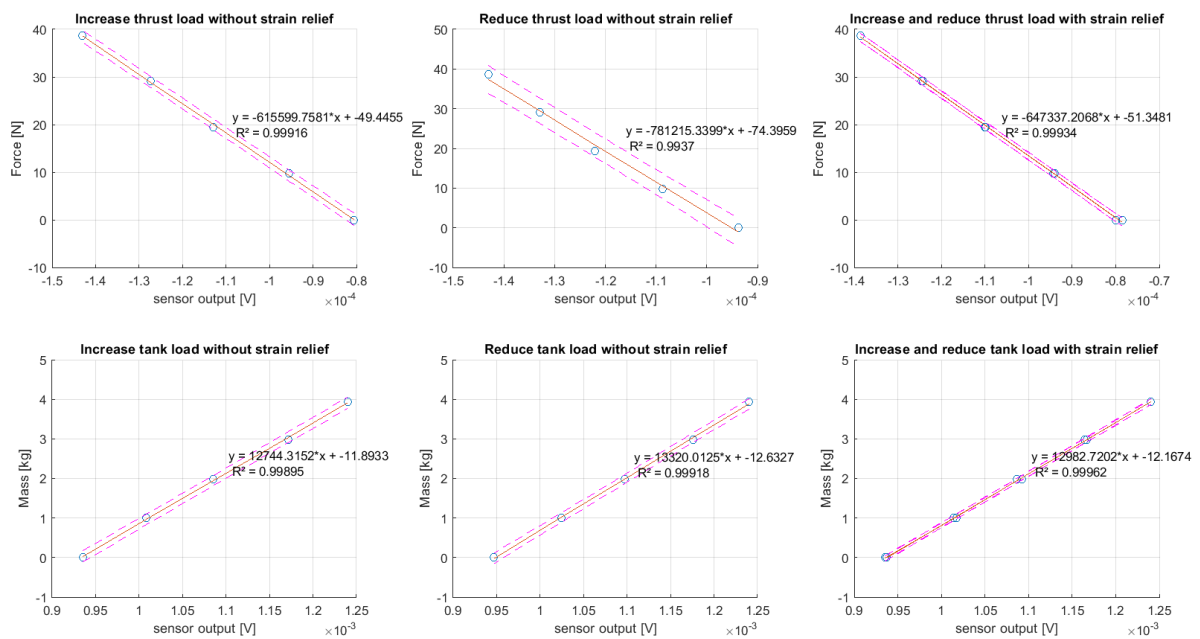


Figure 6.17: Calibration of the load cells

6.4.3. Thermocouples

Standard K-type thermocouples are used to measure the system temperature at a multitude of locations. They function by measuring the potential between the contact of two different metals, which is temperature dependent. For K-type thermocouples these are Ni-Cr and Ni-Al. Calibration of these sensors is not required as they are directly compatible with the cRIO module as long as proper wiring materials are used on all adaptors and internal wiring. On the following locations the temperature will be logged:

- Tank top
- Tank bottom
- Combustion chamber
- Nozzle retainer
- Wall on nozzle side
- Wall on manifold side
- Manifold
- Piezoelectric dynamic pressure sensor

Except for the combustion chamber thermocouple all are standard thermocouple wires that have been applied using conductive aluminium tape. The combustion chamber thermocouple is a sheathed 1mm probe fitted in a pressure gland. It was selected for the earlier monopropellant system with decomposition temperatures around 1100 °C. It is therefore not expected that they will measure the much higher

combustion temperature of ABS and nitrous accurately. When insulated sufficiently with silicone elastomer however it can be used to qualitatively assess the consistency between different tests.

6.4.4. Piezoelectric sensors

Finally, three high frequency piezoelectric sensors have been added to the system: one dynamic pressure sensor, a microphone and an accelerometer. Their datasheets can be found on pages 95 to 99. The first is a model 124A21 water-cooled rocket motor ICP® pressure sensor from PCB electronics. The second is the model 106B52 ICP® Pressure Sensor or acoustic sensor/microphone from the same supplier. It is very sensitive to acoustic pressure variations in a medium and can therefore accurately record the sound from the engine. Finally, the accelerometer is the LDT0-028K from Measurement Specialties and measures the vibration in the longitudinal direction. It should be noted that no combustion instabilities will be investigated as this lays out of the scope of this thesis. The data can instead be used qualitatively to prove consistency between tests, similarly to the thermocouples. In addition, it can give some insight in troubleshooting ignition problems. The generated data is expected to be useful in the future for further studies however. Calibration is not required as the high frequency data is only used for spectrum analysis. In addition, the two sensors from PCB electronics come with accurate calibration values from the supplier so any future quantitative analysis can be performed with these.

6.4.5. Ignition power

The power supplied to the high voltage generator is measured using an Arduino Uno instead of the cRIO as per requirement TEST-10. This is due to the risk of the high voltage damaging expensive components. A cheap isolated circuit is much more suitable for this application. The INA219 breakout board is used to measure the input current and voltage that is supplied to the circuit. A voltage divider is used to measure the output voltage and directly attaches to the ADC of the Arduino. A 21 k Ω and five 1M Ω resistors are used to scale the voltage down within the 0-5V allowable range. The arrangement of the power supply, Arduino data acquisition box, high voltage power supply and the voltage divider on the back of the vertical sensor cable guide can be found in Figure 6.18. A manual button has been added to actuate the high voltage spark in order to set the grain. A procedure that was elaborated upon in subsection 6.1.2 The next section will elaborate on the high voltage generation.

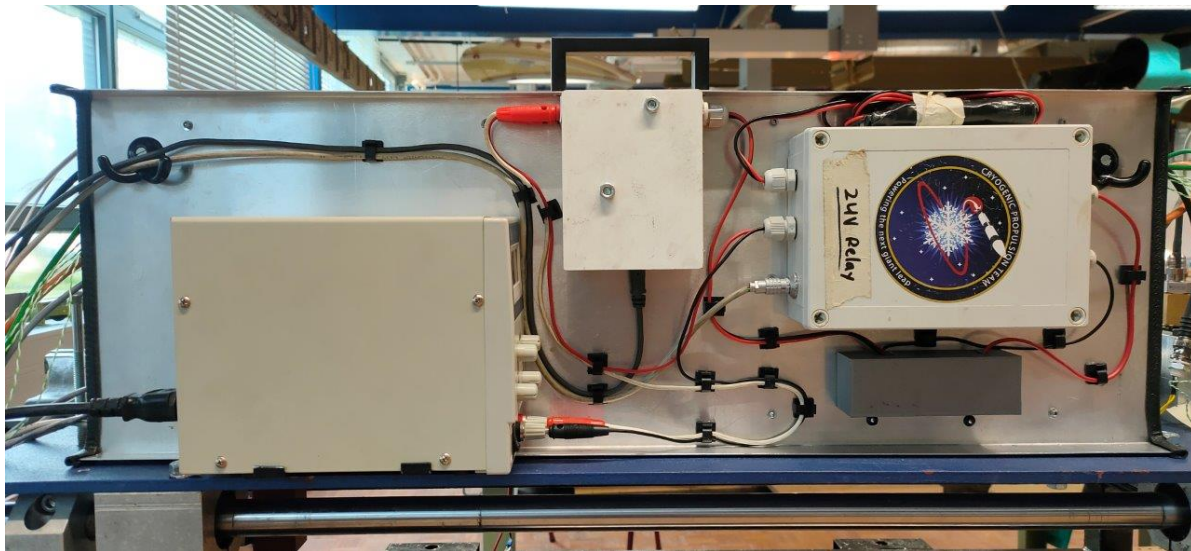


Figure 6.18: Layout of the high voltage system on the back of the vertical sensor cable guide

6.5. High voltage generator

The voltage needed to start the hydrocarbon seeding effect is generated using a Mazzilli driver with a fly back transformer. The assembled system is shown in Figure 6.19. On the right hand side two input wires can be seen as well as a connection for a manual button and a plug to actuate a relay. The relay is used for hot fire procedures so the timing can be done automatically. In order to set the grain the button is used for simplicity's sake. The diagram is shown in Figure 6.20. The driver receives DC from a power supply and outputs a near perfect sine wave. This sine wave is the output of an LC tank, the combination of an inductor and capacitor, and the MOSFETs. As the name suggests, it switches at zero volt, which means very little power is dissipated in the MOSFETs when they switch on and off. The other components on the left hand side provide gate protection to the MOSFETs to prevent them from being destroyed or degraded over time. They function as follows, quoted from Munich [74]:

- "The 470 ohm resistors limit the current that charges the gates as too much gate current can cause damage.
- The 10K resistors pull the gates down to ground to prevent latchup; a process in which the mosfet gets stuck on.
- The Zener diodes prevent the gate voltage from exceeding 12V.
- The UF4007 diodes pull the gates down to ground when the voltage on the opposite leg of the tank is at ground."

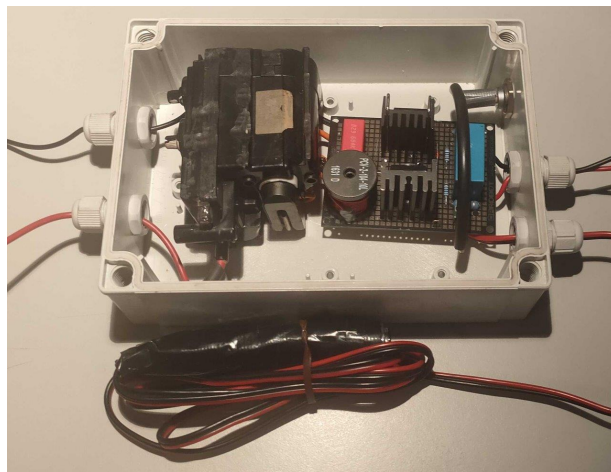


Figure 6.19: Assembled High Voltage Generator

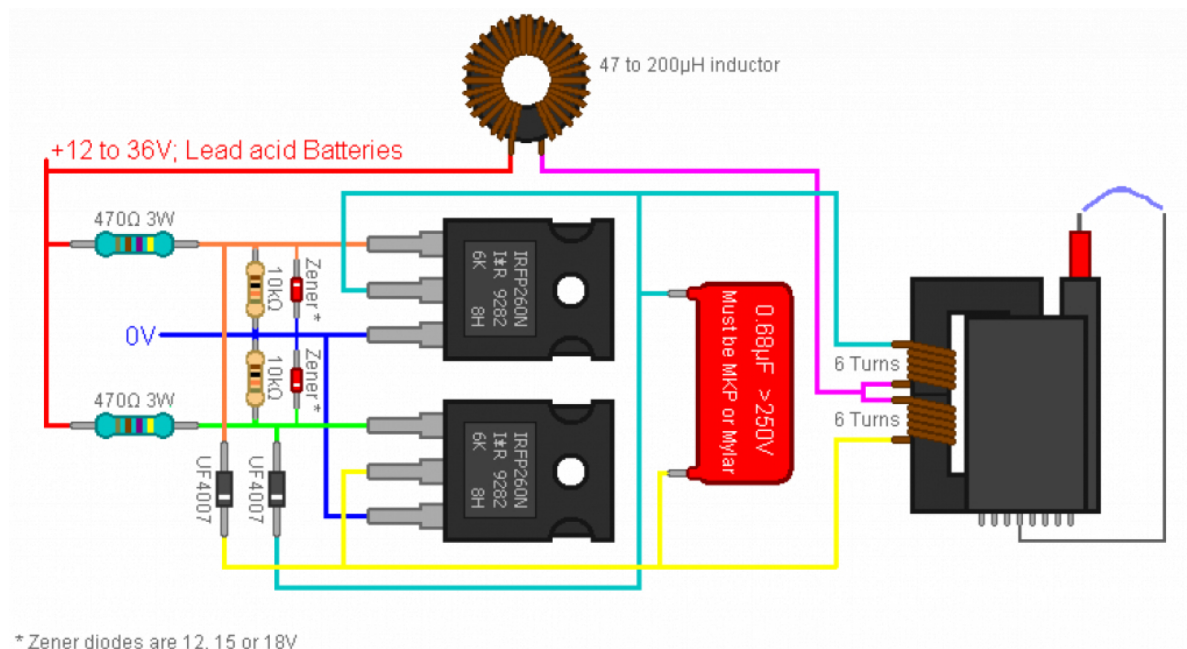


Figure 6.20: The diagram of the ZVS Mazzilli driver [74]

6.6. LabView program

All the data collection and system actuation is managed by the cRIO. This process is programmed using LabView. An interface had to be developed that is intuitive and easy to use to facilitate smooth test days while minimising operator error. This was achieved through a graphical interface that fits exactly on one computer screen and has each relevant section secluded to keep an overview. Some safety features like an actuation enable and sequence arm button have been implemented to prevent misclicks causing incidental actuation.



Figure 6.21: GUI used to control the hybrid engine test setup and log data

On the background the software needed to be optimised significantly in order to achieve the increased data rates since the last iteration. All data was handled in the real time controller which limited the data rate to 2500Hz. At each iteration all the data files were opened and the data was written. This caused incidental overflows as the routine could not keep up. This has been improved using the standard method of writing data to a First In, First Out (FIFO) buffer in the field-programmable gate array (FPGA) and collecting it with the RT controller at a much lower frequency. During the automated sequence all data visualisation, except for the 100 Hz thermocouples, was also disabled to prevent unnecessary use of resources. Finally, the excitation voltage was increased from 3.3V to 10V, reducing sensor noise by a factor of 3 and load cell frequency increased from 2500Hz to 50 kHz to capture ignition events and potential anomalies. The final result is a high frequency data acquisition system where each cRIO module was used to its full capabilities.

6.7. Conclusion

The test setup described in this chapter has been shown to be fit for the purpose of this study: to validate an analytical design tool. Each part of the hardware has been described to a sufficient extend and design decisions have been justified. Two parameters in the engine will be changed in between tests to compare results: the injector ignition to main flow ratio and the grain port geometry. Sensor calibration data has been included to prove the reliability of the collected data.

7

Results

This chapter gives an overview of the test results. Throughout the duration of this study 27 hot fire attempts have been made out of which 10 ignited successfully. First of all, the methods to analyse the collected data are treated in section 7.1. Then a summary of all the processed information is given in section 7.2. Afterwards, section 7.3 gives context to certain anomalous values. Every single anomaly has been investigated and the cause has been determined. For most a solution has been implemented and for the remainder a workaround has been realised. Based on the data and issues encountered a selection will be made of the data that is to be used to validate the software described in chapter 5, which will be executed in section 7.4. Finally, all results will be discussed in section 7.5 and concluded in section 7.6.

7.1. Test Data Analysis Method

An extensive data analysis tool has been written in order to quickly evaluate a test's performance and to allow for re-configuring the setup for another try during a test campaign. It is designed such that minutes after an engine test all the relevant parameters are plotted and saved. This allows for a fast and effective decision making and troubleshooting process between tests. This has been particularly useful in detecting the cause of misfires and attempting solutions. In addition, it smooths the data using a Gaussian filter with a window of 60 samples for the pressure sensors and 100 for the load cells to reduce exacerbated noise in later calculated parameters. Finally, it prepares the data for comparison with other tests or to export it as a csv for comparison with model data. However, before it can be exported some analytical methods have to be employed which will be explained in the following sections.

7.1.1. Time synchronisation

As described in section 6.6, each sensor type is logged at a different speed from a FIFO buffer. This makes alignment of the data streams a challenging process. Even though logging of all the systems is triggered by one shared command, the given timestamps do not match. Instead the $t=0$ mark was found by detecting change in the signals, one per sensor type. The ones used, as they have the most distinct spike at startup, are the thrust load cell and the chamber static and dynamic pressure sensors. From that point it was assumed that the data rate was exactly as specified in the requirements, which, upon closer inspection, was deemed a valid assumption. The result can be seen by the vertical markers in Figure D.6 and Figure D.9. The temperature was logged at an identical frequency to the valve states and can therefore directly be related to the timestamp of the main valve opening.

7.1.2. Mass flow estimate

The mass flow can be acquired by differentiating the tank load cell values. In reality however, the load cell accuracy is only borderline acceptable due to noise. In addition, a slope offset is observed during the tank emptying process. This behaviour aligns with the results from calibrating the load cells as discussed in subsection 6.4.2. When mass was removed a certain amount of strain was kept in the system and the load cell would not return to its correct value until strain relief was applied. For the hot fire tests, this strain relief happens at engine shutoff. The source is likely the sudden closure of the

solenoid valve stopping the momentum of the, albeit compressible, fast flowing vapour. At shutdown an increase of noise can be observed followed by a sudden drop in the measurement. Since the pressure drops are very constant throughout these burns with relatively low velocity subsonic injection velocities, assuming a constant mass flow is a decent assumption. To that end, the mass flow is modelled by averaging all data points before the valve opens and after the valve closes and interpolating a linear decrease between these two values throughout the burn. This assures a very reliable accumulated mass flow over the entire burn duration, yielding accurate average O/F ratio estimates. In the future, the tank mass curve during the burn might be resolved better using a combination of heavy filtering, and comparing the outcome with a system model from CHESS to verify the curve shape.

7.1.3. Performance estimate

The performance parameters have been defined as:

$$I_{sp} = \frac{F_T}{\dot{m} \cdot g_0} \quad c^* = \frac{p_c \cdot A_t}{\dot{m}} \quad C_F = \frac{F_T}{p_c \cdot A_t} \quad (7.1)$$

A throat erosion model identical to the one described in subsection 5.3.7 has been implemented to increase the accuracy of the calculated performance parameters. In the cases where the nozzle disintegrated a change detection was applied that instantaneously increased the nozzle diameter to 15mm, the opening diameter of the retainer ring.

7.1.4. Feed system performance estimate

Discharge coefficients have been modelled by assuming saturated nitrous vapour density based on the measured tank and injector pressures for the valve and injector respectively. For the valve, two valve flow coefficient equations have been attempted as well as four equations for discharge coefficients. These same four are used for the injector plate.

The first valve flow coefficient was calculated using a method described by SAMSON AG [75]. It features two forms for either choked or subsonic flows. The source included other versions for liquids and steam, the one given in Equation 7.2 is specifically intended for gases.

$$\begin{aligned} \text{for } \Delta p < p_1/2 : \quad K_V &= \frac{W}{519} \sqrt{\frac{T_1}{\rho_G \cdot \Delta p \cdot p_2}} \\ \text{for } \Delta p > p_1/2 : \quad K_V &= \frac{W}{259.5 p_1} \sqrt{\frac{T_1}{\rho_G}} \end{aligned} \quad (7.2)$$

Second of all, the standard valve flow coefficient function in the form of volumetric mass flow per hour, using the specific gravity (density relative to water), related to the pressure drop is used:

$$\text{for all } \Delta p : \quad K_V = Q \sqrt{\frac{SG}{\Delta P}} \quad (7.3)$$

In terms of discharge coefficient two choked formulas were used and two simple restricted flow formulas. Three of which have been reverted versions of the formulae in section 5.3

$$C_d = \frac{\dot{m}}{A \cdot \sqrt{2 \rho_1 \Delta P}} \quad (7.4)$$

The following equation is the same as Equation 5.7, but now solved for the discharge coefficient.

$$C_d = \frac{\dot{m}_V}{A \cdot \sqrt{\gamma P_{\text{tank}} \cdot \rho_V \left(\frac{2}{\gamma+1} \right)^{(\gamma+1)/(\gamma-1)}}} \quad (7.5)$$

Similarly this equation has been adapted from Equation 5.8

$$C_d = \frac{\dot{m}_{v, \text{out}}}{A \cdot \sqrt{\frac{2\gamma}{\gamma-1} \rho_v P_{\text{tank}} \left[\left(\frac{P_2}{P_{\text{tank}}} \right)^{2/\gamma} - \left(\frac{P_2}{P_{\text{tank}}} \right)^{(\gamma+1)/\gamma} \right]}} \quad (7.6)$$

7.1.5. Output plots

With these additional parameters derived from the sensor values the plots that are produced for each of the 27 burns are:

1. Raw: show the filtered data compared to the raw source and burn start and end markers
2. Performance: process the data to get engine performance parameters
3. Feed system: pressure drops, ratios and flow coefficients
4. 5 spectrograms: a waterfall plot or spectrogram of the combustion chamber static and dynamic pressure sensors as well as vibration and acoustic sensor.
5. Temperature: collection of all thermocouple data
6. N2O Estimate: nitrous density and temperature estimates from pressure readings
7. Power: input voltage, current and power as well as output voltage of the high voltage supply
8. Piezo: raw data from piezo-electric sensors

An example of these plots partially from tests 6 and 26 has been included in section D.2

7.2. Summary of collected test data and results

Since 12 plots for all 27 tests would be too much data to present here, an overview of the parameters is given in tables 7.1 and 7.2. The first table gives an overview of the parameters that are relevant for all tests, including the misfires and cold flows. The second table includes data only relevant for hot fires such as regression and erosion rates. The method of acquiring these averages and a full explanation of the table and colour labelling will be done in the following subsections. A discussion on these results will be executed later in section 7.3.

7.2.1. Test data summary

A selection of all the available parameters was made to only include values directly relevant for understanding the testing campaign. For example why certain engines had successful ignition and others did not. For clarification the rows have been coloured by their test type: blue for cold flows or misfires and red for hot fires. The test codes are made up of two parts: the first gives an indication of which system configuration was fired and the second part gives the test type and attempt number. 7-C3, for example, means system 7, third cold flow.

The amount of ABS consumed is based off of Table 7.2 and will be further elaborated in the next section. The consumed nitrous is the difference between the initial and final load cell values as described in subsection 7.1.2. The average OF ratio is the ratio between these last two values.

The following columns up to and including the thrust coefficient are all the average values over the entire burn time to give an indication of the type and quality of the respective tests. The maximum temperature is simply the maximum temperature measured by the thermocouple that is inserted into the chamber.

The next three columns deal with ignition parameters. Each has been colour coded to show whether the value is positive or negative. Ignition input voltage describes the voltage at which the power supply was set, for some tests this required starting voltage was higher which is negative as ideally, ignition can be achieved with the smallest possible high voltage generator. The next column is ignition power, which counter-intuitively is coloured inverse. This is due to the fact that once the high voltage starts flowing through the system, the resistance will drop significantly and the current will be the limiting factor, which is set virtually constant between tests. It is therefore beneficial to have a higher ignition power as lower powers indicate no or too little power was supplied to ignite the chamber. This will further be elaborated upon in subsection 7.3.6. Finally, the ignition lead time shows the amount of time between the high voltage turning on and the main valve opening. A shorter duration between the two is deemed beneficial as quick ignition times are required for roll control systems, for example.

The last three columns indicate if the sequence needed to be aborted by a safety officer and if data collection of the ignition power and the chamber pressure was successful. all other data sources were successfully collected during each test.

7.2.2. Hot fire data summary

Table 7.2 shows some overlap with the data in Table 7.1 as the test code, date and number are identical for traceability. The burn time here is indicated as effective burn time, since four nozzles disintegrated about 1 second into the burn. This will be discussed in subsection 7.3.2.

The next four rows give data about the injector and grain configurations used. The first row gives the hole diameter of the single main flow injection element and the two ignition orifices respectively. The next two rows give the total injector area, which was kept as constant as possible, and the ratio of the resulting ignition to main flow. Since it is expected that the smallest ignition flow gives a most uniform burn profile, under the condition that no lower ignition bound is encountered, it has been marked green. The highest ratio was marked red and corresponds to the diagonal hole configuration as shown in subsection 6.1.4.

The following 6 rows correspond to the nozzle performance. The first two indicate whether or not the nozzle disintegrated and what the alignment was with respect to its retainer. Naturally, disintegration and misalignment are negative parameters and have thus been marked red. This will be discussed in subsection 7.3.2. The next four show the nozzle throat and exit diameters as well as the corresponding erosion rates based on their initial value and the effective burn time. Naturally, the exploded nozzles have been excluded from this comparison. Since nozzle erosion was observed not to be fully uniform, 3 radially equidistant measurements were made of each and the resulting average was taken. Lower erosion rates under 0.05mm/s have been marked green, the highest over 0.10mm/s have been marked red.

The next 6 columns associate with the grain used. They give the height and external diameter as to show the consistency between the tests. Then it continues to show the initial and final port diameters which can be used to find the average regression rate. Since each diameter was measured four times, the eccentricity of the final port diameter could be determined. a lower eccentricity corresponds to a rounder port and thus more axisymmetric burning. Of the next group, the first three give the consumed mass. The first value has been calculated based on the fuel density and the difference in port diameters. It represents the amount of mass loss for an ideal regression model. The next value is the mass of the grain before and after the burn. The third gives the assembly mass, that is the grain plus injector manifold. This is deemed the most accurate value as some fuel particles are always lost when the grain is detached from the manifold. The final row gives the ratio between the ideal regression mass difference and the assembly mass difference. Values over 0.8 were marked green and under 0.6 red.

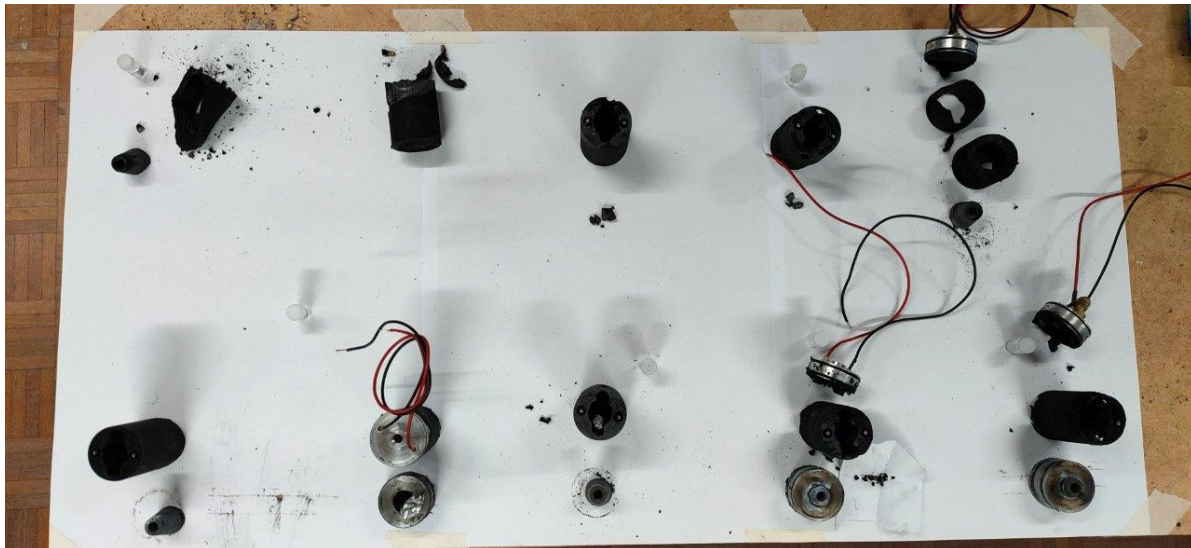


Figure 7.1: Remaining nozzles and fuel grains of all 10 burns counting horizontally from left top to right bottom

Table 7.1: Test data summary of all 27 tests

Test number	Test code	Date	Consumed ABS [g]	Consumed N2O [g]	OF ratio [-]	Burn time [s]	Average mass flow [g/s]	Average Thrust [N]	Total Impulse [Ns]	Average Specific Impulse [s]	Average characteristic velocity [m/s]	Thrust Coefficient [-]	Maximum Temperature [C]	Ignition input voltage [V]	Ignition power [W]	Ignition lead time [s]	Aborted?	Power Data	Pressure data
Test 1	1-C1	26-04	0	520	-	16	32.2	7.8	124.8	29	284	1.01	16.2	22.0	0.1	1	No	Yes	Yes
Test 2	1-H	26-04	55.0	530	9.6	16.0	31.6	46.6	745.4	140	964	1.44	2308	21.1	31.3	2	No	Yes	Yes
Test 3	2-C1	28-04	0	210	-	8	26.2	8.8	70.2	42	377	1.12	19.4	-	-	2	No	No	Yes
Test 4	2-C2	29-04	0	160	-	8	19.9	9.0	71.6	59	475	1.24	14.7	21.9	0.1	2	No	Yes	Yes
Test 5	2-C3	29-04	0	170	-	8	21.3	10.0	80.1	60	465	1.28	14.9	-	-	3	No	No	Yes
Test 6	2-H	29-04	25.0	210	8.3	8	25.4	36.1	288.4	139	1238	1.1	73.5	14.7	15.9	3	No	Yes	Yes
Test 7	3-C1	29-04	0	200	-	8	25.2	11.1	88.5	62	469	1.32	15.5	14.7	0.0	3	No	Yes	Yes
Test 8	3-CH	23-05	0	-	-	7.0	0.6	0.1	0.8	-	-	0.29	24.5	9.5	13.0	1	Yes	Yes	Yes
Test 9	3-H	23-05	12.8	140	11	8	17.4	21.9	175.4	121	1202	0.94	65.6	10.3	13.0	1	No	Yes	Yes
Test 10	4-H	23-05	17.0	160	9.3	8	19.6	28.1	224.4	131	1238	0.98	52.2	9.5	16.8	1	No	Yes	Yes
Test 11	5-C1	23-05	0	200	-	8	24.6	8.7	69.4	39	406	0.93	19.6	9.5	9.2	1	No	Yes	Yes
Test 12	5-C2	23-05	0	170	-	8	21.4	9.3	74.0	47	453	1.02	18.9	9.5	10.6	2	No	Yes	Yes
Test 13	5-C3	24-05	0	190	-	8	23.1	8.8	70.7	30	412	0.71	19.4	-	-	3	No	Part	Yes
Test 14	5-H	24-05	34.9	160	4.5	8	14.2	46.5	371.8	173	-	-	109.8	15.2	16.1	3	No	Yes	Part
Test 15	6-H	24-05	21.7	180	8.1	8	22.0	54.2	433.4	185	-	-	113.9	10.1	13.8	1	No	Yes	No
Test 16	7-C1	24-05	0	140	-	8	17.9	7.8	62.1	39	510	0.72	22.5	10.1	9.4	1	No	Yes	Yes
Test 17	7-C2	25-05	0	180	-	8	22.1	9.4	75.1	35	445	0.76	20.2	15.0	12.9	1	No	Yes	Yes
Test 18	7-C3	25-05	0	170	-	8	21.6	9.7	77.3	34	442	0.73	20.2	15.0	12.7	2	No	Yes	Yes
Test 19	7-C4	25-05	0	160	-	8	19.9	8.1	64.9	37	465	0.76	20.2	15.0	13.2	3	No	Yes	Yes
Test 20	7-H	25-05	4.5	90	20	2.4	36.8	28.9	70.3	74	761	0.76	45.1	15.7	16.2	3	Yes	Yes	Yes
Test 21	8-C1	25-05	0	180	-	8	21.9	9.8	78.5	42	466	0.88	20.5	10.0	5.2	1	No	Yes	Yes
Test 22	8-C2	25-05	0	170	-	8	21.8	9.7	77.3	40	457	0.86	20.7	15	-	1	No	No	Yes
Test 23	8-C3	25-05	0	180	-	8	22.2	8.5	67.8	35	437	0.78	20.4	15	-	3	No	No	Yes
Test 24	8-C4	25-05	0	190	-	8	23.2	8.8	70.0	37	425	0.86	20.3	20	-	3	No	No	Yes
Test 25	8-H	25-05	24.8	150	5.9	8	18.4	52.7	421.9	244	1865	1.28	137.2	19	-	3	No	No	Yes
Test 26	9-H	25-05	21.7	160	7.4	8	19.8	51.3	410.5	220	1799	1.19	108.2	19	-	3	No	No	Yes
Test 27	10-H	25-05	26.2	140	5.3	8	17.5	52.4	418.9	258	-	-	119.7	19	-	3	No	No	Part

Table 7.2: Test data summary of all 10 hotfires

Test Code	1-H	2-H	3-H	4-H	5-H	6-H	7-H	8-H	9-H	10-H	Units
Test Date	26-04-22	29-04-22	23-05-22	23-05-22	24-05-22	24-05-22	25-05-22	25-05-22	25-05-22	25-05-22	-
Test Number	Test 2	Test 6	Test 9	Test 10	Test 14	Test 15	Test 20	Test 25	Test 26	Test 27	-
Burn time	16	1	1	1	8	8	1	8	8	8	s
Injector Configuration	2.2+2x0.5	1.8+2x1	2.3+2x0.2	2.2+2x0.5	1.8+2x1	2.3+2x0.2	2.2+2x0.5	2.3+2x0.2	2.3+2x0.2	2.3+2x0.2	-
Injector Area	4.194	4.115	4.218	4.194	4.115	4.218	4.194	4.218	4.218	4.218	mm ²
Ignition/main flow ratio	0.094	0.382	0.015	0.094	0.382	0.015	0.094	0.015	0.015	0.015	-
Port geometry	Straight	Straight	Straight	Straight	Straight	Straight	Straight	Helical	Straight	Helical	-
Nozzle disintegration?	No	Yes	Yes	Yes	Partial	No	Yes	No	No	No	-
Nozzle interface misalignment	0 deg	<0.1deg	<0.1deg	<0.1deg	<0.1deg	0 deg	0 deg	0 deg	0 deg	0 deg	-
Final nozzle throat diameter	8.53	15	15	15	5.50	4.70	15.40	5.60	4.80	5.53	mm
Erosion rate	0.14	-	-	-	0.09	0.04	-	0.10	0.05	0.10	mm/s
Final nozzle exit diameter	9.03	15	15	15	5.50	7.67	15.4	7.70	7.67	7.70	mm
Erosion rate	0.04	-	-	-	-	0.004	-	0.01	0.004	0.01	mm/s
Grain height	64.6	64.1	64.6	64.4	64.5	64.3	65	64.3	64.8	65.1	mm
Grain diameter	39.3	39.4	39.3	39.4	39.4	39.5	39.3	39.5	39.4	39.3	mm
Initial port diameter	11.4	11.6	11.5	11.6	11.6	11.4	11.6	11.5	11.6	11.6	mm
Final port diameter	33.00	20.15	12.90	19.35	23.15	24.25	14.00	24.95	24.00	24.60	mm
Regression rate	0.68	-	-	-	0.72	0.80	-	0.84	0.78	0.81	mm/s
Eccentricity	0	0.29	0	0.26	0.31	0.34	0	0.31	0.20	0.47	-
Ideal regression mass difference	42.77	12.00	1.52	10.66	17.87	20.32	2.76	21.74	19.76	21.18	g
Grain mass difference	54.73	24.48	12.6	16.8	34.57	21	4.31	24.56	22.33	25.76	g
Assembly mass difference	-	25	12.8	17.04	34.94	21.68	4.46	24.79	21.69	26.19	g
Ideal regression factor	0.78	0.49	-	0.63	0.52	0.97	0.64	0.89	0.88	0.82	-

7.3. Complications during testing

Using the data from the previously presented tables some testing complications can be highlighted. Each section includes a description of an encountered problem, what the hypothesised cause was and how and if the problem was resolved.

7.3.1. Sensor noise

In the past testing power was acquired from facilities next to the testing field on campus. However, relatively recently, access to indoor power plugs of the neighbouring buildings has been prohibited and it is now required to use an engine-generator as the electric power source in the field. The 230V AC that is produced by this generator however is not as well grounded and free of noise as the power on the electric power grid. When this is not dealt with specifically the values on the pressure sensors will oscillate at an amplitude of $\pm 5\text{bar}$ which is over 10% of the sensor's measuring range. An adequate solution has been found by grounding the generator itself with an 1-1.5m aluminium pole that is hammered in the ground. Each part of the testing setup will be connected to this earthing pin using the yellow-green wire on the power reels. The setup itself is electrically insulated from the earth by the use of wooden pallets. If the setup were to be connected to the earth separately from the generator the sensor noise would increase again. This is likely due to a potential between both earthing sources caused mainly by their distance as the generator is placed far from the setup. First of all to prevent it from damaging, losing power and adding fuel to potential anomalies as well as to shield the testing crew from the noise by placing it behind an earth wall.

7.3.2. Nozzles exploding

After a successful 16 second duration test with the first graphite nozzle insert remaining intact, the conical design had been validated. The next three nozzles however each disintegrated about 1 second into their burn. It was hypothesised that this was due to the manufacturing method of these inserts. The first retainer and nozzle were manufactured at the same time as trial pieces in December. This means that the angle of the conical interface, which needs to be set manually on the machine, was identical between the two interfacing parts. All other 9 inserts however have been manufactured on the same day, yielding an identical angle between all of them, but not with respect to the retainers. Although an accuracy of $<0.1^\circ$ had been achieved, the test results showed that this was not sufficient. For all subsequent tests, both the retainers and inserts were resurfaced on the machine, this time with an identical tool angle between them. All subsequent burns, apart from hot fire 7 during test 20, have not resulted in nozzle disintegration and the behaviour was identical to the first hot fire. The reason for the nozzle failure during hot fire 7 is either due to thin and fragile features after re-surfacing operations. The three different final nozzle states are shown in figures 7.2-7.4.



Figure 7.2: Nozzle at the end of test 2

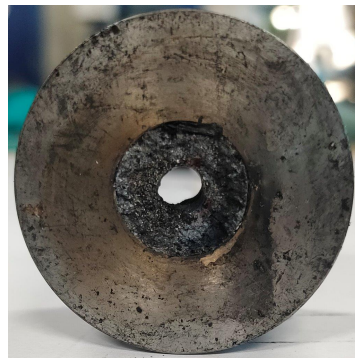


Figure 7.3: Nozzle at the end of test 5



Figure 7.4: Nozzle at the end of test 6

7.3.3. Ignition relay

The initial few failed ignition attempts could not be attributed to the same causes as explained in subsection 7.3.6. Instead they are likely due to a sticky relay. Data collected by the Arduino Uno showed only a very brief 50ms peak at the high voltage output instead of multiple seconds. The lead time was subsequently increased for test 2. Lab tests confirmed the theory as three attempts all failed in succession. When the power was removed, the relay was toggled multiple times in quick succession. Afterwards

the system always consistently produced a multiple second high voltage output. The malfunctioning has been attributed to the absence of a flyback diode which caused it to sustain minor damage over the years. The reason it was missing was because the high voltage generator was built years ago when the data system still had the diodes internally on its output connectors. This has been moved to outside the data system, directly on the valves and relays. For this box however, the adjustments were never made. After a flyback diode had been installed and relay cycling had been added to the test procedures at the beginning of the day and just before every attempt no malfunctioning has been observed anymore.

7.3.4. Ignition data logging

During multiple tests the data logging system failed and components had to be replaced. Interestingly, it failed in different ways, but with similar symptoms. One time the Arduino itself failed, the other times the INA219 current sensing board. The first failure can be attributed to repetitive, but small duration, over current. The board is rated for 3A only and after an in depth analysis it was discovered that the power supply, that ranges from 0-3A, can actually supply up to 3.5A. This caused a peak during the formation of the high voltage, when the potential is building up but not yet crossing the plastic. For subsequent tests the current limitation has been set to 2.5A, which results in only a small duration spike of 3A at startup. The second and most common failure was when the generated voltage potential over the electrodes was not enough to bridge the gap. Normally the voltage drops quickly as the current is conducted through the plastic surface. When the voltage does not drop it means that the ADC of the Arduino is subjected to voltages higher than 5V for an elongated period of time. This generally causes the Arduino to reset without any damage reported, but with the data files lost. After this effect was first observed a 5V Zener diode was added to protect the Arduino in the future. This helped reduce the frequency of the problem occurring, but as the test rate increased so did the probability of a component failing. At the end of test 21, the fourth and final INA219 board was broken and no further power data could be recorded. The ignition input voltage was still logged by reading off the screen of the power supply.

7.3.5. Main valve opening

Throughout the testing campaign some issues arose when the main valve did not open at certain pressures. Plugging out items such as high power lunch equipment seemed to increase the pressure at which the valve could open. At the time, this made sense as the valve in question is a solenoid with a relatively large orifice of 2.6mm, that is known to draw a large amount of power on opening. Similarly, when the generator was set to full throttle the problem seemed to reduce. At the time it was concluded that the valve opening pressure was constrained by power its power draw from the small generator. A few test days later however the problem persisted and the opening pressure lowered even with the previously implemented solutions. When measuring the connector of the valve it was discovered that the valve always opened when a probe was inserted. After opening and re-screwing the crimped wire into its terminal the valve had no more pressure limitations. The connector had been made to industry standards and it was concluded that the problems likely arose due to the test conditions. The setup had been standing outside for a while and even though all equipment was shielded from rain using a tent it is possible that the high humidity still impacted the resistance of this particular connector.

The main valve problems were caught almost every time during the regular pre-burn line purge. However, the misfire during test 8 has been attributed to this problem. The tank pressure was exactly equal to the limiting amount of pressure of the valve at the voltage it got supplied. It barely opened and started repeatedly closing and opening a small gap so after a few seconds a small amount of flow was able to escape resulting in a pulsating flame forming in the engine. A snapshot of one such flame is shown in Figure 7.5.

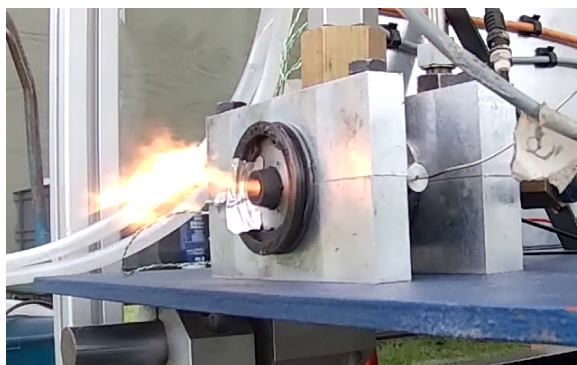


Figure 7.5: Snapshot of the small, subsonic pulsating flame

7.3.6. Misfires

After each misfire only a single parameter was changed in order to assess the exact cause. As a matter of fact, many cold flows were not misfires. They were expected to fail, but still executed in order to eliminate theories as to why the ignition failed. A few theories investigated were: ignition input voltage, input current limitation and lead time. After misfire, first the ignition power draw was assessed. For test 1, 4 and 7, the issue was determined to be the relay refusing to work. For the attempts where a power draw was observed a sequence of changes was followed in order to exclude possibilities and reject theories. First the lead time was increased from 1 to 2 or even 3 seconds. When this did not suffice the input voltage was raised until successful ignition was realised. An important parameter to consider is the injector configuration used. Tests 3-6 and 11-14 were all the injector with the largest ignition flow. This increases the potential for a misfire due to the incoming flow blowing out the ignition source. With the exception of the tests on the 25th of May, which will be left out of consideration for now, all the other grains ignited with relative ease. When a heavy filter is applied to the otherwise very noisy ignition system the ignition voltages of all the logged tests can be compiled together as shown in Figure 7.6. The measuring range is limited to 1150V based on the 5V Arduino ADC and voltage divider.

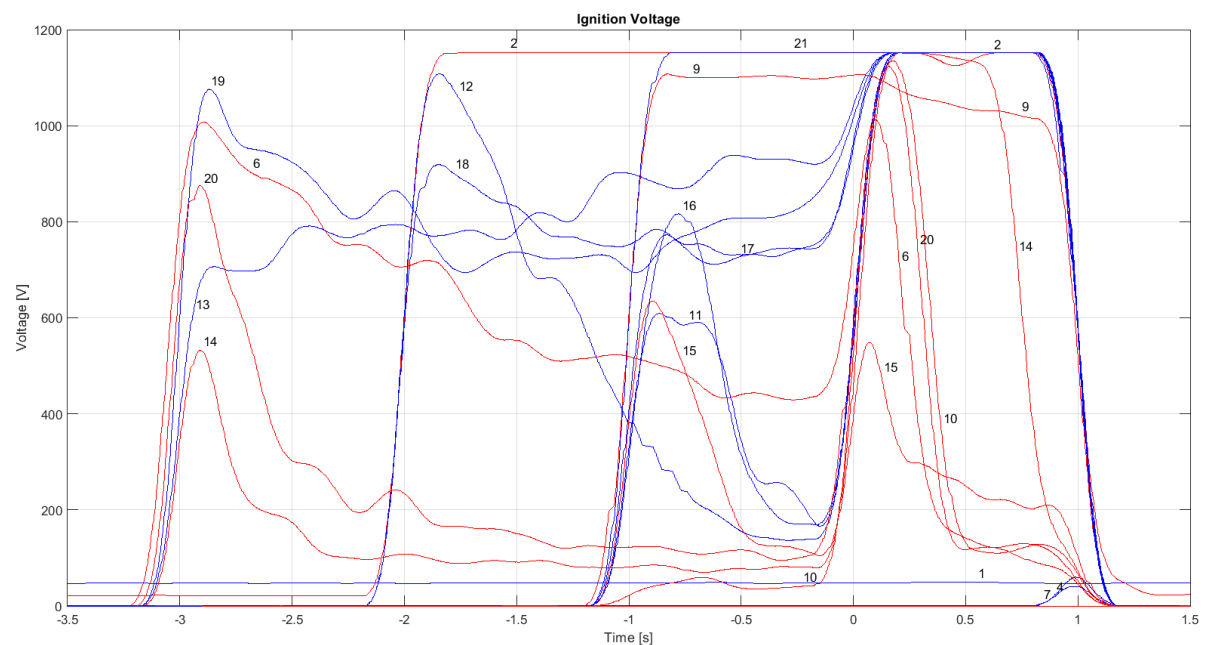


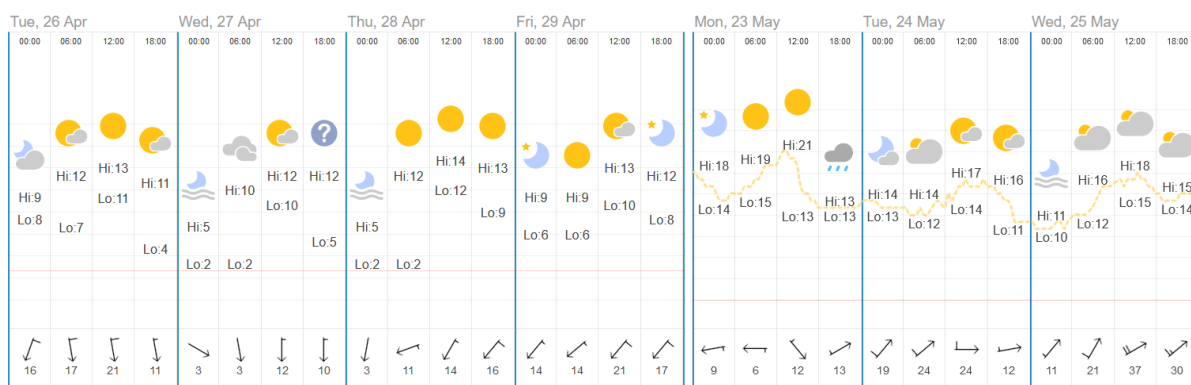
Figure 7.6: Filtered ignition voltage. Red indicates a hot fire, blue a misfire or cold flow. The numbers represent each test.

One trend that can immediately be observed is the fact that every successful ignition had a reduction in ignition voltage after the valve opening at 0 seconds. This indicates that current is flowing and no high static potential is realised. The exception of test 2 can be explained by the higher current of over 3A, but even there a small dip below 1150V can be observed half a second after the valve opening. The three trails (11, 12 and 16) that show a promising trend before 0 seconds but misfire, are the less ideal injector designs. On the opposite side, test 9 achieves successful ignition, when it may not be expected, which is the most optimum injector configuration. All other parameters are identical with power supply voltages being similar and lead times being equal or even longer. When sufficient ignition power was supplied before the introduction of nitrous oxide into the chamber, allowing the hydrocarbon seeding effect to continue, a virtually instantaneous ignition with a delay of only 100 ms was realised for every burn. Table 7.3 shows the ignition rate of each injector separated into two time slots, one before the final test day and one as the final test day. It shows higher ignition rates the lower the ignition flow. This trend however was not continued on the final testing day.

Table 7.3: Overview of success rate of each injector configuration both before and on the 25th of May

Injector configuration	1.8+2x1	2.2+2x0.5	2.3+2x0.5
Success rate before 25/05	2/8	2/4	2/4 (3/4)
Success rate on 25/05	-	1/4	3/7*

On this last day it was discovered that another likely contributor to the ignition difficulties was the weather condition. The wind was significantly stronger with speeds reaching well over 30 km/h as can be seen in the weather reports in Figure 7.7. The speed was 1.5-2 times as high as the other testing days. Normally only two sides were installed on the tent covering the setup to allow for an open escape route for testing personnel, an exit for the flame and clear visibility from the control point. With these wind conditions the two sides acted like a parachute and this meant that all the side panels needed to be removed to prevent the tent from flying away. This caused more free air flow past the system.

Figure 7.7: Weather report of the test days with wind speed given in km/h, retrieved from ¹

It is possible that the whole chamber behind the restricting nozzle functioned as a Helmholtz resonator. As this theory was formulated on the field, tests 26 and 27 were performed with a piece of tape closing off the nozzle. Neither showed any issues with ignition. This theory is supported by comparing spectrograms between the last two tests with tape and all the test on the 25th before. Instead of a stronger band at around 800Hz, test 26 shows a much weaker band around 550Hz before and after the test. During the test the same acoustic instability may have been reinforced or sustained due to the incoming flow from the injector. Nonetheless, even though evidence is supporting this theory more investigation and experimentation is required to confidently prove this theory.

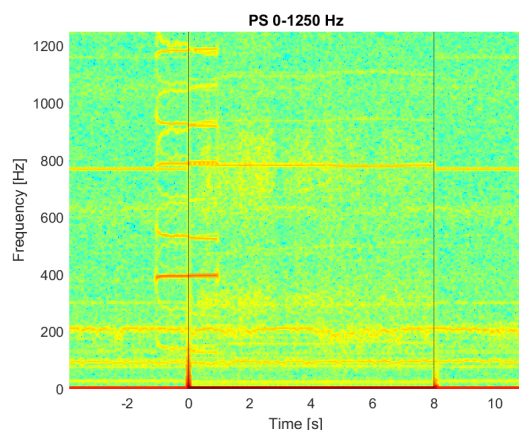


Figure 7.8: Spectrogram of the static pressure during test 21

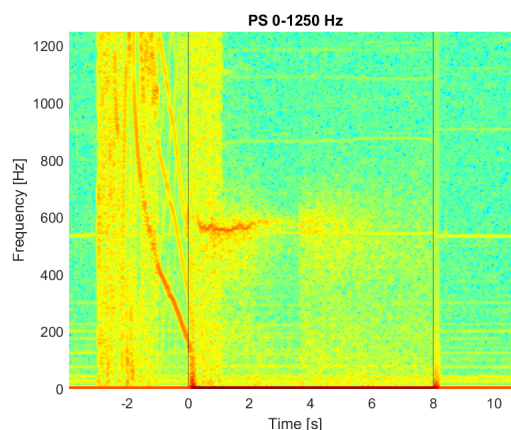


Figure 7.9: Spectrogram of the static pressure during test 26

¹<https://www.timeanddate.com/weather/netherlands/delft>

7.3.7. Pressure sensor malfunctioning

The pressure sensor in the combustion chamber needs to be shielded from the harsh thermal environment. This is done in two ways. First of all, the sensor is attached to a stand-off pipe that keeps a distance between the chamber and the sensor. Secondly, the pipe is filled with regular bearing grease. This grease is able to transmit pressure fluctuations to the sensor but will shield it from the hot gases. On two instances however, the grease must not have been sufficient as the sensor value dropped to negative values during a burn. In addition, during test 15 not all individual sensor values were checked by the operator leading to one additional test without accurate chamber pressure data. Interestingly, the spectrogram of the test still shows comparable results to the other tests indicating that even though the sensor got severely damaged, it was not fully destroyed.

7.4. Validation

From the large pool of data a selection needs to be made that can be used to compare the models to the experimental data. Although each of the 10 hot fires has data that can be used to partially validate the model it was chosen to focus efforts on only two configurations: the straight and helical port both featuring the injector with the lowest ignition mass flow. As shown in subsection 7.5.1, this injector produces the most consistent and ideal regression rate results and is therefore most suitable for model comparison. In addition, for real world application this is also the most ideal case as it preserves the pre-chamber and is likely to allow for a larger amount of restarts. Therefore the sets that will be considered are tests 25 and 26. These are virtually identical to tests 15 and 27, however they both suffered from a failing pressure sensor. This means that the single data set will be used for both the straight and helical port, but their consistency has been validated by the similarity to an almost complete data set as can be seen in figures 7.10 and 7.11.

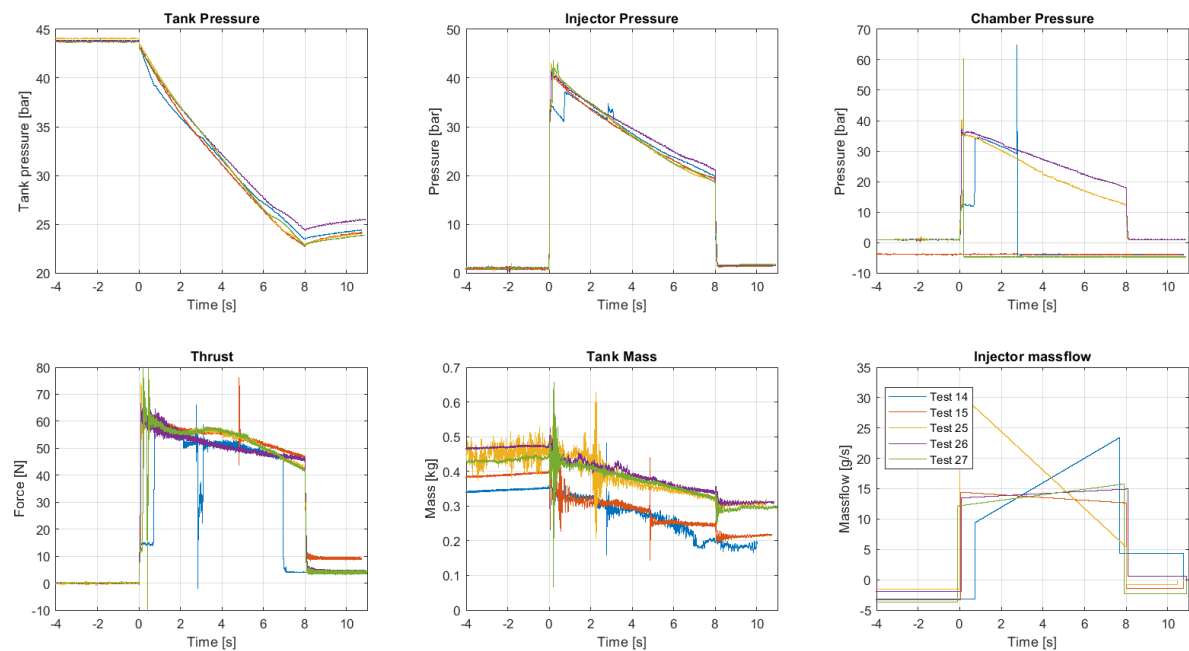


Figure 7.10: Performance comparison of all 8 second burns

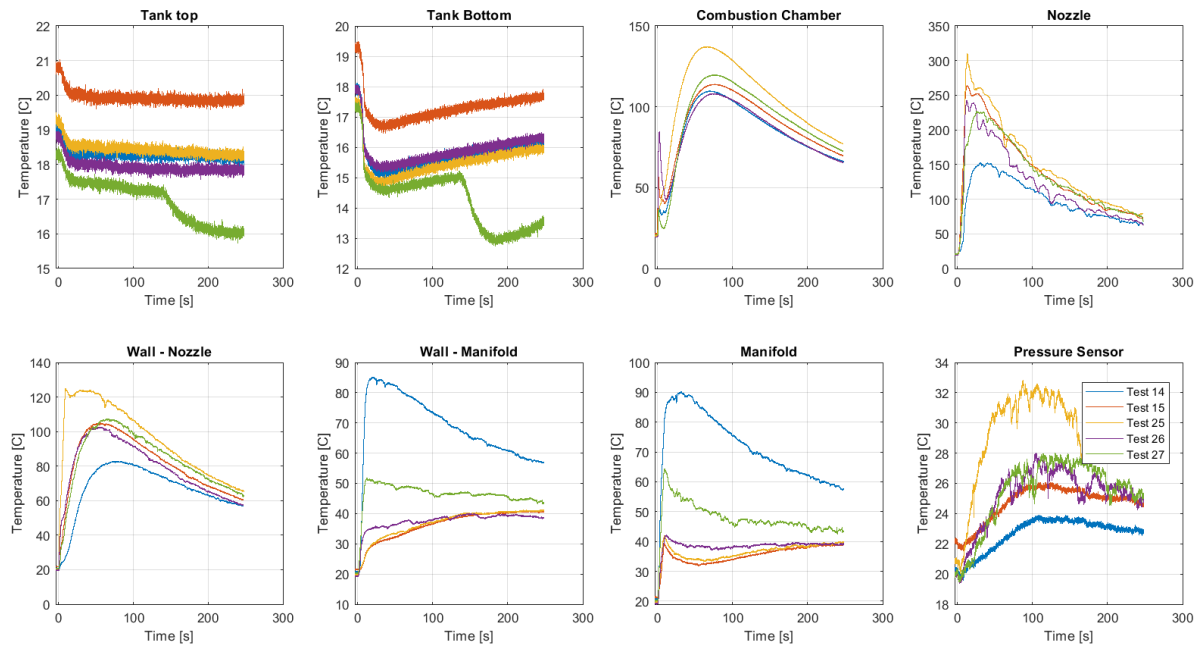


Figure 7.11: Temperature comparison of all 8 second burns

7.4.1. Validation procedure

For validation two aspects will be looked at. First of all the absolute values are compared. They give an indication if models are following the same trend as the experimental data and if the ball park values are correct. Secondly, their percentage difference is plotted. This should give a better idea of the actual quantifiable difference between the two. From the results it is evident that the values for the feed system pressures and thrust output have been proven to be within $\pm 10\%$ of the measured values. However, some of the parameters contributing to these overarching values, such as fuel and oxidiser mass flow and OF ratio show a larger total offset margin of 20%. However, some of the parameters contributing to these overarching values, such as fuel and oxidiser mass flow and OF ratio show a larger deviation. This can be partially attributed to the data analysis method. By including chemical equilibrium calculations into the test data a time resolved fuel regression rate may be found. This requires integration of the data analysis Matlab script into the python based tool CHESS. In addition, different methods to resolve the mass flow more accurately from the available data may be attempted. The second cause may be the use of a simple regression rate model. Proper implementation of more sophisticated models may be able to capture the effects currently treated as a bulk property. This error is further increased when helical structures are attempted to be modelled. Given the fast computational time this is to be expected and a collection of resources and methods have been suggested to decrease the current observed error.

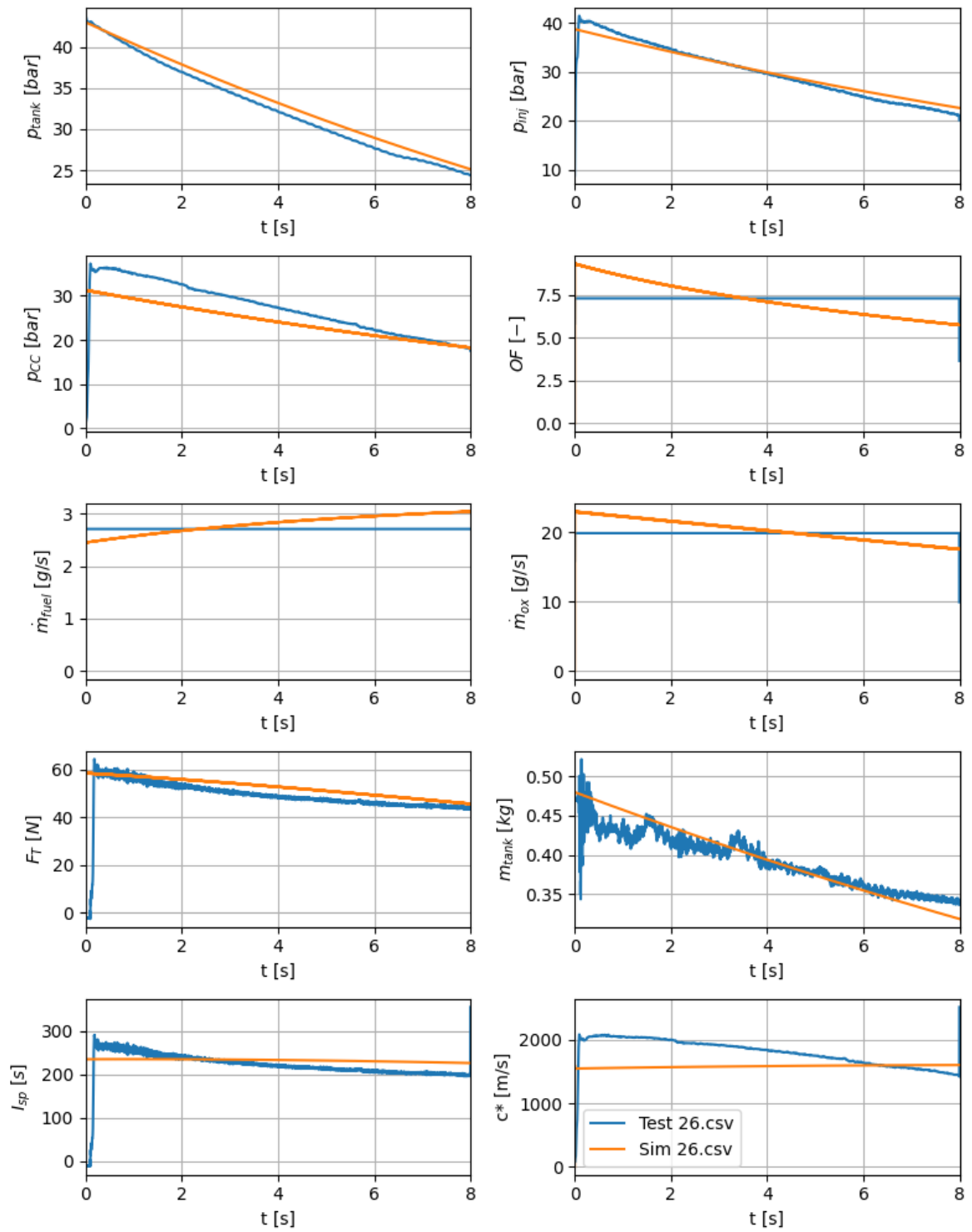


Figure 7.12: Straight grain model comparison absolute values

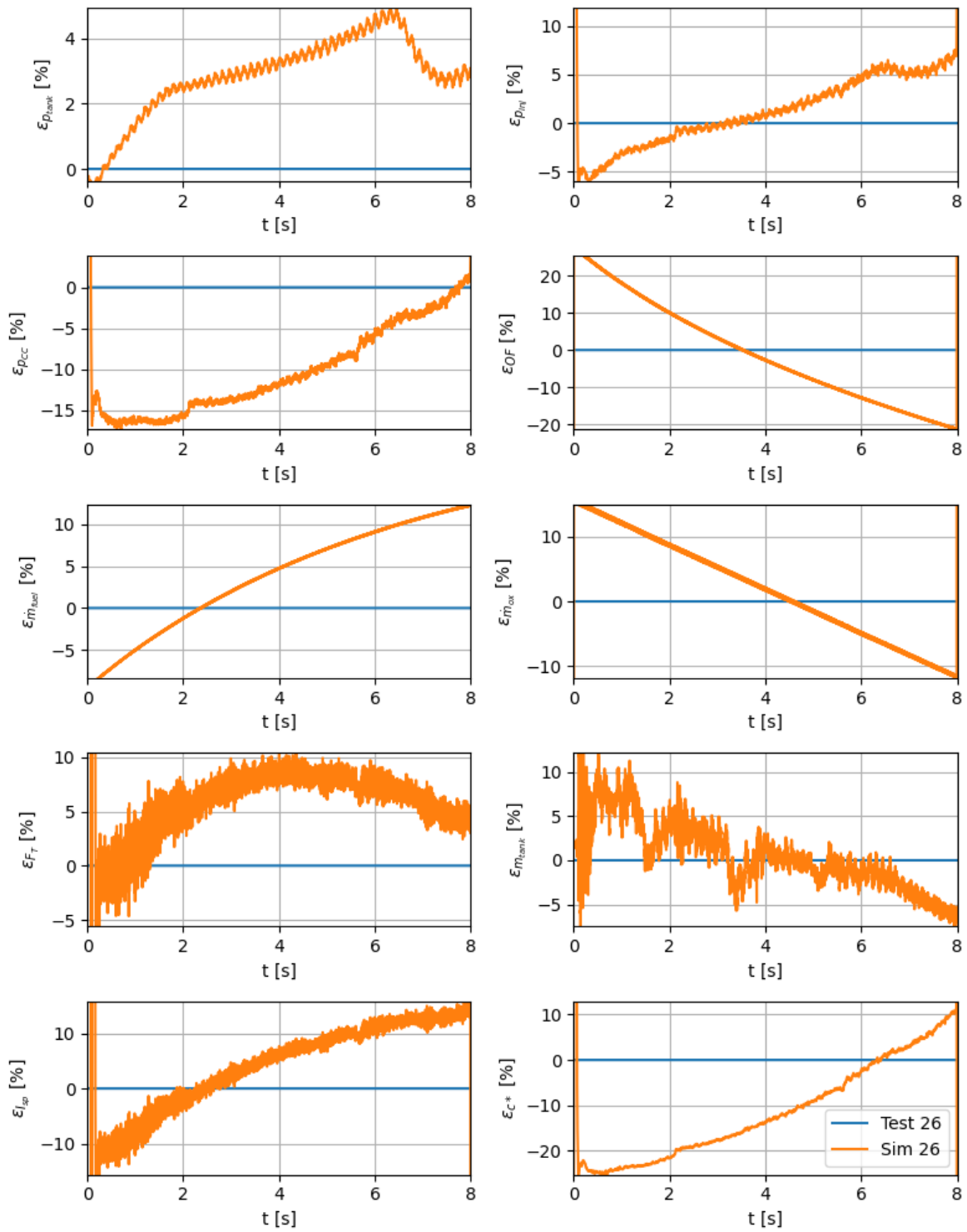


Figure 7.13: Straight grain model comparison percentage error

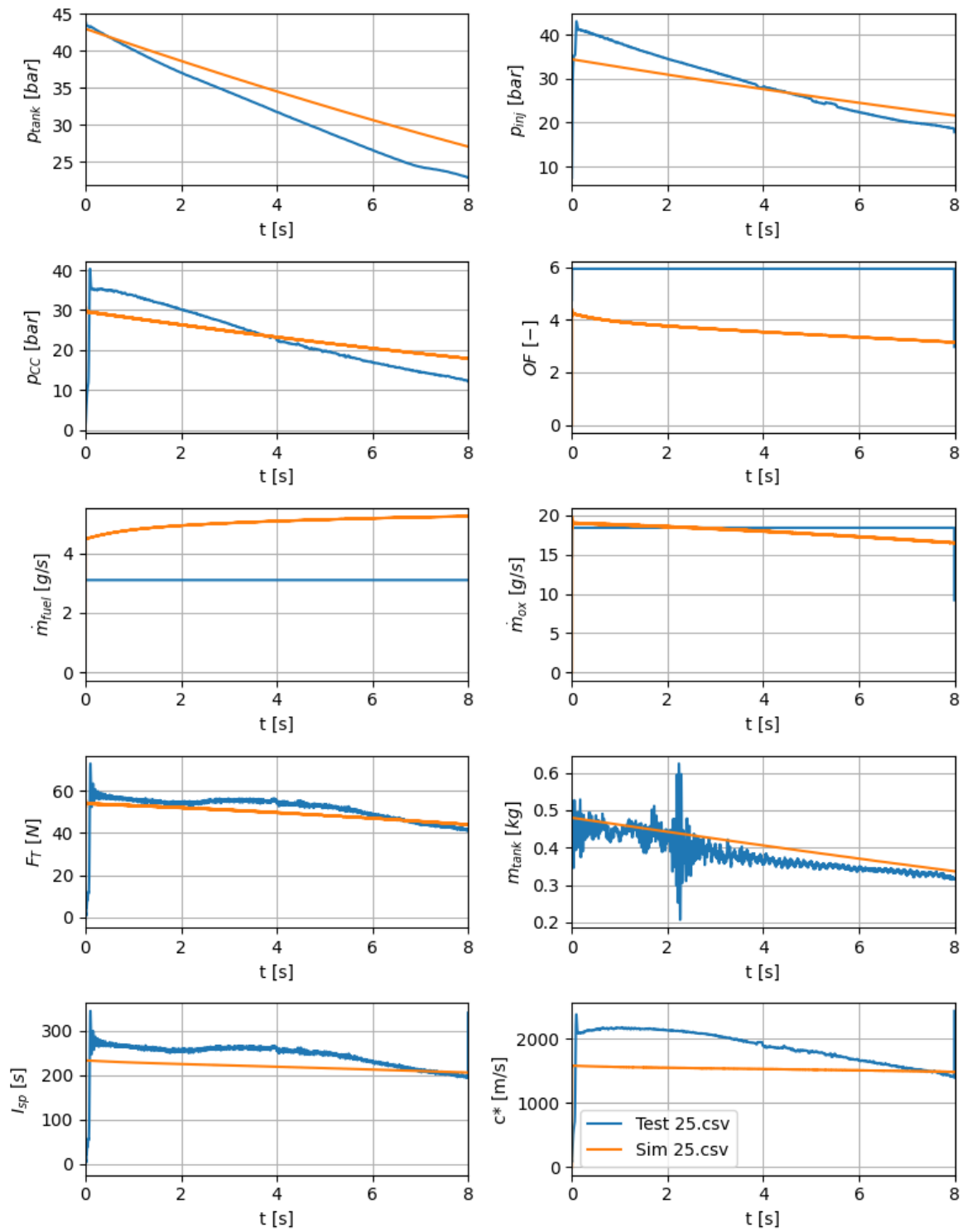


Figure 7.14: Helical grain model comparison absolute values

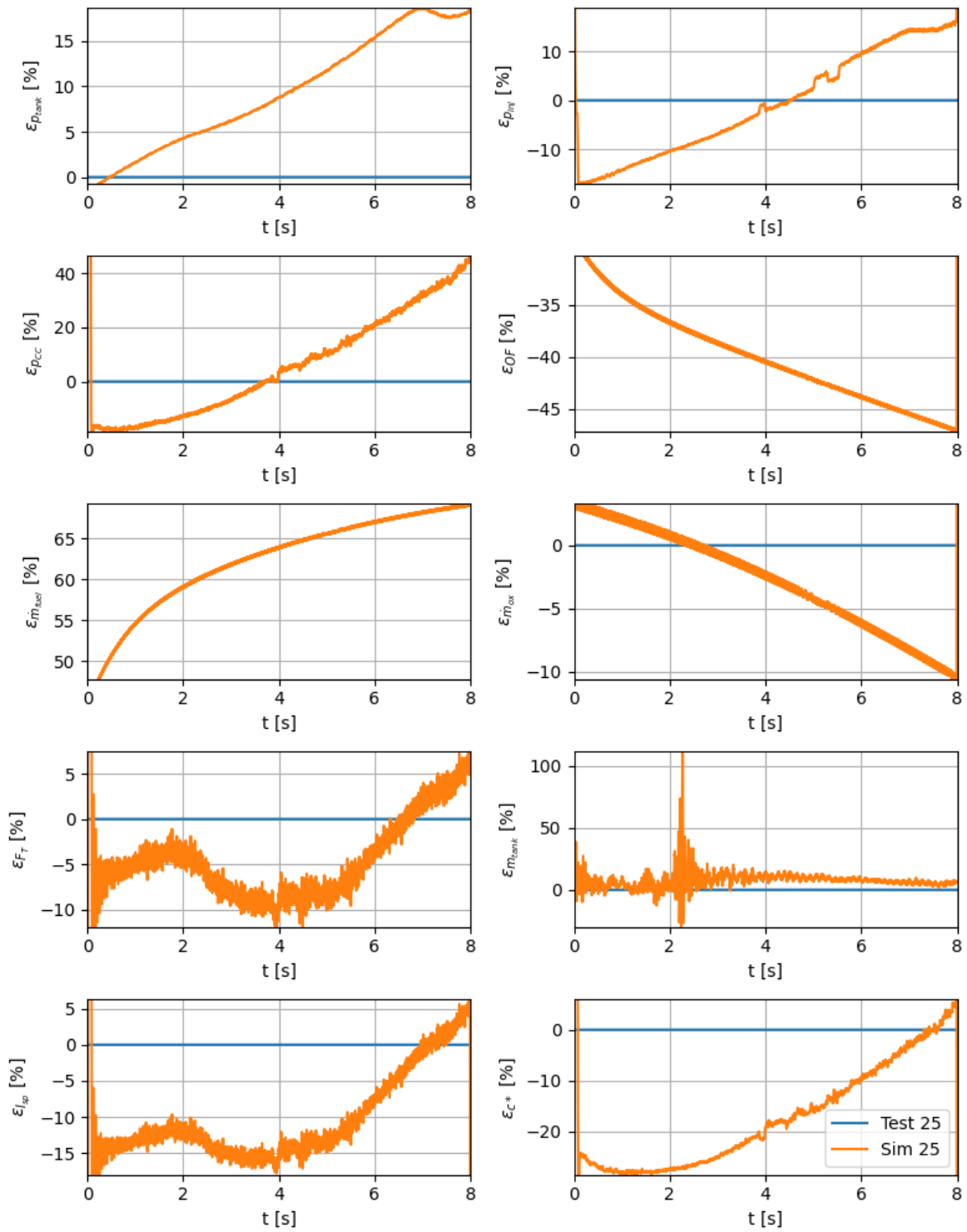


Figure 7.15: Helical grain model comparison percentage error

7.5. Discussion of Results

This section contains some discussion on results that have not been covered in the previous sections.

7.5.1. Injector effect

From the information presented in subsection 7.3.6 it becomes evident that although higher ignition mass flow are harder to ignite, the flows used in this study did not become prohibitively high. However, there is a second effect to consider, which is the effect of the oxidiser flow to the fuel grain. The following three figures show the effect of only a 1 second nominal burn, followed by a low pressure phase due to nozzle disintegration. Already then the difference between the injector design become obvious.



Figure 7.16: Pre-chamber remnants of test 2



Figure 7.17: Fuel grains of tests 3 (left) and 4 (right)

The least optimal injector design of test 2 shows complete combustion of the the pre-chamber and ignition geometry to the point that the connection of the rest of the system is entirely lost. test 3 shows a promising result with only minor damage to the exterior of the grain. The intermediate solution of test 4 shows a small hole on the side from the slightly larger mass flow at the ignition shelves. These observations can be quantified by comparing the ideal regression mass difference with the measured mass loss as described in subsection 7.2.2. The resulting set of fraction can be plotted against the ignition to main flow ratio resulting in the following plot that shows a decent fit with a logarithmic trend line. This is the last bit of confirmation that scaling down the ignition flow rate is beneficial and that extrapolation of this curve can be applied to larger motors with these small paintbrush nozzles. The ignition flow ratio will go even further down yielding increasingly promising perspectives.

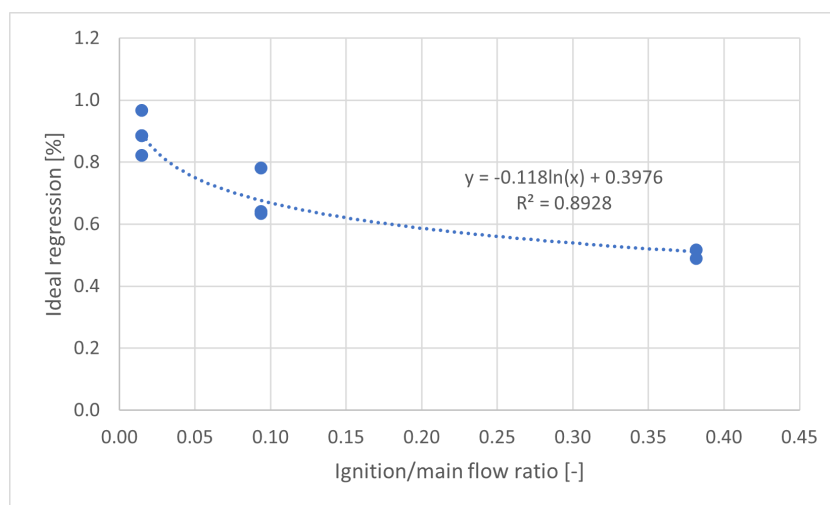


Figure 7.18: Logarithmic curve fit of ignition over main flow ratio to ideal regression factor

7.5.2. Discharge and flow coefficients

Since the pressure drops in the used system were very low, the injector pressure was directly coupled to the engine yielding a very constant pressure ratio over the injector. The result is a relatively constant mass flow and flat thrust curve unlike larger more optimised hybrid systems that use almost the full contents of their tank, utilise the self-pressurising effect of nitrous and have higher margins on their pressure drops. For these systems it becomes important to not only properly model the flow conditions but also include discharge coefficient estimations. Especially when smaller valves are used, such as the solenoid in this study, the pressure losses due to the valve should be attempted to be quantified. From the current tests a strong correlation between the valve pressure ratio or upstream pressure and it's discharge coefficient can be identified. It should be noted however, that the calculated discharge coefficients are heavily dependent on accurate density estimates. In certain circumstances the calculated coefficients exceeded a value of 1 indicating that this assumption, as expected, is not always valid. Therefore, more advanced fluid density calculations also need to be included in any future models. With that implemented, this simple relation has the potential to increase the accuracy of any coupled model on its own already and further investigation is recommended.

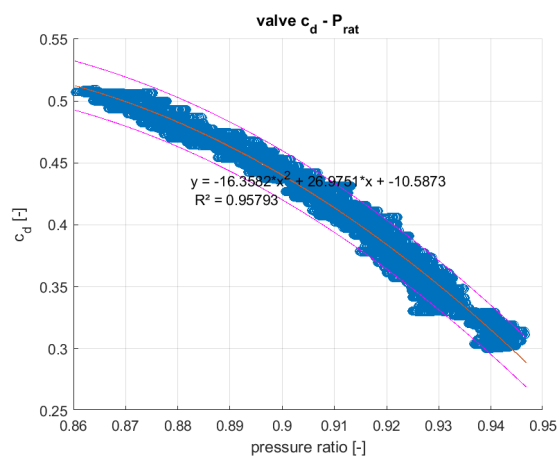


Figure 7.19: Estimated valve discharge coefficient over valve pressure ratio for test 26

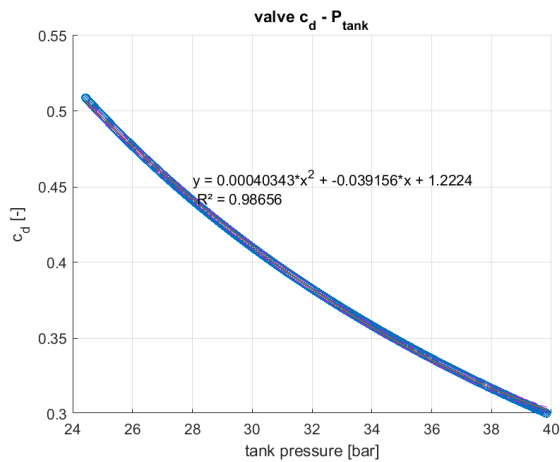


Figure 7.20: Estimated valve discharge coefficient over tank (upstream) pressure for test 26

7.5.3. Nozzle Model

One of the likely sources of inaccuracy is the nozzle model used for both the data analysis and the design tool. From Table 7.2 it can be seen that the linear nozzle erosion rate of hot fire 1 is much higher than that of all the shorter burns afterwards. It is deemed unlikely that this single nozzle was the single one that under-performed significantly. Instead it is likely that the erosion rate is linked to the temperature of the nozzle. In the next 6 images the temperature of the nozzle can be seen to increase during test 26, but only significantly after about 5 seconds.



Figure 7.21: Nozzle at $t = 0$



Figure 7.22: Nozzle at $t = 3$

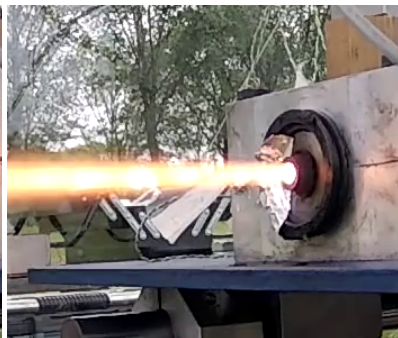


Figure 7.23: Nozzle at $t = 4$

Figure 7.24: Nozzle at $t = 5$ Figure 7.25: Nozzle at $t = 6$ Figure 7.26: Nozzle at $t = 7$

It is thus likely that during the shorter burn, most of the erosion took place in the last three seconds whereas hot fire 1 still had eleven seconds left at this moment in time. Additional evidence to support this theory can be found in the data from tests 25 and 27. These are the helical grains which can be seen to have a much lower O/F ratio, of around 5-7, due to their increased regression rate. Figure 3.8 shows that this range is around the maximum temperature for this propellant combination. Visual inspection of the footage also shows a nozzle with higher temperature during burn 10, which is configured with the helical grain. This difference can be seen in Figure 7.27 and Figure 7.28 where the last frame containing an exhaust flame of each respective test is shown.

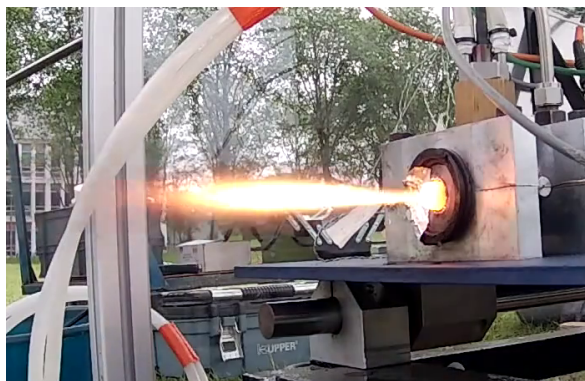


Figure 7.27: Nozzle of hot fire 9 at end of burn

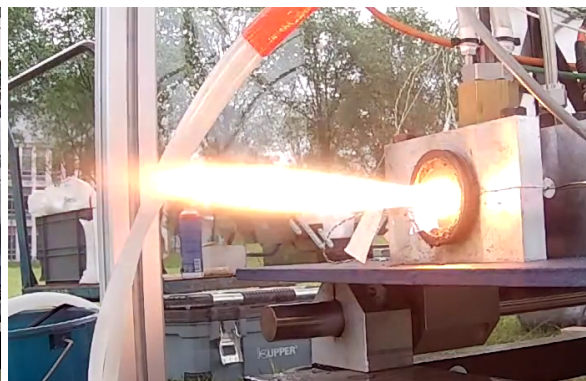


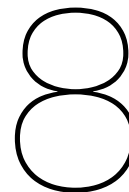
Figure 7.28: Visibly higher temperature during hot fire 10

Two approaches are suggested to improve the existing nozzle erosion model. First of all the nozzle temperature can be calculated using the camera footage and assuming it is a black body radiator. The temperature based erosion can then be scaled to the total erosion of the burn. For this engine in particular, this temperature based erosion rate can be non-dimensionalised by making it time dependant. The second approach however can also be used for different scales of systems. It would take the temperature based erosion rate and use an analytical heat transfer model to estimate the nozzle temperature. It should be noted however, that these heat transfer models have large error bars associated with them. Nonetheless, it is expected to give a significant increase in accuracy as long as the total amount of erosion is identical to the measured dimensions. Alternatively, a pyrolysis time delay can be implemented as suggested by Whitmore [76]. It sets a time from which erosion is allowed to start, assuming that the temperature at which the nozzle material will start to pyrolyse is reached at that moment. The downside of this method is that this parameter will need to be experimentally validated and is expected to vary between systems. This makes it useful for data analysis, but less so for predicting system performance.

7.6. Conclusion

The collected data, though incomplete or anomalous at times, was of sufficient quality to use for validation of the tool. Values for the feed system pressures and thrust output have been proven to be within $\pm 10\%$ of the measured values. However, some of the parameters contributing to these overarching values, such as fuel and oxidiser mass flow and OF ratio show a larger deviation. This can be partially attributed to the data analysis method. By including chemical equilibrium calculations into the test data

a time resolved fuel regression rate may be found. This requires integration of the data analysis Matlab script into the python based tool CHESS. In addition, different methods to resolve the mass flow more accurately from the available data may be attempted. The second cause may be the use of a simple regression rate model. Proper implementation of more sophisticated models may be able to capture the effects currently treated as a bulk property. The observed error is further increased when helical structures or radiation heat transfer are attempted to be modelled. Given the fast computational time, this is to be expected and a collection of resources and methods have been suggested to decrease the current observed error. No absolute boundary conditions for ignition have been observed although larger ignition to main flow ratios have proven more stringent requirements on the power input and lead time of the ignition power. During all burns, a very consistent ignition power has been achieved, although some required higher values depending on their ignition mass flow. This ties in with research question 5e. A low ignition delay can be assured with a sufficiently low ignition mass flow and controlled conditions by shielding the system from environmental effects. Another important factor is that sufficient ignition power was supplied before the introduction of nitrous oxide into the chamber, allowing the hydrocarbon seeding effect to continue and realise a virtually instantaneous ignition with a delay of only 100 ms. Restartability has not been validated completely, but all trends indicate that the grain with the smallest ignition to main flow ratio is the most promising option, due to the lower regression rate of the pre-chamber and ignition area. Control of the grain burn profile has been achieved by adjusting the grain geometry. A lower OF ratio and higher thrust output due to increased mass flow have been observed. However, extra efforts will need to be invested in modelling these helical structures to ensure the user of the tool is able to adjust these parameters and optimise their design.



Conclusion and Recommendations

This chapter will present the final conclusions and recommendations that resulted from this study. First the sub-conclusions of each chapter of this report will be summarised in section 8.1. The report structure, as presented in section 1.4, shows that these chapters have been organised to answer each of the five research questions individually. These summaries will subsequently offer an answer to each research question. Based on these answers, the results with respect to the overall research goal will be assessed. From this conclusion a set of recommendations can be derived which will be given in section 8.2. Each major recommendation is grouped per subsection to provide a better overview.

8.1. Research Conclusions

The first research question addresses the current lack of commercial ventures using hybrid rocket systems by a literature study. While commercial ventures have been unsuccessful in the past, more and more companies are getting in the business of large hybrid motors. New space is reopening the opportunities seen in the 80's that could allow for smaller scale systems to find their way into the space business as well. After all, no prohibitive technological boundaries have been encountered. Large hybrids do have complications with regards to stability, but promising results have followed after attempting fixes. A large contributor to the current lack of commercial applications is a combination of large stakes during experimental testing and the lack of enabling technology to sustain failures. This shows that in the mean time all the student projects and university initiatives are a perfect breeding ground where experience with these systems is gained and the technology can be further researched to further increase its TRL especially in the high thrust range. Designs have been proven to work on smaller scales up to a few tens of kN. Scaling effects together with costs are the current complicating factor, but the new space approach is facilitating new opportunities whose results will be available in the upcoming years. The hybrid engine developed for this study is of a scale small enough not to have to deal with the complications of costs. Also, there is a large body of knowledge available from student efforts at this scale.

The second question focuses on the use of the specific propellant combination of nitrous oxide and ABS. The unique properties that 3D printed ABS has make it a very suitable candidate for applications where hybrids are otherwise not usable. It features restartability with an ignition system that use no toxic propellants or explosives. This makes it a valuable alternative to HTPB or paraffin, even though performance is slightly lower. This marginal performance reduction is however deemed insignificant in comparison to the additional benefits of the ignition method of the ABS plastic. Nitrous oxide is a very accessible oxidiser and easy to use in student applications for its simplicity due to its self pressurising effects.

chapter 4 offers an answer to research question three on the possibility to characterise the ABS fuel. The ratio of monomers has been evaluated using 3 different methods showing globally consistent results. The first is Fourier-transform Infrared spectroscopy. The recorded spectra have been used to correlate peaks to mass percentages of each monomer using calibration curves. The second method is Thermogravimetric Analysis which allows for the measurement of sub-component separation by

thermal decomposition as the mass of a sample is logged together with the sample temperature. Finally, bomb calorimetry gives the higher heating value which can be used to find the heat of formation through chemical equilibrium equations. The component mass ratio can be verified using this method as a different ratio of nitrogen, carbon and oxygen atoms will yield a different total enthalpy of the combustion products when the same heat of formation is used. The combination of results show a deviation in fuel properties of below 1%.

In section 5.3 a list of models, with recommendations for potential future improvements, has been given. Multiple models for self-pressurised tanks are available and are expected to offer sufficient accuracy. These models are strongly coupled to the injector models of which plenty are available for both vapour and liquid phases of nitrous. In terms of hybrid regression rates, only a simple formula has been applied so far but the potential exists to add a large set of more sophisticated models and increase the reliability of the current tool. This collection of models offers the answer to the first part of each sub-question of research question 4. Applicable models have been found, but their accuracy is still to be determined based on a comparison with experimental data.

This data is to be acquired using the test setup described in chapter 6, which has been shown to be fit for the purpose of this study: to validate an analytical design tool. Each part of the hardware has been described to a sufficient extent and design decisions have been justified. Two parameters in the engine have been changed in between tests to compare results: the injector ignition to main flow ratio and the grain port geometry. Sensor calibration data has been included to prove the reliability of the collected data.

The collected data, though partially incomplete or anomalous at times, was of sufficient quality to use for partial validation of the tool. Values for the feed system pressures and thrust output have been proven to be within $\pm 10\%$ of the measured values. However, some of the parameters contributing to these overarching values, such as fuel and oxidiser mass flow and OF ratio show a larger deviation. This can be partially attributed to the data analysis method. The second cause may be the use of a simple regression rate model. Proper implementation of more sophisticated models may be able to capture the effects currently treated as a bulk property. The observed error is further increased when helical structures or radiation heat transfer are attempted to be modelled. Given the fast computational time, this is to be expected and a collection of resources and methods have been suggested to decrease the current observed error. These will be elaborated upon in section 8.2. As such, the tool has been validated only for the system it has currently been applied to, while taking into account that significant margins still exist. This concludes the answer to the aforementioned research question four: the models are both applicable and of sufficient accuracy for this study.

No absolute boundary conditions for ignition have been observed although larger ignition to main flow ratios have proven more stringent requirements on the power input and lead time of the ignition power. During all burns, a very consistent ignition power has been achieved, although some required higher values depending on their ignition mass flow. This ties in with research question 5e. A low ignition delay can be assured with a sufficiently low ignition mass flow and controlled conditions by shielding the system from environmental effects. Another important factor is that sufficient ignition power was supplied before the introduction of nitrous oxide into the chamber, allowing the hydrocarbon seeding effect to continue and realise a virtually instantaneous ignition with a delay of only 100 ms. Restartability has not been validated completely, but all trends indicate that the grain with the smallest ignition to main flow ratio is the most promising option, due to the lower regression rate of the pre-chamber and ignition area. Control of the grain burn profile has been achieved by adjusting the grain geometry. A lower OF ratio and higher thrust output due to increased mass flow have been observed when helical structures were applied.

With the summaries provided in each paragraph the research questions have each been addressed and answered successfully. Therefore the research objective for this study has also been achieved: To experimentally validate a modular analytical design tool for restartable ABS-N₂O hybrid engines.

8.2. Recommendations for future work

Due to the both large scope of the project and the fact that this study is an initialisation for further potential studies there is a multitude of aspects that can be improved upon. Either, simplifying model assumptions can be dropped or further experimental studies can be used to further develop and characterise the system. Due to how the software tool was built up from the start, many engineering models can easily be added. They can each be represented in a module and interchangeably used with the existing pool of models. The compatibility of engineering assumptions between more models should always be checked and included in the form of a warning if an incompatible combination is selected by the user. The following sections each address a caveat or potential improvement of the work currently presented. The data collected in this study as well as the software written to model the system can be requested from the author at rolf.wubben@gmail.com for potential future research.

8.2.1. ABS quantification

The progress that has been made to estimate the properties of the used ABS plastic is deemed sufficient for the purpose of this study. For the future however it is recommended to follow up on the results to gain a better understanding of the actual composition of the fuel. The collected methods have the potential to form a even more reliable basis once accurate results are obtained and compared. This goes for repeatable and accurate bomb calorimeter measurements as well as more accurate results that can be achieved using an AutoStepwise TGA machine. This allows for an accurate determination of the SAN-butadiene ratio and can verify FTIR based measurements. Finally, metal additives can be identified by analysing the residue of these experiments.

8.2.2. Regression rate modelling

At the moment the model only considers ideal radial regression rates. However, surface effects such as vortex shedding in post combustion chamber and reduced regression rates in pre-chamber due to vortex formation could be considered as well. The current experiments were all conducted at approximately identical chamber pressures. In order to validate the applicability of the regression rate models for a wider range of engines it is imperative to include a wider range of chamber pressures as well. The chamber pressure influences the chemical equilibria as well as the regression rate process. In the current form, the grain is discretised, but not all parameters have been iterated over the full grain length to preserve the merit of speed. However, now that it is shown that more accurate engine modelling is required and that even a magnitude increase in computation time is acceptable, it should be investigated if all combustion parameters can be iterated over the grain length. This might include a full range of OF ratios and corresponding chemical equilibrium equations as well. The ideal solution would include an option for the user to turn this feature on, once the preliminary design has been iterated a few times and a more ideal solution is being converged towards. Additionally, extra efforts will need to be invested in modelling helical structures to ensure the user of the tool is able to adjust these parameters and optimise their design. Also, radiation effects can be studied further to get more representative results and explore the application range in which this heat transfer mode is either dominant or significant. Finally, the current experimental model contains no post combustion chamber and nozzle and combustion efficiencies have not been taken into account. Including these estimates and running experiments to validate the changing results can drive future design decisions on the sizing of post combustion chambers to optimise between mass increase and system performance.

8.2.3. Expand propellant combinations

In the current form CHESS is only able to evaluate ABS-N₂O hybrids. In terms of fuel, ABS is very close to HTPB and paraffin amongst the top performing hybrid rocket fuels. The oxidiser however has a lot to win in terms of performance. It's self pressurising properties make the total system mass lower, but for certain applications these mass savings will not outweigh the performance gain. Other propellant combinations can already be used in the rocketCEA model, but no thermodynamic models have been included that can be used to model the oxidiser tank dynamics. Especially if non self-pressurised propellants are used, either a pressurisation model needs to be written or a constant tank pressure and temperature assumed. Both scenarios can be modelled using the REFPROP or Coolprop modules, though with varying complexity. REFPROP stands for Reference Fluid Thermodynamic and Transport Properties Database (REFPROP)[39]. It is a comprehensive collection of thermodynamic properties of

many fluids. Coolprop is a c++ library that can be used as a python wrapper that utilises the full capabilities of REFPROP as well as "Pure and pseudo-pure fluid equations of state and transport properties for 122 components" and "Mixture properties using high-accuracy Helmholtz energy formulations" [77]. A large drawback to introducing a whole range of new possible propellant combination is the need for new regression models. The more advanced models included here are focused on ABS combustion with either nitrous oxide or gaseous oxygen. Achieving comparable accuracy requires an investigation in each propellant combination and performing a literature study to evaluate which combinations have been quantified in greater detail already.

8.2.4. Combustion instabilities

For this study a large amount of (high frequency) data has been collected. Most of the analysed data however was required to be analysed in the temporal domain only to validate the use of engineering models. The consequence is that it completely ignores system behaviour in the frequency domain. With all this information however an in-depth study into combustion stability can be performed. This opens the possibility to resolve the regression rate over time instead of only considering the total amount of regression by measuring the port diameter after a test. The approach from De Zilwa et al. [19, 20] looks at low frequency instabilities caused by Helmholtz acoustic mode and relates it to the instantaneous port diameter. In addition, feed system coupled and high frequency instabilities could be predicted by including a set of analytical instability models. If their applicability can be validated it could be used to optimise the design output from CHESS by minimising the considered oscillation modes. This is particularly interesting when oxidiser are used that use liquid injection instead of vapour.

8.2.5. Scalability

Currently, CHESS has been validated for a single system size only. In order to establish the applicability of the combination of engineering models on different scale systems more test data is required. This data can either be acquired from current literature or another experimental test campaign with different size motors can be executed. The option to look into literature is strengthened if the suggestion in subsection 8.2.3 is worked out in parallel. Expanding the amount of propellant combinations will increase the data pool available in literature. Working on different sized system will be of particular interest for defining flooding and cooking limitations in combination with ignitability and restart capabilities.

8.2.6. Ignition properties

During testing a great variability in ignition success was observed. Certain parameters, such as ignition power, ignition timing and atmospheric conditions have been compared and indicated a trend. However, efforts can still be made to optimise the ignition process both for a single start engine as well as short term restartability for application such as satellite or sounding rocket control. Reducing the ignition lead time will improve the performance of control systems and reducing the ignition power can significantly reduce the system mass. The high voltage system used in this study is capable of producing an output voltage of multiple kilovolts with a power input of several 100 watts. A much smaller generator can be procured or designed that can accurately generate a potential over the ignition electrodes and would not have the potential to destroy the measurement equipment when no current flows over the ignition gap, causing the voltage potential to rise. Apart from reducing the generator size, the gap between the ignition electrodes can also be varied to investigate the sensitivity to distance as well as the power requirements. In this study the variance in this distance was determined to be around $\pm 1\text{mm}$.

8.3. Future applications

Hybrid rocket motors are up and coming especially due to the "new space" approach that is starting to get traction. Their safety, simplicity and low cost access to space make it a promising option for certain applications. However, some complications inherent to hybrid engines, such as limited regression rates, combustion efficiency and instability, will ultimately not allow it to completely replace solids and liquids. Instead, the future looks bright for hybrids to consolidate their spot in the market amongst liquid and solid propulsion systems. Once the technology has matured, an in-depth market analysis could be performed to identify which use case are most applicable the proposed technology and results in a competitive engineering solution. Until then it can first contribute to the scientific community by educating students and applying it to small scale applications as a step up to future missions.

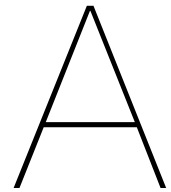
Bibliography

- [1] R. Wubben et al. "Investigation of the in-flight failure of the Stratos III Sounding Rocket". In: *International society of air safety investigators seminar* (2019).
- [2] R. Wubben. *Hydrocarbon Seeded ABS - Nitrous Hybrid Engine Development: A Literature Review*. 2021.
- [3] C. Oiknine. "New perspectives for hybrid propulsion". In: *Joint propulsion conference 42* (2006).
- [4] M. J. Chiaverini and K. K. Kuo. *Fundamentals of Hybrid Rocket Combustion and Propulsion*. Vol. 218. Progress in Astronautics and Aeronautics. AIAA, 2007.
- [5] G. Story et al. "Hybrid Propulsion Demonstration Program 250K Hybrid Motor". In: *39th AIAA/ASME/SAE/ASEE Joint Propulsion Conference and Exhibit*. American Institute of Aeronautics and Astronautics, July 2003.
- [6] D. Pastrone. "Approaches to Low Fuel Regression Rate in Hybrid Rocket Engines". In: *International journal of aerospace engineering 2012* (2012), pp. 1–12.
- [7] G. P. Sutton and O. Biblarz. *Rocket propulsion elements*. 7th ed. John Wiley & Sons, 2001.
- [8] A. Karabeyoglu et al. "Scale-up Tests of High Regression Rate Liquefying Hybrid Rocket Fuels". In: *41st Aerospace Sciences Meeting and Exhibit*. American Institute of Aeronautics and Astronautics, Jan. 2003.
- [9] C. Zaseck et al. "Paraffin Fuel and Additive Combustion in an Opposed Flow Burner Configuration". In: *48th AIAA/ASME/SAE/ASEE Joint Propulsion Conference & Exhibit*. American Institute of Aeronautics and Astronautics, July 2012.
- [10] B. Evans et al. "Characterization of Nano-Sized Energetic Particle Enhancement of Solid-Fuel Burning Rates in an X-Ray Transparent Hybrid Rocket Engine". In: *40th AIAA/ASME/SAE/ASEE Joint Propulsion Conference and Exhibit*. American Institute of Aeronautics and Astronautics, July 2004.
- [11] C. Gotzmer et al. "Improvements of solid fuel burning rates by the addition of nano-sized energetic materials". In: *1st annual national capital region energetics symposium*. Apr. 2009.
- [12] J. Pucci. "The Effects of Swirl Injector Design on Hybrid Flame-Holding Combustion Instability". In: *38th AIAA/ASME/SAE/ASEE Joint Propulsion Conference & Exhibit*. American Institute of Aeronautics and Astronautics, July 2002.
- [13] S. A. Whitmore and S. D. Walker. "Engineering Model for Hybrid Fuel Regression Rate Amplification Using Helical Ports". In: *Journal of propulsion and power* 33.2 (Mar. 2017).
- [14] B. Zandbergen. *Thermal Rocket Propulsion (version 2.07)*. 2018.
- [15] G. Leccese, D. Bianchi, and F. Nasuti. "Modeling of Paraffin-Based Fuels in the Simulation of Hybrid Rocket Flowfields". In: *52nd AIAA/SAE/ASEE Joint Propulsion Conference*. American Institute of Aeronautics and Astronautics, July 2016.
- [16] C. Daniele and R. Giuliano. *HYBRID Project: Demonstrator CFD report - DD-3200-6*. 2013.
- [17] A. Karabeyoglu et al. "Transient Modeling of Hybrid Rocket Low Frequency Instabilities". In: *39th AIAA/ASME/SAE/ASEE Joint Propulsion Conference and Exhibit*. American Institute of Aeronautics and Astronautics, July 2003.
- [18] S. De Zilwa et al. "Combustion Oscillations in High Regression Rate Hybrid Rockets". In: *39th AIAA/ASME/SAE/ASEE Joint Propulsion Conference and Exhibit*. American Institute of Aeronautics and Astronautics, July 2003.
- [19] S. De Zilwa et al. "Time-Resolved Fuel-Grain Regression Measurement in Hybrid Rockets". In: *39th AIAA/ASME/SAE/ASEE Joint Propulsion Conference and Exhibit*. American Institute of Aeronautics and Astronautics, July 2003.

- [20] S. De Zilwa et al. "Time-Resolved Fuel-Grain Port Diameter Measurement in Hybrid Rockets". In: *Journal of propulsion and power* 20.4 (July 2004), pp. 684–689.
- [21] A. Karabeyoglu, J. Stevens, and B. Cantwell. "Investigation of Feed System Coupled Low Frequency Combustion Instabilities in Hybrid Rockets". In: *43rd AIAA/ASME/SAE/ASEE Joint Propulsion Conference & Exhibit*. American Institute of Aeronautics and Astronautics, July 2007.
- [22] B. S. Waxman et al. "Effects of Injector Design on Combustion Stability in Hybrid Rockets Using Self-Pressurizing Oxidizers". In: *50th AIAA/ASME/SAE/ASEE Joint Propulsion Conference*. American Institute of Aeronautics and Astronautics, July 2014.
- [23] D. Pastrone et al. "Acoustic Analysis of Hybrid Rocket Combustion Chambers". In: *43rd AIAA/ASME/SAE/ASEE Joint Propulsion Conference & Exhibit*. American Institute of Aeronautics and Astronautics, July 2007.
- [24] C. Carmicino and A. Russo Sorge. "On the Role of Vortex Shedding in Hybrid Rockets Combustion Instability". In: *44th AIAA/ASME/SAE/ASEE Joint Propulsion Conference & Exhibit*. American Institute of Aeronautics and Astronautics, July 2008.
- [25] C. Carmicino and D. Pastrone. "An Analytical Model to Predict Longitudinal Acoustic Modes Frequency of Hybrid Rockets Combustion Chamber". In: *53rd AIAA/SAE/ASEE Joint Propulsion Conference*. American Institute of Aeronautics and Astronautics, July 2017.
- [26] D. Pastrone et al. "Combustion Instability Involving Vortex Shedding in Hybrid Rocket Motors". In: *49th AIAA/ASME/SAE/ASEE Joint Propulsion Conference*. American Institute of Aeronautics and Astronautics, July 2013.
- [27] K. Akyuzlu. "Modeling Instabilities due to Coupling of Acoustic and Hydrodynamic Oscillations in Hybrid Rocket Motors". In: *43rd AIAA/ASME/SAE/ASEE Joint Propulsion Conference & Exhibit*. American Institute of Aeronautics and Astronautics, July 2007.
- [28] N. S. Uddanti. "Transient Generalized Two Temperatures Approach to Model the Non-acoustic Combustion Instability of a Hybrid Rocket". In: *AIAA Propulsion and Energy 2020 Forum*. American Institute of Aeronautics and Astronautics, Aug. 2020.
- [29] M. Grosse and G. Schlatzke. "Development of a Hybrid Rocket Motor Using a Diaphragm for a Small Test Rocket". In: *44th AIAA/ASME/SAE/ASEE Joint Propulsion Conference & Exhibit*. American Institute of Aeronautics and Astronautics, July 2008.
- [30] M. Grosse. "Effect of a Diaphragm on Performance and Fuel Regression of a Laboratory Scale Hybrid Rocket Motor Using Nitrous Oxide and Paraffin". In: *45th AIAA/ASME/SAE/ASEE Joint Propulsion Conference & Exhibit*. American Institute of Aeronautics and Astronautics, Aug. 2009.
- [31] N. Bellomo et al. "Numerical Investigation of the Effect of a Diaphragm on the Performance of a Hybrid Rocket Motor". In: *46th AIAA/ASME/SAE/ASEE Joint Propulsion Conference & Exhibit*. American Institute of Aeronautics and Astronautics, July 2010.
- [32] N. Bellomo et al. "The "Vortex Reloaded" project: numerical investigation on fully tangential vortex injection in N₂O - paraffin hybrid motors". In: *48th AIAA/ASME/SAE/ASEE Joint Propulsion Conference & Exhibit*. American Institute of Aeronautics and Astronautics, July 2012.
- [33] N. Bellomo et al. "The "Vortex Reloaded" project: experimental investigation on fully tangential vortex injection in N₂O - paraffin hybrid motors". In: *48th AIAA/ASME/SAE/ASEE Joint Propulsion Conference & Exhibit*. American Institute of Aeronautics and Astronautics, July 2012.
- [34] N. Bellomo et al. "Investigation of Effect of Diaphragms on the Efficiency of Hybrid Rockets". In: *Journal of propulsion and power* 30.1 (Jan. 2014), pp. 175–185.
- [35] C. Taylor. *RocketCEA*. 2015. URL: <https://rocketcea.readthedocs.io/en/latest/index.html> (visited on 05/11/2021).
- [36] A. Karabeyoglu. "Mixtures of Nitrous Oxide and Oxygen (Nytrox) as Oxidizers for Rocket Propulsion Applications". In: *45th AIAA/ASME/SAE/ASEE Joint Propulsion Conference & Exhibit*. American Institute of Aeronautics and Astronautics, 2009.
- [37] S. A. Whitmore, Z. W. Peterson, and S. D. Eilers. "Comparing Hydroxyl Terminated Polybutadiene and Acrylonitrile Butadiene Styrene as Hybrid Rocket Fuels". In: *Journal of propulsion and power* 29.3 (May 2013).

- [38] S. Whitmore, Z. Peterson, and S. Eilers. "Analytical and Experimental Comparisons of HTPB and ABS as Hybrid Rocket Fuels". In: *47th AIAA/ASME/SAE/ASEE Joint Propulsion Conference & Exhibit*. American Institute of Aeronautics and Astronautics, July 2011.
- [39] P. Linstrom and W. Mallard. Eds., *NIST Chemistry WebBook, NIST Standard Reference Database Number 69*. National Institute of Standards and Technology, Gaithersburg MD, 20899, (retrieved September 9, 2021).
- [40] B. Genevieve et al. "Performance Modeling of a Paraffin Wax / Nitrous Oxide Hybrid Rocket Motor". In: American Institute of Aeronautics and Astronautics, 2011.
- [41] M. C. Tarifa and L. Pizzuti. "Theoretical performance analysis of hybrid rocket propellants aiming at the design of a test bench and a propulsive system". In: *8th european conference for aeronautics and space sciences (EUCASS)*. 2019.
- [42] S. A. Whitmore et al. "Development of a Power-Efficient, Restart-Capable Arc Ignitor for Hybrid Rockets". In: *Journal of propulsion and power* 31.6 (Nov. 2015).
- [43] S. A. Whitmore et al. "Survey of Selected Additively Manufactured Propellants for Arc Ignition of Hybrid Rockets". In: *Journal of propulsion and power* 32.6 (Nov. 2016), pp. 1494–1504.
- [44] S. A. Whitmore, S. Mathias, and R. Harvey. "High Voltage Breakdown and Arc-Tracking Mechanism of Thermoplastics with Applications to Hybrid Rocket Arc- Ignition". In: *53rd AIAA/SAE/ASEE Joint Propulsion Conference*. American Institute of Aeronautics and Astronautics, July 2017.
- [45] V. Zakirov et al. "Restartable Hybrid Rocket Motor using Nitrous Oxide". In: *57th International Astronautical Congress*. American Institute of Aeronautics and Astronautics, Oct. 2006.
- [46] S. A. Whitmore. "Additively Manufactured Acrylonitrile-Butadiene-Styrene–Nitrous-Oxide Hybrid Rocket Motor with Electrostatic Igniter". In: *Journal of propulsion and power* 31.4 (July 2015), pp. 1217–1220.
- [47] S. A. Whitmore. "Advantages of Using Additive Manufacturing to Build "Green" Fuels for Hybrid Propulsion". In: *International journal of astronautics and aeronautical engineering* 2.1 (June 2017).
- [48] S. A. Whitmore and A. M. Bulcher. "Vacuum Test of a Novel Green-Propellant Thruster for Small Spacecraft". In: *53rd AIAA/SAE/ASEE Joint Propulsion Conference*. American Institute of Aeronautics and Astronautics, July 2017.
- [49] PerkinElmer. *Enhanced Separation of Components in ABS Polymer Using AutoStepwise TGA*. 2012.
- [50] D. Reggio et al. "Characterization of contemporary and historical acrylonitrile butadiene styrene (ABS)-based objects: Pilot study for handheld Raman analysis in collections". In: *Spectrochimica acta part a: molecular and biomolecular spectroscopy* 242 (Dec. 2020), p. 118733.
- [51] J. N. Hahladakis et al. "An overview of chemical additives present in plastics: Migration, release, fate and environmental impact during their use, disposal and recycling". In: *Journal of hazardous materials* 344 (Feb. 2018), pp. 179–199.
- [52] B. D. Gesner. *Analysis of Acrylonitrile-Butadiene-Styrene (ABS) Plastics by Infrared Spectroscopy*. 1970.
- [53] S. Gordon and B. J. McBride. *Computer Program for Calculation of Complex Chemical Equilibrium Compositions and Applications I. Analysis*. 1994.
- [54] B. J. McBride and S. Gordon. *Computer Program for Calculation of Complex Chemical Equilibrium Compositions and Applications II. User Manual and Program Description*. 1996.
- [55] J. E. Zimmerman et al. "Review and Evaluation of Models for Self-Pressurizing Propellant Tank Dynamics". In: *49th AIAA/ASME/SAE/ASEE Joint Propulsion Conference*. American Institute of Aeronautics and Astronautics, 2013.
- [56] ESDU. *Thermophysical properties of nitrous oxide*. 1991.
- [57] S. A. Whitmore and S. N. Chandler. "Engineering Model for Self-Pressurizing Saturated-N₂O-Propellant Feed Systems". In: *Journal of propulsion and power* 26.4 (July 2010), pp. 706–714.

- [58] L. Casalino and D. Pastrone. "Optimal design of hybrid rocket motors for microgravity platform". In: vol. 24. 3. *Journal of Propulsion and Powers*, May 2008, pp. 491–498.
- [59] G. Zilliac and M. Karabeyoglu. "Modeling of Propellant Tank Pressurization". In: *41st AIAA/ASME/SAE/ASEE Joint Propulsion Conference & Exhibit*. American Institute of Aeronautics and Astronautics, July 2005.
- [60] M. M. Fernandez. *Propellant tank pressurization modeling for a hybrid rocket*. Rochester Institute of Technology, 2009.
- [61] J. E. Zimmerman. "Self-pressurizing propellant tank dynamics". PhD thesis. Stanford University, 2015.
- [62] R. Newlands. *Modelling the nitrous run tank emptying*. Aspire Space, 2012.
- [63] J. Dyer et al. "Modeling Feed System Flow Physics for Self-Pressurizing Propellants". In: American Institute of Aeronautics and Astronautics, 2007.
- [64] B. J. Solomon. *Engineering Model to Calculate Mass Flow Rate of a Two-Phase Saturated Fluid Through An Injector Orifice*. Utah State University, 2011.
- [65] B. Waxman, B. Cantwell, and G. Zilliac. "Effects of Injector Design and Impingement Techniques on the Atomization of Self-Pressurizing Oxidizers". In: *48th AIAA/ASME/SAE/ASEE Joint Propulsion Conference & Exhibit*. American Institute of Aeronautics and Astronautics, July 2012.
- [66] G. Marxman and M. Gilbert. "Turbulent Boundary Layer Combustion in the Hybrid Rocket". In: *Proceedings of the 9th international symposium on combustion* (1963), pp. 371–383.
- [67] G. A. Marxman. "Combustion in the turbulent boundary layer on a vaporizing surface". In: *Proceedings of the 10th international symposium on combustion* (Jan. 1965), pp. 1337–1349.
- [68] T. Marquardt and J. Majdalani. "Review of Classical Diffusion-Limited Regression Rate Models in Hybrid Rockets". In: *Aerospace* 6.6 (June 2019).
- [69] S. A. Whitmore. "Three-Dimensional Printing of "Green" Fuels for Low-Cost Small Spacecraft Propulsion Systems". In: *Journal of spacecraft and rockets* 55 (Jan. 2018), pp. 13–26.
- [70] S. A. Whitmore and S. Merkley. "Radiation Heating Effects on Oxidizer-to-Fuel Ratio of Additively Manufactured Hybrid Rocket Fuels". In: *Journal of propulsion and power* 35.4 (July 2019), pp. 863–878.
- [71] S. A. Whitmore et al. "Estimating the Enthalpy of Gasification of Acrylonitrile–Butadiene–Styrene Hybrid Rocket Fuels". In: *Journal of propulsion and power* 31 (July 2015), pp. 1033–1040.
- [72] S. D. Eilers and S. A. Whitmore. "Longitudinally-Variable Hybrid Rocket Regression Rate Model with Radiation and Boundary Layer Effects". In: *49th AIAA/ASME/SAE/ASEE Joint Propulsion Conference*. American Institute of Aeronautics and Astronautics, July 2013.
- [73] K. de Kievit et al. *ET3056TU: Detailed Design Report Detailed Design of a Gimbal Mechanism, Corresponding Test Bench and CNS System*. 2018.
- [74] A. Munich. *ZVS (Mazilli) Driver*. URL: <http://adammunich.com/zvs-driver/> (visited on 05/11/2021).
- [75] SAMSON AG. *Application Notes: KV coefficient - Valve sizing*. 2012.
- [76] S. A. Whitmore. "A Variational Method for Estimating Time-Resolved Hybrid Fuel Regression Rates from Chamber Pressure". In: *AIAA Propulsion and Energy 2020 Forum*. American Institute of Aeronautics and Astronautics, Aug. 2020.
- [77] I. H. Bell et al. "Pure and pseudo-pure fluid thermophysical property evaluation and the open-source thermophysical property library coolprop". In: *Industrial & engineering chemistry research* 53.6 (2014), pp. 2498–2508.



COTS Datasheets

In this appendix the datasheets of the measurement equipment are collected. It contains:

- Pressure transmitter PT5423
- Tank: S-type load cell
- Thrust: miniature in line load cell
- Acoustic sensor
 - Technical drawing
 - Specifications
- Dynamic pressure sensor
 - Technical drawing
 - Specifications
- Vibration sensor
- Arduino uno
- TI INA219
- Material Properties
 - REAL Filemanent
 - TRINSEO MAGNUM™3453 ABS Resin

- The system manufacturer undertakes to perform a risk assessment and to create a documentation in accordance with legal and normative requirements to be provided to the operator and user of the system. This documentation must contain all necessary information and safety instructions for the operator, the user and, if applicable, for any service personnel authorised by the manufacturer of the system.
- Read this document before setting up the product and keep it during the entire service life.
- The product must be suitable for the corresponding applications and environmental conditions without any restrictions.
- Only use the product for its intended purpose (→ Functions and features).
- Only use the product for permissible media (→ Technical data).
- If the operating instructions or the technical data are not adhered to, personal injury and/or damage to property may occur.
- The manufacturer assumes no liability or warranty for any consequences caused by tampering with the product or incorrect use by the operator.
- Installation, electrical connection, set-up, programming, configuration, operation and maintenance of the product must be carried out by personnel qualified and authorised for the respective activity.
- Protect units and cables against damage.

UK



CAUTION

For high medium temperatures, parts of the unit may heat up.

> Risk of burns

► Do not touch the unit

► Protect the housing against contact with flammable substances and unintentional contact.

3 Functions and features

The pressure sensor detects the system pressure and converts it into an analogue output signal.

3.1 Applications

- Type of pressure: relative pressure

Order number	Measuring range		Pressure resistance (max. permissible pressure)		Bursting pressure	
	bar	psi	bar	psi	bar	psi
PT5415 / PU5415	0...6	0...87	15	215	200	2900
PT5404 / PU5404	0...10	0...145	25	360	300	4350
PT5494	-1...10	-14.5...145	25	360	300	4350
PT5414 / PU5414	0...16	0...232	40	580	450	6525
PT5403 / PU5403	0...25	0...360	65	940	600	8700
PT5453	0...30	0...435	65	940	600	8700
PT5443 / PU5443	0...40	0...580	100	1450	800	11600
PT5423 / PU5423	0...60	0...870	150	2175	900	13050
PT5402 / PU5402	0...100	0...1450	250	3625	1000	14500
PT5412 / PU5412	0...160	0...2320	400	5800	1100	15950
PT5401 / PU5401	0...250	0...3625	625	9060	1200	17400
PT5400 / PU5400	0...400	0...5800	1000	14500	1700	24650
PT5460 / PU5460	0...600	0...8700	1500	21750	2400	34800

MPa = bar ÷ 10 / kPa = bar × 100



Avoid static and dynamic overpressure exceeding the specified overload pressure by taking appropriate measures.

The indicated bursting pressure must not be exceeded.

Even if the bursting pressure is exceeded only for a short time, the unit may be destroyed. ATTENTION: Risk of injury!



For units with a final value of the measuring range of 600 bar the limits of the pressure cycles across the lifetime apply. (→ Technical data).



Pressure Equipment Directive (PED):

Units with a final value of the measuring range of 6...400 bar comply with the Pressure Equipment Directive and are designed and manufactured for group 2 fluids in accordance with the sound engineering practice.

Use of group 1 fluids on request!



The units are vacuum resistant.



Pressure Equipment Directive (PED):

The units with a final value of the measuring range of 600 bar comply with the Pressure Equipment Directive. They are designed for group 2 fluids and manufactured and tested according to Module A.

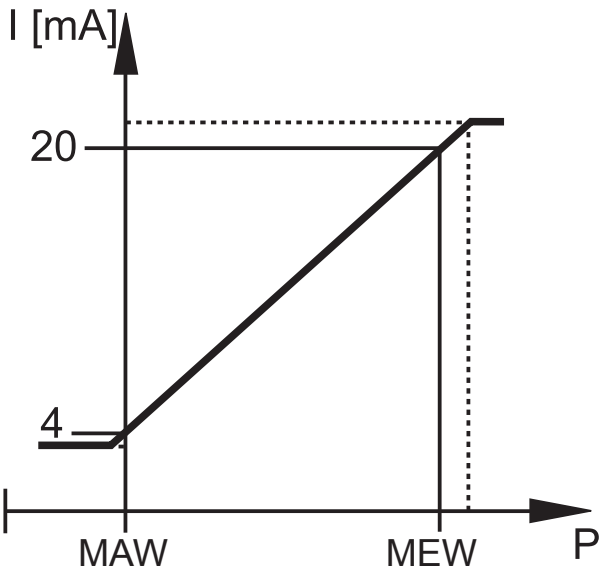
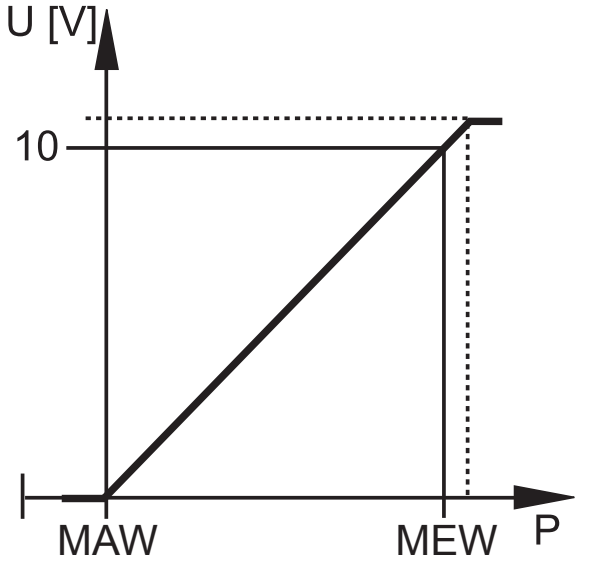
Use of group 1 fluids on request!



If the cable length exceeds 30 m or if used outside buildings, there is a risk of overvoltage pulses from external sources. We recommend to use the unit in protected operating environments and to limit overvoltage pulses to max. 500 V.

UK

4 Functions

Current output 4...20 mA (PT54xx)	Voltage output 0...10 V (PU54xx)
	
P = system pressure, MAW = Initial value of the measuring range, MEW = final value of the measuring range	
In the measuring range the output signal is between 4 and 20 mA. If the system pressure is above or below the measuring range, the analogue output behaves, without achieving the accuracy, as follows: <ul style="list-style-type: none">• System pressure above the measuring range: 20...25 mA.• System pressure below the measuring range: 4...3 mA.	In the measuring range the output signal is between 0 and 10 V. If the system pressure is above the measuring range, the analogue output behaves, without achieving the accuracy, as follows: <ul style="list-style-type: none">• System pressure above the measuring range: 10...11.5 V.

5 Installation



Before installing and removing the unit: make sure that no pressure is applied to the system.

- ▶ Insert the unit in a G ¼ process connection.
- ▶ Tighten firmly. Recommended tightening torque:

Pressure range in bar	Tightening torque in Nm
6...400	25...35
600	30...50
Depends on lubrication, seal and pressure load!	

6 Electrical connection



The unit must be connected by a qualified electrician.
The national and international regulations for the installation of electrical equipment must be adhered to.
Voltage supply to EN 50178, SELV, PELV.



For marine applications (if approval available for the device), additional surge protection is required.

- ▶ Disconnect power.
- ▶ Connect the unit as follows:

PT54xx (4...20 mA analogue)

Core colours		
BN	brown	
WH	white	
		OUT: analogue output 4...20 mA Colours to DIN EN 60947-5-2
Example circuit		

PU54xx (0...10 V analogue)

Core colours	
BN	brown
WH	white
BU	blue

OUT: analogue output 0...10 V
Colours to DIN EN 60947-5-2

Example circuit

UK

7 Technical data



Directive 97/23/EC (pressure equipment directive) stipulates that the following technical data must be provided for units with a final value of the measuring range of 600 bar.

PT5460	
Operating voltage [V]	8.5...36 DC
Analogue output	4...20 mA
PU5460	
Operating voltage [V]	16...36 DC
Analogue output	0...10 V
Medium temperature [°C]	-40...90
Ambient temperature [°C]	-40...90
Storage temperature [°C]	-40...100
Pressure cycles (min.) across lifetime	60 million for 1.2 x nominal pressure
Shock resistance [g]	50 (DIN EN 60068-2-27, 11 ms)
Vibration resistance [g]	20 (DIN EN 60068-2-6, 10...2000 Hz)

More information at www.ifm.com

S-Type Load Cell

SPECIFICATIONS			
PARAMETER	VALUE		UNIT
NTEP/OIML accuracy class	NTEP III & IIIL	Non-Approved	
Maximum no. of intervals (n)	III 5000 single* IIIL10000 single*	2000	
$Y = E_{\max}/V_{\min}$	10000	5000	Maximum available
Standard capacities (E_{\max}) (Aluminum)	5, 10, 20		kg
Standard capacities (E_{\max}) (Steel)	25, 50, 75, 100, 250, 500, 750, 1000, 1500, 2000, 2500, 5000		kg
	250, 300, 500, 750, 1k, 1.5k, 2k, 2.5k, 3k, 5k, 7.5k, 10k, 15k, 20k, 40k		lbs
Rated output—R.O. (Aluminum)	2.0		mV/V
Rated output—R.O. (Steel)	3.0		mV/V
Rated output tolerance	0.25		±% of rated output
Zero balance	1		±% of rated output
Non-linearity	0.020	0.020 (SS: 0.05)	±% of rated output
Hysteresis	0.020	0.020 (SS: 0.05)	±% of rated output
Non-repeatability	0.020		±% of rated output
Creep error (20 minutes)	0.030		±% of rated output
Zero return (20 minutes)	0.030		±% of rated output
Temperature effect on min. dead load output	0.0015	0.0026	±% of rated output/°C
Temperature effect on sensitivity	0.0010	0.0015	±% of applied load/°C
Compensated temperature range	-10 to +40		°C
Operating temperature range	-20 to +60		°C
Safe overload	150		% of R.C.
Ultimate overload	200 (Aluminum) / 300 (Steel)		% of R.C.
Excitation, recommended	10		VDC or VAC RMS
Excitation, maximum	15		VDC or VAC RMS
Input impedance	410±5 (Aluminum) / 385±5 (Steel)		Ω
Output impedance	350±3		Ω
Insulation resistance	>5000		MΩ
Construction	Aluminium or Nickel-plated alloy steel **		
Environmental protection	IP67		

* Capacities 250–20k lbs

** Stainless steel available

All specifications subject to change without notice.

FM Approval

Intrinsically Safe: Class I, II, III; Div. 1 Groups A-G

Non-Incendive: Class I; Div. 2 Groups A-D



FEATURES

- Minimal mounting clearance
- 17-4 PH stainless-steel construction
- For use in both tension and compression
- Utilizes metal foil strain gauge technology
- Adheres to RoHS Directive 2015/863/EU
- Accessories and related instruments available

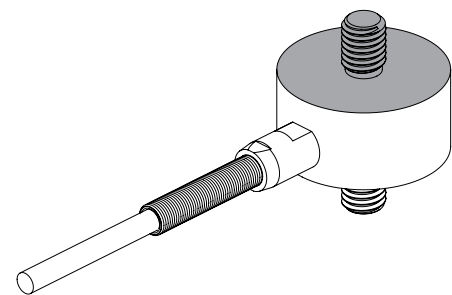
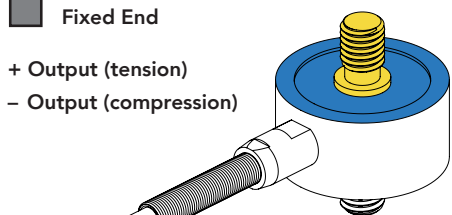
 Non-loading surface, do not contact

 Active End

 Fixed End

+ Output (tension)

– Output (compression)



SPECIFICATIONS

PERFORMANCE

Nonlinearity	±0.25% of RO
Hysteresis	±0.25% of RO
Nonrepeatability	±0.1% of RO

ELECTRICAL

Rated Output (RO)	2 mV/V nom
Excitation (VDC or VAC)	15 max
Bridge Resistance	740 Ohm nom
Insulation Resistance	≥500 MOhm @ 50 VDC
Connection	#28 AWG, 4 conductor braided-shielded PVC cable 10 ft (3 m) long
Wiring/Connector Code	WC1

MECHANICAL

Weight (minus cable)	1.5 oz [42.5 g]
Safe Overload	150% of RO
Deflection	0.001 in [0.03 mm] nom
Material (flexure)	17-4 PH stainless-steel
IP Rating	IP64

TEMPERATURE

Operating Temperature	–45 to 200°F (–42 to 93°C)
Compensated Temperature	60 to 160°F (15 to 72°C)
Temperature Shift Zero	±0.005% of RO/°F (±0.01 of RO/°C)
Temperature Shift Span	±0.02% of load/°F (±0.036 of load/°C)

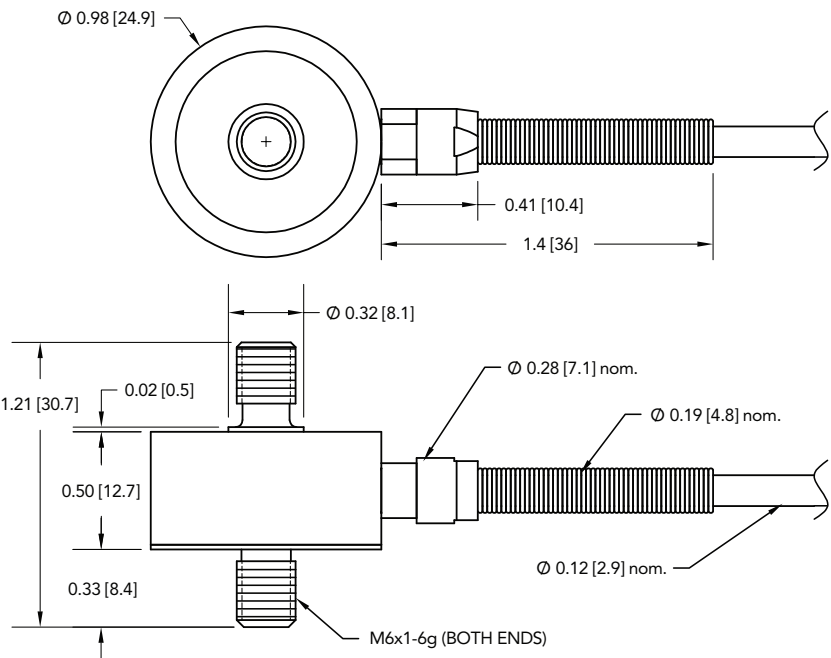
CALIBRATION

Calibration Test Excitation	10 VDC
Calibration (standard)	5-pt Tension
Calibration (available)	Compression
Shunt Calibration Value	100 kOhm

CONFORMITY

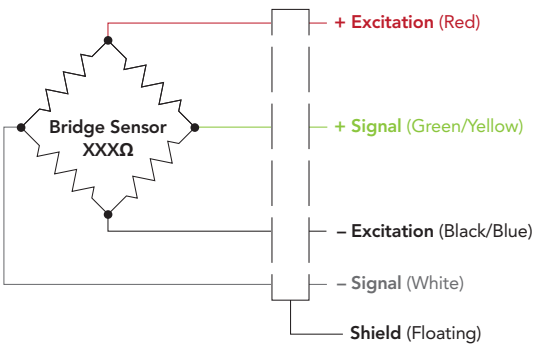
RoHS	EU 2015/863
CE	EN55011; EN61326-1

DIMENSIONS inches [mm]



WIRING CODE (WC1 WITH SHIELD)

RED	+ EXCITATION
BLACK	- EXCITATION
GREEN	+ SIGNAL
WHITE	- SIGNAL
SHIELD	FLOATING



CAPACITIES

ITEM #	lb	N	Natural Frequency (kHz)
FSH03884	50	223	7.5
FSH03885	100	445	10.2
FSH03886	250	1112	16.2
FSH03887	500	2224	22.9
FSH03888	1000	4448	30.1



Drawing Number: FI1059-G

FUTEK reserves the right to modify its design and specifications without notice.
Please visit <http://www.futek.com/salesterms> for complete terms and conditions.

10 Thomas, Irvine, CA 92618 USA

Tel: (949) 465-0900

Fax: (949) 465-0905

www.futek.com



RoHS



U.S. Manufacturer

2

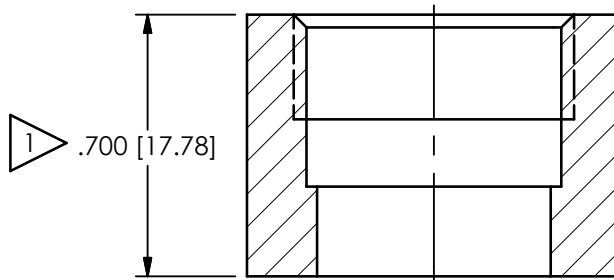
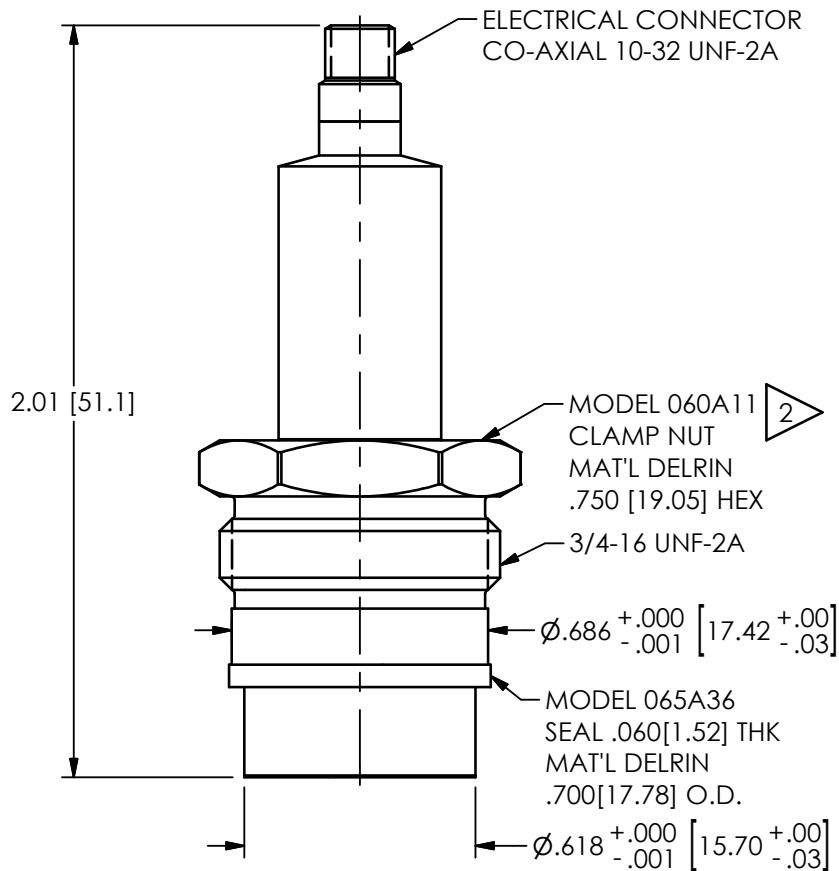
1

PCB Piezotronics Inc. claims proprietary rights in the information disclosed hereon. Neither it nor any reproduction thereof will be disclosed to others without the written consent of PCB Piezotronics Inc.

REVISIONS

REV	DESCRIPTION	DIN
B	UPDATED [15.88] WAS [5.88]	44838

22929



MOUNTING HOLE PREPARATION

$\phi .625$ [15.88] THRU
 $\perp \phi .703$ [17.86] $\nabla .460$ [11.68]
3/4-16 UNF-2B $\nabla .28$ [7.1]

2 RECOMMENDED MOUNTING TORQUE ON 3/4 HEX 3-5 FT LBS [.415-.691 Kg-m]

1 DIMENSIONS SHOWN ARE FOR .700 [17.78] THICK WALL. COUNTERBORE THICKER WALLS.

UNLESS OTHERWISE SPECIFIED TOLERANCES ARE:

DRAWN

CHECKED

ENGINEER

PCB PIEZOTRONICS

3425 WALDEN AVE. DEPEW, NY 14043
(716) 684-0001 E-MAIL: sales@pcb.com

CODE
IDENT. NO.
52681

DWG. NO.

22929

SCALE:



2X

SHEET

1 OF 1

2

1

Model Number 106B52	ICP® PRESSURE SENSOR		Revision: B ECN #: 33741	
Performance Measurement Range(for ±5V output) 1 psi 6.89 kPa Sensitivity(± 15 %) 5000 mV/psi 725 mV/kPa Maximum Pressure(Dynamic) 10 psi 68.9 kPa Maximum Pressure(static) 50 psi 345 kPa Resolution 0.02 mpsi .00013 kPa Resonant Frequency ≥ 40 kHz ≥ 40 kHz Rise Time(Reflected) ≤ 12.5 µ sec ≤ 12.5 µ sec Low Frequency Response(-5 %) 2.5 Hz 2.5 Hz Non-Linearity ≤ 1 % FS ≤ 1 % FS [1]			OPTIONAL VERSIONS Optional versions have identical specifications and accessories as listed for the standard model except where noted below. More than one option may be used. E - Emralon coating Coating Emralon Emralon Electrical Isolation 10 ⁸ ohm 10 ⁸ ohm J - Ground Isolated [3] N - Negative Output Polarity W - Water Resistant Cable [4] Supplied Accessory : Model 060A11 Delrin clamp nut 3/4-16-2A thd 3/4" hex (1) WM - Water Resistant Cable [4] Supplied Accessory : Model 060A13 Metric Delrin clamp nut M20 x 1.5-6g thd 20 mm hex (1)	
Environmental Acceleration Sensitivity ≤ 0.002 psi/g ≤ 0.0014 kPa/(m/s ²) Temperature Range(Operating) -65 to +250 °F -54 to +121 °C Temperature Coefficient of Sensitivity ≤ 0.03 %/°F ≤ 0.054 %/°C Maximum Shock 1000 g pk 9807 m/s ² pk			NOTES: [1] Zero-based, least-squares, straight line method. [2] See PCB Declaration of Conformance PS023 for details. [3] Used with optional mounting adaptor. [4] Clamp nut installed prior to cable attachment	
Electrical Output Polarity(Positive Pressure) Positive Positive Discharge Time Constant(at room temp) ≥ 0.2 sec ≥ 0.2 sec Excitation Voltage 24 to 27 VDC 24 to 27 VDC Constant Current Excitation 2 to 20 mA 2 to 20 mA Output Impedance <100 ohm <100 ohm Output Bias Voltage 7 to 14 VDC 7 to 14 VDC			SUPPLIED ACCESSORIES: Model 060A11 Delrin clamp nut 3/4-16-2A thd 3/4" hex (1) Model 060A13 Metric Delrin clamp nut M20 x 1.5-6g thd 20 mm hex (1) Model 065A36 Seal, .687" OD x .625" ID x .060", Delrin (3)	
Physical Sensing Geometry Compression Compression Sensing Element Quartz Quartz Housing Material 17-4 Stainless Steel 17-4 Stainless Steel Diaphragm 316L Stainless Steel 316L Stainless Steel Sealing Welded Hermetic Welded Hermetic Electrical Connector 10-32 Coaxial Jack 10-32 Coaxial Jack Weight 1.2 oz 35 gm			Entered: <u>OMW</u> Engineer: <u>NIL</u> Sales: <u>KWJ</u> Approved: <u>EB</u> Spec Number: Date: <u>8/24/10</u> Date: <u>8/24/10</u> Date: <u>8/24/10</u> Date: <u>8/24/10</u> 22933	
 [2] All specifications are at room temperature unless otherwise specified. In the interest of constant product improvement, we reserve the right to change specifications without notice. ICP® is a registered trademark of PCB Group, Inc.			 PCB PIEZOTRONICS® PRESSURE DIVISION 3425 Walden Avenue, Depew, NY 14043 Phone: 716-684-0001 Fax: 716-686-9129 E-Mail: pressure@pcb.com	

124-1210-90

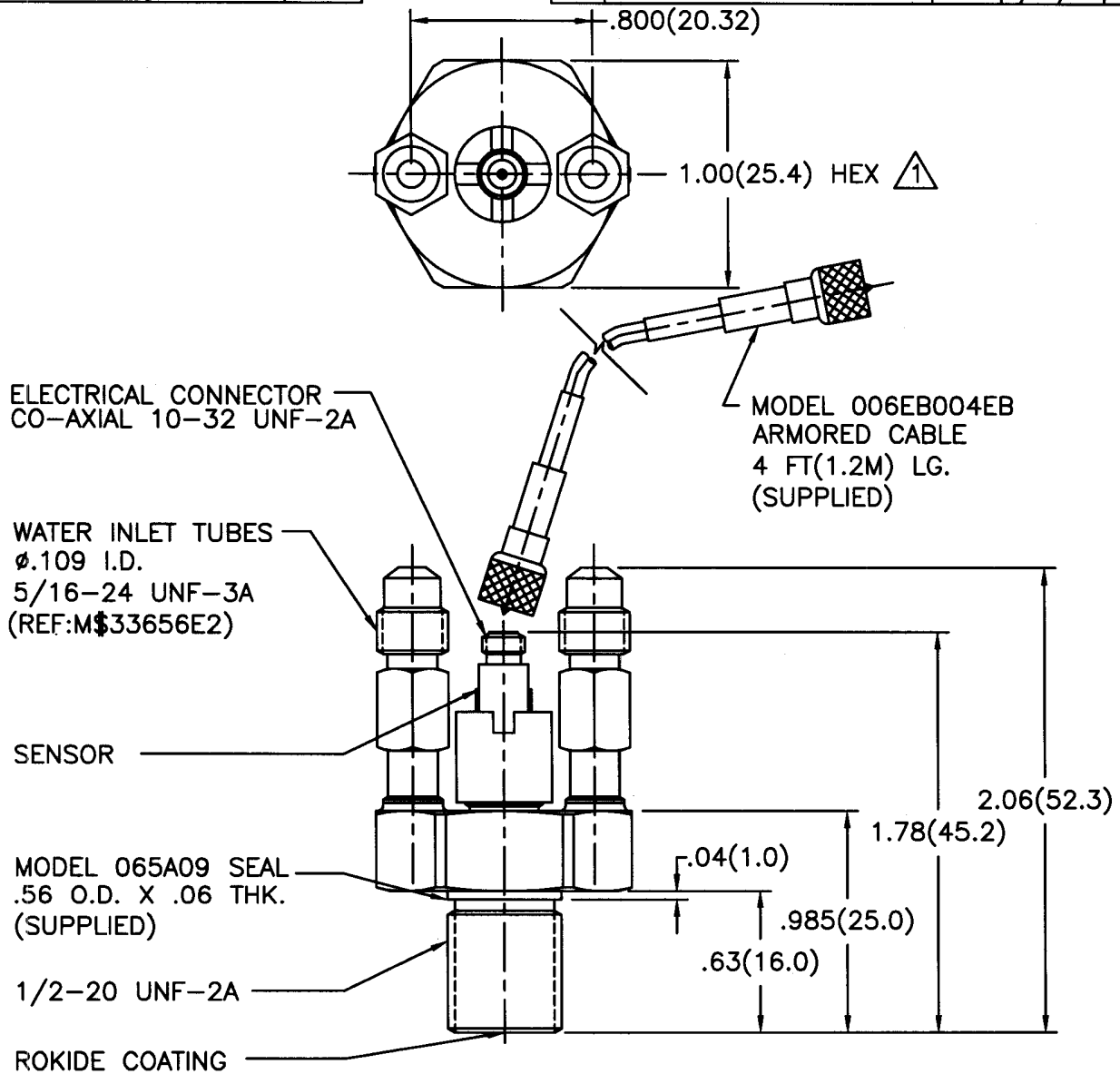
PCB Piezotronics Inc. claims proprietary rights in the information disclosed herein. Neither it nor any reproduction thereof will be disclosed to others without written consent of PCB Piezotronics Inc.

APPLICATION

NEXT ASS'Y	USED ON	VAR

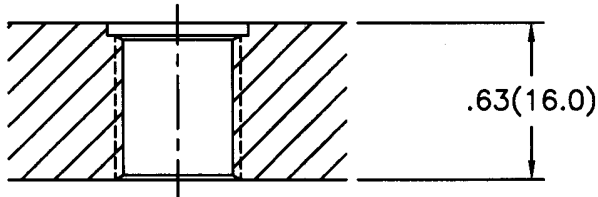
REVISIONS

REV	DESCRIPTION	ECN	DATE	APP'D
D	REVISED PER ECR	20202	7/14/04	DM7/04



MOUNTING HOLE PREPARATION:

Ø.453
THRU
1/2-20 UNF-2B
THRU
Ø.562
X .050 $\nabla 2$



$\nabla 2$ SEAL SURFACE MUST BE FLAT AND FREE OF TOOL MARKS WITH AT LEAST $\nabla 63$ FINISH.

$\nabla 1$ MOUNTING TORQUE ON 1.00 HEX 10-15 FT. LBS.

UNLESS SPECIFIED TOLERANCES

DIMENSIONS IN INCHES	DIMENSIONS IN MILLIMETERS
DECIMALS XX $\pm .03$	[IN BRACKETS] DECIMALS X ± 0.8
XXX $\pm .010$	XX ± 0.25
ANGLES ± 2 DEGREES	ANGLES ± 2 DEGREES
FILLETS AND RADII .003 - .005	FILLETS AND RADII [0.07 - 0.13]

DRAWN	CHK'D	APP'D	TITLE
EB	EM	RF	OUTLINE DRAWING
7/14/04	7/14/04	7/14/04	MODEL 124A21, A22, A24
MFG	ENGR	SALES	WATER COOLED SENSOR
KL6	BVH	DAC	
7/14/04	7/14/04	7/14/04	

PCB PIEZOTRONICS
3425 WALDEN AVE. DEPEW, NY 14043
(716) 684-0001 EMAIL: SALES@PCB.COM

CODE IDENT. NO. 52681	DWG. NO. 124-1210-90
SCALE: 1.33X SHEET 1 OF 1	

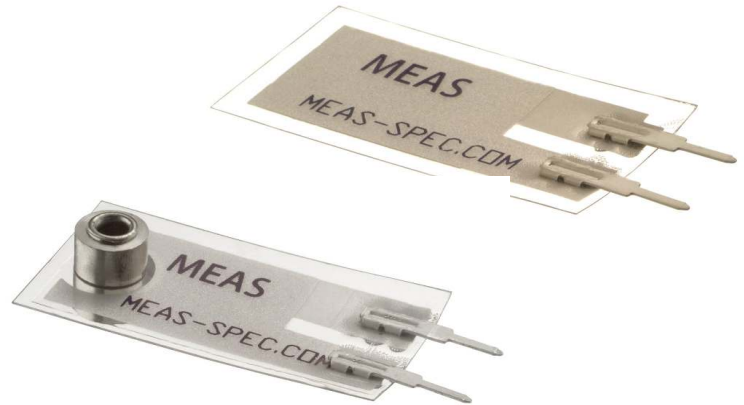
DD011 REV. C 01/21/03

Model Number 124A21		Revision: K ECN #: 51279	
Performance Measurement Range(for ±5V output) Useful Overrange(for ±7V output) Sensitivity(± 15 %) Maximum Pressure Resolution Resonant Frequency Rise Time(Reflected) Low Frequency Response(- 5 %) Non-Linearity Environmental Acceleration Sensitivity Temperature Range(Operating) Temperature Coefficient of Sensitivity Maximum Flash Temperature Maximum Vibration Maximum Shock Electrical Output Polarity(Positive Pressure) Discharge Time Constant(at room temp) Excitation Voltage Constant Current Excitation Output Impedance Output Bias Voltage Electrical Isolation Physical Sensing Geometry Sensing Element Housing Material Diaphragm Sealing Electrical Connector Weight Cable Type Cable Length Water Flow Rate(at 50 psi)	ENGLISH 250 psi 350 psi 20 mV/psi 5,000 psi 0.005 psi ≥ 15 kHz ≤ 30 μsec 0.50 Hz ≤ 1.0 % FS ≤ 0.002 psi/g -100 to +250 °F ≤ 0.03 %/°F 5,000 °F 2,000 g pk 10,000 g pk Positive ≥ 1.0 sec 20 to 30 VDC 2 to 20 mA ≤ 100 Ohm 8 to 14 VDC 10 ⁸ Ohm Compression Quartz Stainless Steel Invar Welded Hermetic 10-32 Coaxial Jack 3.9 oz 006 Ruggedized Low Noise 4.0 ft 1.2 gal/min	SI 1,724 kPa 3,448 kPa 2.90 mV/kPa 34,475 kPa 0.034 kPa ≥ 15 kHz ≤ 30 μsec 0.50 Hz ≤ 1.0 % FS ≤ 0.0014 kPa/(m/s ²) -73 to +121 °C ≤ 0.054 %/°C 2,670 °C 19,600 m/s ² pk 98,070 m/s ² pk Positive ≥ 1.0 sec 20 to 30 VDC 2 to 20 mA ≤ 100 Ohm 8 to 14 VDC 10 ⁸ Ohm Compression Quartz Stainless Steel Invar Welded Hermetic 10-32 Coaxial Jack 110 gm 006 Ruggedized Low Noise 1.3 m 1.2 gal/min	[1] <

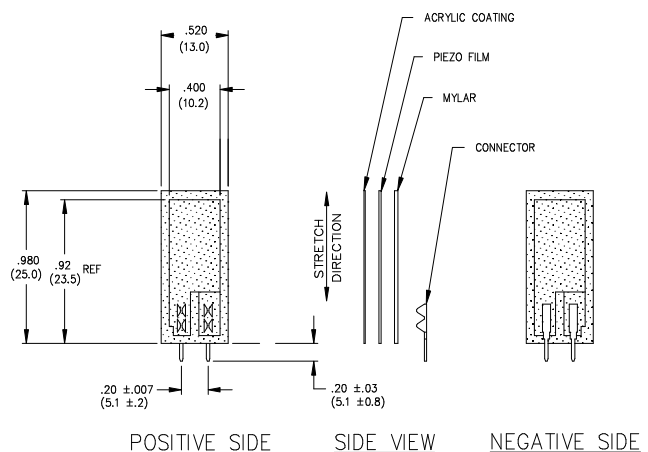
LDT with Crimps Vibration Sensor/Switch

Piezo Film Sensors
High Sensativity
AC Coupled
Laminated
Robust

The **LDT0-028K** is a flexible component comprising a 28 μm thick piezoelectric PVDF polymer film with screen-printed Ag-ink electrodes, laminated to a 0.125 mm polyester substrate, and fitted with two crimped contacts. As the piezo film is displaced from the mechanical neutral axis, bending creates very high strain within the piezopolymer and therefore high voltages are generated. When the assembly is deflected by direct contact, the device acts as a flexible "switch", and the generated output is sufficient to trigger MOSFET or CMOS stages directly. If the assembly is supported by its contacts and left to vibrate "in free space" (with the inertia of the clamped/free beam creating bending stress), the device will behave as an accelerometer or vibration sensor. Adding mass, or altering the free length of the element by clamping, can change the resonant frequency and sensitivity of the sensor to suit specific applications. Multi-axis response can be achieved by positioning the mass off center. The LDTM-028K is a vibration sensor where the sensing element comprises a cantilever beam loaded by an additional mass to offer high sensitivity at low frequencies.



dimensions

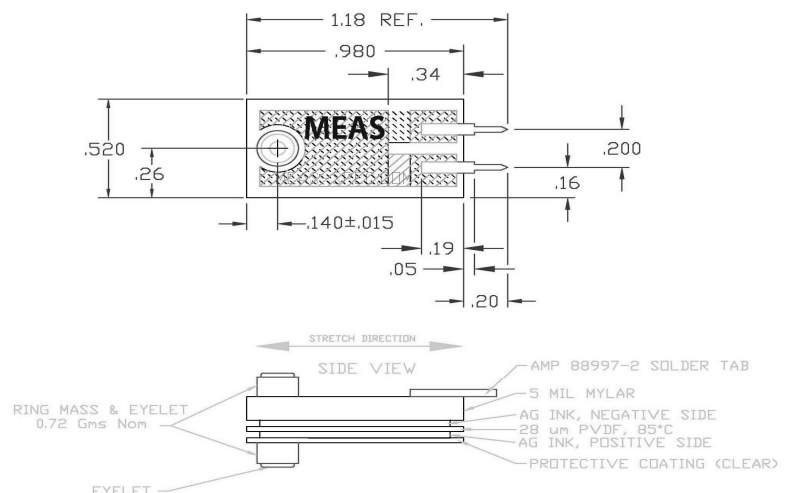


FEATURES

- Solder Tab Connection
- Both No Mass & With Mass Version
- Withstands High Impact
- Operating Temperature: 0°C to 85°C
- Storage Temperature: -40°C to 85 °C
- Higher Temperature Version up to 125 °C available on a Custom Basis

APPLICATIONS

- Vibration Sensing in Washing Machine
- Low Power Wakeup Switch
- Low Cost Vibration Sensing
- Car Alarms
- Body Movement
- Security Systems

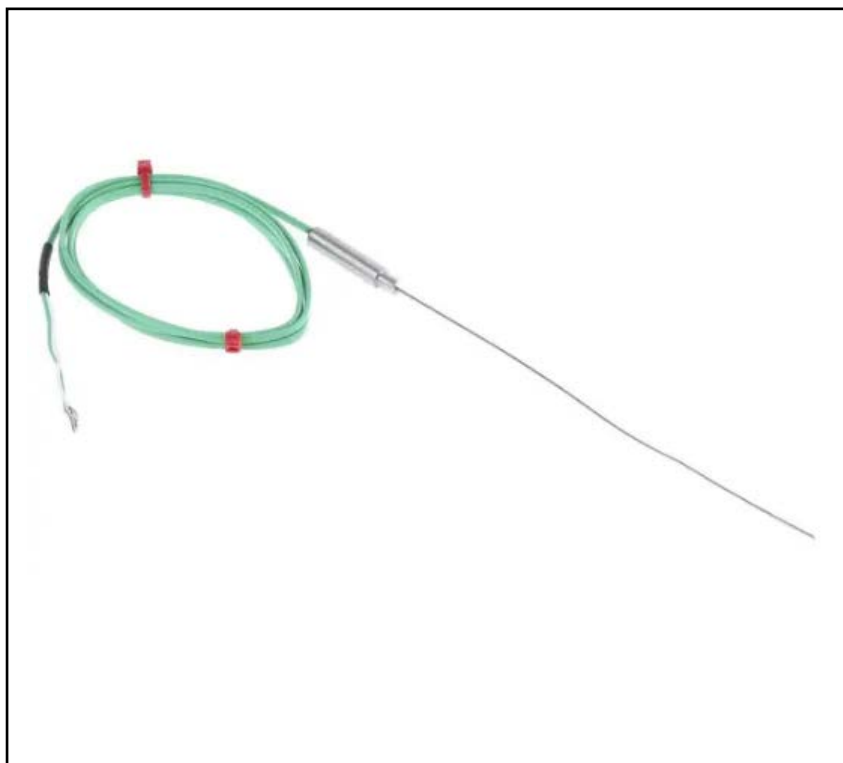


FEATURES

- Mineral insulation for flexibility
- Durability and high performance
- Insulated hot junction for reduction in electrical interference
- Plain pot seal with a temperature rating of 200°C.

RS PRO Type K Thermocouple 150mm Length, 1mm Diameter → +1100°C

RS Stock No.: 787-7696



RS Professionally Approved Products bring to you professional quality parts across all product categories. Our product range has been tested by engineers and provides a comparable quality to the leading brands without paying a premium price.

Product Description

These sensors or probes have a durable construction and feature a stainless steel 310 probe sheath and a PFA insulated lead. The mineral insulated flexible probe sheath can be bent and formed to suit a wide range of applications. The thermocouple has a single element insulated hot junction for a reduction in electrical interference and a plain pot seal with a temperature rating of 200°C.

General Specifications

Thermocouple Type	Type K
Construction	Flexible mineral insulated probe with stainless steel sheath, plain pot seal & 1 metre extension cable
Measuring Junction	Underground
Application	high pressure and vacuum applications, and able to withstand high levels of vibration

Mechanical Specifications

Probe Diameter	1mm
Probe Length	150mm
Probe Body Material	Stainless Steel
Insulation / Sheath Material	310 Stainless steel
Termination Type	Cable

Approvals

Standards Met	IEC
----------------------	-----





Features

- **ATMega328P Processor**
 - **Memory**
 - AVR CPU at up to 16 MHz
 - 32KB Flash
 - 2KB SRAM
 - 1KB EEPROM
 - **Security**
 - Power On Reset (POR)
 - Brown Out Detection (BOD)
 - **Peripherals**
 - 2x 8-bit Timer/Counter with a dedicated period register and compare channels
 - 1x 16-bit Timer/Counter with a dedicated period register, input capture and compare channels
 - 1x USART with fractional baud rate generator and start-of-frame detection
 - 1x controller/peripheral Serial Peripheral Interface (SPI)
 - 1x Dual mode controller/peripheral I2C
 - 1x Analog Comparator (AC) with a scalable reference input
 - Watchdog Timer with separate on-chip oscillator
 - Six PWM channels
 - Interrupt and wake-up on pin change
- **ATMega16U2 Processor**
 - 8-bit AVR® RISC-based microcontroller
- **Memory**
 - 16 KB ISP Flash
 - 512B EEPROM
 - 512B SRAM
 - debugWIRE interface for on-chip debugging and programming
- **Power**
 - 2.7-5.5 volts

INA219 Zero-Drift, Bidirectional Current/Power Monitor With I²C Interface

1 Features

- Senses Bus Voltages from 0 to 26 V
- Reports Current, Voltage, and Power
- 16 Programmable Addresses
- High Accuracy: 0.5% (Maximum) Over Temperature (INA219B)
- Filtering Options
- Calibration Registers
- SOT23-8 and SOIC-8 Packages

2 Applications

- Servers
- Telecom Equipment
- Notebook Computers
- Power Management
- Battery Chargers
- Welding Equipment
- Power Supplies
- Test Equipment

3 Description

The INA219 is a current shunt and power monitor with an I²C- or SMBUS-compatible interface. The device monitors both shunt voltage drop and bus supply voltage, with programmable conversion times and filtering. A programmable calibration value, combined with an internal multiplier, enables direct readouts of current in amperes. An additional multiplying register calculates power in watts. The I²C- or SMBUS-compatible interface features 16 programmable addresses.

The INA219 is available in two grades: A and B. The B grade version has higher accuracy and higher precision specifications.

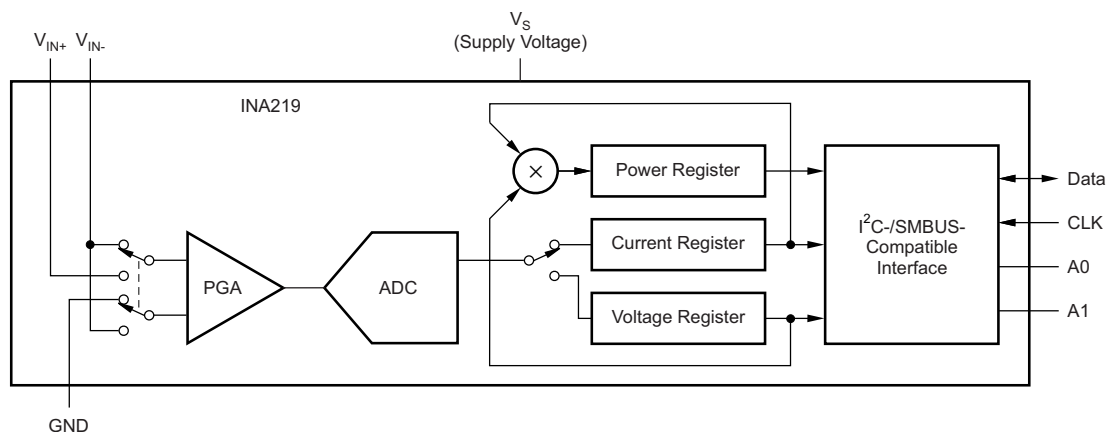
The INA219 senses across shunts on buses that can vary from 0 to 26 V. The device uses a single 3- to 5.5-V supply, drawing a maximum of 1 mA of supply current. The INA219 operates from –40°C to 125°C.

Device Information⁽¹⁾

PART NUMBER	PACKAGE	BODY SIZE (NOM)
INA219	SOIC (8)	3.91 mm x 4.90 mm
	SOT-23 (8)	1.63 mm x 2.90 mm

(1) For all available packages, see the orderable addendum at the end of the data sheet.

Simplified Schematic



An IMPORTANT NOTICE at the end of this data sheet addresses availability, warranty, changes, use in safety-critical applications, intellectual property matters and other important disclaimers. PRODUCTION DATA.

INA219

SBOS448G –AUGUST 2008–REVISED DECEMBER 2015

www.ti.com

7 Specifications

7.1 Absolute Maximum Ratings

over operating free-air temperature range (unless otherwise noted)⁽¹⁾

		MIN	MAX	UNIT
V _S	Supply voltage		6	V
Analog Inputs IN+, IN–	Differential (V _{IN+} – V _{IN–}) ⁽²⁾	–26	26	V
	Common-mode (V _{IN+} + V _{IN–}) / 2	–0.3	26	V
SDA		GND – 0.3	6	V
SCL		GND – 0.3	V _S + 0.3	V
Input current into any pin			5	mA
Open-drain digital output current			10	mA
Operating temperature		–40	125	°C
T _J	Junction temperature		150	°C
T _{stg}	Storage temperature	–65	150	°C

- (1) Stresses beyond those listed under *Absolute Maximum Ratings* may cause permanent damage to the device. These are stress ratings only, which do not imply functional operation of the device at these or any other conditions beyond those indicated under *Recommended Operating Conditions*. Exposure to absolute-maximum-rated conditions for extended periods may affect device reliability.
- (2) V_{IN+} and V_{IN–} may have a differential voltage of –26 to 26 V; however, the voltage at these pins must not exceed the range –0.3 to 26 V.

7.2 ESD Ratings

		VALUE	UNIT
V _(ESD)	Electrostatic discharge		
	Human body model (HBM), per ANSI/ESDA/JEDEC JS-001, all pins ⁽¹⁾	±4000	V
	Charged device model (CDM), per JEDEC specification JESD22-C101, all pins ⁽²⁾	±750	
	Machine Model (MM)	±200	

- (1) JEDEC document JEP155 states that 500-V HBM allows safe manufacturing with a standard ESD control process.
- (2) JEDEC document JEP157 states that 250-V CDM allows safe manufacturing with a standard ESD control process.

7.3 Recommended Operating Conditions

over operating free-air temperature range (unless otherwise noted)

	MIN	NOM	MAX	UNIT
V _{CM}		12		V
V _S		3.3		V
T _A	–25		85	°C

7.4 Thermal Information

THERMAL METRIC ⁽¹⁾		INA219		UNIT
		D (SOIC)	DCN (SOT)	
		8 PINS	8 PINS	
R _{θJA}	Junction-to-ambient thermal resistance	111.3	135.4	°C/W
R _{θJC(top)}	Junction-to-case (top) thermal resistance	55.9	68.1	°C/W
R _{θJB}	Junction-to-board thermal resistance	52	48.9	°C/W
ψ _{JT}	Junction-to-top characterization parameter	10.7	9.9	°C/W
ψ _{JB}	Junction-to-board characterization parameter	51.5	48.4	°C/W
R _{θJC(bot)}	Junction-to-case (bottom) thermal resistance	N/A	N/A	°C/W

- (1) For more information about traditional and new thermal metrics, see the *Semiconductor and IC Package Thermal Metrics* application report, [SPRA953](#).

7.5 Electrical Characteristics:

At $T_A = 25^\circ\text{C}$, $V_S = 3.3\text{ V}$, $V_{IN+} = 12\text{ V}$, $V_{SHUNT} = (V_{IN+} - V_{IN-}) = 32\text{ mV}$, $\text{PGA} = /1$, and $\text{BRNG}^{(1)} = 1$, unless otherwise noted.

PARAMETER		TEST CONDITIONS	INA219A			INA219B			UNIT
			MIN	TYP	MAX	MIN	TYP	MAX	
INPUT									
V _{SHUNT}	Full-scale current sense (input) voltage range	PGA = /1	0		±40	0		±40	mV
		PGA = /2	0		±80	0		±80	mV
		PGA = /4	0		±160	0		±160	mV
		PGA = /8	0		±320	0		±320	mV
Bus voltage (input voltage) range ⁽²⁾		BRNG = 1	0		32	0		32	V
		BRNG = 0	0		16	0		16	V
CMRR	Common-mode rejection	V _{IN+} = 0 to 26 V	100	120		100	120		dB
V _{OS}	Offset voltage, RTI ⁽³⁾ vs Temperature	PGA = /1		±10	±100		±10	±50 ⁽⁴⁾	μV
		PGA = /2		±20	±125		±20	±75 ⁽⁴⁾	μV
		PGA = /4		±30	±150		±30	±75 ⁽⁴⁾	μV
		PGA = /8		±40	±200		±40	±100 ⁽⁴⁾	μV
		T _A = −25°C to 85°C		0.1			0.1		μV/°C
PSRR	vs Power Supply	V _S = 3 to 5.5 V		10			10		μV/V
Current sense gain error vs Temperature				±40			±40		m%
		T _A = −25°C to 85°C		1			1		m%/°C
IN+ pin input bias current		Active mode		20			20		μA
IN− pin input bias current V _{IN−} pin input impedance		Active mode		20 320			20 320		μA kΩ
IN+ pin input leakage ⁽⁵⁾		Power-down mode		0.1	±0.5		0.1	±0.5	μA
IN− pin input leakage ⁽⁵⁾		Power-down mode		0.1	±0.5		0.1	±0.5	μA
DC ACCURACY									
ADC basic resolution				12			12		bits
Shunt voltage, 1 LSB step size				10			10		μV
Bus voltage, 1 LSB step size				4			4		mV
Current measurement error over Temperature				±0.2%	±0.5%		±0.2%	±0.3% ⁽⁴⁾	
		T _A = −25°C to 85°C			±1%			±0.5% ⁽⁴⁾	
Bus voltage measurement error over Temperature				±0.2%	±0.5%		±0.2%	±0.5%	
		T _A = −25°C to 85°C			±1%			±1%	
Differential nonlinearity				±0.1			±0.1		LSB
ADC TIMING									
ADC conversion time		12 bit		532	586		532	586	μs
		11 bit		276	304		276	304	μs
		10 bit		148	163		148	163	μs
		9 bit		84	93		84	93	μs
Minimum convert input low time			4			4		μs	
SMBus									
SMBus timeout ⁽⁶⁾				28	35		28	35	ms
DIGITAL INPUTS (SDA as Input, SCL, A0, A1)									
Input capacitance				3			3		pF
Leakage input current		0 ≤ V _{IN} ≤ V _S		0.1	1		0.1	1	μA
V _{IH} input logic level			0.7 (V _S)		6	0.7 (V _S)		6	V
V _{IL} input logic level			−0.3	0.3 (V _S)		−0.3	0.3 (V _S)		V

(1) BRNG is bit 13 of the Configuration register 00h in Figure 19.

(2) This parameter only expresses the full-scale range of the ADC scaling. In no event should more than 26 V be applied to this device.

(3) Referred-to-input (RTI)

(4) Indicates improved specifications of the INA219B.

(5) Input leakage is positive (current flowing into the pin) for the conditions shown at the top of the table. Negative leakage currents can occur under different input conditions.

(6) SMBus timeout in the INA219 resets the interface any time SCL or SDA is low for over 28 ms.

INA219

SBOS448G –AUGUST 2008–REVISED DECEMBER 2015

www.ti.com
Electrical Characteristics: (continued)

At $T_A = 25^\circ\text{C}$, $V_S = 3.3\text{ V}$, $V_{IN+} = 12\text{ V}$, $V_{SHUNT} = (V_{IN+} - V_{IN-}) = 32\text{ mV}$, $\text{PGA} = /1$, and $\text{BRNG}^{(1)} = 1$, unless otherwise noted.

PARAMETER	TEST CONDITIONS	INA219A			INA219B			UNIT
		MIN	TYP	MAX	MIN	TYP	MAX	
Hysteresis			500			500		mV
OPEN-DRAIN DIGITAL OUTPUTS (SDA)								
Logic 0 output level	$I_{\text{SINK}} = 3\text{ mA}$		0.15	0.4		0.15	0.4	V
High-level output leakage current	$V_{\text{OUT}} = V_S$		0.1	1		0.1	1	μA
POWER SUPPLY								
Operating supply range		3		5.5	3		5.5	V
Quiescent current			0.7	1		0.7	1	mA
Quiescent current, power-down mode			6	15		6	15	μA
Power-on reset threshold			2			2		V

7.6 Bus Timing Diagram Definitions⁽¹⁾

		FAST MODE		HIGH-SPEED MODE		UNIT
		MIN	MAX	MIN	MAX	
$f_{\text{(SCL)}}$	SCL operating frequency	0.001	0.4	0.001	2.56	MHz
$t_{\text{(BUF)}}$	Bus free time between STOP and START condition	1300		160		ns
$t_{\text{(HDSTA)}}$	Hold time after repeated START condition. After this period, the first clock is generated.	600		160		ns
$t_{\text{(SUSTA)}}$	Repeated START condition setup time	600		160		ns
$t_{\text{(SUSTO)}}$	STOP condition setup time	600		160		ns
$t_{\text{(HDDAT)}}$	Data hold time	0	900	0	90	ns
$t_{\text{(SUDAT)}}$	Data setup time	100		10		ns
$t_{\text{(LOW)}}$	SCL clock LOW period	1300		250		ns
$t_{\text{(HIGH)}}$	SCL clock HIGH period	600		60		ns
$t_{\text{F DA}}$	Data fall time		300		150	ns
$t_{\text{F CL}}$	Clock fall time		300		40	ns
$t_{\text{R CL}}$	Clock rise time		300		40	ns
$t_{\text{R CL}}$	Clock rise time for $\text{SCLK} \leq 100\text{ kHz}$		1000			ns

(1) Values based on a statistical analysis of a one-time sample of devices. Minimum and maximum values are not ensured and not production tested.

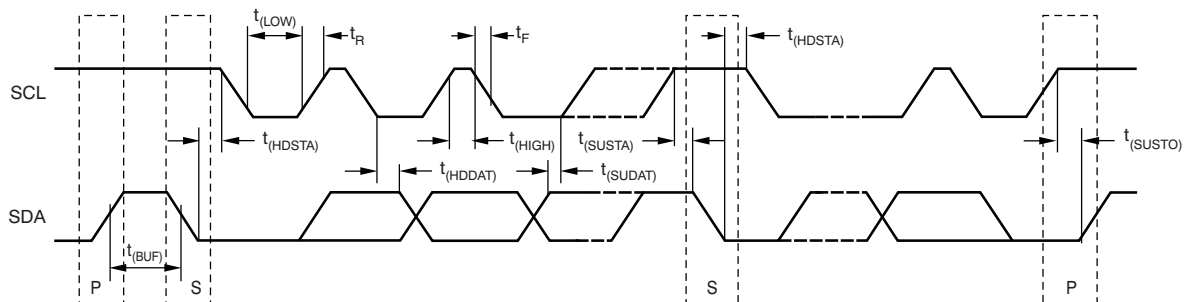


Figure 1. Bus Timing Diagram



Safety Data Sheet

According to EU Directive 1907/2006, as amended

Product name: Real filament ABS

Date of issue: 23-7-2018

1. Identification of the substance/preparation and of the company

- 1.1 Trade name:** Real filament ABS
- 1.2 Use of the product:** 3Dprinter Filament
- 1.3 Supplier:**
ReprapWorld B.V.
Wagenmaker 6a
2631 RL Nootdorp, The Netherlands
Phone: +31 (0)85 0091531

2. Hazards identification

- 2.1 Classification of the substance or mixture**
According to Regulation (EC) No 1272/2008 [CLP]
This mixture is classified as not hazardous
- 2.2 Label elements**
Labelling (CLP)
Hazard statements: not applicable
Safety precautions: not applicable
Labelling (67/548/EEC or 1999/45/EC)
R phrase(s): not applicable
S phrase(s): not applicable
- 2.3 Other hazards**
Dust: Can cause skin, eye and respiratory tract irritation.
Fine dust: explosive
The melted product can cause severe burns.
Swallowing may cause gastrointestinal irritation and pain of guts.

3. Composition/information on ingredients

- 3.1 Mixtures:**
Chemical characterization: Polymer mixture, enhanced for 3D printing
CAS No. 9003-56-9: > 98 % Styrene-acrylonitrile-butadiene copolymer
CAS No. 100-42-5: < 0,1 % Styrene

4. First aid measures

- 4.1 Description of first aid measures**
- General information: Immediately remove any contaminated clothing, shoes or stockings.
- After inhalation: Provide fresh air. Put victim at rest and keep warm.
Seek medical attention
- In case of skin contact: The melted product can cause severe burns. Do not attempt to remove molten product, or molten product that has cooled, from skin without medical assistance. After contact with molten product, cool skin area rapidly with cold water. Consult physician.
- After eye contact:
IF IN EYES: Rinse cautiously with water for several minutes. Remove contact lenses, if present and easy to do. Continue rinsing. Consult an eye specialist in the event of irritation.

MAGNUM™ 3453

ABS Resin

Overview

'MAGNUM™ 3453 ABS is a general purpose injection moulding resin suitable for a wide range of applications. The product combines a medium to high impact performance with good flowability. The mass (continuous process) ABS technology ensures an ABS resin that combines excellent processability with a stable light base colour that is ideal for self-colouring.

Applications:

- Household appliances
- Telephones
- Electrical and computer equipment
- Consumer goods
- Toys

Physical	Nominal Value (English)	Nominal Value (SI)	Test Method
Density	1.05 g/cm ³	1.05 g/cm ³	ISO 1183
Apparent (Bulk) Density	0.65 g/cm ³	0.65 g/cm ³	ISO 60
Melt Mass-Flow Rate (MFR) (220°C/10.0 kg)	15 g/10 min	15 g/10 min	ISO 1133
Molding Shrinkage	4.0E-3 to 7.0E-3 in/in	0.40 to 0.70 %	ISO 294-4
Mechanical	Nominal Value (English)	Nominal Value (SI)	Test Method
Tensile Modulus	331000 psi	2280 MPa	ISO 527-2
Tensile Stress (Yield)	6530 psi	45.0 MPa	ISO 527-2/50
Tensile Strain (Yield)	2.5 %	2.5 %	ISO 527-2/50
Flexural Modulus ¹	334000 psi	2300 MPa	ISO 178
Flexural Stress ¹	9860 psi	68.0 MPa	ISO 178
Impact	Nominal Value (English)	Nominal Value (SI)	Test Method
Charpy Notched Impact Strength 73°F (23°C), Injection Molded	8.6 ft-lb/in ²	18 kJ/m ²	ISO 179/1eA
Thermal	Nominal Value (English)	Nominal Value (SI)	Test Method
Heat Deflection Temperature 264 psi (1.8 MPa), Annealed	212 °F	100 °C	ISO 75-2/A
Vicat Softening Temperature	207 °F	97.0 °C	ISO 306/B50
Flammability	Nominal Value (English)	Nominal Value (SI)	Test Method
Flame Rating ²			UL 94
0.04 in (1.0 mm)	HB	HB	
0.12 in (3.0 mm)	HB	HB	
Carbon Emission ²	25.0 µg/g	25.0 µg/g	VDA 277
Additional Information	Nominal Value (English)	Nominal Value (SI)	Test Method
Fogging ²	97 %	97 %	ISO 294-4
Injection	Nominal Value (English)	Nominal Value (SI)	
Drying Temperature	176 to 194 °F	80 to 90 °C	
Drying Time	2.0 to 4.0 hr	2.0 to 4.0 hr	

Notes

These are typical properties only and are not to be construed as specifications. Users should confirm results by their own tests.

¹ 0.079 in/min (2.0 mm/min)

² This rating not intended to reflect hazards presented by this or any other material under actual fire conditions.

B

Engineering drawings and production

This appendix is a collection of the engineering drawings of the components of the experimental engine setup. The drawings of the more intricate parts have a section that elaborates upon the machining method used. There have been many lessons learnt working with soft materials like copper and PEEK that require high tolerances or with the brittle graphite piece that features no parallel concentric surfaces. The exact steps that need to be followed for each part are given on their respective drawing. This guide serves as context for these operations and as a reference for future endeavours that also require high precision machined components.

B.1. Manifold

The manifold is made from aluminium as a lightweight easy to machine material. Its thickness is constrained by its features, not the strength to withstand the internal pressure of the motor. On the exterior it has two grooves for O-rings to seal the high pressure manifold from both the engine and the exterior. The edges here are relatively thin however and prohibit the use of a regular three chuck clamp on the external machined surface. Therefore soft jaws are used that have been machined to exactly fit a 40mm shaft. They will continue to be used on the setup of the mill, which required some creative clamping of the lathe chuck. With a larger budget and more time, custom tooling can also be developed for the mill to circumvent this approach. A white plastic ring with high tolerance parallel surfaces was used to provide a reference surface for the back of the manifold during re-clamping procedures. This ring and the soft jaw setup can be seen in Figure B.1. Please note that the same clamping setup is used on the lathe to face off this side of the stock material after the external features have been made.



Figure B.1: Close up of the clamping of the manifold and alignment of the diagonal injection hole.

First off all, the axisymmetric features are made on the lathe. Then the chuck is moved to the mill and fixed to the machining bed. After the vertical features are made the mill head can be rotated to machine the optional diagonal injection holes. This setup is shown in Figure B.2 as well as the clamping method of the chuck. The center drilling operation is done when the machine is suspended vertically after which alignment is done by eye against the back surface left by the center drill. Be sure to observe no flex in the drill when it starts touching the material or it will snap!

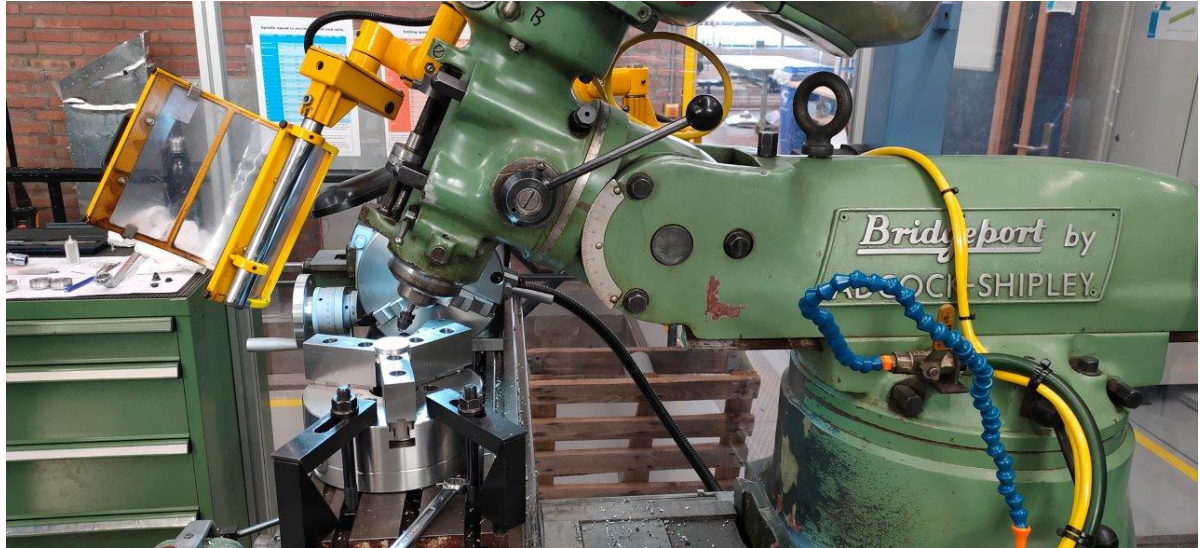


Figure B.2: The Bridgeport mill set at a 25 degrees angle to drill two injector holes. Also note the clamping setup of the chuck.

When the features on the front of the manifold have been finished the last operation is the 4mm hole for lateral ignition nozzles and pressure sensor. The chuck now needs to be suspended vertically which can be done on two aluminium slot profiles that are constrained in the T-slots of the machining bed, shown in Figure B.3. The chuck is clamped on the internal surface on the back. Use a soft material like a few 1mm aluminium strips to protect the surface of the chuck from damages by the clamping operation. Vertical alignment of the work piece is done with a digital or analog level. This level should be placed on two high tolerance shafts inside the press fit holes. These two shafts form the horizontal feature.

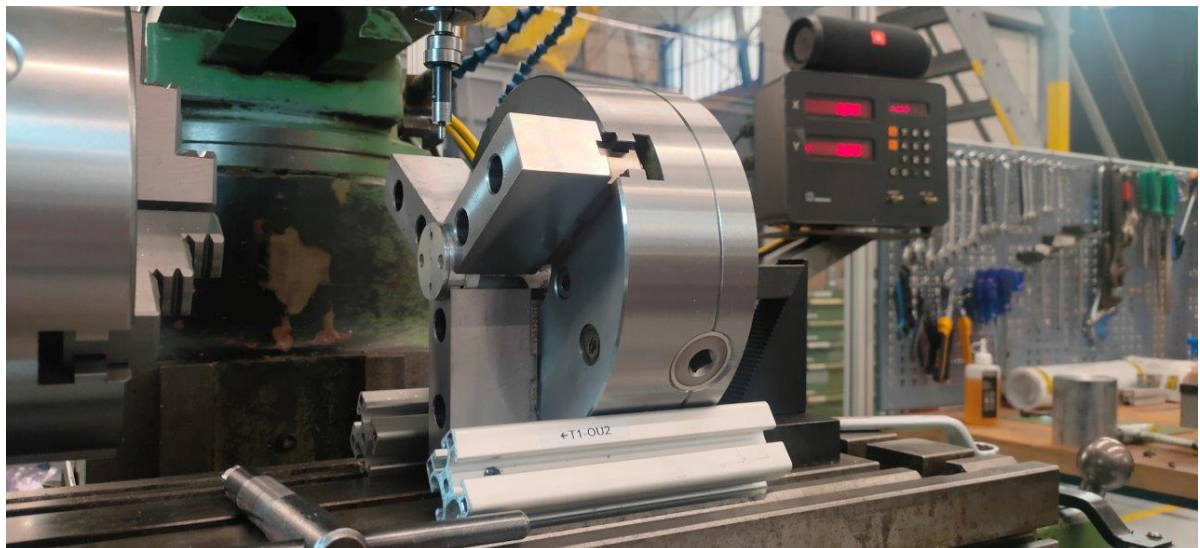


Figure B.3: Vertical clamping setup of chuck on the mill bed.

B.2. HV Pressfit

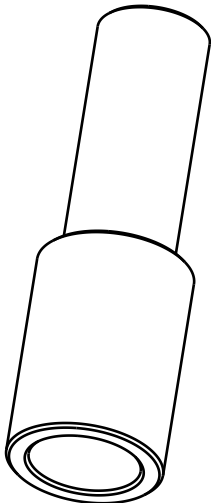
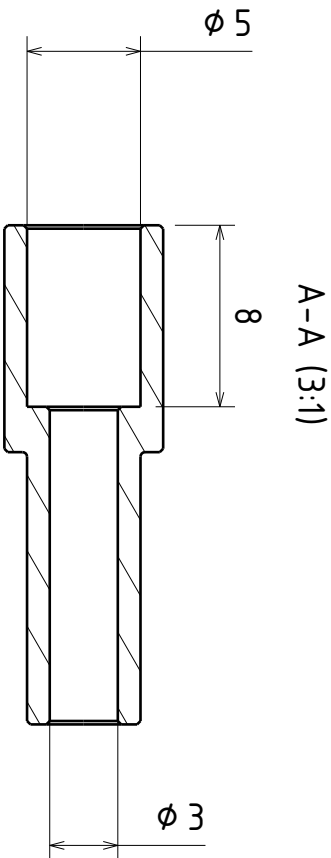
The HV press fit and HV connector are fairly similar in their machining approach. Both are soft materials that heat up quickly and are easy to deform. Their machining steps also follow the same pattern. PEEK is easier to machine however so most information will be given in the next section. The HV press fit fits in between the manifold and HV connector and offers electrical insulation for the high voltage ignition system. PEEK was chosen as it is one of the most heat resistant, accessible, plastics around with a melting point of almost 350 °C. PEEK heats up significantly when machined, especially internal operations such as drilling or milling a bore. The external surface therefore should be clamped in a collet to prevent warping of the material. Also, be careful when taking the part out of the machine, it can burn your fingers!

B.3. HV Connector

The HV connector fits tightly in the HV press fit and is the component that feeds the high voltage leads into the combustion chamber. Copper is used as it is an excellent conductor and easy to solder. It is important that no bare copper sticks out of the top of the press fit in the manifold as it may cause sparks to jump to the manifold (ground) over the surface of the PEEK. The downside of copper is that it easily warms up during machining and becomes very ductile. Also, the manual machines used go up to a rotation speed of 3000 rpm which is far lower than the required speed for these small features in a soft material. Throughout the machining process it should therefore be suspended from a rotating center to prevent bending due to machining forces. A collet should be used instead of a three chuck as well as it provides even clamping on a small, relatively soft, surface. Especially for the second side it is imperative that it is clamped in a collet over it's full length as otherwise the drilling operation will deform the outer surface and distort the high tolerance external diameter. Another complication is in the drilling of small holes. The stock material should be sufficiently cooled otherwise it will gradually warm up over the day when multiple parts are made in a row. This will make the difference between the drill breaking or not. Finally, on the manual machines available it is difficult to chamfer the soft copper as it tends to push the edge away instead of removing it. The solution is to reduce the speed and use fine grid sandpaper to smoothen the edges as shown in Figure B.4. Make sure there is nothing on or around the machine that you can get caught in and be ready to turn off the machine at any time!



Figure B.4: Sanding of the edges on a HV connector as it is clamped in a collet and suspended in a rotating center



$\phi 7 \begin{matrix} +0.110 \\ +0.095 \end{matrix}$

22

12

$\phi 5 \begin{matrix} +0.070 \\ +0.055 \end{matrix}$

(3:1)

R 0.2 (Tool radius)

$0.15 \pm 45^\circ$
TYP

TOOLS NEEDED

1. Lathing tool
2. Small parting tool
3. Fine grid sandpaper
4. 5 mm end mill
5. Center drill
6. 3mm drill bit

PRODUCTION STEPS

1. Leave ~30mm of stock sticking out of the chuck and face the end
2. Insert sharp centerpoint in soft plastic
3. Lathe outer diameter to 7mm
4. Lathe section of outer diameter to 5mm
5. Smoothen surface and edges with sandpaper
6. Use small parting tool to part off the piece
7. Reclamp on 5mm collet and face to 22mm length
8. Use the end mill to make 5mm bore
9. (Center)drill 3mm hole all through

Delft Aerospace Rocket Engineering (DARE) - Chimera

TOLERANCES (unless indicated otherwise)

DRAWN BY:
Rolf Wubben

CHECKED BY:

DATE:
25-05-2022

APPROVED BY CHIEF ENG.:

PART NAME:
HVInjector_Pressfit_Drawing_V2

Dimensions
 ± 0.1 [mm]

Angles
 ± 0.5 [deg]

Surface Roughness
1.6 [μ m]

AMOUNT:
1

MATERIAL:
Plastic: PEEK

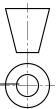
MASS [g]:
0.476

M: add mobile phone of person who drew part

T:

This drawing is DARE property; it cannot be reproduced or communicated without our written agreement.

SIZE:
A4

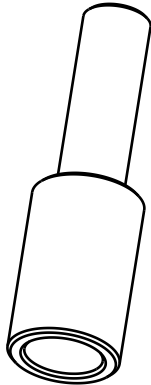
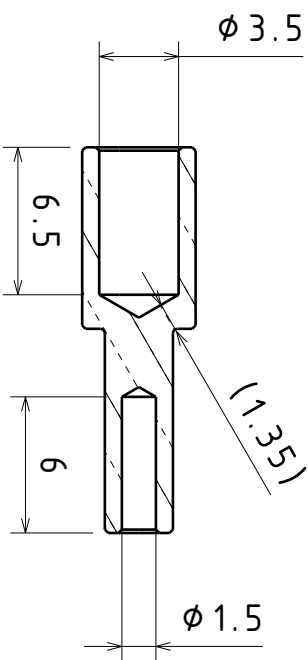


SCALE:
3:1

REVISION:
A.1

SHEET
1 / 1

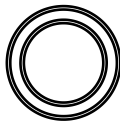
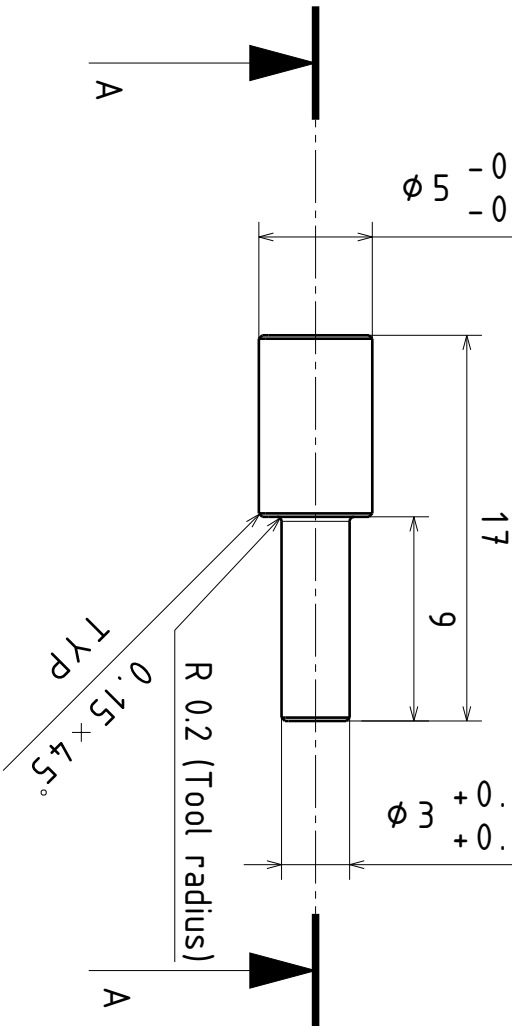
Follow the exact production steps or the soft material will warp during machining. The pressfit is designed to be H7/p6 (medium tight, assembly at the press). Tolerance given is based on the dimensons created by the tools in the manifold.



$\phi 5 \begin{matrix} -0.260 \\ -0.275 \end{matrix}$

$\phi 3 \begin{matrix} +0.050 \\ +0.035 \end{matrix}$

(3:1)



TOOLS NEEDED

1. Lathing tool
2. Small center drill
3. 15mm drill bit
4. Fine grid sandpaper
5. Parting tool
6. 35mm drill bit

PRODUCTION STEPS

1. Leave 25mm of stock sticking out of the chuck and face the end
2. Carefully (center)drill 15mm hole 6mm deep and insert centerpoint
3. Lathe outer diameter to 5mm
4. Lathe section of outer diameter to 3mm
5. Smoothen surface and edges with sandpaper
6. Use parting tool to part off the piece
7. Recamp on 5mm collet and face to 17mm length
8. (Center)drill 35mm hole 6mm deep

Follow the exact production steps or

the soft material will warp during

machining. The pressfit is designed

to be H7/p6 (medium tight, assembly

at the press). Tolerance given is

based on the dimensons created by

the tools in the pressfit.

DRAWN BY:
Rolf Wubben

CHECKED BY:

DATE:

25-05-2022

APPROVED BY CHIEF ENG.:

M: add mobile phone of perpson who drew part

T:

SIZE:

A4

Delft Aerospace Rocket Engineering (DARE) - Chimera

PART NAME:

HVInjector_Connector_Drawing_V2

DATE:

25-05-2022

APPROVED BY CHIEF ENG.:

M: add mobile phone of perpson who drew part

T:

TOLERANCES (unless indicated otherwise)

Dimensions

± 0.1 [mm]

Angles

± 0.5 [deg]

Surface Roughness

16 [μ m]

AMOUNT:

1

MATERIAL:

Copper

MASS [g]:

130

This drawing is DARE property. It cannot be reproduced or communicated without our written agreement.

REVISION:

A.1

SHEET

1 / 1

B.4. Nozzle Insert

The nozzle insert is a challenging piece due to the material, graphite, and the design which features no parallel surfaces. Graphite comes off the work piece as a fine conductive dust cloud. It should therefore be contained and kept away from electronics. This is achieved by holding a vacuum cleaner with appropriately small filter close by the work piece as it is machined. The heavier particles will still fall down and are to be caught by cloths soaked in machining coolant to capture them. The proposed setup is shown in Figure B.5.



Figure B.5: Graphite dust collection setup on a lathe

First the external diameter is machined down and then the throat and convergent section are made. After the piece is parted it should not be clamped in a three chuck but a collet to ensure proper alignment and distribute the clamping force over the thinner piece. After it is faced to the correct length the divergent is machined with a conical mill. In order to ensure an identical expansion ratio between each nozzle, a hard stop that fits exactly around the mill is made out of white plastic. It has been made to create an exit diameter of 7.6mm, but it is a feature that is very difficult to measure exactly. However, even if there is a small unquantifiable deviation it will be consistent between nozzles meaning no difference should be observed between tests.



Figure B.6: Machining of nozzle divergent using a conical mill and custom hard stop.

Finally the piece is aligned for machining of the exterior surface. This is done by suspending it between two conical features. One is the Nozzle Tooling Flange that is clamped in a collet and interfaces with the nozzle convergent section. The exit diameter is fit in a piece of PVC with a small step exactly equal to the exit diameter to create a tight fit. This PVC interfaces with a piece of steel that has a hole for a rotating center to be inserted. This chain of high tolerance components, shown in Figure B.7, results in shaft runout of less than 10 micron.

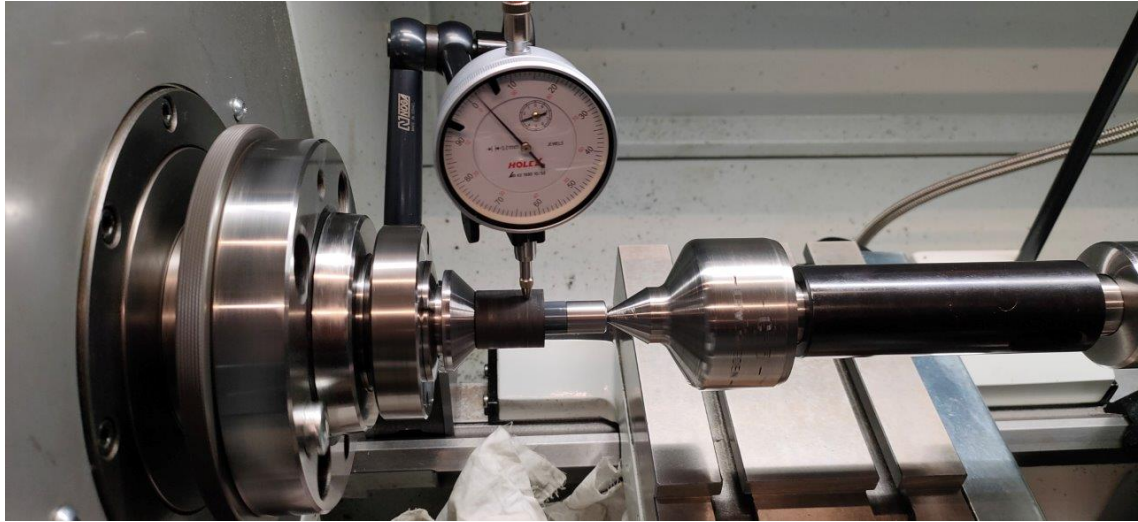


Figure B.7: Clock dial showing less than 10 micron misalignment over a full rotation.

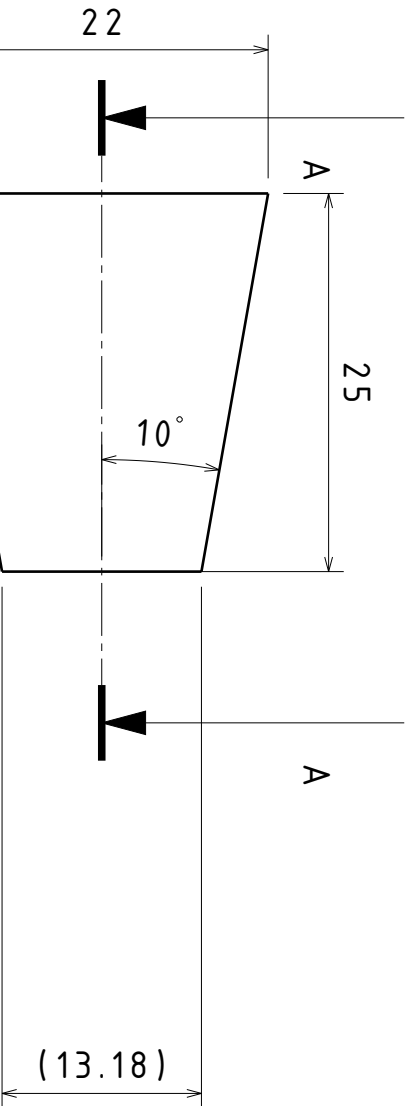
Machining of the external conical surface, shown in Figure B.8, needs to be done at the exact same tool angle as the retainer it fits in. A misalignment of less than 0.01° will result in nozzle disintegration during testing. The tolerance on the drawing however does not need to be accurate: both parts simply need to be made within the specified $\pm 0.1^\circ$.



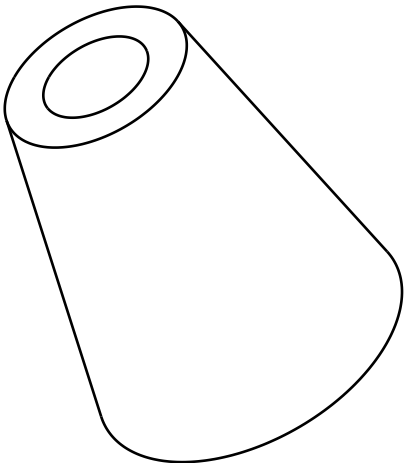
Figure B.8: Machining of external conical surface.

B.5. Nozzle Retainer

Alignment of the nozzle interfacing surface should again be ensured by using the 40mm soft jaws instead of a three chuck. As indicated in the previous section, that interfacing surface needs to be made at the exact same tool angle as the nozzle external conical surface. This means the smaller diameter of the cone will be facing the machinist and thus a sufficiently large hole needs to be drilled to allow for enough space for the tool to fit in and have some visibility of the operation.

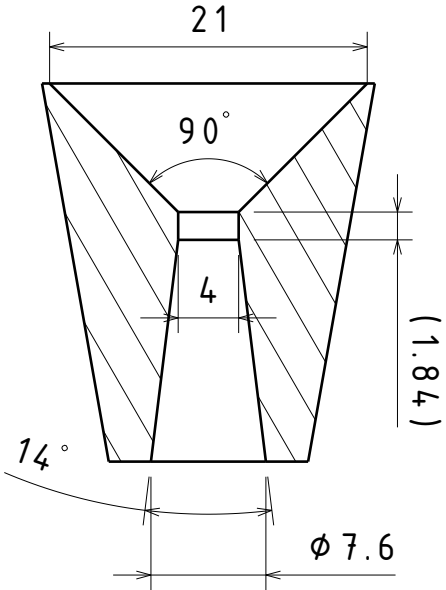


Conical surface needs to be manufactured at the exact same tool angle as the mating retainer. On a manual machine <0.01° accuracy is not enough. The surfaces need to be machined at the same time.



TOOLS NEEDED	
1:	Lathing chisel
2:	Center drill
3:	3.8mm drill
4:	90° countersink
5:	4.0mm reamer
6:	Parting tool
7:	14° conical mill

PRODUCTION STEPS	
1:	Leave ~30mm of stock sticking out of the chuck and face the end
2:	Centerdrill 3.8 m hole 30mm deep
3:	Machine converging (90°) section
4:	Ream throat
5:	Part/saw workpiece
5:	Clamp in 22mm collet
6:	Face and machine diverging (14°) section with conical mill and standoff
7:	Clamp custom tooling in collet and constrain workpiece with centerpoint and nozzle insert
8:	Lathe external cone



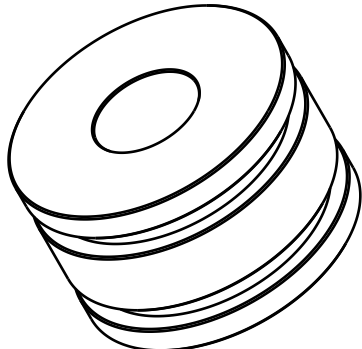
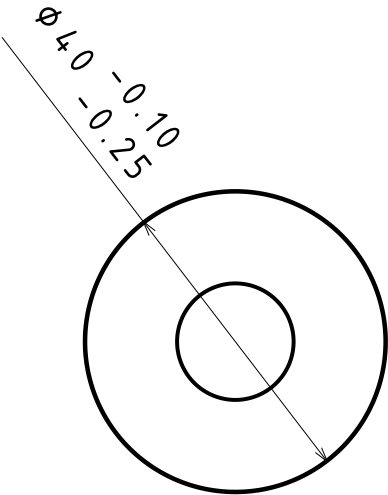
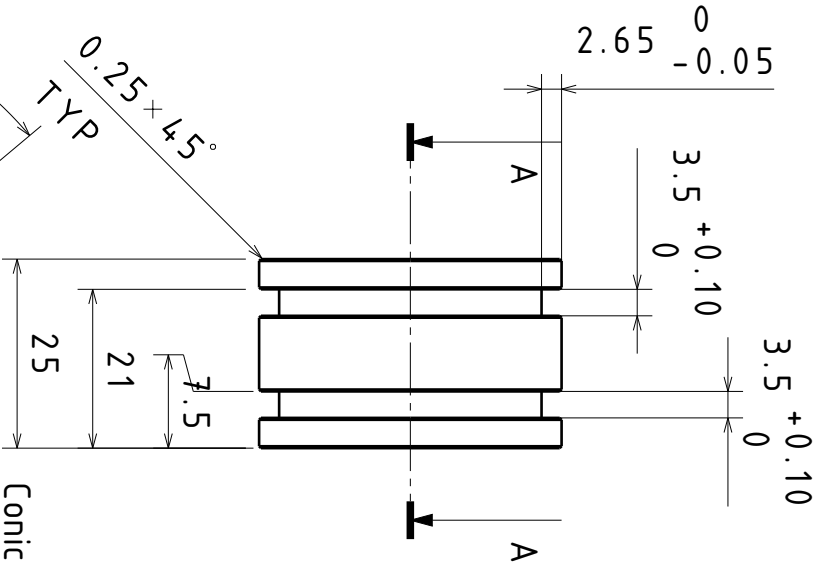
DRAWN BY: Rolf Wubben		Delft Aerospace Rocket Engineering (DARE) - Stratos IV		TOLERANCES (unless indicated otherwise)	
CHECKED BY: XXXXXXXXXX		PART NAME: Stratos4_Tank_RollControl_TestThrus ter_NozzleInsert_Drawing V1.1		Dimensions	
DATE: 29-03-2022		M:		Angles	
APPROVED BY CHIEF ENG.: XXXXXXXXXXXX		T:		Surface Roughness	
SIZE: A4		SCALE: 2:1		AMOUNT:	
				MATERIAL:	
				MASS [KG]:	
				REVISION:	
				SHEET	
				1 / 1	

D

C

B

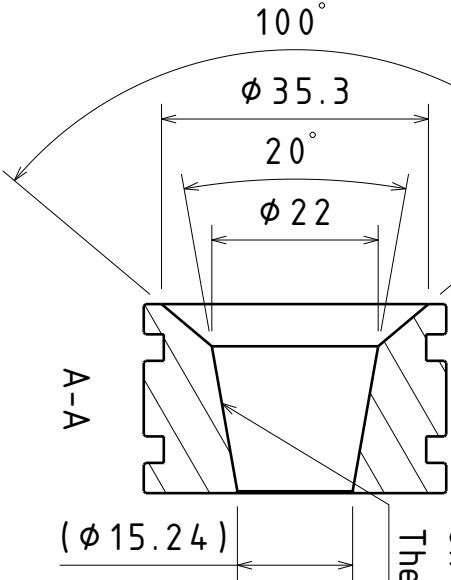
A



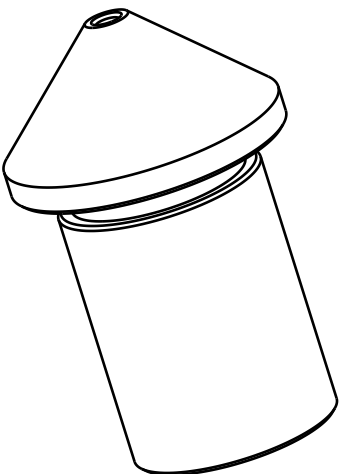
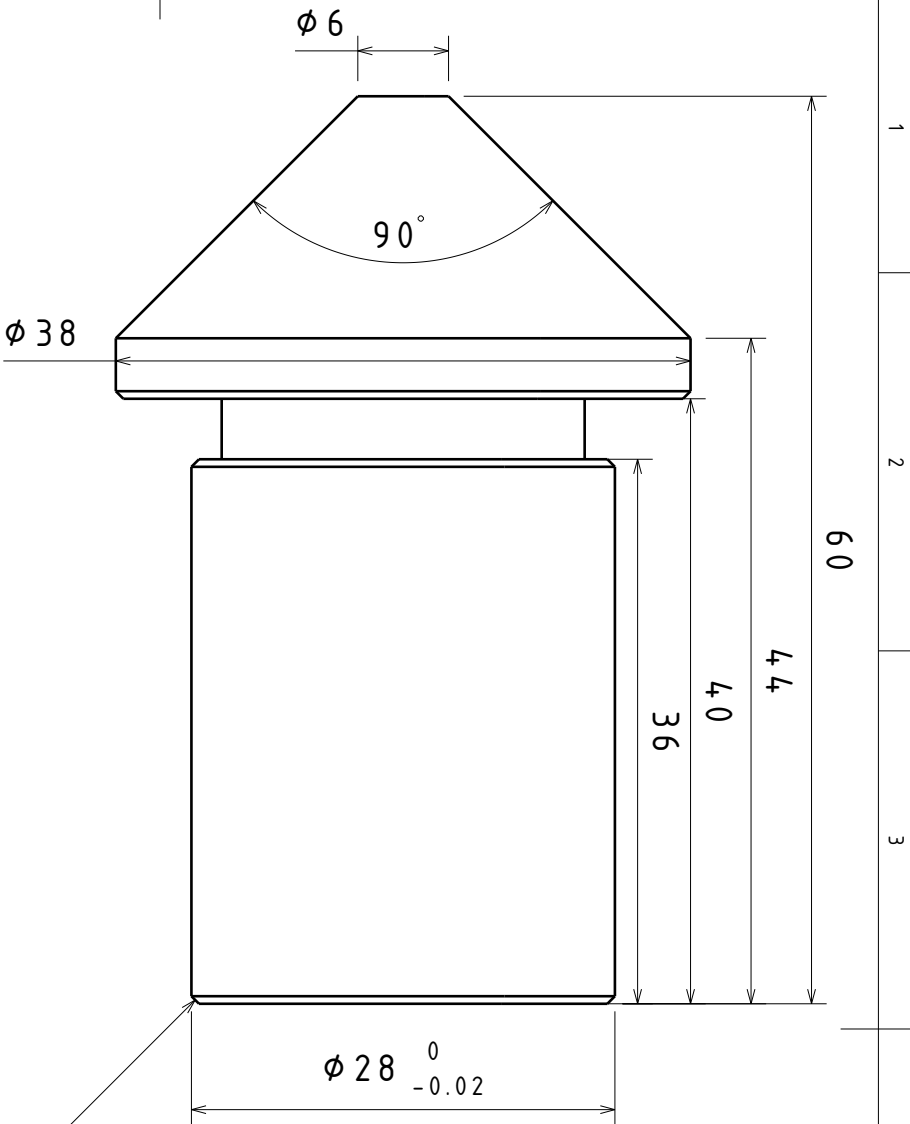
Conical surface needs to be manufactured at the exact same tool angle as the mating insert. On a manual machine $<0.01^\circ$ accuracy is not enough. The surfaces need to be machined at the same time.


TOOLS NEEDED	
1:	Lathing chisel
2:	Parting tool
3:	Chamfer tool
4:	Center drill
5:	14mm drill
6:	Internal lathing chisel
7:	90° countersink

PRODUCTION STEPS	
1:	Leave ~30mm of stock sticking out of the chuck and face the end
2:	Lathe outer diameter to tolerance
3:	Make grooves with parting tool
4:	Chamfer all edges
5:	(Center) drill 14mm hole
6:	Machine converging (100°) section
7:	Part off the workpiece
8:	Flip part and clamp in soft jaws
9:	Face to length and chamfer edges
10:	Machine internal cone (10°) and chamfer edge with countersink



DRAWN BY: Rolf Wubben		Delft Aerospace Rocket Engineering (DARE) - Stratos IV		TOLERANCES (unless indicated otherwise)	
CHECKED BY: XXXXXXXXXX		PART NAME: Stratos4_Tank_RollControl_TestThruster_Nozzle_Drawing V1.1		Dimensions	
DATE: 29-03-2022		APPROVED BY CHIEF ENG: M: T:		Angles	
XXXXXXXXXXXX		SCALE: 2:1		Surface Roughness	
SIZE: A4		MATERIAL: Steel		AMOUNT: 1	
		MASS [KG]: 0.159		REVISION: C.1	
		SHEET 1 / 1			



DRAWN BY: Rolf Wubben	Delft Aerospace Rocket Engineering (DARE) - Stratos IV			TOLERANCES (unless indicated otherwise)		
CHECKED BY: XXXXXXXXXX	PART NAME: Stratos4_Tank_UpperSkirt_TestThrust erBattleship_Nozzle_ToolingFlange_Dra wing V1.0	Dimensions		± 0.1 [mm]		
		Angles		± 0.5 [deg]		
		Surface Roughness		1,6 [µm]		
DATE: 26-11-2021			AMOUNT:	1		
APPROVED BY CHIEF ENG: XXXXXXXXXXXX			MATERIAL:	Stainless 430F		
			MASS [KG]:			
			This drawing is DARE property; it cannot be reproduced or communicated without our written agreement.			
SIZE: A4		SCALE: 2:1	REVISION: A.1	SHEET 1 / 1		

B.6. ABS grain printing

For the printing of the grain very specific settings are required to achieve good results. These settings will vary between every different ABS blend and 3d printer used. During this thesis with REAL Filament ABS grey on an Ultimaker S5 the ideal settings were iterated in order to find acceptable results. These were found to be:

- Extruder temperature of 255 °C
- Bed temperature of 105 °C
- Print speed of 30mm/s



Figure B.9: Bad layer adhesion

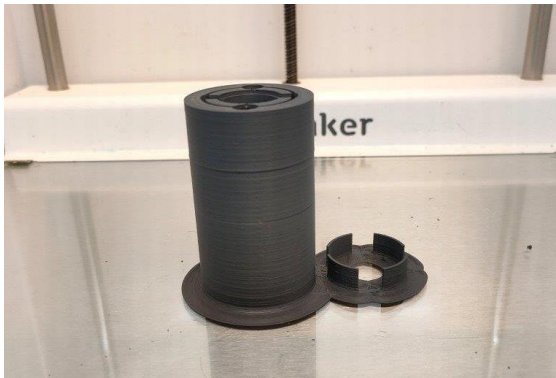


Figure B.10: Small amount of layer separation

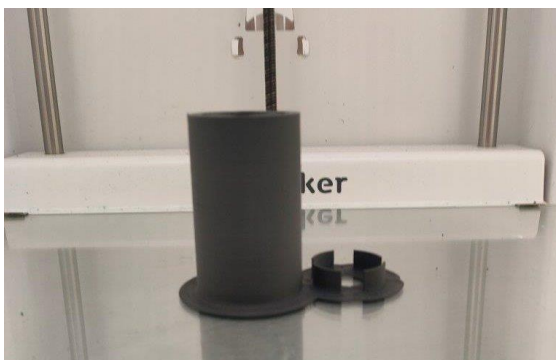


Figure B.11: No layer separation

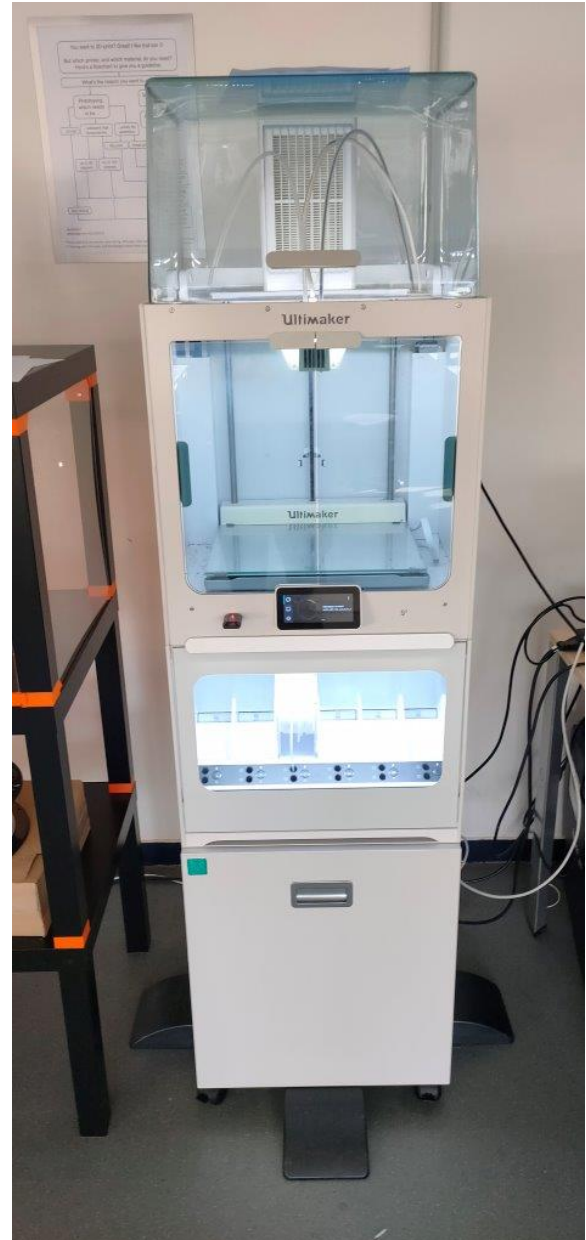
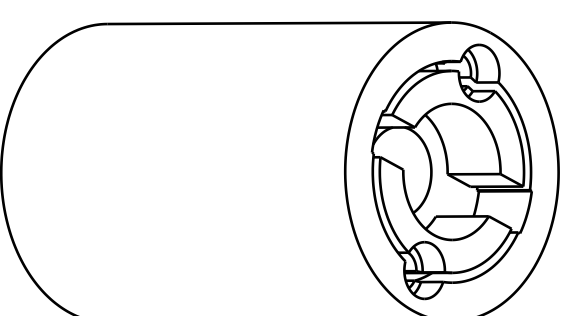
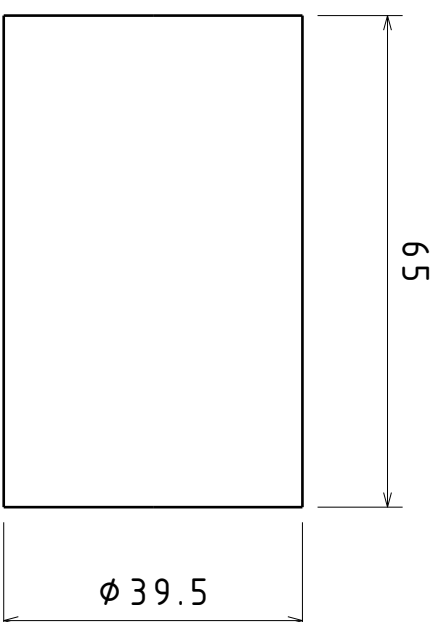
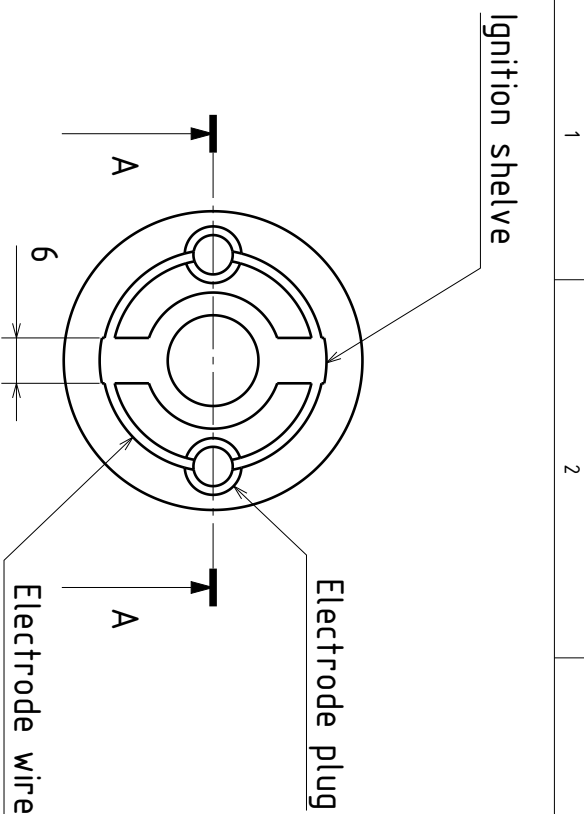
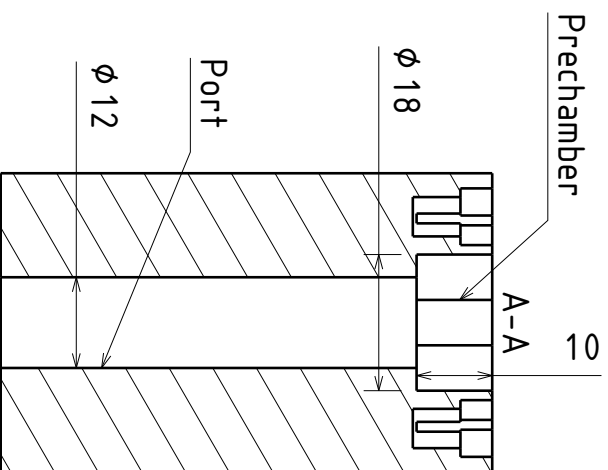


Figure B.12: Ultimaker S5 3D printer

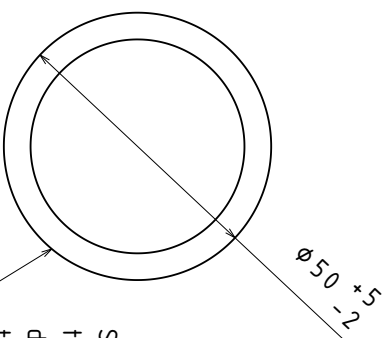
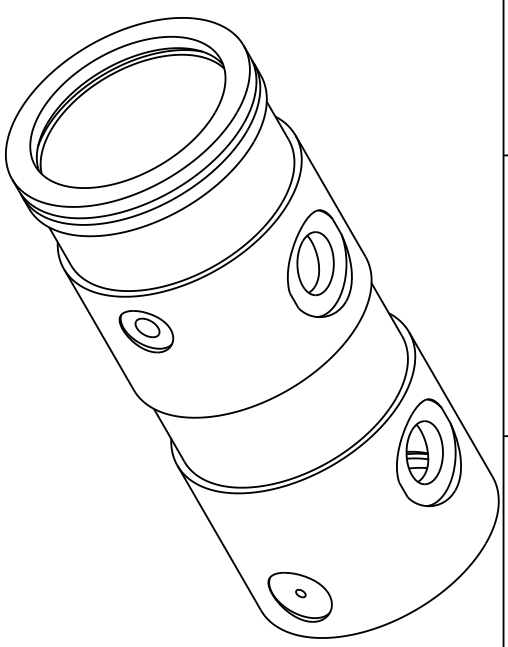
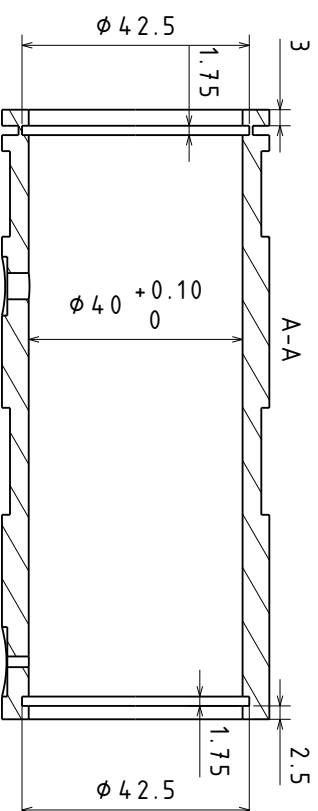
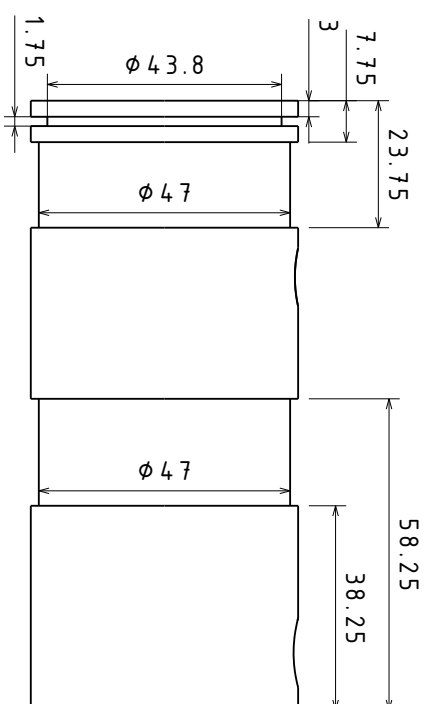
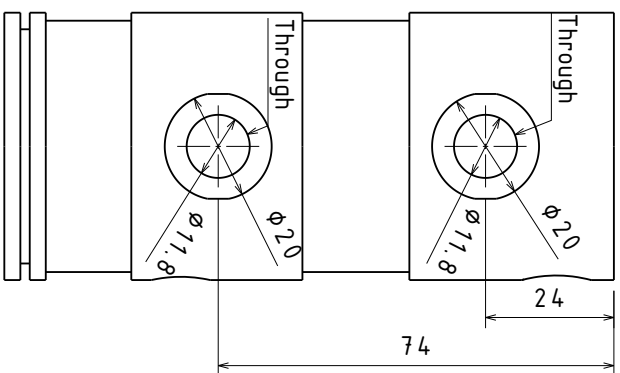


Print duration ~22hrs

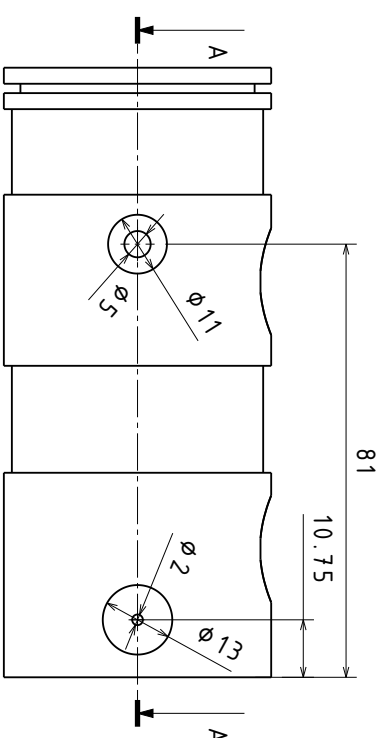
When using REAL filament ABS gray with 2.85mm thickness: 3D print at an extruder temperature 255°C, bed temperature of 105°C and a print speed of 30mm/s. Artificially set infill to 100% with a wall thickness >7mm for a circular infill pattern. A brim is required for proper adhesion. Ensure that the bed is cleaned and sprayed with adhesive. Best results have been achieved with an Ultimaker 5S.




DRAWN BY: Rolf Wubben	Delft Aerospace Rocket Engineering (DARE) - Stratos IV				TOLERANCES (unless indicated otherwise)	
DATE: 05-06-2022	PART CODE: ABSgrain_Reference				Dimensions	± 0.2 [mm]
APPROVED BY PROC. MAN.	PART DESCRIPTION:				Angles	± 0.5 [deg]
N/A	ABS Grain Straight Port				Surface Roughness	1.6 [µm]
APPROVED BY CHIEF ENG.:	M:				AMOUNT:	1
N/A	T:				MATERIAL:	ABS
					MASS [KG]:	0.072
SIZE: A4	SCALE: 1/2				REVISION: A.1	
					SHEET 1 / 1	

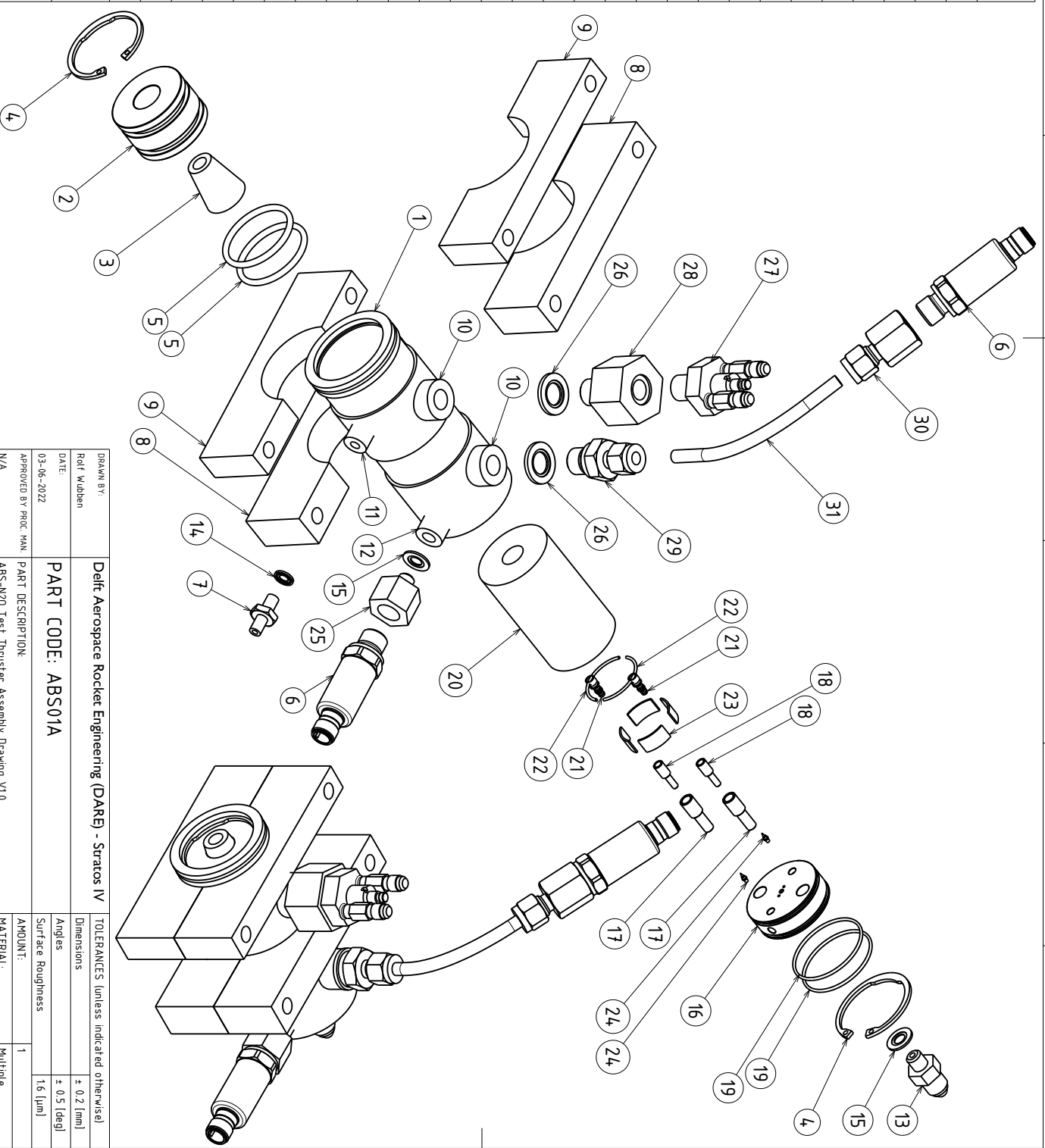


Simply smoothen the stock. The diameter that is then left is acceptable.

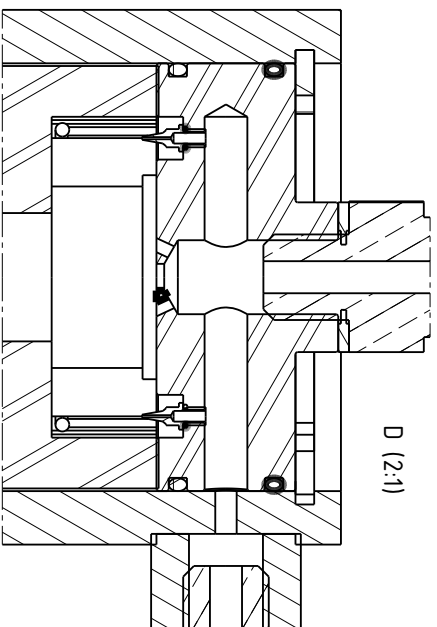


DRAWN BY: Ref: Wubben		Delft Aerospace Rocket Engineering (DARE) - Stratos IV		TOLERANCES (unless indicated otherwise)	
DATE: 22-01-2019		PART CODE: TRC-T02A		Dimensions	± 0.1 (mm)
APPROVED BY PROJ. MAN:		PART DESCRIPTION: Testchamber Battleship drawing V12		Angles	± 0.5 (deg)
APPROVED BY CHIEF ENG:		M:		Surface Roughness	16 (µm)
T:		AMOUNT: 1		MATERIAL:	Steel
		MASS (KG): 0.530		This drawing is DARE property. It cannot be reproduced or transmitted without our written consent.	
SITE: A3				SCALE: 1:1	SHEET 1 / 1

A			Material
Item No.	Quantity	Description	
1	1	Chamber	Steel
2	1	Nozzle Retainer	Steel
3	1	Nozzle Insert	Graphite
4	2	Snapping	Spring Steel
5	2	Nozzle O-Ring	Rubber
6	2	ifm Pressure Sensor	StainlessSteel 316
7	1	TC Pressure Gland	StainlessSteel 316
8	2	Back Clamp	Aluminium
9	2	Front Clamp	Aluminium
10	2	Pressure Flange	Steel
11	1	Thermocouple Flange	Steel
12	1	Injector Flange	Steel
13	1	Inlet Adapter	Brass
14	1	Dowty Seal M6	-
15	2	Dowty Seal M8	-
16	1	Manifold	Aluminium
C			
17	2	HV Pressfit	PEEK
18	2	HV Connector	Copper
19	2	Manifold O-Ring	Rubber
20	1	ABS Fuel Grain	ABS
21	2	Electrode Plug	Bronze
22	2	Electrode Wire	Copper
23	1	ABS Fuel Grain Filler	ABS
24	2	Injector Nozzle	StainlessSteel 316
25	1	Pressure Adapter	Brass
26	2	Dowty Seal 1/4"	-
E			
27	1	IEPE-124A21	StainlessSteel 316
28	1	IEPE-124A21-Adapter	Brass
29	1	SS-400-1-4RS-Swagelok	StainlessSteel 316
30	1	SS-400-7-4RJ-Swagelok	StainlessSteel 316
F			
31	1	Standoff Pipe	StainlessSteel 316

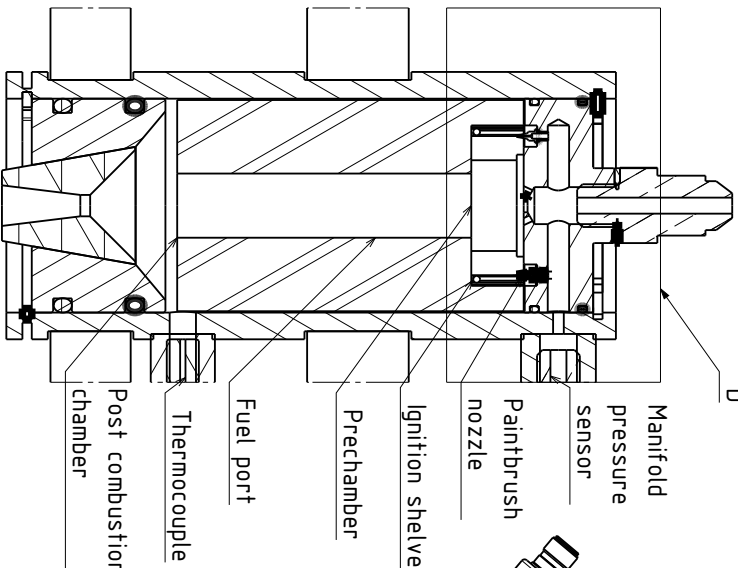


DRAWN BY: Rolf Wubben		Delft Aerospace Rocket Engine Engineering (DARE) - Stratos IV	
DATE: 03-06-2022	PART CODE: ABS01A	TOLERANCES (unless indicated otherwise)	
APPROVED BY PROC. MAN: N/A	PART DESCRIPTION: ABS-N2O Test Thruster Assembly Drawing V1.0	Dimensions	± 0.2 [mm]
APPROVED BY CHIEF ENG.: N/A	M:	Angles	± 0.5 [deg]
SIZE: A3	T:	Surface Roughness	1.6 [µm]
SCALE: 1:2		AMOUNT:	1
REVISION: A1		MATERIAL:	Multiple
SHEET 1 / 1		MASS [KG]: 2.081	
		This drawing is DARE property! It cannot be reproduced or communicated without prior written agreement.	



B-B (1:1)

D



D (2:1)

Dynamic pressure sensor

A-A (1:1)

Static pressure sensor

Snap ring

Snap Ring

Nozzle Insert

Nozzle Retainer

Test bench clamps

ABS Fuel grain

Chamber wall

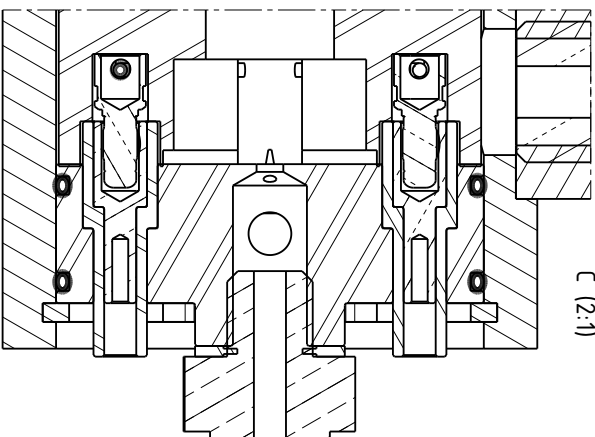
Manifold

High Voltage Connector

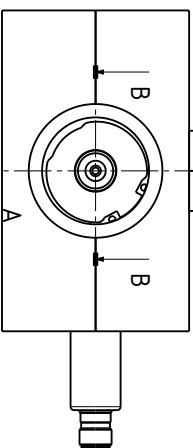
Nitrous inlet


Snap ring

C (2:1)



Manifold assembly, grain assembly and nozzle assembly are all to be prepared individually. The manifold and grain are then mated outside the combustion chamber with silicone elastomer. When dried the manifold+grain assembly can be inserted into the chamber and secured with a snap ring. After applying more silicone elastomer to the external of the nozzle assembly, it can be inserted from the bottom and secured with a snap ring. Ensure that the nozzle is sitting tightly against the snap ring.



DRAWN BY: Ref't Wulben		Delft Aerospace Rocket Engineering (DARE) - Stratos IV		TOLERANCES (unless indicated otherwise)	
DATE: 03-06-2022		PART CODE: ABS01A		Dimensions	± 0.2 [mm]
APPROVED BY PROC. MAN		PART DESCRIPTION: ABS-NZO Test Thruster Assembly Drawing V1.0		Angles	± 0.5 [deg]
N/A		M:		Surface Roughness	1.6 [µm]
APPROVED BY CHIEF ENG:		T:		AMOUNT:	1
N/A		SCALE:		MATERIAL:	Multiple
SIZE: A3				MASS [KG]:	2.081
This drawing is DARE property, it cannot be reproduced or disseminated without our written agreement.					
				REVISION	SHEET 1 / 1

C

CHESS

The software written to model the system can be requested from the author at rolf.wubben@gmail.com for future research. It uses Python 3.9 and will require the standard packages Numpy and Matplotlib that can be downloaded using the `pip install` command. PyQt5 is used as the basis of the code to allow for a user friendly front end. Like the other packages it can simply be installed using `pip install`. Finally `rocketCEA`, a very useful python wrapper of NASA's CEA software, is required. However, it comes with a few complications during its installation process, especially on Windows.

C.1. Installing `rocketCEA`

Some additional work that was needed to get it running has been collected here. Nonetheless, the best place to start is <https://rocketcea.readthedocs.io/en/latest/quickstart.html>. At the moment of writing it will tell you that Python3.8 and 3.9 are not yet fully support and an additional command is needed. In my experience however everything works as normal without complications. Installing `gfortran` can be done easily by following their suggested steps. However, when running `pip install rocketcea` you will probably get an error message stating you need Microsoft Visual C++ build tools 14.0. Installing should be done using the settings in Figure C.1 as suggested by Ewindar ¹.

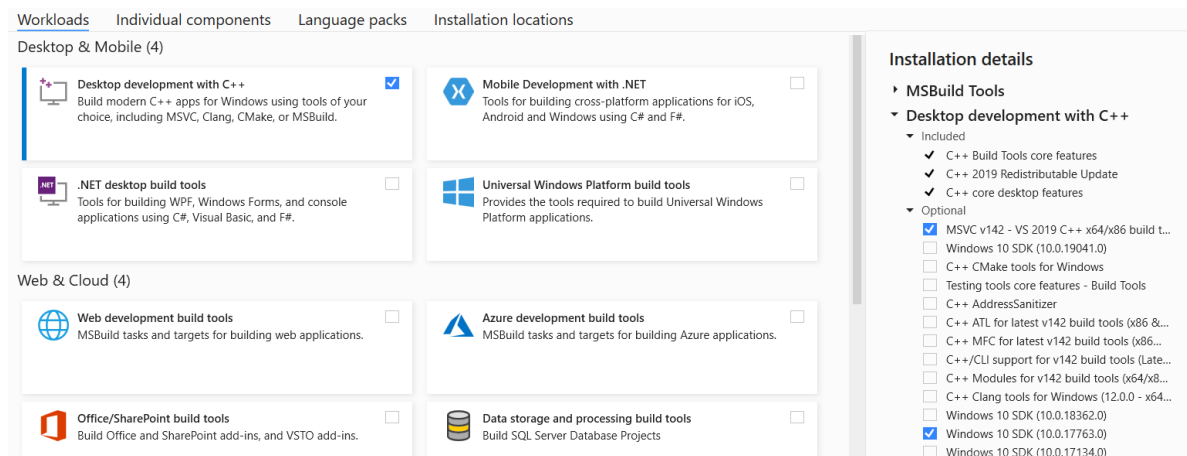


Figure C.1: Use exactly these settings that have been shown to work

¹<https://answers.microsoft.com/en-us/windows/forum/all/microsoft-visual-c-140/6f0726e2-6c32-4719-9fe5-aa68b5ad8e6d>

Now rocketCEA can be installed but upon running it will likely bring up the error: *ImportError: DLL load failed while importing py_cea: The specified module could not be found*. This is due to the fact it cannot find its own .dll which needs to be moved inside the rocketCEA directory. Simply copy it from " \Python39\Lib\site-packages\rocketcea \libs" and move it up a folder. In order to use the ABS fuel blend a new propellant card needs to be added as well. This can be done by copying the following part into the input_cards.py file under the header fuels. Please note that these numbers are only valid using our specific blend of ABS and other brands will need to be characterised as documented in chapter 4:

fuel ABS(S) C 5.216 H 5.898 N 0.284 wt%=100.00
h,cal=14954.5889 t(k)=298.15 rho=1.04

C.2. Example Output

This section contains four example output plots of CHESS. The first one gives some engine properties over time such as the chamber pressure, thrust produced and mass flows. Figure C.3 and Figure C.4 show the cross sections of the grain and nozzle over time respectively. They each show three relevant variables plotted alongside. Finally the mass species over time are shown in Figure C.5.

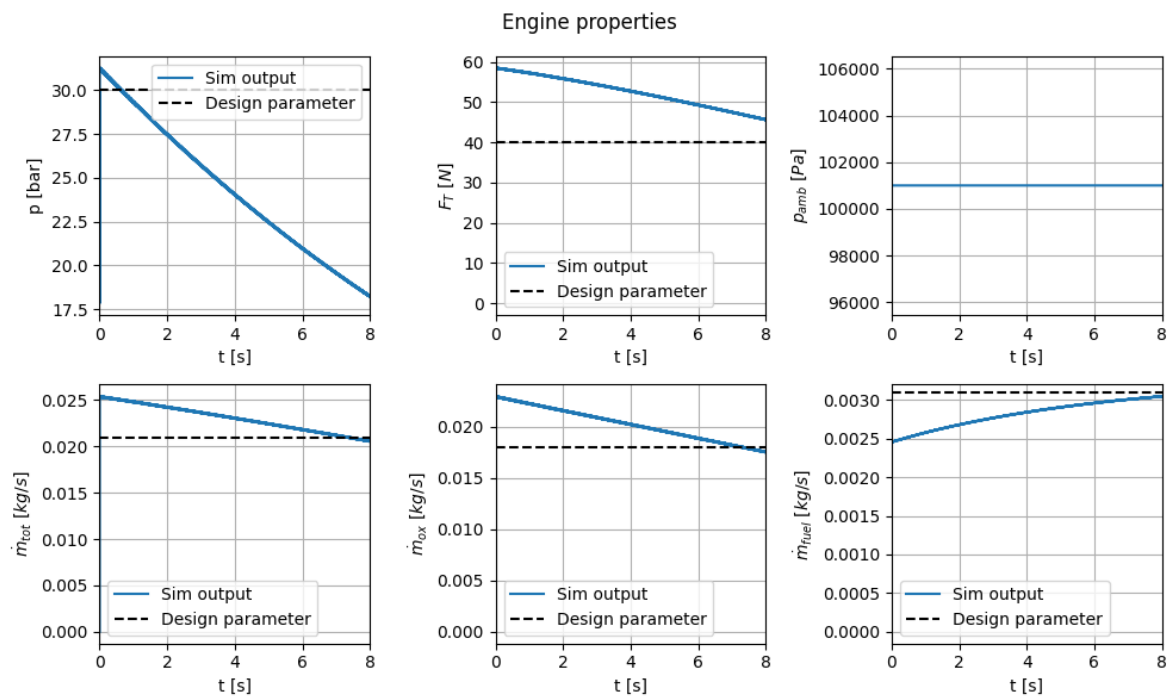


Figure C.2: CHESS engine properties output

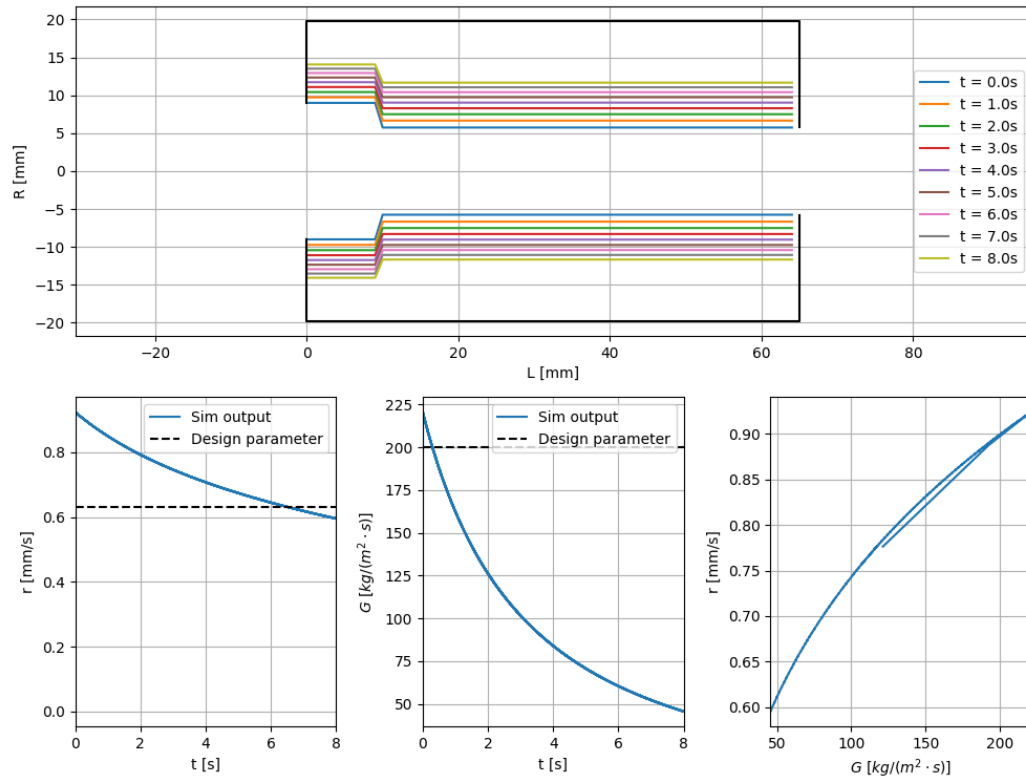


Figure C.3: CHESSE grain cross sections output

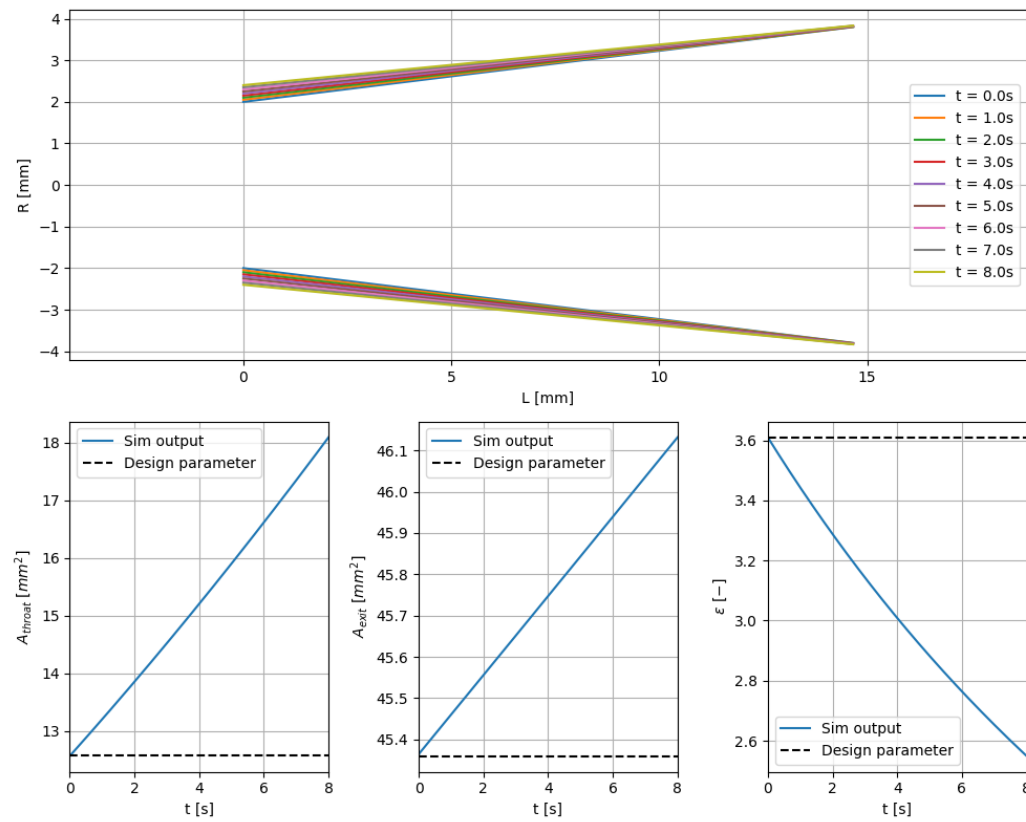


Figure C.4: CHESSE nozzle cross sections output

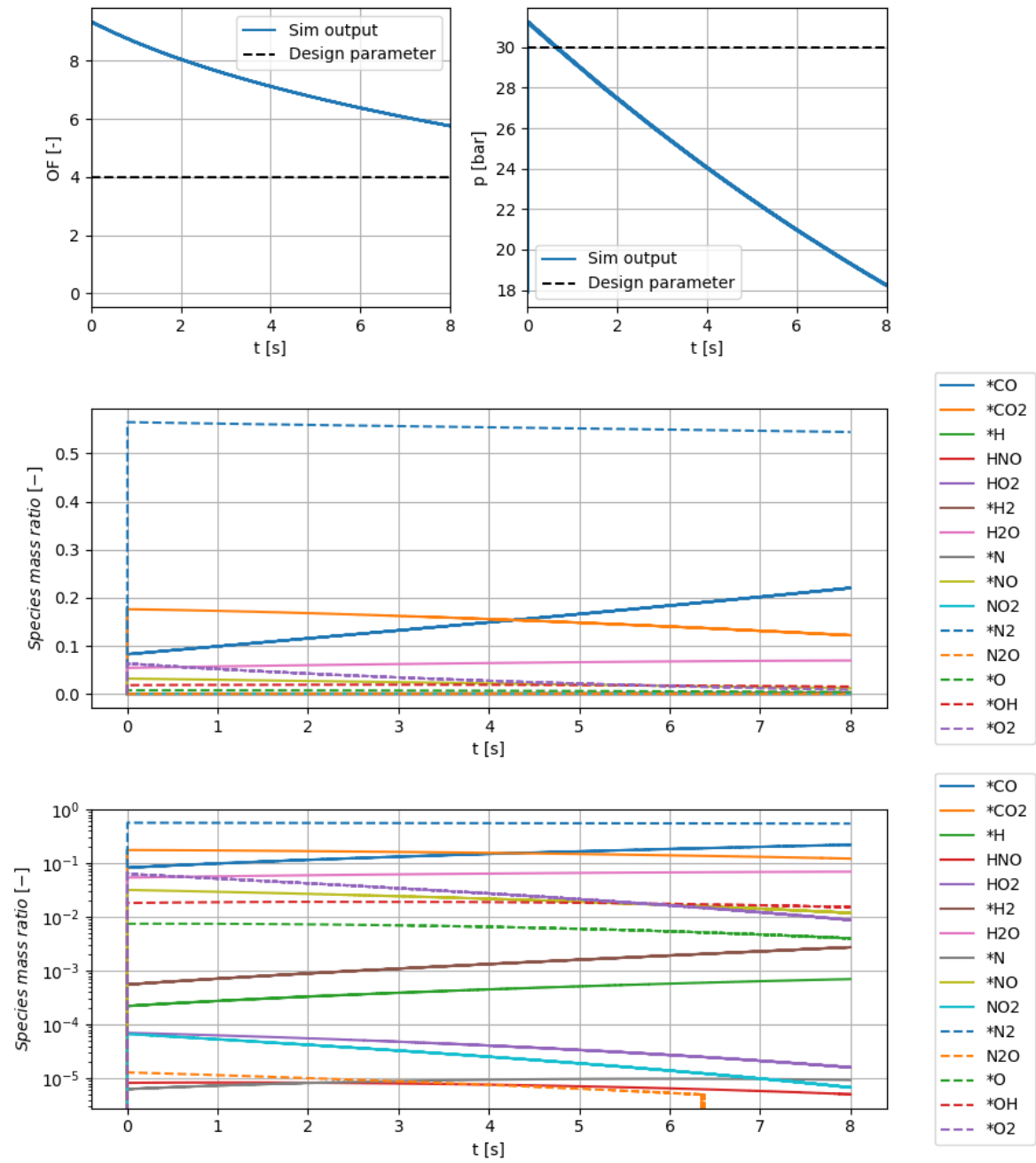


Figure C.5: CHES species mass ratio output

Engine Sizing

System sizing

System design performance

Results

Progress and Control

☒ Average thrust and burn time
☐ Average thrust and total impulse
☐ Total impulse and burn time

Total impulse

320.00

Ns

Burn time

8.00

s

Average thrust

40.00

N

Nozzle

☐ Expansion ratio

3.609

A_e/A^*

☒ Exit pressure

1.429

bar

☐ Pressure ratio

21.0

P/P_e

Convergence angle

50.00

°

Divergence angle

14.00

°

Nozzle efficiency

0.90

-

Fuel

%A

28.40

%B

34.10

%S

37.50

Heat of formation

62.57

kJ/mol

Density

1.04

g/cm³

Oxidizer

Tank pressure

43.00

Drawing

Liquid

Tank liquid level

Flat

Tank bulkhead level

>

Tank L/D

4.00

Chamber Geometry

Area ratio

2.50

A_{exit}/A^*

Height ratio

0.20

L_{grain}/L_{exit}

Diameter ratio

2.00

D_{exit}/D_{throat}

Length ratio

0.10

L_{nozzle}/L_{exit}

Nozzle seat ratio

0.80

-

Injector sizing

Discharge coefficient

0.45

-

Number of ignition holes

2

-

Number of main holes

1

-

Ignition-main ratio

0.01

-

Atmospheric pressure (avg)

1.01

bar

Specific Impulse

215.41

s

c*

1565.0

m/s

Chamber Temperature

3057.7

K

Molar mass

24.16

g/mol

Gamma

1.23

-

Viscosity

0.0001

kg/ms

	Value	Unit	Status
m_prop	0.55	kg	✓
mdot	0.021	kg/s	✓
m_fuel	0.07	kg	✓
mdot_fuel	0.0031	kg/s	✓
m_ox	0.48	kg	✓
mdot_ox	0.018	kg/s	✓
t_fuel	14.0	mm	✓
D_throat	4.0	mm	✓
A_throat	12.57	mm²	✓
D_exit	7.6	mm	✓
A_exit	45.36	mm²	✓
exp_ratio	3.61	-	✓
D_port	11.5	mm	✓
A_port	103.87	mm²	✓
D_grain	39.5	mm	✓
D_pre	18.0	mm	✓
L_grain	65.0	mm	✓
L_pre	10.0	mm	✓
V_fuel	90.8	cm³	☐

Reset

Load

Save

Generate

Next

?

×

Figure C.6: CHESS sizing GUI

Figure C.7: CHESS solving GUI

Figure C.7: CHESS solving GUI

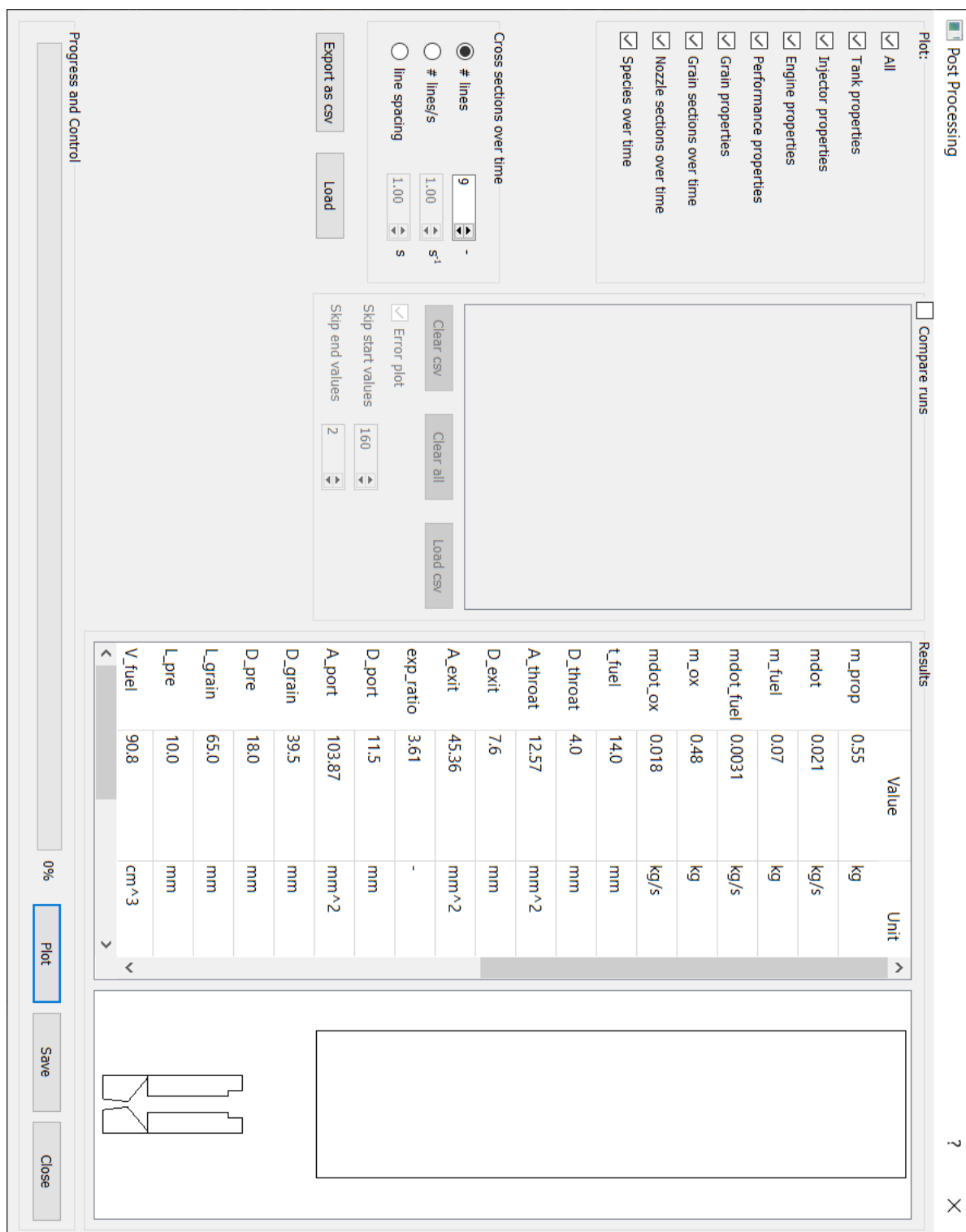


Figure C.8: CHES post-processing GUI

D

Data

This appendix includes all the data that was not directly relevant for the conclusions of the main report. As mentioned in chapter 8 however, this data can provide a solid baseline for future studies or further development of similar systems and has therefore been included for future reference.

D.1. TGA results

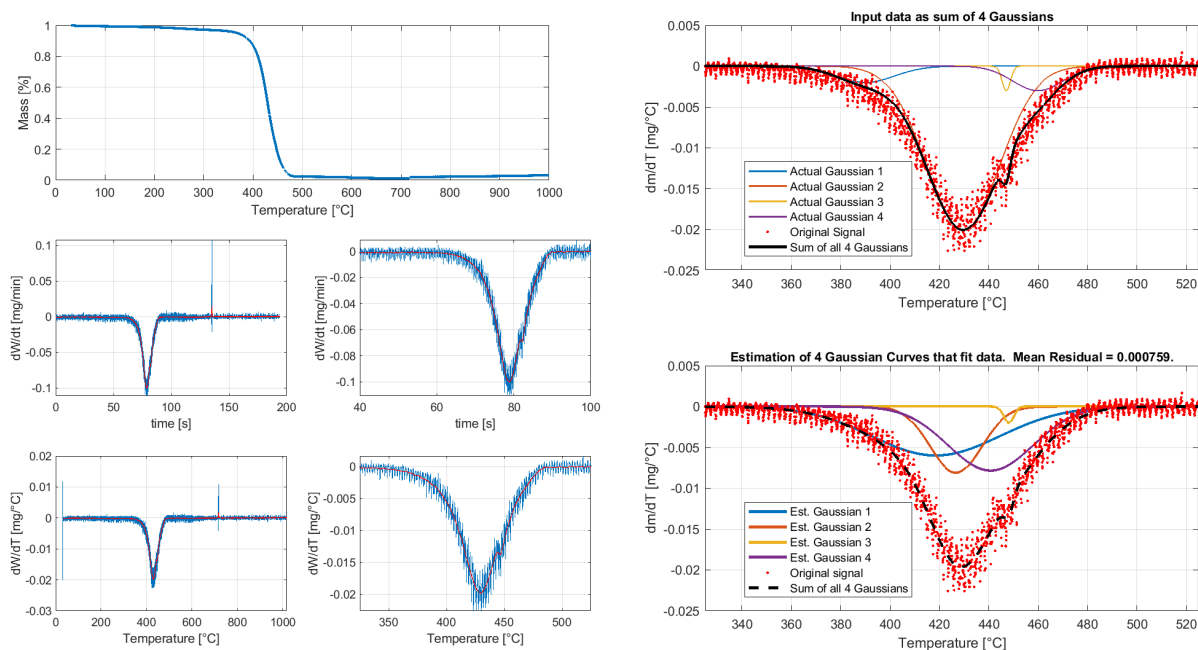


Figure D.1: Mass over temperature of an ABS sample at 5 °C/min including Gaussian fit

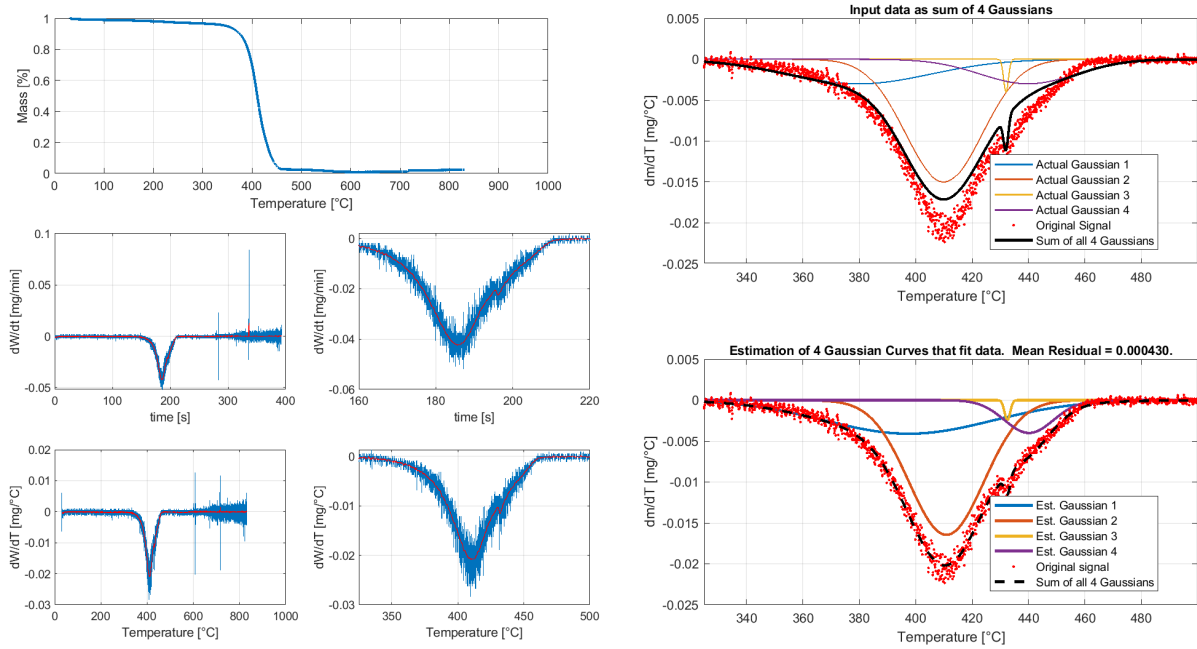


Figure D.2: Mass over temperature of an ABS sample at 2 °C/min including Gaussian fit

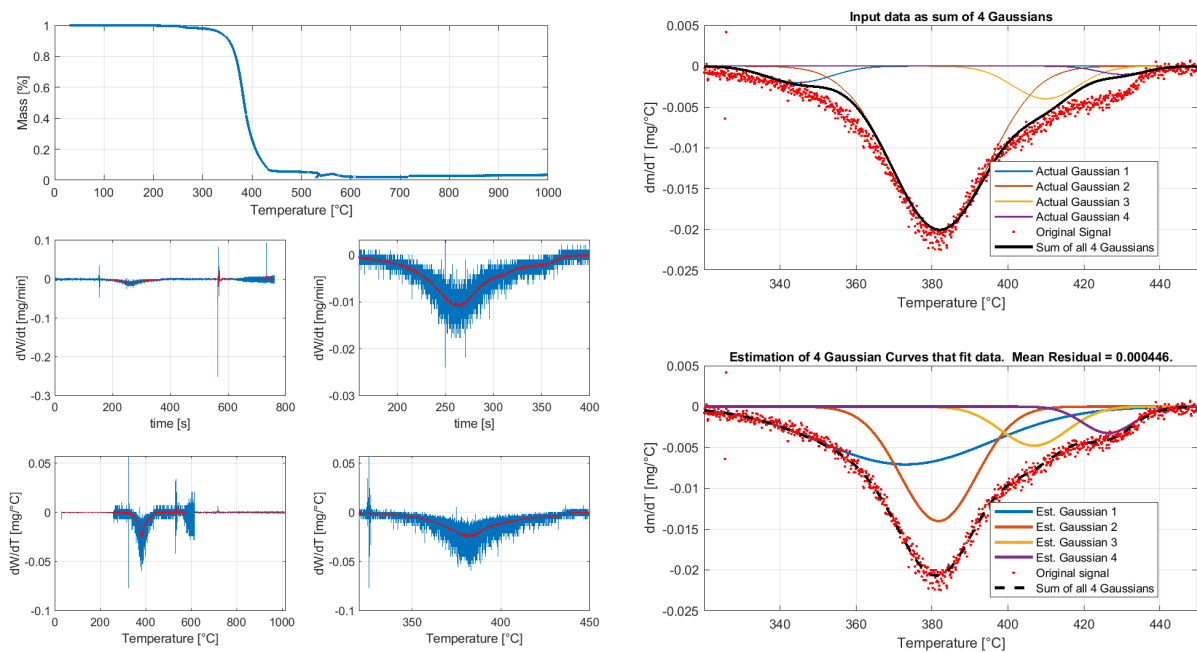


Figure D.3: Mass over temperature of an ABS sample at 0.5 °C/min including Gaussian fit

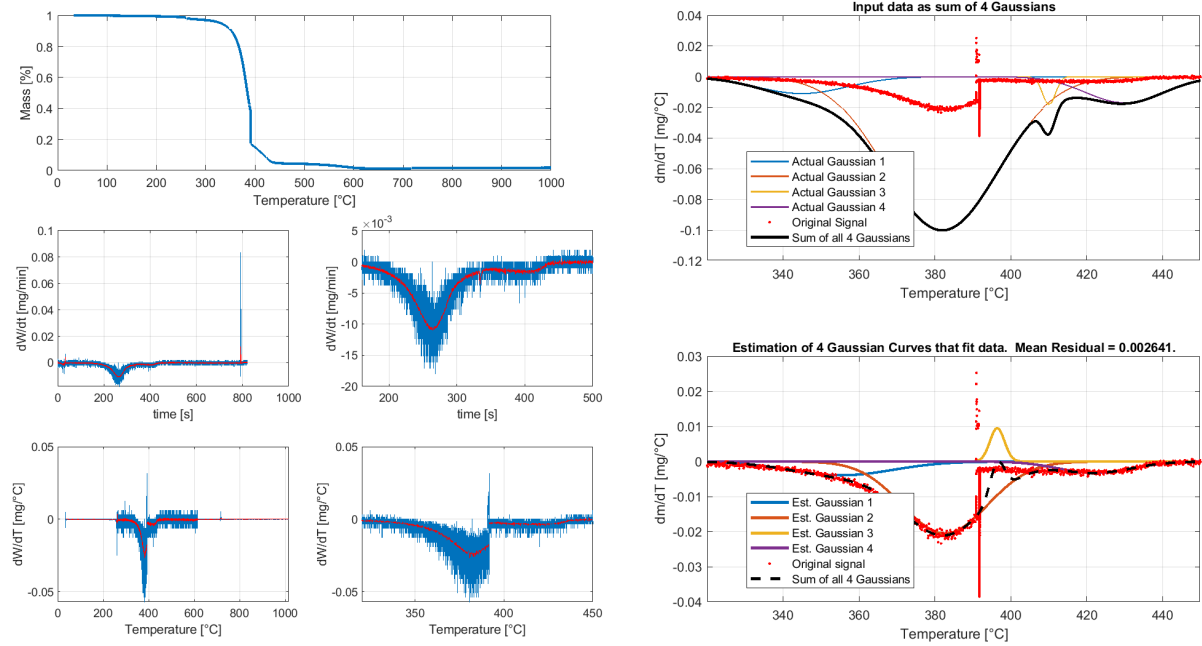


Figure D.4: Mass over temperature of an ABS sample at 5 °C/min with isothermal step including Gaussian fit

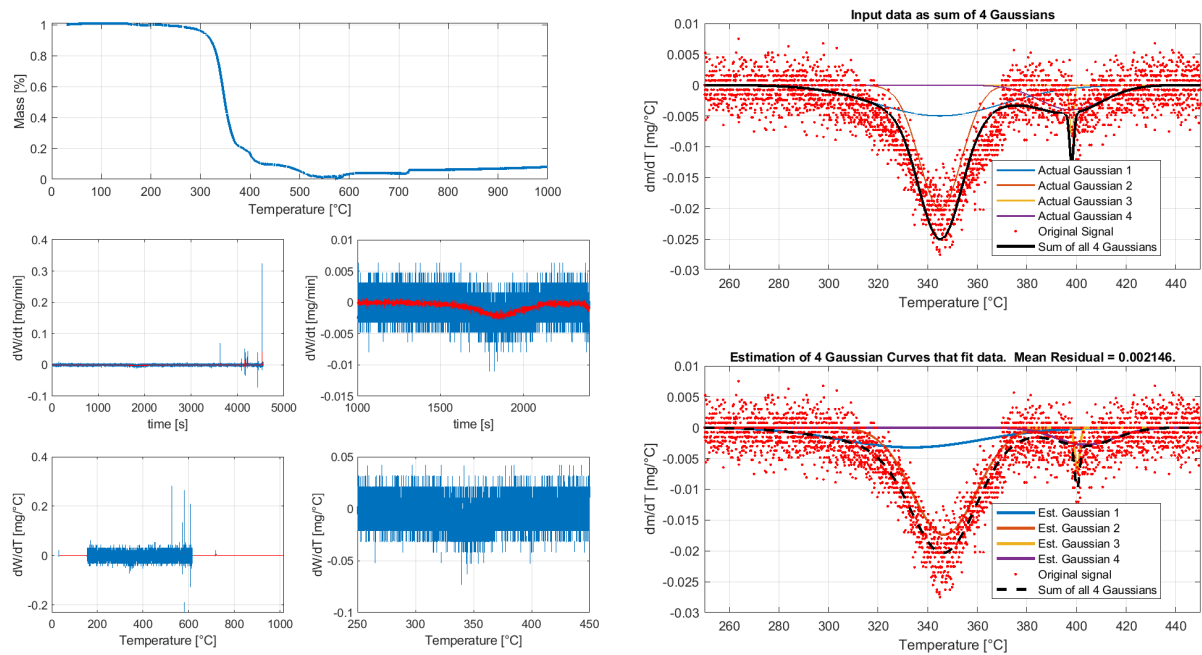


Figure D.5: Mass over temperature of an ABS sample at 0.1 °C/min including Gaussian fit

D.2. Data Analysis Output Example

As an example, the data of tests 26 will be displayed here. The power plots and spectrograms of test 6 are given.

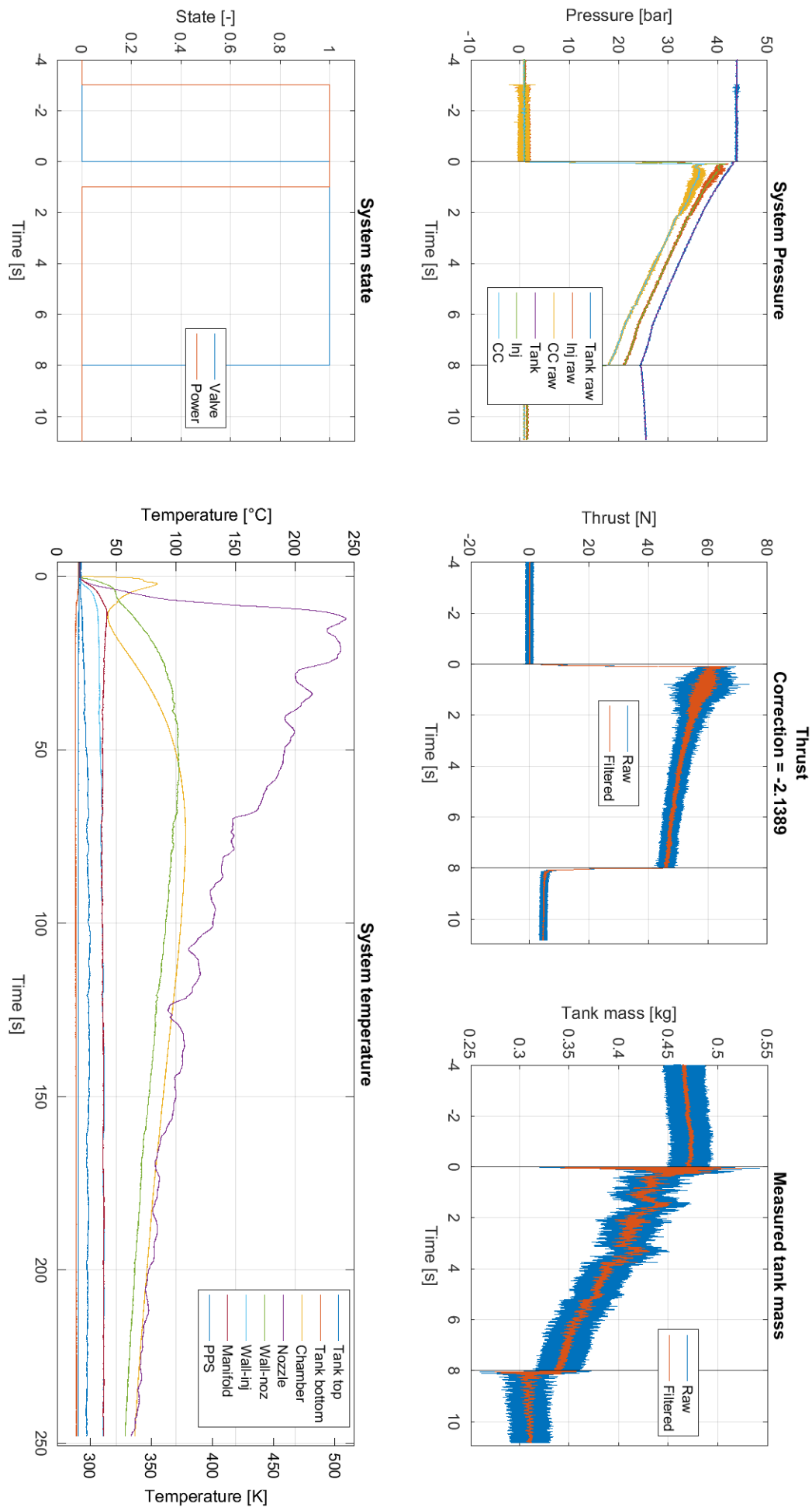


Figure D.6: Raw and filtered data comparison of test 26

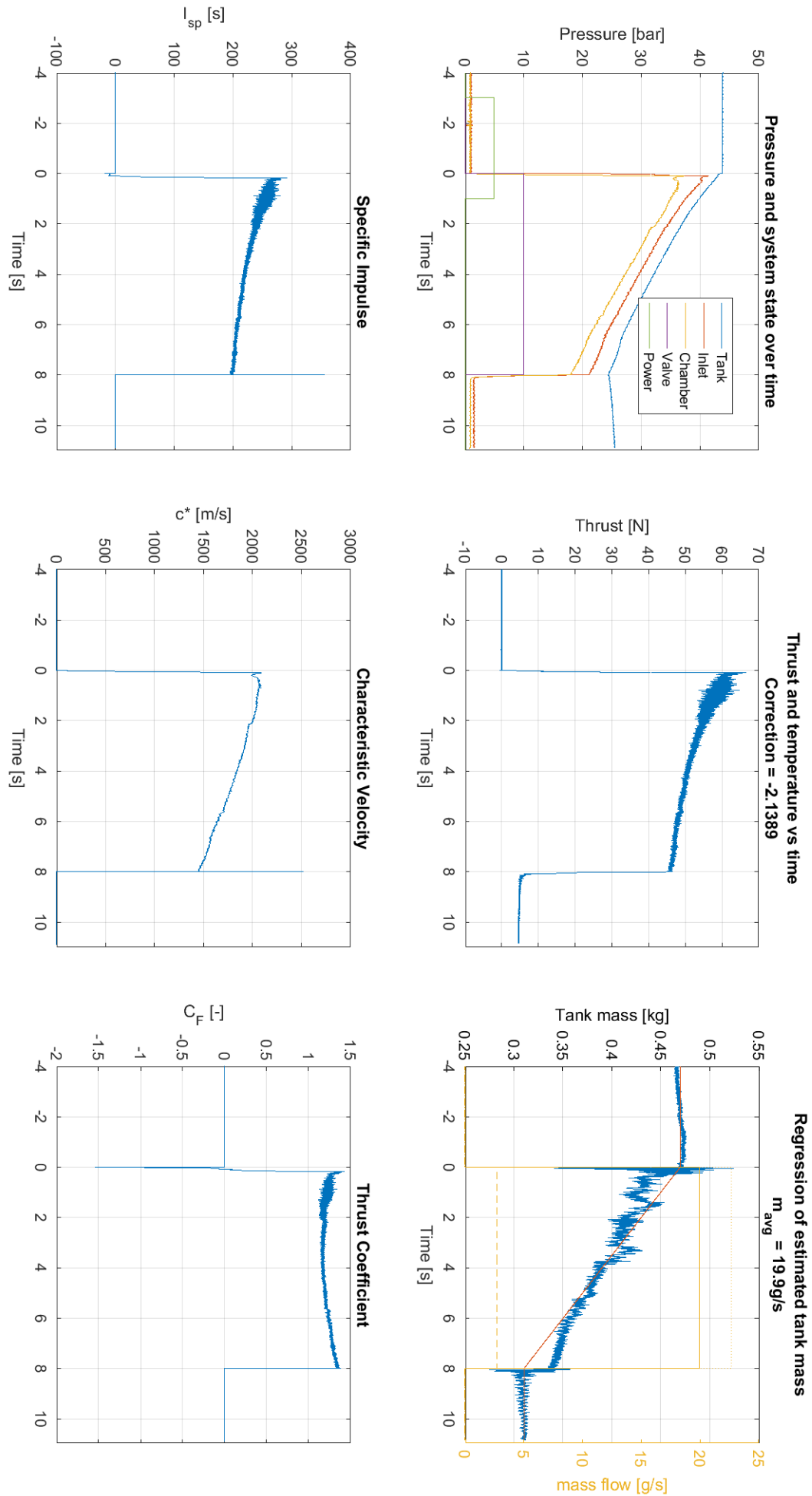


Figure D.7: Calculated engine performance of test 26

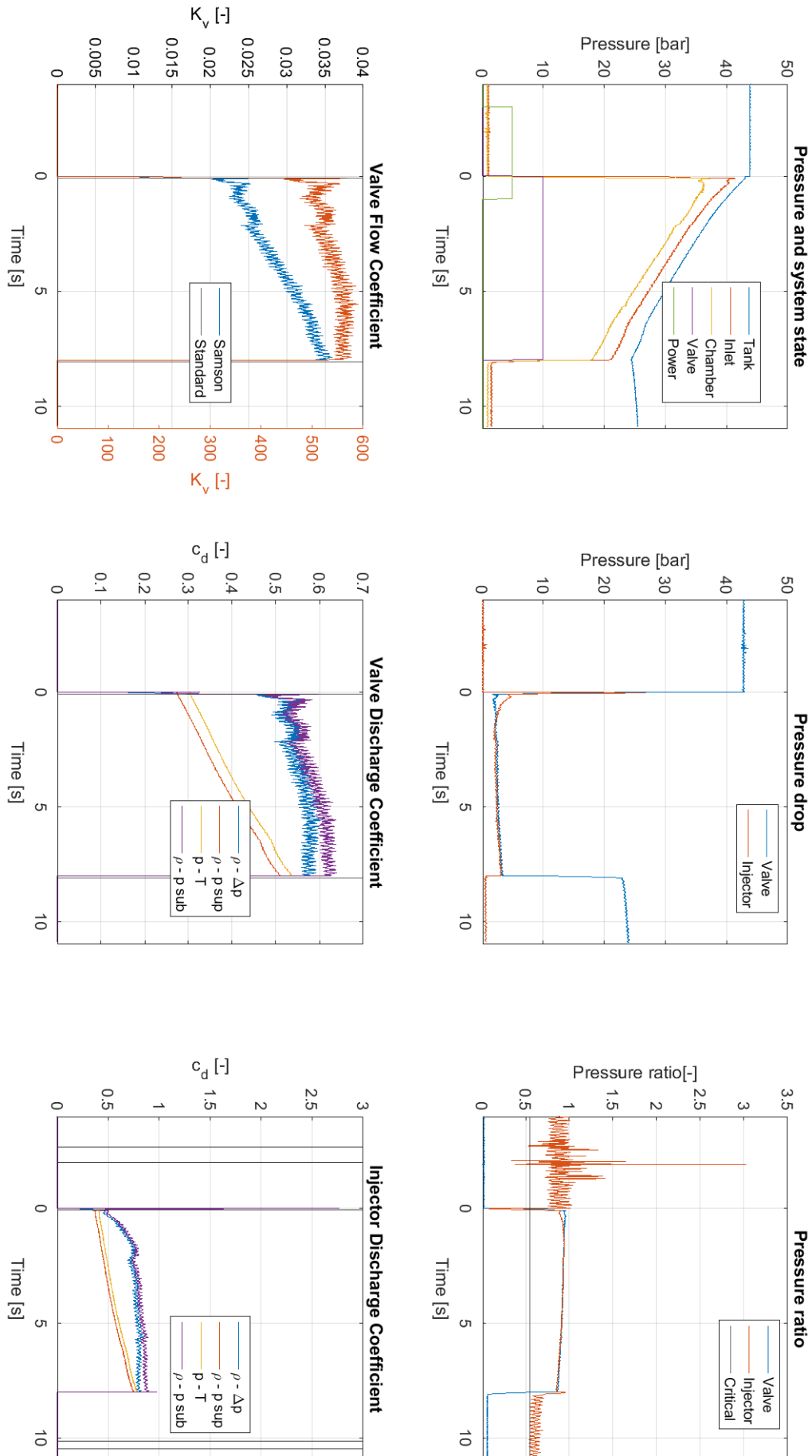


Figure D.8: Calculated feed system performance of test 26

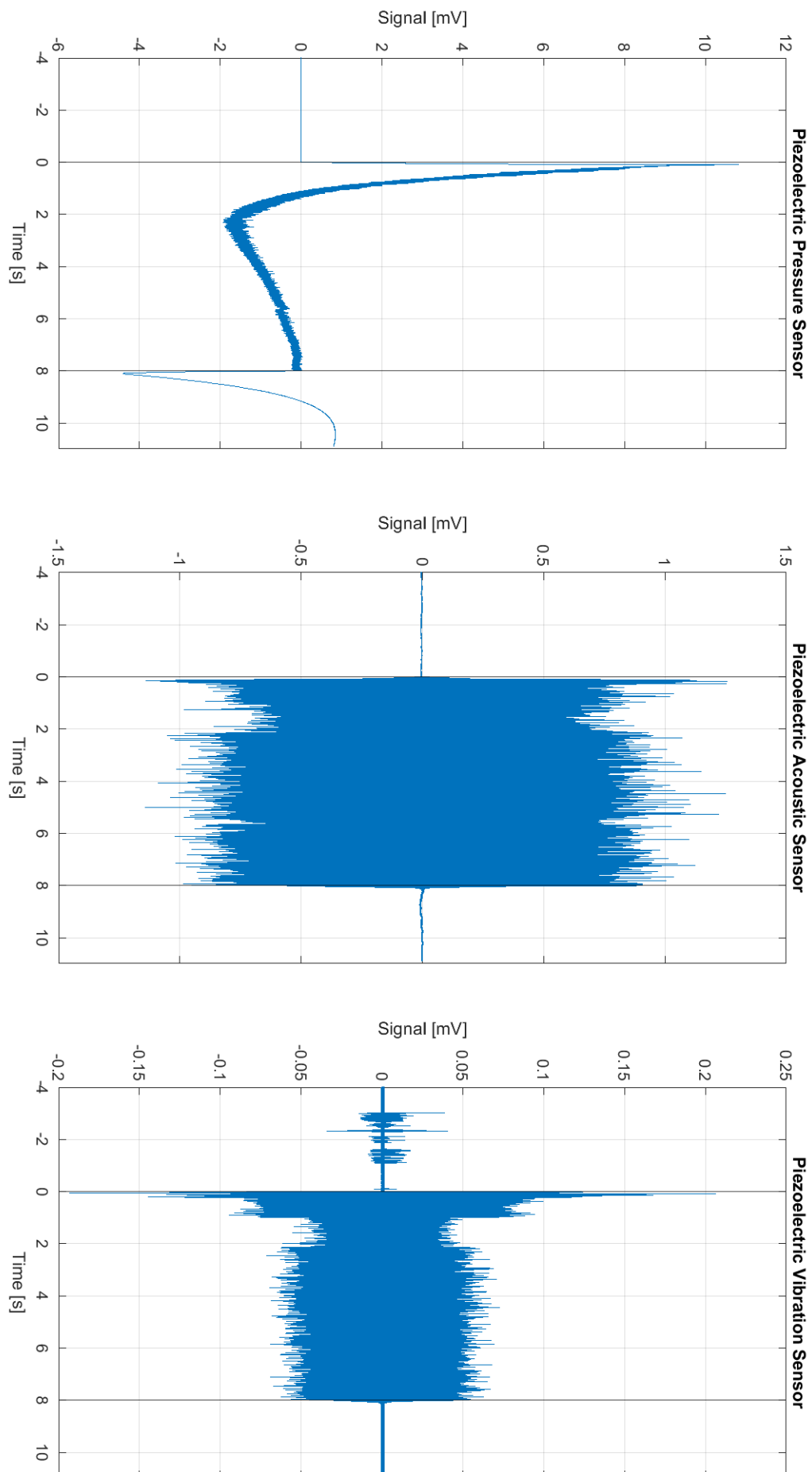


Figure D.9: Piezoelectric data from dynamic pressure sensor, microphone and accelerometer of test 26

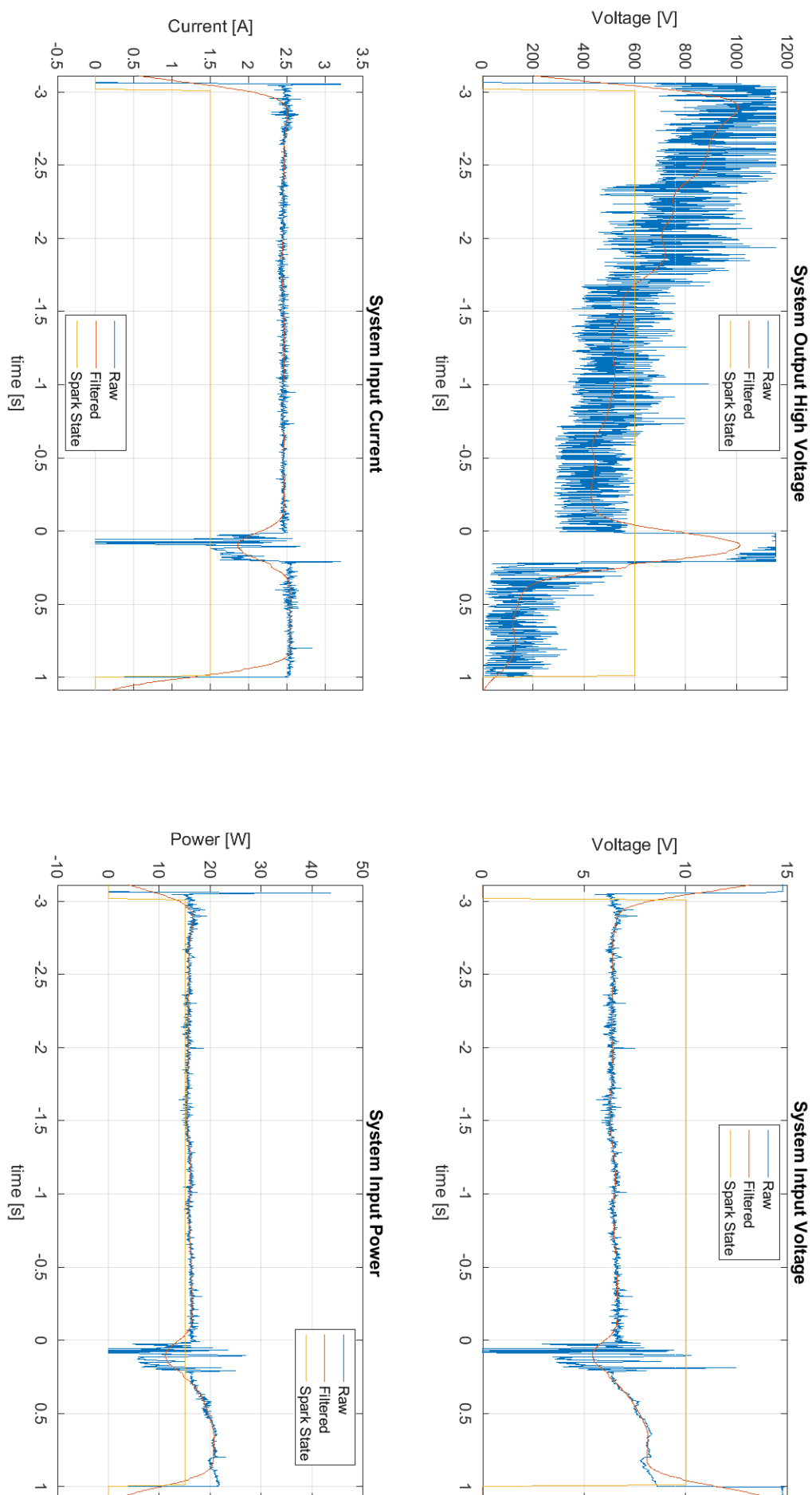


Figure D.10: Power data of test 6

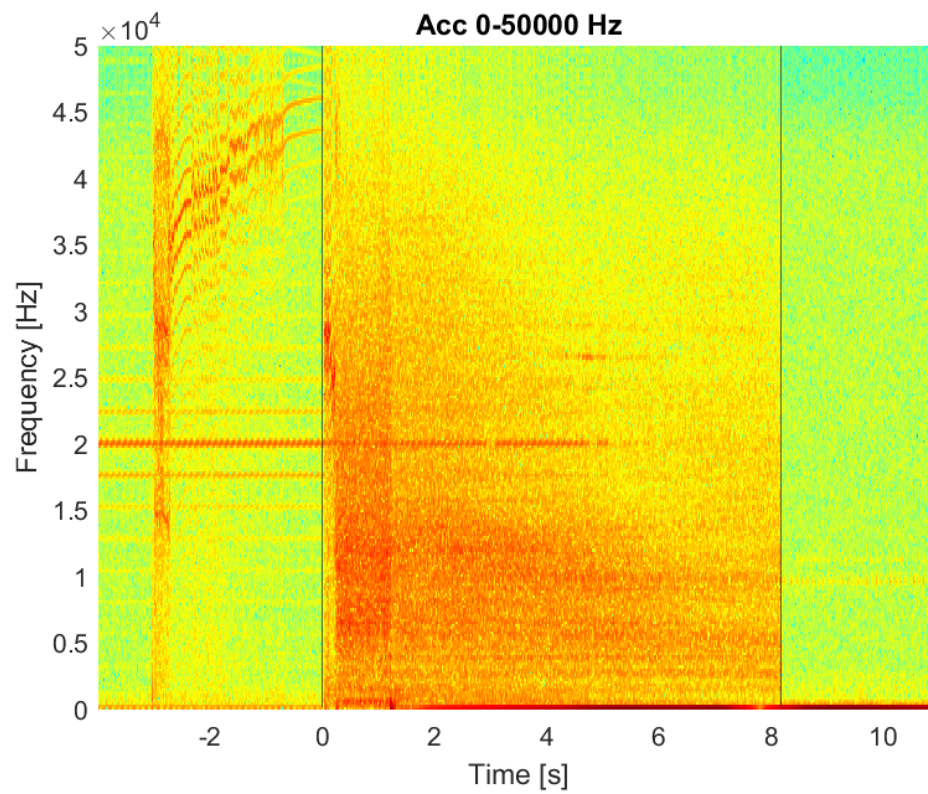


Figure D.11: Spectrogram of accelerometer recording of test 6

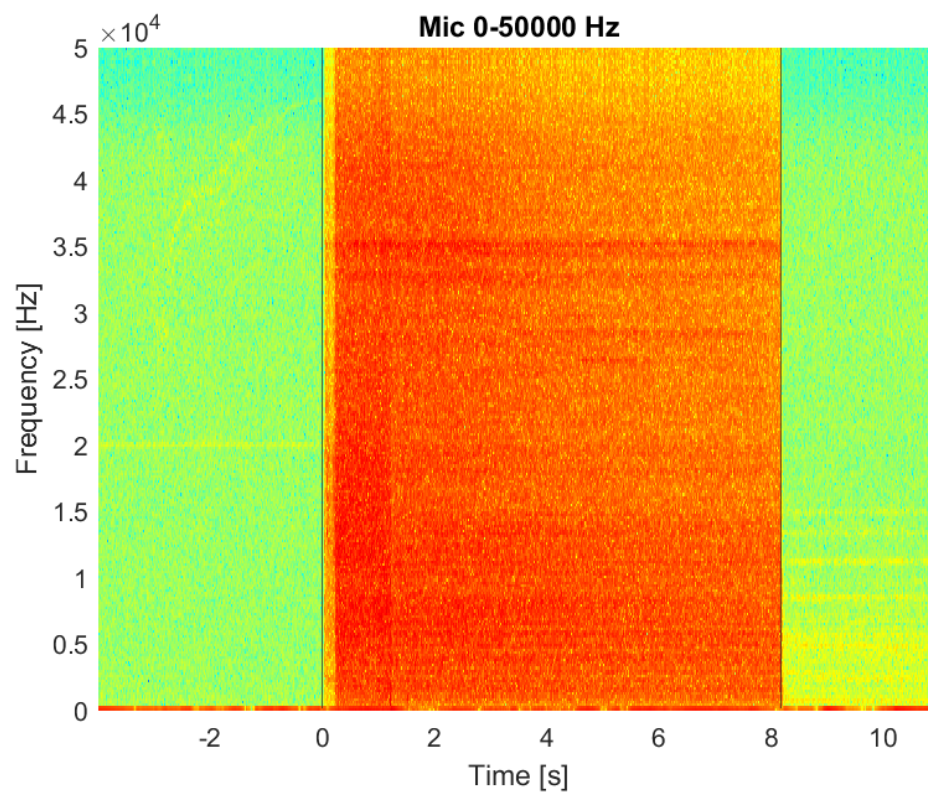


Figure D.12: Spectrogram of microphone recording of test 6

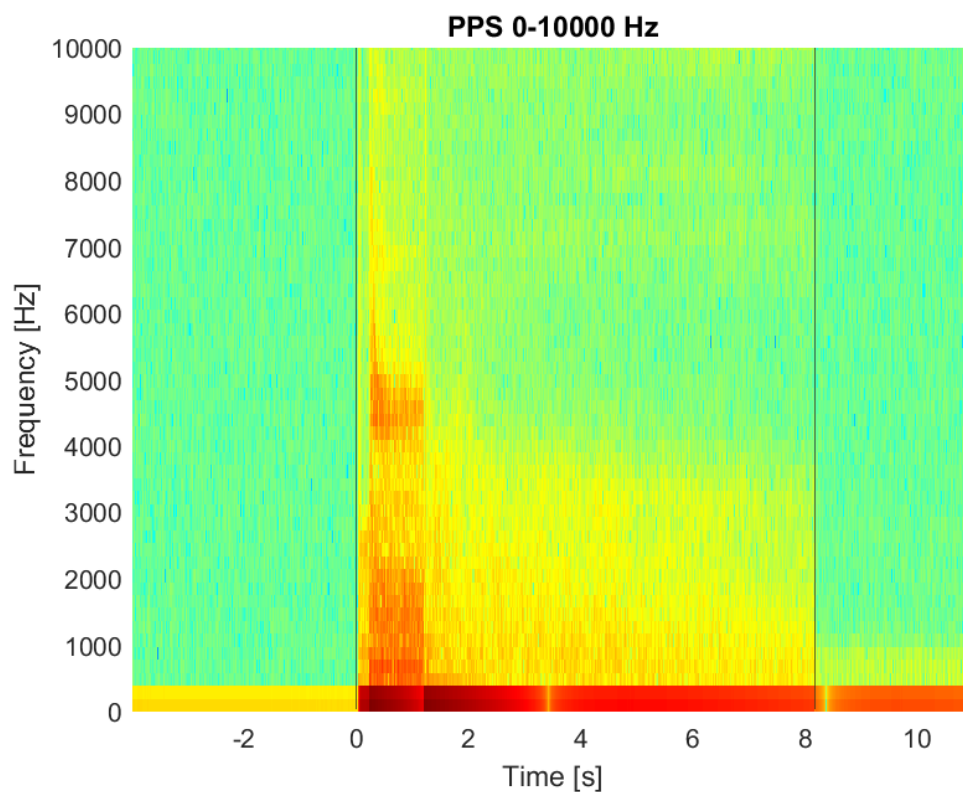


Figure D.13: Spectrogram of dynamic pressure sensor recording of test 6 in the range 0-10,000Hz

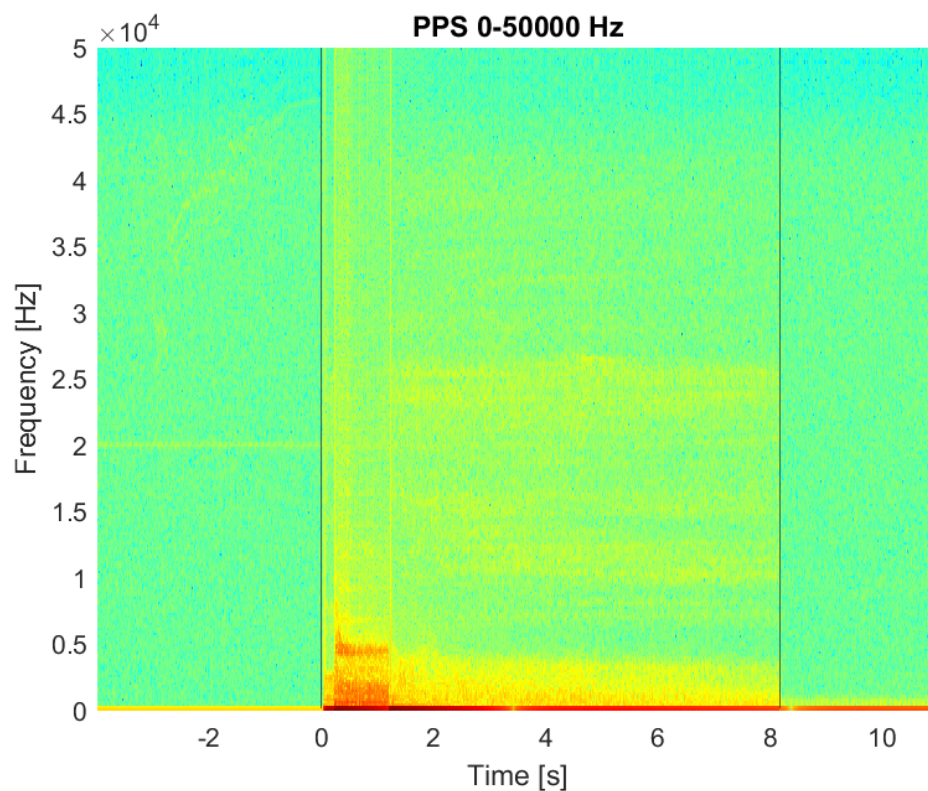


Figure D.14: Spectrogram of dynamic pressure sensor recording of test 6 in the range 0-50,000Hz

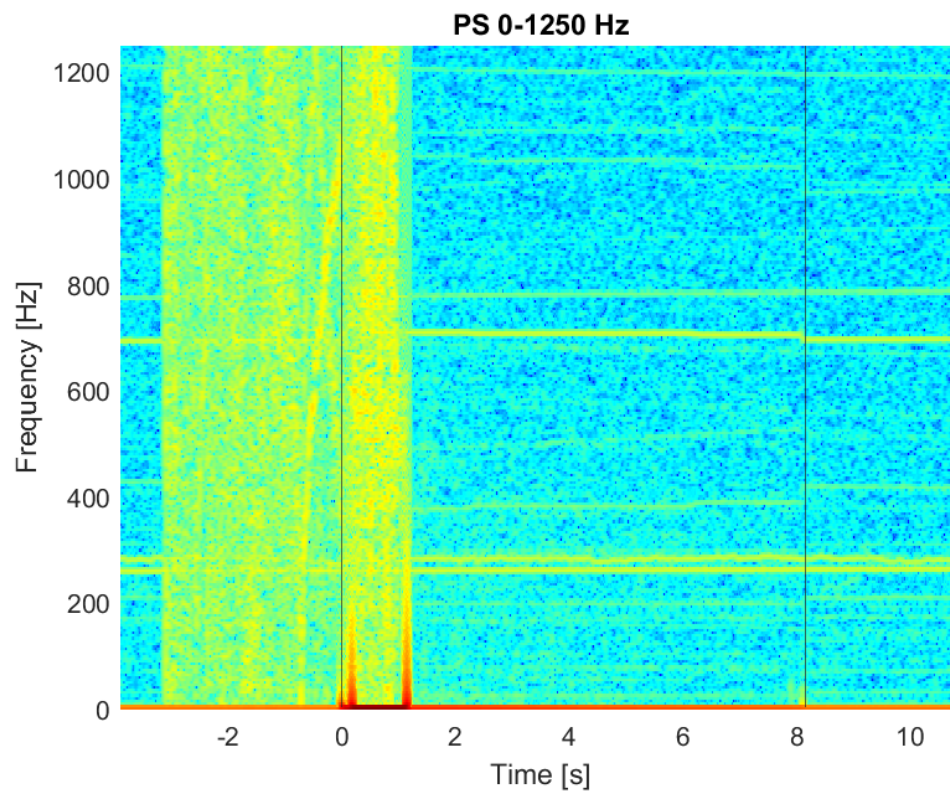


Figure D.15: Spectrogram of chamber pressure recording of test 6

D.3. Compilation of all test data

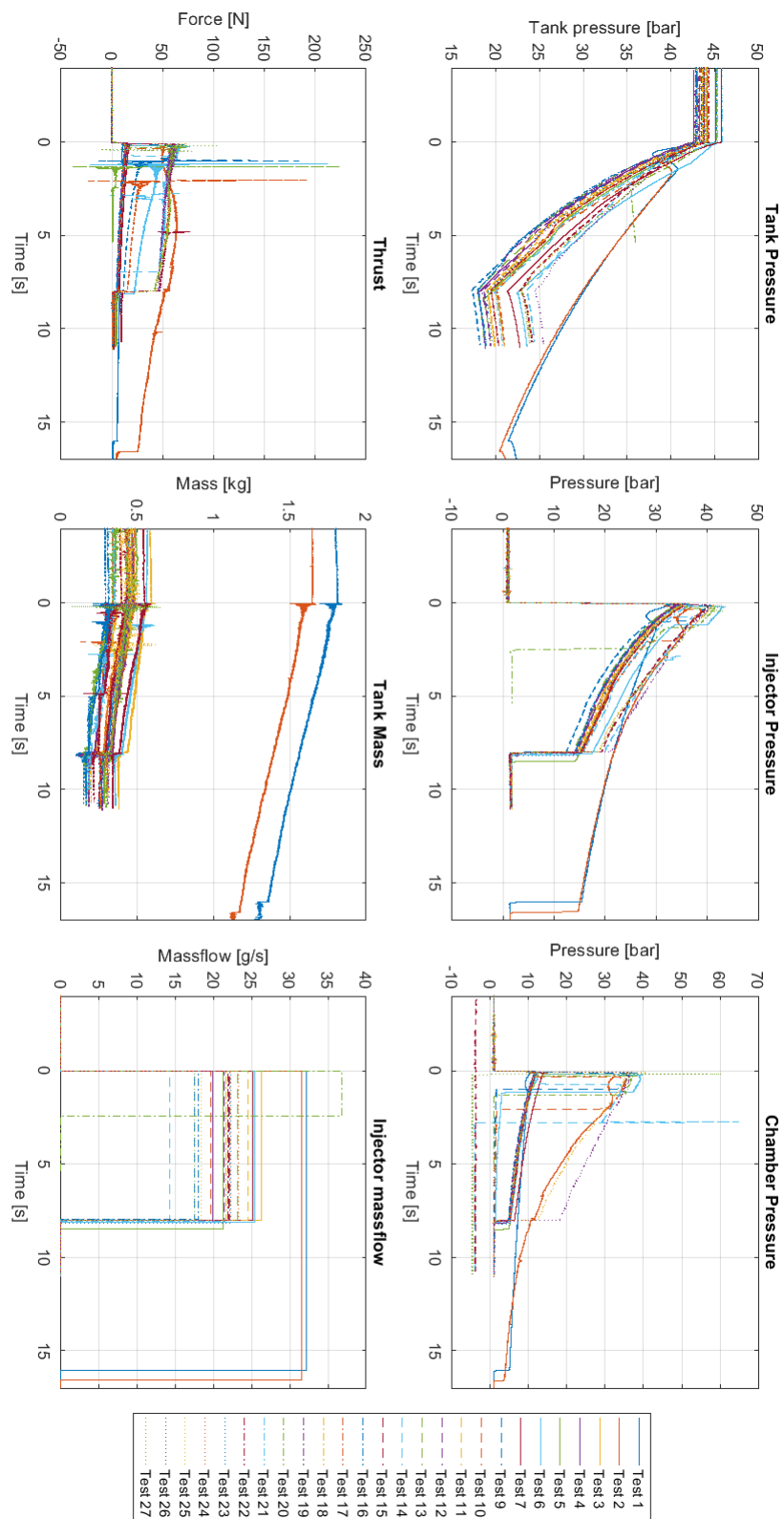


Figure D.16: Performance comparison of all flows

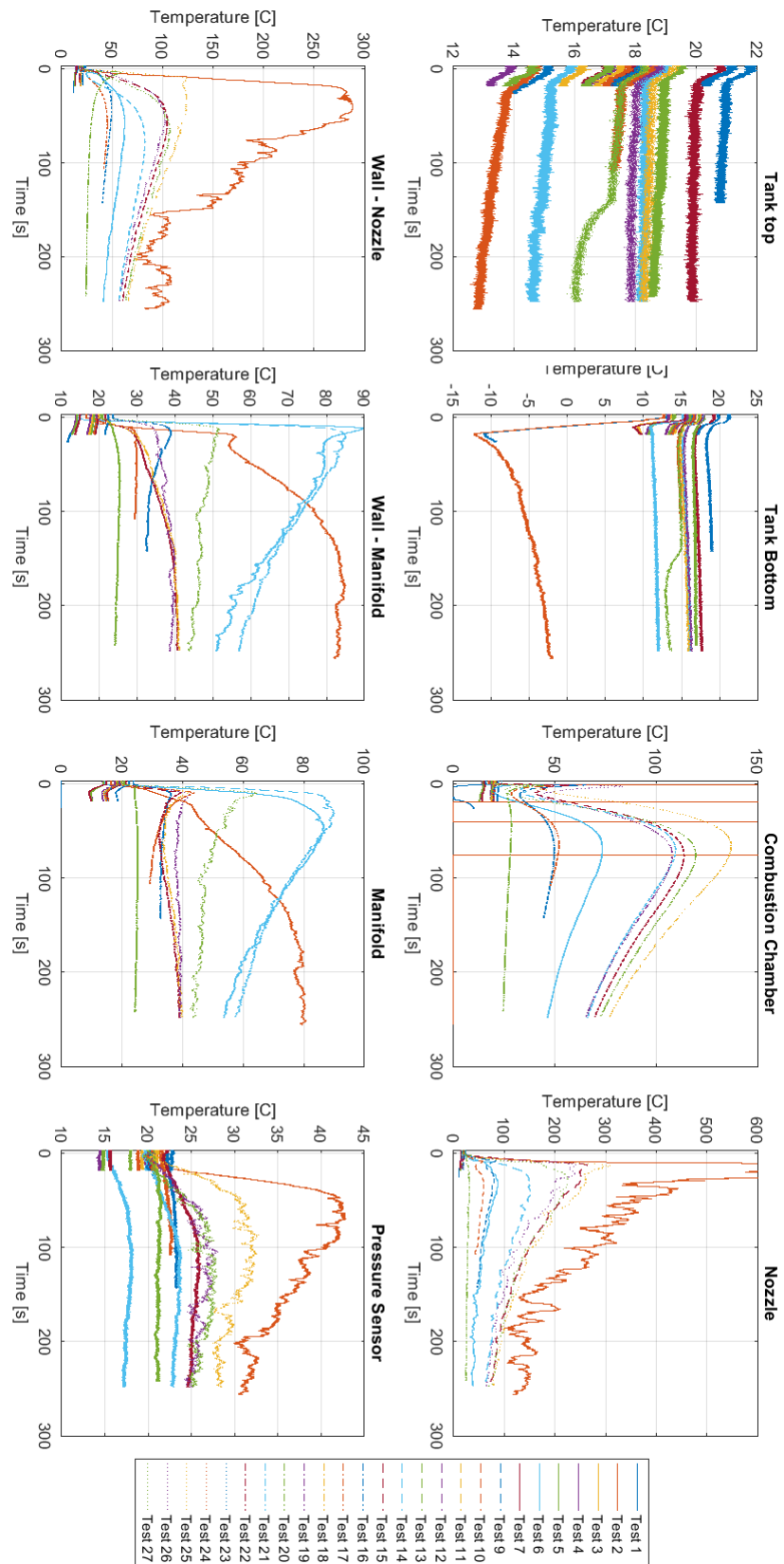


Figure D.17: Temperature comparison of all flows